SCHRIFTEN DES INSTITUTS FÜR MIKROSTRUKTURTECHNIK
AM KARLSRUHER INSTITUT FÜR TECHNOLOGIE (KIT)

Band 46

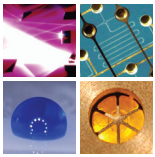

SIMON TERNES

In Situ Characterization and Modelling of Drying Dynamics for Scalable Printing of Hybrid Perovskite Photovoltaics

KIT Scientific Publishing

Simon Ternes

In Situ Characterization and Modelling of Drying Dynamics for Scalable Printing of Hybrid Perovskite Photovoltaics

Schriften des Instituts für Mikrostrukturtechnik
am Karlsruher Institut für Technologie (KIT)
Band 46

Hrsg. Institut für Mikrostrukturtechnik

Eine Übersicht aller bisher in dieser Schriftenreihe
erschienenen Bände finden Sie am Ende des Buchs.

In Situ Characterization and Modelling of Drying Dynamics for Scalable Printing of Hybrid Perovskite Photovoltaics

by
Simon Ternes

KIT Scientific Publishing

Karlsruher Institut für Technologie
Institut für Mikrostrukturtechnik

In Situ Characterization and Modelling of Drying Dynamics
for Scalable Printing of Hybrid Perovskite Photovoltaics

Zur Erlangung des akademischen Grades eines Doktors der Ingenieurwissenschaften von der KIT-Fakultät für Elektrotechnik und Informationstechnik des Karlsruher Instituts für Technologie (KIT) genehmigte Dissertation

von Simon Ternes, M.Sc.

Tag der mündlichen Prüfung: 4. Juli 2022
Hauptreferent: Tenure-Track-Professor Dr. Ulrich W. Paetzold
Korreferent: Prof. Dr. Wilhelm Schabel

Impressum

KIT Scientific Publishing

Karlsruher Institut für Technologie (KIT)
KIT Scientific Publishing
Straße am Forum 2
D-76131 Karlsruhe

KIT Scientific Publishing is a registered trademark
of Karlsruhe Institute of Technology.
Reprint using the book cover is not allowed.

www.ksp.kit.edu

Print on Demand 2023 – Gedruckt auf FSC-zertifiziertem Papier

ISSN 1869-5183
ISBN 978-3-7315-1255-4
DOI 10.5445/KSP/1000152603

Abstract

Hybrid perovskites are a promising material class for next-generation photovoltaic (PV) modules. Due to the exceptional optoelectronic properties of polycrystalline perovksite thin-films and the possibility of solution-processing these films, significant progress has been achieved since the emergence of perovskite PV in 2005. At the release date of this work, champion power conversion efficiencies (PCEs) surpass 25% in perovksite solar cells and 20% in (small-scale) perovskite PV modules. Furthermore, by tuning the bandgap of hybrid perovskites as a function of their chemical composition, wide-bandgap perovskite devices combined with silicon in a so-called tandem configuration exceeding a PCE of 30% could be demonstrated. However, for the successful commercialization of the technology, several challenges must still be addressed. The stability of perovskite devices needs to be increased to the industry standard of 30 years of operation, the PCEs of perovskite-incorporating tandem devices need to surpass around 33% to justify the additional architectural complexity with the associated costs and the device areas need to be scaled up to market-relevant sizes of square metres. The focus of this work lies on the last challenge – in particular on the transfer of perovskite solution processes from spin coating to linear deposition techniques like blade coating. In a second priority, this work covers the replacement of potentially toxic solvents with green alternatives that are of minor concern for workers and the environment.

The specific methodology used in this work is the fundamental analysis of drying dynamics by extensive *in situ* characterization, on the one side, and modelling of the involved dynamics backed by precise measurements of heat and mass transfer, on the other side. First, the drying dynamics of two typical perovskite precursor solutions are compared – methylammonium lead iodide (MAPI) dissolved in N,N-dimethylformamide (DMF) as well as caesium, formamidinium and methylammonium lead iodide bromide, called triple cation perovskite (TCP), dissolved in a mixture of DMF and dimethylsulfoxide (DMSO). The drying dynamics as measured by *in situ* interferometry in a

laminar air flow channel are in accordance with a simple, analytical drying model – assuming the dynamics are fully controlled by convection in the gas phase and concentration gradients within the solution film can be neglected. Numerical simulation shows a convergence with the analytical model if the analogous mass transfer Biot number remains smaller than 10^3, which is satisfied in all presented experiments – under the assumption that the drying process is effectively controlled by the diffusion coefficient of the remaining solution when the crystal phase precipitates. However, in the case of the TCP precursor, the assumption of an additional drying regime with a significantly reduced solvent activity is necessary ($\gamma_{DMSO} = 0.05$), which is attributed to the formation of an intermediate solute-solvent phase. Second, in accordance with a qualitative investigation of LaMer's model for crystal growth and nucleation, a criterion for processing homogeneous polycrystalline perovskite thin-films with high surface coverage is identified: A threshold of mass/heat transfer coefficients must be exceeded exactly at the critical concentration for nucleation. This threshold differs significantly for MAPI and TCP, which is due to the reduced solvent activity in the TCP solution film before the onset of the crystallization ($\alpha > 500\,\mathrm{W\,m^{-2}K^{-1}}$ for TCP and $\alpha > 25\,\mathrm{W\,m^{-2}K^{-1}}$ for MAPI). For the determination of these thresholds, the laminar air flow with well-defined heat and mass transfer is compared to a focussed slot-jet of high-pressure gas. The local heat transfer coefficient of the slot-jet is measured accurately by recording a thermochromic liquid crystal coating with a commercial camera and fitting the resulting data to empirical correlations of the Nusselt number for a variety of different jet parameters. With the above-described criterion at hand, not only blade coated MAPI perovskite solar cells with the same PCE as spin coated devices (PCE>15%) can be fabricated in the laminar air flow by choosing a sufficiently high air flow velocity. With the same concept, the coating windows of MAPI and TCP films that are dynamically moved under the narrow slot-jet are determined, enabling the processing of decently efficient perovskite solar cells (PCE>15%). Consistently, an extensive coating test with varying web speed and air velocity confirms that the coating windows predicted by the model are indeed in correlation with the morphology of experimentally fabricated perovskite thin-films as characterized by large-area Whitelight Interferometry.

To advance the capabilities of *in situ* characterization, the newly designed *In situ* Multichannel Imaging technique is described in this work. The technique combines the advantage of imaging large areas quickly and obtaining not only reflectance but also photoluminescence intensity and emission wave-

length images quasi-simultaneously. Using this novel technique, defects in the evolving thin-film morphology can be localized and classified quickly. The classification is achieved by comparing the different imaging channels of the technique. Furthermore, the evolution of the optical properties of perovskite solution films during drying and crystallization can be measured. We demonstrate that the so-recorded transients for MAPI solution films are not only in accordance with state-of-the art literature knowledge but also enable the distinction between favourable and detrimental thin-film morphologies as produced by different processing parameters.

Besides the analysis of drying dynamics in the laminar air flow and a slot jet of high-pressure gas, this work covers a possible up-scaling of anti-solvent immersion – a process called 'anti-solvent quenching' – with commercial airbrush guns. Furthermore, the difference between the one-step deposition process – where the perovskite is deposited from a solution containing all components – and the two-step process – where a layer of lead iodide is deposited independently, which is subsequently immersed with a solution of the (organic) cations in Isopropanol – is discussed. While the one-step process is performed with the conventional solvent mixture – DMF and DMSO – and a green solvent mixture – DMSO and Ethylene Glycol Monobutyl Ether (EGBE), the two-step process is directly transferred to blade coating using solely the latter green solvent mixture. In a final analysis, all processing and respective quenching methods are compared. It is shown that the anti-solvent process, despite occasionally yielding performant devices, is problematic to control both in terms of reproducibility and scalability. Additionally, the introduction of green solvents to this process leads to a PCE offset that cannot be corrected by extensive optimization. In the two-step process, devices where the first layer is blade coated and the second layer is spin coated do not fall significantly behind fully spin coated devices in terms of PCE. However, a decrease in PCE and reproducibility is still noticeable when the second step is performed by blade coating, as well. The process of one-step deposition combined with dynamic slot-jet drying, supported by the modelling concepts mentioned above, is most promising for industrial fabrication. The reasons are that the complexity of the drying setup is manageable, that the process can be exactly predicted from the provided models and that the results show a high reproducibility (however still without the use of green solvents). To achieve good results, a fine-tuning of the web speed and the gas output velocity is needed, which is fully determined by the drying models. In summary, the comparison of different processing methods demonstrates the fundamental

advantages of dynamic drying combined with a narrow slot dryer. In addition, the *in situ* characterization techniques and the modelling concepts could be used in future works to optimize the perovskite deposition early-on in the fabrication process – possibly using automated optimization systems – in order to maintain a good quality of perovskite PV on large areas. On top of that, the design of drying and coating machines without the need for extensive testing campaigns becomes possible.

Zusammenfassung

Hybride Perowskite sind eine vielversprechende Materialklasse für die nächste Generation von Photovoltaikmodulen. Aufgrund der außergewöhnlich guten optoelektronischen Eigenschaften von polykristallinen Perowskitdünnschichten und der Möglichkeit diese Schichten nass abzuscheiden konnten große Fortschritte seit dem Beginn der Entwicklung von Perowskitphotovoltaik im Jahre 2005 erzielt werden. Zur Zeit der Fertigstellung dieser Arbeit erreichen Perowskitsolarzellen bereits Wirkungsgrade über 25% und (Mini-)Perowskitmodule erreichen Wirkungsgrade über 20%. Darüber hinaus können aufgrund der Durchstimmbarkeit der Bandlücke als Funktion der chemischen Zusammensetzung des Perowskits Solarzellen mit breitem Bandabstand gefertigt werden, die mit Silizium kombiniert Wirkungsgrade über 30% in der sogenannten Tandem-Konfiguration erreichen. Dennoch gibt es noch einige Herausforderungen, die gemeistert werden müssen, um die neue Technologie erfolgreich zu kommerzialisieren. Die Stabilität von Perowskitphotovoltaik muss verbessert werden, sodass die industrieüblichen 30 Jahre Betriebszeit möglich werden, der Wirkungsgrad von Perowskit-enthaltenden Tandemsolarzellen muss etwa 33% betragen, um die zusätzliche Komplexität der Architektur und die damit verbundenen Kosten zu rechtfertigen und die aktive Fläche der Module muss auf marktrelevante Größen von Quadratmetern hochskaliert werden. Diese Arbeit behandelt hauptsächlich die letztgenannte Herausforderung, das heißt insbesondere den Prozesstransfer von der Rotationsbeschichtung („spin coating“) zu linearen Beschichtungstechniken wie dem Rakelverfahren („blade coating“). In zweiter Priorität handelt diese Arbeit von dem Ersatz potentiell toxischer Lösemittel durch grüne Alternativen, die nahezu unbedenklich für den Menschen und die Umwelt sind.

Die spezifische Methodik dieser Arbeit ist die grundlegende Analyse von Trocknungsprozessen durch umfassende *In-Situ*-Charakterisierung auf der einen Seite und die Modellierung der zugehörigen Dynamik gestützt durch präzise Messung des Stoff/Wärmetransportes auf der anderen Seite. Zunächst

wird die Trocknungsdynamik von zwei typischen Perowskit-Ausgangslösungen verglichen – Methylammonium-Bleiiodid (MAPI) gelöst in N,N-Dimethylformamid (DMF) sowie Cäsium-, Formamidinium- und Methylammonium-Bleiiodid-bromid, das sogenannte Dreifachkationenperowskit (TCP), gelöst in DMF und Dimethylsulfoxid (DMSO). Die Trocknungsdynamiken, gemessen durch *in-situ* Interferometrie in einem laminaren Strömungskanal, stimmen mit den Vorhersagen eines einfachen, analytischen Trocknungsmodells überein, das auf den Annahmen basiert, die Trocknung sei vollständig kontrolliert durch den Stofftransport in der Gasphase und Konzentrationsgradienten in der Lösung seien vernachlässigbar. Eine numerische Simulation konvergiert mit den analytischen Gleichungen, sofern die analoge Biot-Zahl für Stofftransport kleiner 10^3 bleibt, was in allen hierin beschriebenen Experimenten erfüllt ist – unter der Annahme, dass beim Ausfällen der Kristallphase die verbleibende Trocknung durch den Diffusionskoeffizienten der verbleibenden Lösung bestimmt wird. Im Falle der TCP-Lösung ist jedoch die Hypothese eines zusätzlichen Trocknungsbereiches mit deutlich reduzierter Lösemittelaktivität notwendig ($\gamma_{\mathrm{DMSO}} = 0{,}05$), was mit der Bildung einer Zwischenphase aus Lösemittel- und Perowskitkomponenten erklärt werden kann. Als nächster Schritt wird aus einer qualitativen Betrachtung des LaMer-Modells für Kristallwachstum und -nukleation ein Kriterium für die Herstellung homogener, polykristalliner Perowskitdünnschichten mit hoher Flächenabdeckung hergeleitet. Das Kriterium besagt, dass ein bestimmter Schwellwert des Wärme/Stofftransportkoeffizienten genau dann überschritten werden muss, wenn die Lösung die kritische Konzentration für die Nukleation der Kristalle erreicht. Dieser Schwellwert unterscheidet sich für MAPI und TCP signifikant, was durch die reduzierte Lösemittelaktivität im TCP Lösemittelfilm vor dem Einsetzen der Kristallisation zustande kommt ($\alpha > 500\,\mathrm{W\,m^{-2}K^{-1}}$ für TCP und $\alpha > 25\,\mathrm{W\,m^{-2}K^{-1}}$ für MAPI). Zur Bestimmung dieser Schwellwerte wird eine Laminarströmung mit wohl definiertem Stoff- und Wärmeübertrag verglichen mit einer Strömung von Druckluft durch einen schmalen Schlitz, deren lokaler Wärmeübertragskoeffizient durch die Aufnahme einer thermochromen Kristallschicht mit einer handelsüblichen Kamera und Fitten der resultierenden Daten an empirische Korrelationen der Nußeltzahl für eine Vielzahl an Düsenparametern bestimmt wird. Mithilfe des oben genannten Kriteriums können nicht nur gerakelte MAPI Solarzellen im laminaren Luftstrom durch eine angemessene Strömungsgeschwindigkeit hergestellt werden, deren Wirkungsgrad denen von rotationsbeschichteten Zellen entspricht (>15%). Mit dem gleichen Modell können die Prozessfenster für MAPI und TCP Filme bestimmt werden, die dynamisch unter den Hochdruck-Schlitztrockner fahren,

sodass die Herstellung von Solarzellen mit respektablem Wirkungsgrad (>15%) möglich wird. Eine umfangreicher Beschichtungstest mit variierender Band- und Luftgeschwindigkeit bestätigt in konsistenter Weise, dass die durch das Modell vorhergesagten Porzessfenster mit den mit Weißlichtinterferometrie vermessenen Morphologien experimentell gefertigter Perowskitdünnschichten korrelieren.

Um den Umfang der *In-Situ*-Charakterisierung zu erweitern, wird zusätzlich die neu entwickelte *In-Situ*-Multikanal Bildgebung (IMI) in dieser Arbeit beschrieben. Diese Messtechnik kombiniert die Vorteile von schneller Bildgebung auf großen Flächen mit der Fähigkeit, nahezu gleichzeitig reflektive Bilder und Bilder der Photolumineszenzintensität und -emissionswellenlänge aufzunehmen. Durch Verwendung dieser innovativen Messtechnik können Defektstellen in der Dünnschichtmorphologie schnell lokalisiert und klassifiziert werden. Hierbei wird die Klassifizierung durch den Vergleich der unterschiedlichen Bildkanäle durchgeführt. Darüber hinaus kann IMI zur Aufnahme und Analyse von Transienten der optischen Eigenschaften der trocknenden und kristallisierenden Dünnschichten eingesetzt werden. Beim Trocknen von MAPI Dünnschichten zeigt sich, dass diese Transienten nicht nur den Vorhersagen aktueller Forschung entsprechen, sondern auch die Unterscheidung vorteilhafter und unvorteilhafter Dünnschichtmorphologien ermöglichen, die infolge unterschiedlicher Prozessparameter entstehen.

Neben der Analyse der Trocknungsdynamiken von Perowskitlösungsschichten in Laminar- und Schlitzströmung, enthält diese Arbeit die Beschreibung möglicher Hochskalierungskonzepte mit Anti-Lösemittel Exposition – ein Prozess, der in der Literatur als „Anti-Solvent Quenching“ bekannt ist – durch handelsübliche Air-Brush Pistolen. Zusätzlich wird der Unterschied zwischen dem Einschritt-Prozess, in dem das Perowskit von einer alle Komponenten enthaltenden Lösung abgeschieden wird, und dem Zweischritt-Prozess erläutert, in dem zunächst eine Schicht von Bleiiodid aufgetragen wird, die anschließend der (organischen) Kationen-Lösung (basierend auf Isopropanol) ausgesetzt wird. Während der Einschritt-Prozess sowohl mit der konventionellen Lösemittelformulierung aus DMF und DMSO als auch mit grünen Lösemitteln, einer Mischung aus DMSO und Ethylenglycolmonobutylether (EGBE), durchgeführt wird, erfolgt der Zweischrittprozess ausschließlich mit den oben genannten grünen Lösemitteln direkt beim Transfer zum Rakelverfahren. In einer Analyse am Ende der Arbeit werden schließlich alle oben aufgeführten Prozesse basierend auf den jeweiligen Quenching-Methoden verglichen. Es stellt sich heraus, dass der Anti-Lösemittelprozess trotz ver-

einzelter Erfolge bei der Herstellung effizienter Solarzellen in Hinsicht der Reproduzierbarkeit und der Skalierbarkeit Mängel aufweist. Darüber hinaus führt der Einsatz grüner Lösemittel beim Anti-Lösemittelprozess zu einem signifikanten Einbruch des Wirkungsgrades, der auch durch langwierige Optimierung nicht ausgeglichen werden kann. Im Vergleich hierzu fällt der Wirkungsgrad von Solarzellen, deren Absorber durch Rakeln der ersten Schicht und darauffolgende Rotationsbeschichtung der Kationenlösung hergestellt wurden, kaum hinter komplett rotationsbeschichteten Zellen zurück. Bisher sind die Verluste des Wirkungsgrades und der Reproduzierbarkeit jedoch noch höher, wenn die zweite Schicht ebenfalls durch Rakelbeschichtung appliziert wird. Allen voran ist der Einschritt-Prozess basierend auf der dynamischen Trocknung mit der Schlitzströmung, gestützt durch die vorher beschriebene Modellierung, die vielversprechendste Variante für die zukünftige industrielle Fertigung. Die Gründe hierfür sind die beschränkte Komplexität der nötigen Fertigungsstrecke, die Vorhersehbarkeit der Ergebnisse durch die beschriebenen Modelle und die gleichzeitige hohe Reproduzierbarkeit der Ergebnisse (jedoch bisher ohne den Einsatz grüner Lösemittel). Um mit diesem Prozess gute Resultate zu erzielen, ist das Fine-Tuning der Bandgeschwindigkeit zur Gasgeschwindigkeit von großer Bedeutung, was durch die Trocknungsmodelle vollständig vorhergesagt wird. Zusammenfassend lässt sich also sagen, dass der Vergleich verschiedener Prozessierungsmethoden in dieser Arbeit die grundsätzlichen Vorteile der dynamischen Trocknung durch einen schmalen Schlitztrockner demonstriert. Darüber hinaus können die *In-Situ*-Charakterisierungsmethoden sowie Modellierungskonzepte dieser Arbeit in Zukunft dafür verwendet werden, die Perowskitabscheidung zu einem frühen Zeitpunkt im Herstellungsprozess zu optimieren – möglicherweise unter Verwendung automatisierter Optimierungstechnik – und somit eine hohe Qualität der Perowskitphotovoltaik auf großen Flächen sicherzustellen. Zusätzlich wird die Auslegung großer Beschichtungs- und Trocknungsmaschinen mit den bereitgestellten Modellen ohne große Pilot-Kampagnen möglich.

Contents

Part I.

Introduction

1. Motivation

Climate change is one of the greatest challenges of the 21st century [1]. The reason is that the global average temperature, determining the total amount of thermal energy in our atmosphere, impacts nearly all spheres of human, animal and plant life[2]. It is a consensus within the meteorological research community that the increase of the global average temperature as compared to pre-industrial times is human-induced and originates from the emission of green-house gases, among which carbon dioxide (CO_2) as produced by the combustion of fossil fuels is the biggest contributor[3]. The Intergovernmental Panel on Climate Change (IPCC) recently released the second part of its Sixth Assessment Report covering Impacts, Adaptation and Vulnerability related to climate change[4]. It highlights the interdependence of the global average temperature and the associated risks for life on our planet, listing five major Reasons For Concern (RFC):

- **RFC1:** Dangers for unique and threatened systems (human or ecological) that are geographically constrained by climate-related conditions (for example coral reefs, the arctic, glaciers etcetera)
- **RFC2:** Extreme weather events that pose high risks to human heath, livelihoods and biodiversity hotspots (for example heatwaves, heavy rain, droughts and wildfires, flooding)
- **RFC3:** Distribution of impacts – risks that affect particular groups due to their exposure or vulnerability (for example populations of islands or deserts)
- **RFC4:** Global aggregate impacts, that is global socio-ecological impacts (for example monetary damage, species lost, lives affected, etcetera)
- **RFC5:** Large-scale singular events that happen abruptly and are sometimes irreversible (for example ice sheet disintegration or thermohaline circulation slowing)

According to the IPCC report, RFC1 and RFC2 are already observable due to the global warming that started with the industrial revolution until the present day. In contrast, the impact of RFC3-RFC5 is still moderate to undetectable. However, this will definitely change within the next ten years – potentially threatening entire biospheres and civilizations. The likelihood of these risks depends directly on the relative global temperature rise as compared to pre-industrial standards. Therefore, the IPCC defined the 1.5°C-goal as a desirable scenario in which the worst risks could be mitigated and, most importantly, the process of further global warming could be limited [5].

In order to predict possible scenarios of the future evolution of the global average temperature, complex climate models are applied taking into account the green house gas emissions as a result of human behaviour (see Figure 1.1).

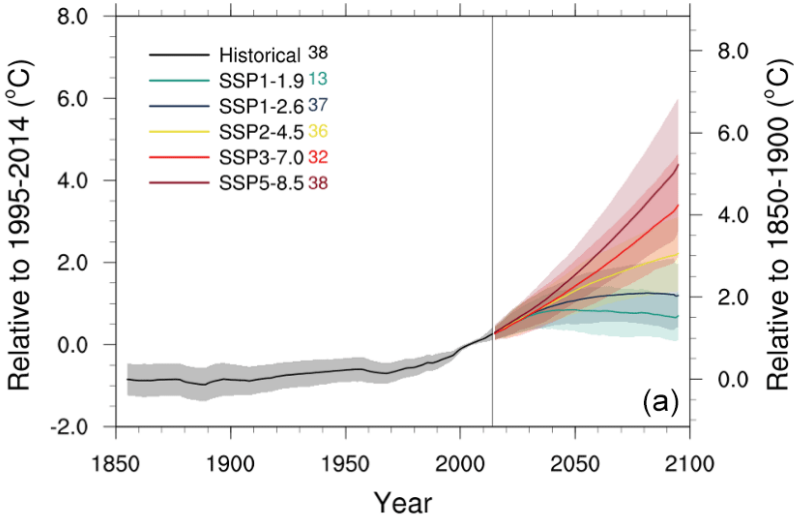

Figure 1.1.: Global average temperature time series (11-year running average) as measured historically (black line) and predicted from climate models (coloured lines) starting from the present until the year 2100 for different socio-economic pathways (SSP1-SSP5). Thick lines are the mean values and the shaded area represents the $\pm 1.64\sigma$ interval generated from an ensemble of different computations. (reproduced with permission from Tebaldi *et al.* [6]: Figure 1a licensed under CC BY 4.0 [7])

The predicted temperature evolution depends on the so-called shared socio-economic Pathway (SSP) scenarios which are a complex prediction of human society in terms of global population, global Gross Domestic Product (GDP), land use, energy production and consumption as well as the resulting emitted greenhouse gases which cause the increase in global surface temperature[8]. Consistently, as shown in Figure 1.1, the predicted global average temperature strongly depends on the kind of SSP scenario. Here, we will shortly summarize the main assumptions for the first three of these[9]:

- **SSP1 sustainability – taking the green road**
  The economy decouples partially from material and energy resources. Social acceptance of renewable energy production is high and renewable technologies develop faster than conventional ones.
- **SSP2 middle-of-the-road**
  Global energy demand will continue to grow with the same rate as today. The social acceptance of technologies and energy sources does not change significantly and the transformation of the energy production continues.
- **SSP3 rivalry – a rocky road**
  There is a fast increase in human population, but economic progress and environmental awareness stagnates for large parts of this population. Energy production is only slowly modernized and domestic coal and biomass is preferred to global energy trade.

Figure 1.2 shows the assumptions for the development of the global energy production that were made in the scenarios SSP1, SSP2 and SSP3 (technically, each SSP scenario has a subcategory designated by the assumed maximum radiative forcing $\left[\mathrm{W\,m^{-2}}\right]$ in the atmosphere as induced by differences in the assumed technological development. Here, we selected SSP1-2.6, SSP2-4.5 and the SSP3 baseline as plausible scenarios, while others can be found in [9]. The baseline assumes no use of carbon capture and storage nor novel nuclear technologies.). We find that one of the major differences between scenarios SSP1, SSP2 and SSP3 is the growth of the renewable energy sector (other technologies such as carbon capture and storage, nuclear energy concepts and the total energy consumption also play a vital role.). Renewable energies have the advantage of (close-to) zero net emission of additional greenhouse gases. A very promising renewable energy source is solar power, and in particular photovoltaics (PV), taking a large share of the energy production in the scenarios SSP1 and SSP2. The International Energy Agency (IEA) predicts

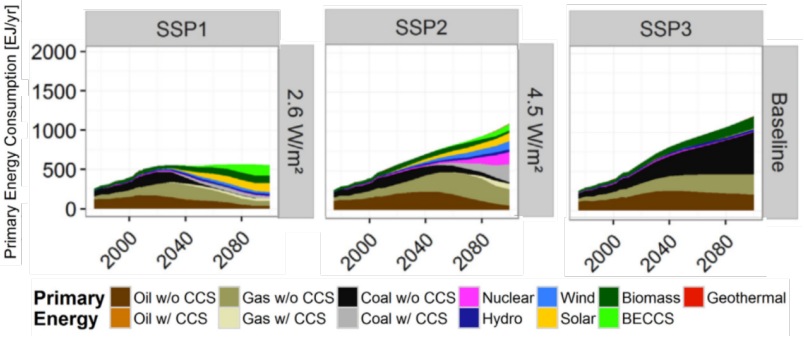

Figure 1.2.: Assumptions for the partition and development of global primary energy use until the year 2100 in the shared socio-economic pathways SSP1-2.6 and SSP2-4.5 and SSP3-Baseline in comparison[10]. The second number indicates the assumed radiative forcing in $\left[\mathrm{W\,m^{-2}}\right]$ in the atmosphere and depends on the technological innovation. While in the $2.6\,\mathrm{W\,m^{-2}}$ case, bioenergy with carbon capture and storage (BECCS) is assumed to show a strong increase, in the $4.5\,\mathrm{W\,m^{-2}}$ case, novel nuclear energy concepts as well as coal with carbon capture and storage (w/ CCS) are assumed to play a major role in future energy production. In the baseline case, neither of these novel technologies is assumed to have an impact in the future and today's technologies are assumed to prevail. (reproduced with permission from Bauer *et al.* [9]: Figure 5a used under CC BY 4.0 [7], cropped in extracts and rearranged)

that the global renewable energy capacity will rise by 2026 to over 4.8 TW (which is over 60% of 2020's global electricity generation capacity) with PV providing more than half of this capacity[11]. It has to be noted that IEA prognoses on renewable energy growth are commonly very conservative[12]. Indeed, considering that the global cumulative PV capacity has most likely surpassed 1 TW recently and that the newly installed PV capacity in 2022 will probably exceed 200 GW, the IEA prognosis on PV growth appears realistic[13]. A key figure for PV is the total price per watt of generated power, that is its 'levelized cost of electricity' (LCOE) measured over the whole operation lifetime including costs for installation, operation and maintenance, land use, electronics and scrubbing as well as an estimate of the annual discount rate of the investment. The development of the LCOE influences, in relation to the prices of other energy sources, how fast global PV capacity will grow in the future[14] (in addition to the decisions of policy makers and the development of electric grid as well as energy storage technologies needed to manage decentralized and volatile energy production[15]). The reason is that

a technological transition on global scales most likely requires the combined effort of green policies (CO_2 prices, subsidies, investments,...) and economic incentives such as a promised return of investment for PV systems matching (at least) the global economic growth. In state-of-the-art PV systems, the so-called 'balance of system costs' (price of inverting electronics, batteries, mounting, etcetera) already surpass the module prices themselves[16]. Therefore, further lowering of the LCOE of PV is most-effectively achieved by increasing the power conversion efficiency (PCE) – or more precisely the energy yield[17]) – of commercially available PV modules instead of further reducing their fabrication costs. For this reason, the development of novel PV technologies is of utmost importance. In particular, technologies beyond the market-dominating mono-crystalline silicon PV will become increasingly important in the future. The reason is that mono-crystalline silicon PV is predicted to reach is physical efficiency limit around 2030 [16]. The hybrid perovskite PV covered in this work could provide a contribution to a next generation of commercial PV modules overcoming these limitations (as will be detailed later).

In conclusion, it is crucial to make global efforts to maintain the global surface warming – in the ideal case staying in the scenario SSP1 (that is SSP1-1.9 or SSP1-2.6). In this way, a maximum global temperature increase of 1.5°C – 2°C as compared to pre-industrial times could be maintained, instead of an uncontrolled heating with devastating impacts on all species of life according to the scenario SSP3-7.0. A decisive factor for the likelihood of the different scenarios are the methods of primary energy production. The rate of innovation of PV as compared to other technologies could be a key indicator for a achieving the 1.5°C-goal – in particular in situations where regulative measures are insufficient and the cost-effectiveness of technologies is the decisive factor. Hybrid perovskite PV is a very promising candidate for a new generation of PV modules, surpassing the physical efficiency limitations of mono-crystalline PV (if combined with another semiconductor as detailed below).

2. Structure, grammar, and contributions

In order to increase readability and outline the general connection of the covered topics, the sections of this work are structured in a logical rather than a chronological succession. That is to say that the content is not ordered by the release date of the main publications (which is a very common convention in cumulative PhD theses), but by the logical connections of different aspects contained in these publications. To still provide the reader with the ability to quickly recognize if a certain section reviews one or multiple previous publications, footnotes with the symbols ★, †, ‡ are added to the respective section headlines (these footnotes are just for convenience, proper reference is provided independently at each statement where it is necessary). Following this convention, sections that are uniquely appearing in this thesis (covering literature knowledge, background information or so-far unpublished results) are not marked with a respective footnote.

The concrete structure is the following. After this introduction, the second part *'Fundamentals and Methods'*, covers all necessary background knowledge from literature on the topic of hybrid perovskites and thin film solar cells as well as the set of standard experimental methods that were used in the fabrication and characterization of perovskite solar cells. The third part *'Results and Discussion'* covers three main sections of results that were achieved during the work in this thesis. First, a gas phase controlled drying model is introduced and adapted to perovskite precursors, deriving novel analytical equations. The so-obtained quantitative predictions of drying dynamics are compared to interferometric measurements recorded in a well-defined laminar air flow environment. In a similar way, state-of-the-art crystallization models are applied to perovskite thin-films resulting in a qualitative simulation of the polycrystalline morphology evolution that is correlated with experimentally fabricated thin-film morphologies. In succession, the development of extended characterization techniques for the scaling of drying and

crystallization processes is discussed. A special emphasis is put on the newly developed *In situ* Multichannel Imaging, which is designed to assess the perovskite thin-films in real-time and on large areas early on in the formation of the material. In the next chapter, we list all investigated perovskite processing methods ordered according to the method used for drying/quenching the precursor (that is laminar air flow, anti-solvent or slot-jet) and, in subordinate hierarchy, according to the type of the original process and precursor (one step methylammonium lead iodide, one step triple cation, two step double cation). Each of these sections is written in the mindset of, first, showing the effect of the optimization of process parameters on the thin-film morphology as well as device performances and, second, determining how these empirical findings can be explained by the earlier derived knowledge about the drying and crystallization dynamics of the respective precursor. In this context, special emphasis is put on the formulation of a coating window, that is a parameter space in which industrial coating can be performed in the future. Finally, all investigated processes are compared in terms of device performances and their prospects and limitations for an industrial fabrication line (section 8.4).

Before we come to the contributions to the results described in this work, a short note on English grammar is necessary. In the whole manuscript, the pronoun *'we'* is used as the substantive performing actions and thought processes. This can, in some parts of this work, be interpreted as a tribute to the fact that most of the presented findings are a product of constructive team work between students, PhD candidates, principal investigators and the author, as detailed below. However, to maintain consistency in grammar, the pronoun *'we'* is also used in sections or statements that were conceived solely by the author himself. In these phrases, *'we'* is either used to designate the imaginary, didactic team of the reader and the author (*'We can write equation... as ...', 'Let us focus on... ', 'We can safely assume that...'* [synonym: *'you'*]) or it is simply a synonym of an imaginary group of people who would come to the same conclusion (*'We note that...', 'We usually set ...','We assume that...'*, [synonym: *'one'* or *'the author'*]). This deliberate choice of consistent grammar was preferred to the use of the rather narrative or autobiographic than scientific pronouns *'I'* and *'you'* as well as excessive use of the passive voice.

Let us now come to the contributions. Nowadays, significant progress of science and technology is nearly impossible without productive team work. It is therefore not only necessary but also a sign of the reliability and solidity of

scientific results to highlight the work of all those who contributed, reviewed and tested these hard earned results. To give proper credit to all these people, we will apply the 'CRediT' taxonomy for the main publications [18]. Other contributions are given by student theses that were supervised by the author, occasionally in cooperation with colleagues. These will be listed after the main publications. At this point, it must be stated that the formal authorship of this thesis as associated with the task of writing, editing, graphics design and structuring is solely attributed to the author and remains untouched by these contributions.

Firstly, 'Drying Dynamics of Solution-Processed Perovskite Thin-Film Photovoltaics: In Situ Characterization, Modeling, and Process Control' was published in Advanced Energy Materials in 2019 with the authors *Simon Ternes (S.T), Tobias Börnhorst (B.T.), Jonas A. Schwenzer (J.A.S), Ihteaz M. Hossain (I.M.H), Tobias Abzieher (T.A.), Waldemar Mehlmann (W.M.), Uli Lemmer (U.L.), Philip Scharfer (P.S.), Wilhelm Schabel (W.S.), Bryce S. Richards (B.S.R.), Ulrich W. Paetzold. (U.W.P)* [19]. In addition to the citation mark, sections containing content of this publication will be marked with a ⋆-symbol and a corresponding footnote, for convenience. It should to be noted that the work is succession of *Benjamin Schmidt-Hansberg's (B.S.H.)* work on organic photovoltaics to whom the authors are grateful, in particular. The 'CRediT' is given in the following table:

Term	**Authors**	**Details**
Concept	*S.T., T.B., P.S., W.S., B.S.R & U.W.P*	conceptualization of flow channel setup by *B.S.H.* under supervision of *W.S.* and *P.S.*, adjustment to hybrid perovskite deposition by S.T. and others
Methodology	*S.T., T.B., W.S., P.S. & U.W.P*	development of drying models and experimental procedures to test these.
Software	*S.T., P.S., W.S.*	LabView software for data acquisition by *B.S.H*, *P.S.* and *W.S.*, data analysis and processing by *S.T.*.

Term	Authors	Details
Validation	*S.T., T.A., T.B. & W.M.*	AFM/SEM top view measurements by S.T., SEM cross section measurements by T.A., Drying experiments and interpretation by S.T., T.B. and W.M.
Formal Analysis	*S.T.*	Evaluation of interferometric data, fitting of drying rates and/or drying models to data
Investigation	*S.T., J.A.S., I.M.H., B.S.R & U.W.P*	Development of solar cell stack, fabrication and testing.
Resources	*J.A.S., I.M.H.*	Supply with spin-coated reference cells, fabrication processes and materials
Data Curation	*S.T.*	Creating of 'database' of drying experiments
Writing—Draft	*S.T.*	-
Writing—Review	*T.B.,U.L., B.S.R, P.S. & U.W.P*	-
Visualization	*S.T., B.S.R & U.W.P*	Original plots by *S.T.*, revised by *B.S.R* and *U.W.P*
Supervision	*U.L.,P.S., W.S., B.S.R & U.W.P*	-
Project Administration	*U.L., P.S., W.S., B.S.R & U.W.P*	-
Funding Acquisition	*U.L., P.S., W.S., B.S.R & U.W.P*	-

Second, 'Correlative In Situ Multichannel Imaging for Large-Area Monitoring of Morphology Formation in Solution-Processed Perovskite Layers' was published in Solar RRL in 2021 with the authors *Simon Ternes (S.T.), Felix Laufer (F.L.), Philip Scharfer (P.S.), Wilhelm Schabel (W.S.), Bryce S. Richards*

(B.S.R.), Ian A. Howard (I.A.H.) and Ulrich W. Paetzold (U.W.P.) [20]. In addition to the citation mark, sections containing content of this publication will be marked with a †-symbol and a corresponding footnote, for convenience. It is important to note that *S.T.* and *F.L.* contributed equally to the work. The 'CRediT' is given in the following table:

Term	**Authors**	**Details**
Concept	*S.T.& I.A.H*	conceptualization of IMI setup
Methodology	*S.T., F.L., I.A.H. & U.W.P*	application of IMI on the drying channel at different drying parameters
Software	*S.T., F.L.*	camera operation, data post-processing
Validation	*S.T., F.L.*	comparison with spectral one-point probe PL setup by F.L., comparison with literature by S.T.
Formal Analysis	*S.T., F.L.*	Data evaluation and interpretation
Investigation	*S.T., F.L.*	Conducting of IMI experiments by F.L and S.T., chemical engineering of devices by S.T..
Resources	*I.A.H., P.S. & W.S.*	Supply with components for electronics, mounting and operation
Data Curation	*S.T., F.L.*	Creating of 'database' and detection of trends by F.L. and S.T. , defect analysis by S.T.
Writing—Draft	*S.T.*	-
Writing—Review	*F.L., B.S.R, I.A.H. & U.W.P*	-
Visualization	*S.T.,F.L., B.S.R, I.A.H. & U.W.P*	Original plots by *S.T. & F.L.*, revised by *B.S.R, I.A.H. & U.W.P*
Supervision	*P.S., W.S., B.S.R, I.A.H. & U.W.P*	-

Term	Authors	Details
Project Administration	*P.S., W.S., B.S.R, I.A.H. & U.W.P*	-
Funding Acquisition	*P.S., W.S., B.S.R, I.A.H. & U.W.P*	-

The last publication "Drying and Coating of Perovskite Thin-Films: How to Control the Thin-Film Morphology in Scalable Dynamic Coating Systems" was published in ACS Applied Materials & Interfaces in 2022 with the authors *Simon Ternes (S.T.), Jonas Mohacsi (J.M.), Nico Lüdtke (N.L.), Hoang Minh Pham (H.M.P), Meriç Arslan (M.A.), Philip Scharfer (P.S.), Wilhelm Schabel (W.S.), Bryce S. Richards (B.S.R.), Ulrich W. Paetzold (U.W.P.)* [21]. In addition to the citation mark, sections containing content of this publication will be marked with a ‡-symbol and a corresponding footnote, for convenience. The 'CRediT' is given in the following table:

Term	Authors	Details
Concept	*S.T.*	conceptualization of coating setup and modelling
Methodology	*S.T., J.M., N.L., H.M.P.*	operation of high-pressure slot-nozzle and dynamic coating by *S.T., N.L. & H.M.P.*, TLC measurements by *S.T. & J.M.*
Software	*S.T., J.M., N.L., M.A. & , H.M.P., P.S. & W.S.*	motor operation by *N.L., M.A. & H.M.P.*, TLC evaluation by *J.M., P.S. & W.S.*, data analysis and drying simulation by *S.T.*
Validation	*S.T., J.M., N.L., H.M.P. and M.A.*	experiments of static and dynamic gas quenching by *N.L., H.M.P& M.A.*, validation of heat transfer coefficients by *S.T., J.M.* and validation of drying models by *S.T.*

Term	Authors	Details
Formal Analysis	*S.T.*	Data evaluation, simulation of drying dynamics and interpretation
Investigation	*S.T., N.L., M.A. & , H.M.P.*	Investigation of perovskite morphology evolution under different mass transfer conditions
Resources	*S.T., J.M., P.S. & W.S.*	air nozzle and TLC setup by J.M., P.S. & W.S., integration and adjustments by S.T.
Data Curation	*S.T.*	Simulation and modelling
Writing—Draft	*S.T.*	-
Writing—Review	*J.M., B.S.R, & U.W.P*	-
Visualization	*S.T., B.S.R, & U.W.P*	Original plots by *S.T.* , revised by *B.S.R & U.W.P*
Supervision	*P.S., W.S., B.S.R, & U.W.P*	-
Project Administration	*P.S., W.S., B.S.R& U.W.P*	-
Funding Acquisition	*P.S., W.S., B.S.R & U.W.P*	-

Besides the main publications, this work reviews results of multiple Bachelor's and Master's theses, some of which were supervised with the help of the colleagues Tobias Börnhorst and Fabian Schackmar, which will be indicated accordingly. During the supervision of a student, the most common distribution of tasks is that the supervisors will conceptualize a methodology and goal, give suggestions for the respective, subsequent experiment and give concise guidelines how to interpret the data. The student conducts the experiments, evaluates the data with the given method and gives their opinion on possible issues and solutions. However, there are also cases where students develop unexpected ideas and perform self-designed experiments beyond the framework given by the supervisor, which can lead to unexpected

solutions of problems. These cases of excellent, independent research will be indicated in the list below. This work reviews (partially) content of the following theses:

- Bachelor's thesis of *Waldemar Mehlmann* on the topic "Optimization of the deposition and crystallization of a perovskite solution film in a flow channel." co-supervised with *Tobias Börnhorst*. This work contributed to the first drying experiments of MAPI in the laminar air flow channel as detailed in section 8.1.1.
- Bachelor's thesis of *Louis Kressibuch* on the topic "Optimization of the deposition and crystallization of a triple cation perovskite solution film in a flow channel" co-supervised with *Tobias Börnhorst*. This work contributed to the basis of the optimization of the anti-solvent spray quenching of one-step triple cation perovskite detailed in section 8.2.
- Master's thesis of *Virajini Palakonda* on "Green solvent Engineering of Triple Cation Solar Cells" continuing Mr. Kressibuch's work by solely using green solvents in the precursor.
- Master's thesis of *Kristina Geistert* with the topic "Investigation of solvent systems with non-hazardous volatile components for blade coating of homogenous lead iodide layers for perovskite solar cells." co-supervised together Fabian Schackmar. This work laid the basis for the section 8.1.2 detailing on the two-step green solvent deposition of PbI_2 in the laminar air flow. Remarkably, Ms. Geistert optimized the parameter space of surfactants, solvent concentrations and coating parameters very independently.
- Master's thesis of Vashu Kamboj continuing Ms. Geistert's work with the topic "Scalable sheet-to-sheet-coating of double cation perovskite solar cells based on green solvent systems." Her work was the basis for the process transfer of the second step, that is the deposition of the cations, by blade coating.
- Master's thesis of *Felix Laufer* on the topic "Large-area luminescence imaging of perovskite photovoltaics for in situ characterization" which laid the basis the IMI technique and the second publication (see † symbol for the chapters concerned by this). Mr. Laufer worked in an excellent independent way continuously pushing the capabilities of the system and the depth of image post-processing beyond the initial

expectations during his work time (he is therefore shared first author of the publication as detailed above).

- Bachelor's thesis of *Huang Minh Pham* on the topic "Design and Optimization of an air knife for the drying of a triple cation perovskite precursor film.". This work laid the basis for the (static) quenching of triple cation perovskite with a narrow jet of high-pressure air (section 8.3.). Remarkably, Mr. Pham overcame a fundamental problem of this method by his idea to use very narrow slot-widths very close to the drying thin-film.
- Bachelor's thesis of *Meriç Arslan* on the topic "Fabrication of Blade Coated Triple Cation Perovskite Solar Cells by Gas Quenching With a Slot-Die Nozzle" continuing the work of Mr. Pham to produce the first functional, dynamically quenched triple cation solar cells.
- Master's thesis of *Nico Lüdke* on the topic "Optimization of scalable slot-nozzle drying of perovskite solar cells" finalizing the application of the dynamic gas quenching method. It must be noted that Mr. Lüdke worked with high experimental precision and meticulousness to find the optimum parameters and fill the necessary parameter space for the final comparison of the drying model and experiment. His results were the foundation of the third publication [21].

Additionally, the author had the honour to supervise students whose work is not detailed on herein (Teresa Dagenbach, Alexander Diercks [co-supervised with Tobias Börnhorst], Malte Haupt, Aynur Demir, Roja Thatichetty Sudhakumar & Ryan Schork [co-supervised with Fabian Schackmar]). This is however not correlated in any sense to their performance (which was mostly excellent) but rather to the conceptual focus of this thesis. Nevertheless, their work was pivotal to frame the final path that this work has taken, which was not predictable at that time.

Finally, the author wants to give credit to the inspiring and fundamental literature sources that are frequently referenced throughout this work:

1. VDI Heat Atlas[22] published by the chemical engineering branch of the German Engineers Society (VDI-GVC).
2. 'Fundamentals of Heat and Mass Transfer sixth edition' by F. P. Incorpera, D. P. DeWitt, T. L. Bergman, and A. S. Lavine [23]

3. 'Crystal Growth for Beginners. Fundamentals of Nucleation, Crystal Growth and Epitaxy, Third Edition' by Ivan V. Markov [24].
4. "Physics of Solar Cells From Basic Principles to Advanced Concepts" by Peter Würfel and Uli Würfel [25]
5. "Perovskite Solar Cells on the Way to Their Radiative Efficiency Limit – Insights Into a Success Story of High Open-Circuit Voltage and Low Recombination" by Wolfgang Tress [26].

Part II.

Fundamentals and methods

3. Hybrid perovskite photovoltaics

3.1. Background, state-of-the-art, and challenges

Hybrid perovskite optoelectronics have attracted significant research interest in the last 15 years[27, 28, 29]. The term perovskite originates from the characteristic, ionic crystal structure with stoichiometry ABX_3, which is well-known in crystallography[30]. The positions of ions in the crystal can be described by a (cubic) unit cell whose face centred positions are occupied by the X-anions, while the A and B sites are occupied by the singly charged A- and the doubly charged B-cation at the body centred and corner positions, respectively (see Figure 3.1). To make the formation of the perovskite structure possible, the ions must fulfil size-ratio constraints, as schematically indicated by the size of the spheres in Figure 3.1. In a nutshell, the X-anion must be around 1.3 times the size of the B-cation, while the A-cation must be around 1.5 times the size of the X-anion (more details can be found in the figure caption). Therefore, the cations A and B are often distinguished by the attributes 'big-' and 'small cation', respectively.

The term 'hybrid' is used to indicate that organic cation molecules, such as Methylammonium, $CH_3NH_3^+$, and Formamidinium, $CH(NH_2)_2^+$, (with occasional use of Cs^+) occupy the A-site, while the B-site is occupied by metallic anions like Pb^{2+}, Sn^{2+}, Ge^{2+}, and the X-site by halogens like iodide, bromide or chloride. In an alternative definition of the perovskite crystal structure, eight hexagons spanned by the X-anions with the B-cation in their centre (see shaded hexagon Figure 3.1) surround every large A cation. This description is often preferred in hybrid perovskites because the hexagonal units are more rigid than their bounds with the large (organic) cations, such that crystal phase transitions can be described by mutual displacement and rotation of these hexagons[31, 32]. Furthermore, these hexagons appear similarly in PbI_2 or $PbBr_2$ solutions, which are common precursors of hybrid perovskites. In that sense, the formation of the perovskite can be seen as an assembly

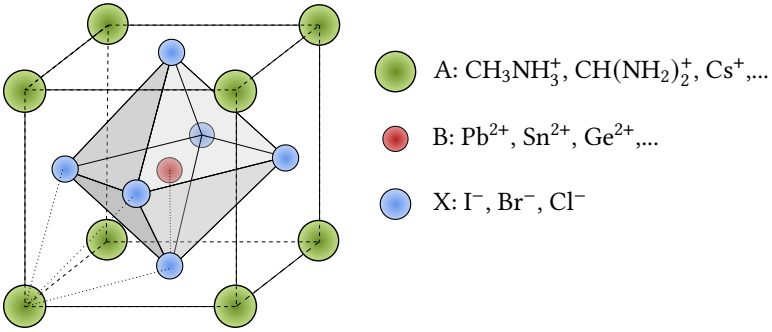

Figure 3.1.: Cubic perovskite unit cell with the stoichiometry ABX_3. The structure is possible if the radii of the composite ions, R_A, R_B and R_X, satisfy $0.81 < t \leq 1.11$, where t is the Goldschmidt factor defined as $R_A + R_X = t\sqrt{2}(R_B + R_x)$ and $0.44 < R_B/R_X < 0.90$ [28]. This implies that the A species must be bigger than the other ions. Alternative to the shown (cubic) unit cell, the structure can be described by the positions (and rotations) of BX_6 octahedra (grey shaded polygon) that surround the A cations (only one shown here).

between these hexagons and the large (organic) cations[33, 34]. The different large cations and halide anions (as well as the metal cations) in the perovskite crystal structure can be mixed in different molar ratios to modify the properties of the perovskite (such as the absorption onset, stability, crystal morphology etcetera). In this work, we will investigate three hybrid perovskite systems, in particular: Methylammonium lead iodide (MAPI) with the stoichiometry $MAPbI_3$ dissolved in N,N-Dimethylformamide (DMF), Triple cation perovskite (TCP) with the stoichiometry $Cs_{0.1}(FA_{0.83}FA_{0.17})_{0.9}Pb(I_{0.83}Br_{0.17})_3$ (in most cases) dissolved in a 4:1 volume ration of DMF and Dimethylsulfoxide (DMSO) and double cation perovskite (DCP), with a two-step processing of PbI_2 and cations in separate solutions of DMSO with 10% (volume) Ethylene glycol monobutyl ether (EGBE) and Isopropanol respectively. (Historically, MAPI was the first system investigated intensively for optoelectronic applications because of its simple stoichiometry. Subsequently, the research focus transitioned to the more complex multi-cation perovskites because of their increased stability.)

Although hybrid perovskites were investigated for optoelectronic applications already 25 years ago[35], it was from 2006 on, that the exceptional optoelectronic properties of hybrid perovskite thin-films were (re-)discovered

when applying it as a sensitizer in combination with a nanoporous TiO_2 electrode[36]. Remarkably, these optoelectronic properties, as listed below, are preserved even when the thin-films are characterized by a polycrystalline morphology[37]. Hybrid perovskite thin-films have the following advantageous properties:

- A strong absorption over the optical wavelength range whose onset is as sharp as in direct semiconductors[38].
- Exciton binding energies on the order of $kT_R \approx 25\,\text{meV}$ such that excitons dissociate to free excited charge carriers at room temperature, $T_R \approx 293\,\text{K}$ [39].
- Comparatively long excited charge carrier lifetimes (30 μs and 2.7 ms in polycrystalline and single crystals respectively) and diffusion lengths (23 μm and 650 μm in films and crystals respectively)[40] due to a high tolerance toward intrinsic defects[41, 42].
- Tunability of the bandgap over a wide range of energies from 1.2 eV to almost 2.4 eV by compositional engineering[43].
- Abundance of the perovskite precursor materials (which is not necessarily true for other functional layers in a device stack)[44, 45] and low-energy consumption during production [46, 47].
- Possibility of solution processing on flexible substrates[29] (thermal co-evaporation is another popular fabrication route [48]).

After the discovery of these properties, a fast growing community formed, researching perovskite films for a multitude of optoelectronic applications such as x-ray detectors[49, 50], light emitting diodes[51, 52], lasers[53, 54] and photovoltaics (PV). This work focusses on perovskite PV (which encompasses perovskite solar cells [PSCs] and modules consisting of multiple, electrically connected PSCs[55]). The perovskite PV community was very successful in increasing the power conversion efficiency (PCE) of PSCs rapidly over the last 10 years, which is commonly brought forward as a principal argument to invest in research on perovskite PV. The chart of champion solar cells, which is continuously updated by the National Renewable Energy Laboratory (NREL) in the United States[56] ,partially re-plotted in Figure 3.2, illuminates that the certified, record PSCs reach PCEs beyond those of concurrent thin film technologies like Copper indium gallium selenide (CIGS) and Cadmium telluride (CdTe). Furthermore, record PSCs are almost on the same level with

the most established PV technology, mono-crystalline silicon (Si), which has been under development for almost half a century. Although this achievement seems very remarkable, we have to take into account that perovskite PV profited strongly from the scientific advancements in PV research (that is models, analytical methods and deposition tools) that were developed for concurrent technologies before, in particular for organic PV. Additionally, the possibility of solution processing inherently increases the rate of technological increments as compared to technologies that rely on crystallization from a vapour or melt.

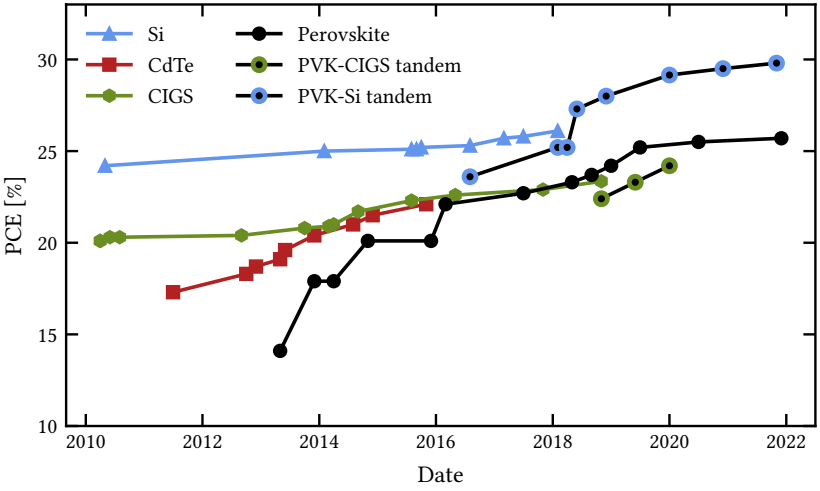

Figure 3.2.: Power conversion efficiencies of champion solar cells over date of certification. The data is adapted from the NREL chart [56]

It is crucial to stress that the record PCEs depicted in Figure 3.2 represent small-scale ($\approx 1\ cm^2$) champion solar cells, which were fabricated and measured under optimal conditions in the laboratory. Although a view on Figure 3.2 can be used to judge the 'potential' of a certain technology as a converter of solar irradiation power to electrical power, it provides merely an idealized comparison of technologies which is, first of all, an academic concern. Figure 3.2 alone is insufficient to answer the question if a commercial application of a technology will become economically feasible or sensible. An answer to this much more general question depends not only on many more technological

parameters (device stability, module architecture, scalability, light management, production complexity, etcetera) but also on many socio-economical factors (material and energy prices, labour cost, demand, legislation and incentives, etcetera). The main focus of the following paragraphs will lie on the comparison of different perovskite PV applications among themselves and with other technologies from a purely technological point of view. However, even if economy is very hard to predict, possible real-life applications should be mentioned in a work covering a topic of electrical engineering. Therefore, we will give a short overview of the business ideas developed by popular (start-up) companies in the perovskite PV community before the technology-focussed discussion. We also note which properties of hybrid perovskite would become important in which application. The main business concepts are:

- **Cost-effective thin-film photovoltaics**: The company Microquanta plans to enter the PV market soon by making cost-effective perovskite thin-film photovoltaics, already having a 5 GW-capacity pilot line operational[57]. By the end of 2019, they demonstrated a 14.2% efficient module with an area of $20 \times 80\,\mathrm{cm}^2$ [58] (their state-of-the-art solar modules are probably exceeding this value). Recently, they claimed a record of a PCE of 21.4% on a small active area[59] (the exact area is not specified, but the last record was set on $20\,\mathrm{cm}^2$). Likewise, GCL New Energy works on a 100 MW-capacity pilot line with the goal to produce 18% efficient modules and to reduce the price of production cost by 70% as compared to crystalline silicon PV[57]. Other big players in this field are Panasonic and Toshiba, demonstrating record modules PCEs of 15.1% on $703\,\mathrm{cm}^2$ in 2019 and 17.3% on $>800\,\mathrm{cm}^2$ in 2020, respectively[60]. The properties of hyrbid perovskites which are exploited in this application is the cost-effectiveness of the precursor materials, the low-energy production, the layer thickness smaller 1 μm and, potentially, the cost reduction by large-scale solution processing. In this context, it is worth mentioning that cost-effectiveness is not only an economic advantage but also an ecological one if the energy payback times with respect to silicon PV can be reduced[47].
- **Tandem photovoltaics**: Two-terminal tandems are proposed as an effective way to enter the PV market by the companies Oxford PV and Swift solar[61, 62]. Their argument for using this more complex architecture is that PCE will be come more and more important in the future to reduce the cost per watt[61]. The reason is that module prices

are already below the added cost of installation and electronics such as inverters and/or transformers[16]. Oxford PV has demonstrated some of the champion PCEs for two-terminal perovskite-silicon tandems shown in Figure 3.2. However, it must be noted that these are all small-area devices (around 1 cm^2) and the company has, so far, not published any data on the PCEs of their $15.6 \times 15.6\,cm^2$ modules. Their goal is to reach above 30% in PCE for these wafer-sized modules that could be installed in a grid forming a large panel later. In 2019, some of the founders of Swift Solar demonstrated PCEs of 23% and 21.3% in small scale rigid and flexible perovskite-perovskite tandem respectively[63]. Their main argument for using the all-perovskite architecture is a reduction in weight that could enable new integrated PV [62] (see next application). The property that is exploited in perovskite tandem PV is the bandgap tunability of hybrid perovskites via their chemical composition, which is used to make wide-bandgap ($\approx$ 1.7 eV) devices[64] (while the bandgap of crystalline silicon is fixed at around 1.1 eV).

- **Flexible and lightweight photovoltaics**: Saul technologies and Swift Solar propose that flexible and lightweight perovskite foils could be used in many appliances[65, 66].. These are aesthetic PV foils on rooftops, solar blinds or windows and integrated PV on vehicles or devices that are battery-powered and use the PV to recharge these batteries (partially) by using the surface area on the appliance The property that is most important in this context is the strong absorption of hybrid perovskites enabling comparatively thin absorber layers (<1 μm) as well as flexibility of many perovskite stacks.

Despite the existence of the above business plans and company investments, so far, no hybrid perovskite PV is available on the market to the knowledge of the author. Evidently, for the large-area PV applications, it is partially due to the fact that the capacity for industrial fabrication is still being established. However, there are some fundamental challenges in the field that still need to be addressed before production can be started with manageable risk:

- Further **increase in PCEs** to above 30% or even 33% of perovskite incorporating devices
- Increase of **stability** of perovskite PV to around 30 years
- **Scale-up** to market relevant sizes of m^2
- Management of **toxicity** due to lead incorporation or solvent systems

This thesis mainly focusses on the challenge of up-scaling and, in second priorety, on the replacement of toxic solvents in perovskite precursors, that is the toxicity. Before getting into these main topics, we will detail the other two challenges in a short paragraph each.

Since the emergence of commercially available PV around the year 1980, the PV module price in € per watt has roughly followed a learning rate of 25%. In detail, an increase in the cumulative production capacity in GW by a factor of two has lead to a decrease in the module price in € per watt by 25% [16]. This learning rate can only be continued if module PCEs keep increasing by about 0.6% absolute per year. With the physical limit of silicon modules around 29% and the current PCEs of commercial silicon modules at around 23% [16], a new technology beyond single-junction, mono-crystalline silicon PV must start taking over the main market share by 2030. This new technology could be, for a example, a two-junction tandem module incorporating at least one perovskite absorber. When planning the production of these novel modules, it must be taken into account that PCE is a moving target. Therefore, it would be beneficial if the new generation is ahead of the current commercial module PCE by at least five years (or more) such that the scale-up of industrial production for meeting global demand is feasible in that time. Depending on the time of market entry, a PCE of at least 30% is therefore desirable for research modules. In some research projects, even 33% is defined as a goal[67], which is possible according to simulations[68]. Even if the NREL efficiency chart looks promising with respect to achieving the 30% goal, it must be noted again that the active areas of these devices are yet far from commercial standards, as will be detailed after the next paragraph.

As stated above, we will detail shortly on the topic of stability, as well. First of all, with suitable architecture and encapsulation, perovskite modules can maintain 95% of their PCE for 1000 h even in harsh conditions of 85°C and 85% humidity[69]. In 2020, Microquanta was the first company to claim having passed this damp heat test for 3000 h without any loss in performance (along with a degradation of less than 2% for 100 kWh of UV irradiation), which are equivalent to 3 times and 6.5 times the IEC standards for silicon PV[70]. These results are however to be seen with caution because the standards were defined for silicon PV and already commercialized thin-film technologies[71]. It is hard to judge if these tests are suitable for perovskite PV until the first field application has been tested for 30 years (which is two times longer than the time perovskite PV has been researched). However, even if the stability of 30 years was not entirely met (the current record is 10,000h [72] or a little

longer than one year) a commercialization might still be possible if the profit due to a higher PCE outweighs the sacrifice of a shorter lifetime (and thus replacing/refurbishing the modules earlier) because the important figure is the total cost of generated energy (for a module of a given size) as an average over these 30 years and not the absolute operation time of the module itself.

Let us now come to the principal challenge addressed in this work - the scaling of perovskite PV to market-relevant sizes. Within the perovskite PV community, the NREL chart of record solar cells (Figure 3.2) is shown more frequently than the NREL chart of record module PCEs[60]. The reason is probably that on the module-scale, perovskite PV still falls behind most concurrent technologies. Figure 3.3 shows the last 12 years of this NREL module chart for the same technologies as in Figure 3.2 along with some recent PCE-data from press releases of different companies and research institutes, which have not (yet) completed the process of certification needed to include them in the official chart. We find that only two uncertified modules

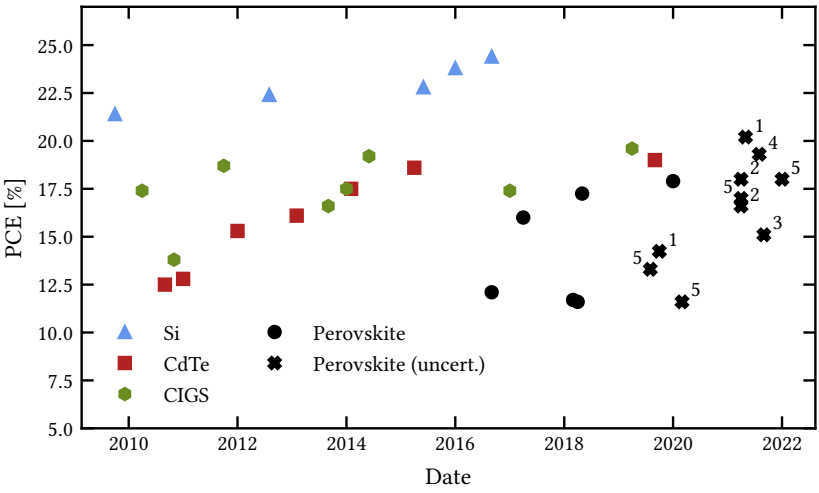

Figure 3.3.: PCEs of record modules over date of certification/date of press release. The data is adapted from the NREL module chart [60]. Recent yet uncertified results released by companies and research institutes were added to illuminate the state-of-the-art: Microquanta (1), KIT (2), Toshiba (3), NREL (4) [73, 74, 75, 60, 76]

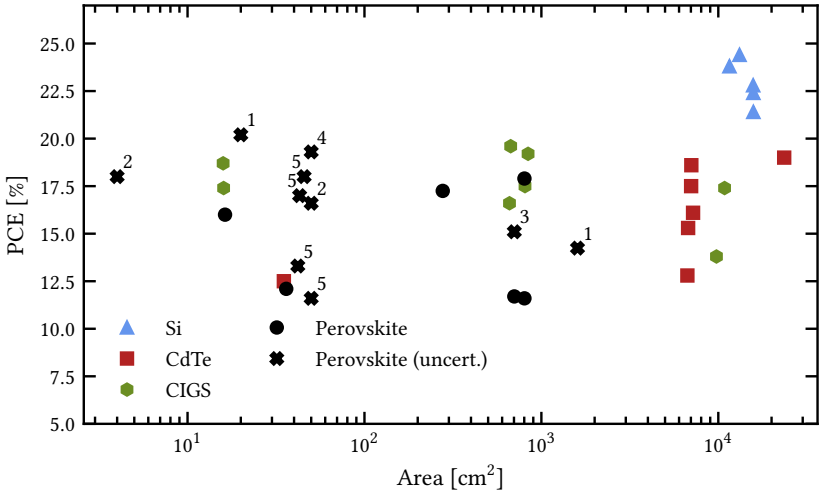

Figure 3.4.: Same data as in Figure 3.3, however PCEs are now plotted over module aperture area. Recent yet uncertified results released by companies and research institutes were added to illuminate the state-of-the-art: Microquanta (1), KIT (2), Toshiba (3), NREL (4) [73, 74, 75, 60, 76]

fabricated by Microquanta and NREL are on a similar PCE-level as the state-of-the-art of CdTe and CIGS modules. However, comparing module PCEs is only fair, when the aperture area is taken into account. When plotting the very same module PCEs over their area in Figure 3.4, it becomes evident that the state-of-the-art of all concurrent technologies is still above hybrid perovskite PV. The scaling loss, that is the drop in PCE with increasing device area, is much higher in perovskite PV than in the other technologies, which makes up-scaling a major challenge that must be solved before perovskite PV can join the competition. One could argue that areas of 10^3 cm^2 could be enough to make a large module that is comprised of many wafer-size sub-modules. However, this also introduces an upscaling loss and it remains to be shown that the total module built in that way can reach the same PCE like CdTe or CIGS where modules at the m^2-scale are already commercially available. Afterall, Figure 3.4 illuminates the still apparent technological dominance of mono-crystalline silicon because it achieves highest PCE on the m^2-scale (at a low production cost). This scale-comparison is a main reason (combined

with economical factors) why silicon PV is still dominating the market over thin-film technologies.

As a last topic, we want to address the toxicity. It is argued that the incorporation of lead in the perovskite thin-films in the form of water soluble lead salts might be problematic[77] (and tin salts being discussed as even more toxic, which rules out tin based perovskites as a viable alternative). However, effective lead recycling, device encapsulation and containment strategies were demonstrated[78, 79, 80]. Nevertheless, it is undeniable that lead incorporation will always cause a certain risk, such that the question is not purely a technological but also a legislative one. Societies must assess if the remaining risk and amount of possible intoxication of soil, ground water, animal life or the consumers is to be justifiable for the possible merit of boosting photovoltaics technology further in PCE to prevent the risks associated with climate change. For large-scale production however, the toxicity of the used solvent systems might become an issue for the workers or the environment, as well[81]. Of course, this problem depends on the grade of automation, the effectiveness of fume collecting ventilators and the organization of the work space. The most commonly used solvent in perovskite solution processing, N,N-Dimethylformamide (DMF), is listed as a CMR-chemical due to its toxicity on unborn children and its mutagen impact on liver cells[82, 83] and the threshold for work places is limited to $15\,\mathrm{mg\,m^{-3}}$ in Germany or $10\,\mathrm{mg\,m^{-3}}$ in the United States[84]. This is definitely a very low threshold given that in the spin coating of one $\mathrm{cm^2}$-sized substrate about 30 mg liquid DMF is used (A similar argument holds for the nowadays less used solvent N-Methyl-2-pyrrolidone [NMP] with a threshold of $82\,\mathrm{mg\,m^{-3}}$ in Germany [85]). In recent reports, DMF was replaced by the more volatile Methylglycol or 2-Methoxyethanol (2-ME) [86]. However, this solvent is also very toxic to reproduction in both men and women and was therefore almost fully replaced in industry [87]. The maximum threshold for work places lies at $3.2\,\mathrm{mg\,m^{-3}}$ in Germany[84]. It would be a great relief for the perovskite community if these toxic solvents could be replaced in production entirely by green alternatives, which are (close-to) non-toxic. The reason is that, for a future industrial fabrication on the $\mathrm{m^2}$-scale, fully gas-sealed systems such as gloveboxes would be very expensive and that every ventilation system or automated coating system can fail and will need hands-on repairs (not speaking of the efforts to ensure safe and environmentally friendly transport, handling and disposal of huge amounts of these solvents). Unfortunately, if we compare the average PCEs of a large number of publications (as given by

the open-access perovskite database [88]), it becomes clear that the majority of works used either DMF, NMP or 2-Me (see Figure 3.5). Further, the average published PCEs of works avoiding the use of these toxic solvents are not only significantly lower but also seem to stagnate in PCE over last three years (compare datapoints in Figures 3.5a and 3.5b as well as solid and dashed trend line in Figure3.5b, which are obtained from polynomial fits). This shows that there is still a great potential in finding ways around toxic precursor solvents, while maintaining the PCE, which is a second focus of this work.

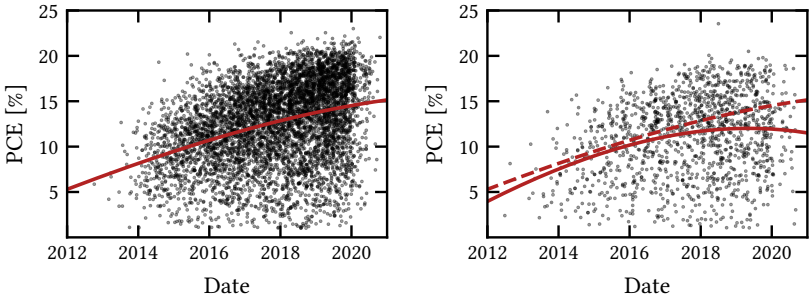

(a) Average of device PCEs for all works using either DMF, NMP or 2-Me (or multiple of these).

(b) Average of device PCEs for all works using neither DMF, NMP nor 2-Me.

Figure 3.5.: Data from the perovskite open access-database[88] ordered by the usage of solvents. Each black point represents the average of the PCEs as measured by backward JV of one publication. The solid red lines are a fit of a third order polynomial to the respective data, while the dashed line in (b) is a copy of the solid line from (a) for better comparison of the two trends.

3.2. Large-scale solution processing and chemical dynamics

Solution processing is a popular route for fabricating perovskite solar cells[29]. The most common solution processing method is spin coating, where a drop of solution is cast onto a substrate that is rotated rapidly[89]. Due to the centrifugal forces the solution is sheered over the substrate forming a thin

solution film that dries homogeneously. The advantages of spin coating are its constant smoothing of the film surface during drying and the fast repetition rate of individual samples. The disadvantages are scalability issues due to the growing stress on the substrate with the distance from the rotation centre and the growing irregularity of coating due to the radial dependence of the involved forces as well as the high solution wastage[90]. (Besides, due to the complex entanglement between sheer/viscous forces, surface tension, centrifugal forces and solvent evaporation, it is very challenging to isolate drying dynamics from sheering dynamics, which makes it not a good candidate for modelling of the drying dynamics as described in this work.)

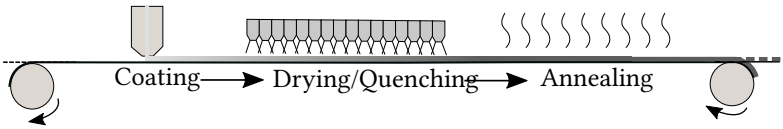

Figure 3.6.: Schematic of a typical production line for solution-processes perovskite PV with slot-die coating, gas jet drying and annealing. The dashed lines indicate a rigid glass substrate, while the solid lines indicate a flexible substrate (=Roll-to-Roll coating).

As a conclusion, spin coating is not a viable method for making perovskite photovoltaics on an industrial scale (which is greater 100 cm^2 as we discussed above). Instead, linear coating as shown in Figure 3.6 would be desirable. Such machine typically includes the following processing steps:

- **Coating:**
  The solution is coated on a linearly moving substrate (which could be a flexible foil or a rigid glass substrate as indicated by the dashed lines) by slot-die coating, spray coating, screen printing, inkjet printing, etcetera.
- **Drying/Quenching:**
  The substrate is driven under a big drying machine to extract the solvent, for example by nozzles of high-pressure air. Technically, this is a drying process, but the perovskite community typically uses the term ‘quenching’ (which the process of driving a solution film quickly into supersaturation such that homogeneous nucleation is induced). Such quenching step is optionally combined with anti-solvent immersion or infra-red pulses.

- **Annealing:**
  Finally, the substrate is driven in an annealing chamber of elevated temperature (around 100°C) or is irradiated by infra-red light. This step is important to remove defects from the crystal structure, re-crystallize polycrystalline thin film to a certain desired micro-structure and remove potential residuals.

These principal processing steps are in accordance with a variety of reports on pilot lines for perovskite solution processing[29]. (In general, the same principal steps exist as well in smaller scale batch-to-batch fabrication lines or even spin coating processes.) Similar solution printing concepts were already proposed for organic electronics before[91] and could potentially accomplish high-throughput fabrication in a cost-effective way. However, perovskite solution processing has a principal difference in the formation dynamics. In organic electronics, the solution contains (mixtures of) polymer chains that form an amorphous network upon drying[92]. In this case, different structural properties arise from different phase segregation dynamics and/or mixture and order parameters of the polymer network[93, 94]. In perovskite solution films however, a different process dominates the morphology formation starting at a certain concentration of solute and continuing until all solvent has evaporated – the nucleation of crystal grains and their growth (re-crystallization can happen also afterwards during annealing). Figure 3.7 shows a schematic of the perovskite formation stages. These are:

1. **Liquid film formation**: Formation of a liquid solution film with a defined surface on the substrate
2. **Drying**: Evaporation of solvent from the solution film and diffusion of solvent to the film surface
3. **Crystallization**: Nucleation of crystal grains from the solution and growth of these grains
4. **Recrystallization**: Reforming and refining of the polycrystalline morphology as well as healing of defects

Figure 3.7 further shows the main parameters that affect each formation stage and demonstrates that the formation stages can be mapped to the processing steps discussed earlier. It is crucial to note that this mapping is to be interpreted as the approximative relation ‘occurs around the same time’ rather than a unique one-to-one map. The exact onset of formation stages may vary with the chosen perovskite solution process and it is even possible

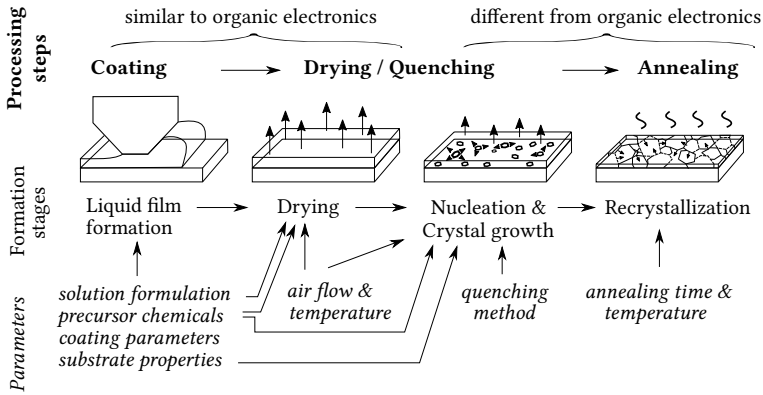

Figure 3.7.: Conceptual depiction of the processing steps and formation stages involved in hybrid perovskite solution processing along with the parameters impacting these stages. The arrows (X→Y) under the pictograms are to be understood as *'X depends on Y'*.

that formation stages overlap temporarily or happen at the same time. Let us now analyse the parameters affecting the formation stages. The liquid film formation is controlled by the coating parameters (these are the speed, blade gap and solution volume for blade coating but differ for other coating methods), the viscosity of the solution, its surface tension and its surface energy on the substrate. In turn, the latter parameters depend on the solvents (and additives) employed, on the solute chemicals and the texture and surface treatment of the substrate. The main parameters affecting the drying stage are the applied temperature and the convection over the solution film, that is the air flow geometry. Beyond these, the initial wet film thickness of the previously formed wet film, the vapour pressures of the solvents, the diffusion coefficients of these solvents in the solute, as well as, possible changes in solvent activity due to solvent-solute interaction can impact the drying dynamics (these considerations refer to the 'drying stage' designating the physical process of evaporation of solvent from a thin-film, as defined in item 2. above, and not to the 'drying/quenching process' which is the action that an operator initiates to supersaturate the perovskite solution as detailed earlier). Nucleation and crystal growth are influenced by the final state and rate of drying, by the present temperature and convection during the process, by

the precursor chemicals chosen as well as the substrate surface (in particular, in case of heterogeneous nucleation). Evidently, in case anti-solvents and/or infrared radiation are used during the quenching, the crystallization dynamics will be heavily impacted by the quenching method beyond the above parameters. We note that in some of the publications of this work, nucleation and crystal growth are listed as separate formation stages[19, 20]. This is conceptually sensible but not temporally because they usually happen at the same time as we will show in section 6.2.4 on LaMer's model, which is why we combined them here into one step. The recrystallization happens after the initial crystal growth and nucleation are completed, in particular when the temperature is increased for annealing. This may involve the coalescence of crystal-grains[95], morphological transformations[96], Ostwald ripening[97] and healing of defects[98]. These processes are influenced by the annealing time and temperature as well as the morphological state at the beginning of the annealing process.

3.3. Research goal and questions

Given the complexity of the perovskite morphology formation explained in the last section, it is not astonishing that up-scaling these dynamics is a major challenge. The scaling losses mainly originate from the inability to produce homogeneous thin-films without coating defects[99]. This problem of scaling solution processing is what this work tries to tackle in a fundamental way. In detail, the main goal is to provide the research community with a fundamental analysis of the involved drying and crystallization processes and thereby offer a versatile toolbox of *in situ* characterization methods as well as modelling concepts. In practice, engineers conceptualizing large-scale perovskite printing should obtain concrete design guidelines and profound knowledge for the interrelation of experimental parameters from this work. Of course, in a technology driven field such as perovskite PV, testing ranges of solvents, precursor components and processing methods is also necessary to commit relevant results to the field. However, the topic of this thesis is less the optimization of the PCE of perovskite solar cells but more the question how accurate analysis and modelling of the fundamental perovskite formation dynamics can help with the process transfer from spin coating to linear deposition techniques. If possible, the emergence of coating windows (these are parameter ranges, where the fabrication is successful) is investigated

in great detail. Special emphasis is laid on the scalability and generality of the so-obtained insights such that they can later be applied in a variety of fabrication lines. In fact, most methods and models are so general that they can be applied to the general problem of depositing any homogeneous, polycrystalline layer from a thin solution film. In more detail, this work attempts answering the following research questions.

1. **Drying dynamics:** How to model and measure the drying dynamics of perovskite solutions films
2. **Crystal growth and nucleation:** How to optimize crystal growth and nucleation simultaneously in solution processed perovskite thin-films
3. **Advanced *in situ* characterization:** How to monitor crystallization dynamics in real-time during large-scale perovskite solution printing
4. **Device performance:** How different drying and quenching methods influence the achievable PCE, yield and repeatability in perovskite solar cells processed by blade coating
5. **Green solvents:** How the measures discussed above change when toxic solvents are replaced by green alternatives

This work is dedicated to answer these questions in a detailed way. We will refer to the respective questions in the beginning and end of each chapter in the Results and Discussion, part III, to guide the reader through this work. Finally, in the conclusion, we will assess to which extent the questions could be answered and what further questions could be part of future research.

4. Solar cells

4.1. Charge carrier dynamics in solid state materials

In a solid state material, the electromagnetic potentials of its unit cells (which are made up of atoms, ions or molecules) merge in a way that a continuum of quantum mechanical states forms (in contrast to the discrete states available in a single unit). These continuous states are grouped in the so-called bands with index n, which are defined by a dispersion relation between energy ε_n and momentum $\vec{k}$ [100, p.353-355] (as we will see later, these bands are energy regions of high state density, while between them there are gaps of very low state density). Accordingly, the dynamics of electrons in these bands are comparable to a confined, electron gas in vacuum. In a semi-classical model they behave as particles with the effective mass tensor [100, p.372-373]

$$[(m^*)^{-1}]_{njk} = \frac{1}{\hbar^2}\frac{\partial^2 \varepsilon_n(\vec{k})}{\partial k_j \partial k_k}, \tag{4.1}$$

where $\hbar$ is the reduced Planck constant and the equation of motion

$$\frac{d\vec{v}_n}{dt} = [(m^*)^{-1}]_n \vec{F}, \tag{4.2}$$

where $\vec{v}_n$ is the velocity of the electron in the band n. Consequently, if an electric field, $\vec{E}$, is applied to the material, we would get an acceleration of electrons $a_n = \frac{d\vec{v}_n}{dt} = e[(m^*)^{-1}]_n \vec{E}$. It is important to note that $\varepsilon_n(\vec{k})$ is in general a periodic function, which also lets $[(m^*)^{-1}]_{njk}$ oscillate with $\vec{k}$. This oscillation leads to a vanishing net current in completely filled bands because for every electron moving with $\vec{v}_n(\vec{k})$ we can find a symmetric electron moving with $-\vec{v}_n(-\vec{k})$ [100, p.377]. Only in partially filled bands this is

no longer the case such that non-vanishing, net currents can flow. In the following, we assume that at least one partially filled band, n, is available at the present temperature, in which we find a significant density of charge carriers, $n_{i,n}$ $\left[\mathrm{cm}^{-3}\right]$ (that is to say we are not dealing with an insulator). The index i is added to designate the charge carrier species. These charge carriers can be electrons in almost empty bands or, in almost completely filled bands, one usually treats electron vacancies, or commonly called 'holes', as positive charge carriers with polarity 1. Hence, the polarities $z_i = -1$ (electrons) and $z_i = 1$ (holes) are possible.

Charge carriers in a (classically conducting) material are only accelerated for a certain range, which is statistically equal to their mean free path, until they scatter with other electrons or lattice vibrations in the material. Continuing with the case of the external electric field, we can calculate the mean velocity $< v_{i,n} >$ that a charge carrier accelerated with $a_{i,n}$ reaches until it is scattered. For this calculation we assume that the probability that an electron is not scattered is $p(t) = \exp\left(-t/\tau_{i,n}\right)$ with a characteristic decay time $\tau_{i,n}$. We obtain

$$< v_{i,n} >= \int_0^\infty a_{i,n} p(t) dt = \int_0^\infty \frac{z_i e E}{m^*_{i,n}} \exp(-t/\tau_{i,n}) dt = \frac{z_i e}{m^*_{i,n}} \tau_{i,n} E \equiv z_i \mu_{i,n} E, \tag{4.3}$$

where E is the amount of the electric field vector, $m^*_{i,n}$ is the average effective mass of the charge carriers and $\mu_{i,n} = e\tau_{i,n}/m^*_{i,n}$ is defined as the charge carrier mobility $\left[\mathrm{cm}^2\,\mathrm{V}^{-1}\mathrm{s}^{-1}\right]$ and we get the so-called *drift current* (or *field current*) as

$$j_{i,n,\mathrm{field}} = z_i e n_{i,n} < v_{i,n} >= e n_{i,n} \mu_{i,n} E \equiv \sigma_{i,n} E \tag{4.4}$$

$\left[\mathrm{A\,m}^{-2}\right]$, where $\sigma_{i,n}$ is the conductivity $\left[\,\Omega^{-1}\mathrm{m}^{-1}\right]$ (for constant $\sigma_{i,n}$ the above relation becomes Ohm's law.) [25, p. 107]. It is important to remember that due to $z_i^2 = 1$ the field current has always the same polarity independent of the charge carrier polarity and that the above expression for $j_{i,n,\mathrm{field}}$ is only for one species of charge carriers, i, in one band, n. We will see later that in semiconductors we have in general bipolar conduction of holes in the valence and electrons in the conduction band; so we must add-up two

expressions of the type above. Further, we must account for the fact that (spatially varying) fields can be produced by all the internal charged species in a material (these are electrons, holes, rigid atom cores and, in particular in hybrid perovskites, mobile ions or ion vacancies as detailed in section 4.6). So, we must technically replace E with the total field, $E_{\text{tot}} = -\nabla\phi_{\text{net}} + E$, containing also the net contribution of the electromagnetic potentials of these internal charges, $-\nabla\phi_{\text{net}}$ (which vanishes everywhere in a completely neutral homogeneous material, but not in a pn-junction, for example, as we will see below). It is important to keep in mind that $\nabla\phi_{\text{net}}$ is, first of all, a mathematical contribution and can in most cases not be directly measured with a voltmeter.

In the case where charge carriers accumulate in a certain region, Equation 4.4 does not describe the full physics (which is the reason why $\nabla\phi_{\text{net}}$ does not correspond to the measured field over a semiconductor in general). The reason is that, thermodynamically, the charge carriers will always try to maximize their entropy (that is to say distribute as homogeneously as possible in a material). This implies that if an inhomogeneous distribution of $n_{i,n}$ is present, a diffusion current from regions of high $n_{i,n}$ to regions of low $n_{i,n}$ according to Fick's law will arise. Such *diffusion current* can be written as

$$j_{i,n,\text{diff}} = -z_i e D_{i,n} \nabla n_{i,n}, \tag{4.5}$$

where $D_{i,n}$ $\left[\text{m}^2\,\text{s}^{-1}\right]$ is the diffusion coefficient of the charge carriers [25, p. 108]. We note that, because each charge carrier combines the properties of its position and its charge, statistical mechanics yields the Einstein-Relation [25, p. 108], which interrelates the diffusion coefficient, $D_{i,n}$, and the charge carrier mobility, $\mu_{i,n}$, as

$$\frac{\mu_{i,n}}{D_{i,n}} = \frac{e}{kT}. \tag{4.6}$$

Whenever the (electrical) energy of charge carriers is discussed, it is handy to express the total current, $j_{i,n,\text{tot}} = j_{i,n,\text{diff}} + j_{i,n,\text{field}}$, in terms of the gradient of the so called electrochemical potential [25, p. 109] as

$$j_{i,n,\text{tot}} = -\frac{\sigma_{i,n}}{z_i e} \nabla \eta_{i,n} \tag{4.7}$$

with

$$\eta_{i,n} = kT \ln(n_{i,n}/N_{i,n}) + z_i e \phi_{\text{tot}}, \tag{4.8}$$

where $kT \ln(n_{i,n}/N_{i,n})$ is chemical potential of the species (the constant $N_{i,n}$ does not alter the equations of motion, but by convention, it equals the effective density of states, N_{C} or N_{V} introduced later), and ϕ_{tot} is the total electrical potential present in the material factoring in all internal fields, such that $E_{\text{tot}} = -\nabla\phi_{\text{tot}}$. We note that in a bipolar conductor (as for example an illuminated semiconductor where one band is partially filled with electrons and one band is partially filled with holes) [25, p. 109], we need to write

$$j_{\text{bi,n,tot}} = \frac{\sigma_{\text{e},n}}{e} \nabla \eta_{\text{e},n} - \frac{\sigma_{\text{h},n}}{e} \nabla \eta_{\text{h},n}. \tag{4.9}$$

We note that, in general, the electron and hole current are not equal in magnitude (neither are the respective diffusion and drift currents, which is a common misconception). It can be shown that this [25, p. 109] expression can be written in terms of the Quasi Fermi levels, ε_{FV} and ε_{FC} we will introduce in section 4.3 as

$$j_{\text{bi,n,tot}} = \frac{\sigma_{\text{e},n}}{e} \nabla \varepsilon_{\text{FC}} + \frac{\sigma_{\text{h},n}}{e} \nabla \varepsilon_{\text{FV}}, \tag{4.10}$$

which is identical to Equation 4.9 except for the sign change in the hole current.

4.2. Thermodynamic distribution of charge carriers

The thermodynamic distribution of electrons in a solid state material is given by a minimization of their free energy $F = E - TS$, where E is their total energy and S is the entropy of the system, while the Pauli principle for fermions must be fulfilled. This implies that, in thermodynamic equilibrium with the environment temperature T, electrons fill energetic states according to the so-called Fermi-Dirac distribution [25, p. 43]

$$f_e(\varepsilon_e) = \frac{1}{\exp\left[\left(\varepsilon_e - \varepsilon_F\right)/kT\right] + 1}, \tag{4.11}$$

where ε_F is the *Fermi level*, that is the highest energy which would be occupied, hypothetically, at $T = 0\,\mathrm{K}$. It can be shown that $\varepsilon_F = \eta_e = -\eta_h$ in the dark [25, p. 59-63]. Further, the number of electrons per volume, dn, occupying states with the energy ε_e is given as

$$dn(\varepsilon_e) = D_e(\varepsilon_e) f_e(\varepsilon_e) d\varepsilon_e, \tag{4.12}$$

where $D_e(\varepsilon_e)$ is the density of available states at this energy [25, p. 42]. This density is fully determined by the band structure and can be computed as

$$D_e(\varepsilon_e) = \frac{2}{(2\pi)^3} \int\limits_{S_{\varepsilon_e}} \frac{dS_\varepsilon}{|\vec{\nabla}\varepsilon(\vec{k})|}, \tag{4.13}$$

where the integration is carried out on the surface in momentum space where $\varepsilon(\vec{k}) = \varepsilon_e$ [100, p.352]. We note that D_e represents the whole band structure. It varies from regions of very high density of states, the actual band, to regions of almost no density, the spaces between bands. Materials can be classified according to the relative position of the Fermi-Level in the band structure. In metals and semi-metals, ε_F lies within a band, that is in region of high D_e producing a partially filled band with many charge carriers potentially available for electric currents. In insulators and semiconductors ε_F lies in a region of low D_e. The lowest partially filled band is then referred to as the valence band with index V, while the subsequent band with higher energy is referred to as the conduction band with index C. The energy difference between the lower edge of the conduction band and the upper edge of the valence band, is called the bandgap, ε_G. By convention, we call a material a semiconducting, if its bandgap is on the order of 0.5 eV to 3 eV, which in turn specifies a maximum and a minimum of the charge carrier density in the valence and conduction band at room temperature [100, p. 469]. The density of electrons in the conduction band (in the dark) can be calculated as

$$n_e^0 = \int\limits_{\varepsilon_C}^{\infty} D_e(\varepsilon_e) f_e(\varepsilon_e) d\varepsilon_e \approx N_C \exp\left(-\frac{\varepsilon_C - \varepsilon_F}{kT}\right), \tag{4.14}$$

where $N_C = 2(2\pi m^*_{e,C} kT/h^2)^{3/2}$ is the effective density of states of the conduction band and ε_C is the energy of the lower conduction band edge [25, p. 48]. Analogously, we can define the density of unoccupied states in the valence band, the holes, (in the dark) by

$$n_h^0 = \int_{-\infty}^{\varepsilon_V} D_e(\varepsilon_e)[1 - f_e(\varepsilon_e)]d\varepsilon_e \approx N_V \exp\left(-\frac{\varepsilon_F - \varepsilon_V}{kT}\right) \tag{4.15}$$

with $N_V = 2(2\pi m^*_{h,V} kT/h^2)^{3/2}$ and ε_V as the energy of the upper valence band edge. From this, we can calculate the intrinsic density of charge carriers, n_i^0, (in the dark) [25, p. 49] as

$$n_i^0 = \sqrt{n_e^0 n_h^0} = \sqrt{N_C N_V} \exp\left(-\frac{\varepsilon_G}{2kT}\right). \tag{4.16}$$

We note that for a doped semiconductor, we can artificially set $n_e^0 \approx n_D$ (n-doped) or $n_h^0 \approx n_A$ (p-doped) where n_D and n_A are concentrations of p and n-dopants respectively. The Fermi level then shifts according to the Equations 4.14 and 4.15, while ε_G remains approximately unchanged [25, p. 55-56].

4.3. Absorption and emission of light in semiconductors

Let us now come to the absorption of light in the semiconductor, which can be described by the Lambert-Beer law

$$j_\gamma(x) = j_\gamma(0) \exp(-\alpha x), \tag{4.17}$$

where the absorption coefficient, α, is proportional to the combined density of states at the band edge, $D_{comb}(h\nu)$ [25, p. 66]. For direct semiconductors, we have approximately

$$D_{comb} \propto (h\nu - \varepsilon_G)^{(1/2)} \tag{4.18}$$

if $h\nu$ is close to the ε_G [25, p. 66]. It was shown that hybrid perovskites behave like direct semiconductors [101]. Accordingly, as visible in Figure 4.1, Equation 4.18 is approximately fulfilled.

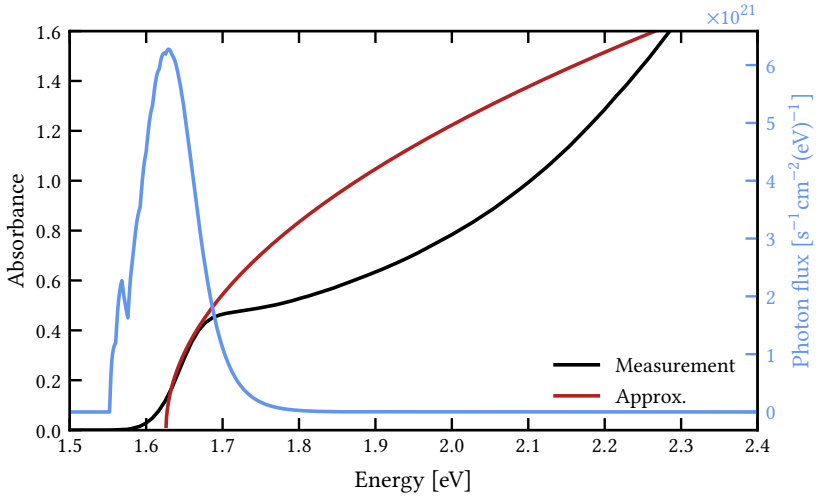

Figure 4.1.: Absorbance (negative logarithm of transmission) of MAPI as measured by UV-VIS spectroscopy, along with close to bandedge approximation for direct semiconductors (Equation 4.18) and calculated emitted photon flux by radiative recombination according to Equation 4.22 (with assumption $\Delta\eta = 1.32\,\text{eV}$). The left side of the peak is noisy because the absorption measurements hits its noise limit there. (The the so-called Urbach-tail is where the measured absorbance deviates from Equation 4.18 at around 1.63 eV.)

From the viewpoint of quantum mechanics, when photons of frequency ν impinge on a semiconducting material, they can be absorbed in a process called the 'photovoltaic effect'. In this process, they transfer all their energy, $h\nu$, to an electron in the valence band which is then lifted to the conduction band if $h\nu > \varepsilon_G$. If however $h\nu < \varepsilon_G$ there is no available state for the electron to go in an ideal semiconductor and therefore the material appears transparent to photons with these energies. (In a real semiconductor a certain density of sub-bandpap states is always available defining the *sub-bandgap absorption.*) The excess energy, $h\nu - \varepsilon_G$, of the absorbed photons is converted to heat shortly ($10^{-12}s$) after the absorption by electron-electron as well as

electron-phonon scattering in the conduction and/or the valence band – a process called thermalization [25, p. 57-58]. Afterwards, the electrons occupy a state close to the conduction band edge, while the holes occupy a state close to the valence band edge. These excited states can be semi-stable and have lifetimes from nanoseconds to microseconds depending on the available recombination pathways, which will be detailed later.

In conclusion, a present flux of photons onto a semiconductor leads to an accumulation of additional electrons in the conduction band and holes in the valence band. To describe the quasi static distribution of these species, two so-called Quasi Fermi distributions with the shifted Fermi energies $\varepsilon_{\mathrm{FC}}$ and $\varepsilon_{\mathrm{FV}}$ are introduced. It can be shown that (thanks to the definition of η_i) these are equivalent to the chemical potentials of the electrons and holes η_{e} and $-\eta_{\mathrm{h}}$ respectively (which are not equal in magnitude any more as in the case of the semiconductor in the dark) [25, p. 59-63]. The effective densities of charge carriers under irradiation then become

$$n_{\mathrm{e}} \approx N_{\mathrm{C}} \exp\left(-\frac{\varepsilon_{\mathrm{C}} - \varepsilon_{\mathrm{FC}}}{kT}\right), \tag{4.19}$$

$$n_{\mathrm{h}} \approx N_{\mathrm{V}} \exp\left(-\frac{\varepsilon_{\mathrm{FV}} - \varepsilon_{\mathrm{V}}}{kT}\right) \tag{4.20}$$

and the intrinsic carrier density becomes

$$n_{\mathrm{i}} = \sqrt{n_{\mathrm{e}} n_{\mathrm{h}}} = \sqrt{N_{\mathrm{C}} N_{\mathrm{V}}} \exp\left(\frac{\varepsilon_{\mathrm{G}}}{2kT}\right) \exp\left(\frac{\varepsilon_{\mathrm{FC}} - \varepsilon_{\mathrm{FV}}}{2kT}\right) = n_{\mathrm{i}}^{0} \exp\left(\frac{\Delta\eta}{2kT}\right), \tag{4.21}$$

where $\Delta\eta = \varepsilon_{\mathrm{FC}} - \varepsilon_{\mathrm{FV}}$ is called *Quasi Fermi level splitting* [25, p. 58]. Because $\Delta\eta$ determines the potential energy difference between electrons and holes, it plays a major role in the conversion of chemical to electrical power in solar cells, as we will show later.

If absorption of photons is possible due to the photoelectric effect, time invariance of energy and momentum conservation implies that the temporally reversed process must be allowed, as well, which is called radiative recombination. We can calculate the flux of emitted photons $dj_{\gamma,\mathrm{em}}(E)$ per photon energy $E = h\nu$ as

$$\frac{dj_{\gamma,\mathrm{em}}(E)}{dE} = \frac{\Omega}{4\pi^3\hbar^3c_0^2}\frac{a(E)E^2}{\exp([E-\Delta\eta]/kT)-1} \equiv a(E)\phi_{BB}(E-\Delta\eta) \quad (4.22)$$

$\left[\#\text{photons}\,\mathrm{s}^{-1}\mathrm{cm}^{-2}(\mathrm{eV})^{-1}\right]$, where $a(E) = a(h\nu) = [1-r(\nu)][1-\exp(-\alpha(\nu)d)]$ is the so-called *absorptance*, d is the thickness of the film, $r(\nu)$ its reflectivity, Ω is the detection angle and c_0 is the speed of light in vacuum [25, p.99]. The function $\phi_{\mathrm{BB}}(E)$ is the black body radiation spectrum as introduced by Planck [26, p.3]. Figure 4.1 depicts a luminescence spectrum as calculated from Equation 4.22 based on the absorbency data plotted as the solid black line.

It is crucial to note that this radiative 'loss' is an unavoidable consequence of the inverse photovoltaic effect, (limiting the theoretical power conversion efficiency of an infinite junction solar cell illuminated with fully concentrated light to about 86% which is only slightly above the efficiency of an ideal Carnot heat engine connected to a black absorber of 85% [25, p.102]). In an ideal semiconductor, this radiative recombination pathway would be the only available one for excited charge carriers to decay to their initial state (neglecting Auger recombination that is a highly charge-carrier-density dependent three-particle process and is not relevant under non-concentrated sunlight conditions for hybrid perovskites[26, p.7]). However, as we will detail in the following section, substantial non-radiative pathways are available in a real semiconductor (the most common of which are Shockley-Read-Hall recombination at defect sites and surface recombination [25, p.75-85]). These pathways decrease the lifetime, $\tau(n)$, of the excited charge carriers [26, p.5] as

$$\frac{1}{\tau(n)} = \frac{1}{\tau_{\mathrm{rad}}(n)} + \frac{1}{\tau_{\mathrm{non-rad}}} + \frac{1}{\tau_{\mathrm{non-rad2}}} + \dots. \quad (4.23)$$

This equation hints to the fact that the more non-radiative recombination is suppressed as compared to radiative recombination, the more the charge-carrier lifetime approaches its ideal value, $\tau(n) = \tau_{\mathrm{rad}}(n)$. This is reflected in the so-called Internal quantum efficiency of luminescence [26, p.5]

$$\mathrm{IQE} = \frac{\tau(n)}{\tau_{\mathrm{rad}}(n)}. \quad (4.24)$$

Equation 4.24 highlights the importance of photoluminescence measurements, where the semiconductor is excited by a monochromatic, high-intensity light source of known intensity and wavelength. In an ideal case, where all parameters are known, this allows for the determination of the external quantum efficiency EQE_{PL}. Although it may be complex to determine the relation between EQE_{PL} and IQE [102], relative comparability can still yield information about differences in the IQE assuming light propagation in two samples is roughly identical. The same is true even if no proper EQE_{PL} measurement is performed but just a PL intensity response at constant excitation is measured. In a nutshell, highly luminescent materials are a good candidate for solar cell production. However, in a solar cell stack, also the properties of the charge extraction layers and contacts as well as the external bias can influence the magnitude of the photoluminescence response [103, 104]. Accounting for all these influences imposes a principal challenge for interpreting (photo)luminescence measurements.

4.4. Power generation in ideal solar cells

A solar cell is a device that makes use of the chemical energy of excited charge carriers created by the photovoltaic effect and converts it into electrical energy. For this purpose, the electrons and holes created by the incident photons need to separate and must be extracted at two different electrodes, which are typically metals or transparent conductive oxides (TCOs). Shortly after the absorption of a photon, the created electron and hole can form a so-called exciton due to their electromagnetic attraction. However, these electron-hole pairs are separated by temperature (that is to say phonon-exciton interactions) in hybrid perovskites [39] such that the electrons and holes can move freely in the conduction and valence band, respectively. for a successful, monopolar extraction of these charge carriers at different electrodes, these electrodes – or, more precisely, the junctions leading to the electrodes – need to be *charge selective*. This is to say these junctions need to act as 'membranes' that have a high conductivity only for one type of excited charge carriers. In classical silicon solar cells, charge sensitivity is achieved by a pn-junction close to one of the electrodes. However, in thin-film photovoltaics, it is a popular approach to sandwich the absorber between an n-type and a p-type material. These are also referred to as *electron transport layer* (ETL) and *hole transport layer* (HTL) [25, p.129-131]. The energy diagram of such a device (in the

dark) is depicted in Figure 4.2a. The x-axis shows the material stack from one electrode M_1, the ETL (*n*-type), the absorber (intrinsic or *i*), the HTL (*p*-type) to the second electrode M_2. The y-axis shows the energy of the valence band edge, ε_V, Fermi-level ε_G and the conduction band edge ε_C followed by the electrostatic potential of free charge carriers separated from the conduction band edge by the work function χ_e. The grey shaded area can be seen as the band, while the white area is the bandgap/vacuum.

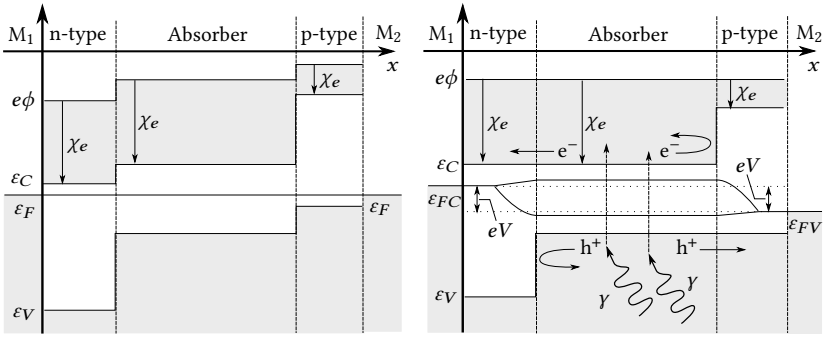

(a) Energy diagram of thin film solar cell in the dark

(b) Energy diagram of thin film solar cell in the light.

Figure 4.2.: Energy diagrams of sandwich structure of a thin-film solar cell. In the dark (a), the charge carrier redistribution leads to a constant Fermi-level over all the device. In the illuminated device (b), Fermi-level splitting is present by the accumulation of electrons in the conduction band and holes in the valence band. Due to Fermi-level splitting, a (chemical) potential difference is present at the electrodes, which is the terminal voltage. Non-radiative recombination and the load resistance then determine how much this potential difference rises (The maximum value is the Fermilevel-splitting.)

Let us now fundamentally explain the charge carrier conduction over the individual junctions in the device stack in the dark (see Figure 4.2a). When two semiconducting materials are in contact, the charge carriers redistribute in the vicinity of the junction until a constant Fermi level is reached (see Fermi level in Figure 4.2a). In detail, when a *p*- and an *n*-doped material come into contact, some of the electrons that were in the *n*-material before flow into the *p*-material to occupy some of the available energy states in the *p*-material, thereby increasing their total entropy and decreasing their mean total mean free energy $F = E - ST$ (in bipolar systems this implies

that electrons flow from *n* to *p* in the conduction band and holes flow from p to n in the valence band). In the case of an *n-i* or *p-i* junction (as in the thin-film device stack we will detail shorty), the involved mechanisms are essentially the same, since the *i*-material appears relatively *p*-doped to the *n*-material and vice versa. (The only difference is the band alignment between the conduction and valence bands, which are usually chosen in a way to maximize the conductivity over the conduction bands and minimize conductivity over valence bands the in the *n-i* configuration and vice versa for *p-i* configuration.) Because charge carrier redistribution in a neutral material comes at the expense of the potential energy of separating the electrons from the rigid positive atom cores (which is essential an increase in E), an equilibrium state at minimum free energy $F = E - ST$ reached, in which no further redistribution happens. In a *pn*-contact, a finite region of low charge carrier density forms as result – the depletion region. (While an *n*-material conducts mainly in the conduction band and a *p*-material in the valence band, in the depletion region, both charge carrier densities are low because they diffuse along the gradient of their respective concentration according to Equation 4.5 away from the depletion region, leading to a low total conductivity.) In *n-i* or *p-i* junctions, a similar redistribution happens, but the intrinsic material has less electrons/holes that can redistribute such that the depletion region is charged less and must therefore be wider due to charge conservation. In the *n-i-p* or *p-i-n* configuration, the depletion region can extend over the whole intrinsic semiconductor (this is the case in typical silicon *p-i-n* diodes with an intrinsic layer thickness of 10 μm to 100 μm [105]). It is crucial to note that for every material junction, depending on the relative alignment of conduction and valence bands (and other effects as band bending, tunnelling or polarization which we will omit herein for simplicity), the hole and electron mobilities over the junction and in the materials might differ. This effect leads to differences in their respective conductivity over the junction as described by Equation 4.4, which achieves the required charge carrier selectivity.

In this context, an important side note has to be made on the proper definition of fields and voltages (that is potential differences) in a device stack because this topic is prone to misconception in literature. As stated above, it is often argued that the separation of charge carriers from atom cores leads to the build-up of an 'internal field' or 'built-in field', $-\nabla\phi$, over a semiconductor junction or even a full device. However, this internal field is not associated with a measurable potential difference (that is an energy difference) neither

over the junction nor the electrodes, which is a common misconception. In contrast, when calculating the real, net field over a junction or device, we need to use the gradient of the electrochemical potential $\nabla\eta_i/e$ as in Equation 4.7 for electrons and holes, respectively. Consistently, after the contacting, both species of charge carriers follow any real fields $\nabla\eta_{\text{tot}}$ until $\nabla\eta_{\text{tot}} = 0$ (in other words a constant Fermi level is reached), which is what we would intuitively expect to happen in any non-insulating material (mathematically, the internal field is accounted for in the electrical potential in Equation 4.9, but only the total electrochemical potential determines the equations of motion and therefore any measurable potential differences). The above argument implies that the internal field alone cannot be a relevant parameter for any dynamic process, in particular not for separating electron-hole pairs or free charge carriers (which is another common misconception), because a single charge carrier moving through the device would not 'see' this mathematical field contribution but only the total electrochemical potential (therefore, as stated before, the ETL and HTL junction act as a 'membrane' rather than an 'energy barrier'). If the term 'internal field' is used correctly, it is a figure of merit for the amount of charge redistribution over a junction or device, which is actually a measurable quantity [106, 107, 108] . However, this is a very delicate argument that can be misleading. This is why we always mean $\nabla\eta_{\text{tot}}/e$ or $\Delta\eta_{\text{tot}}/e$ (and not $-\nabla\phi$) when we talk about fields or voltage in the following. We note that such real field can exist in the device, if an external source constantly provides energy to keep it up as for example given by external electromagnetic fields (which is sunlight in case of a solar cell) or heat sources.

Upon illumination, Fermi level splitting is present in the absorber as explained in the last section. This implies that the electrochemical potentials at the contacts no longer equilibrate such that the voltage $(\varepsilon_{\text{FC}} - \varepsilon_{\text{FV}})/e = \Delta\eta/e$ is present at the terminals (see Figure 4.2b). As stated earlier, the precondition for this voltage are different conductivities of holes and electrons over the respective ELT and HTL junctions. Otherwise the generated electrons and holes would 'use' the intermediate energy state of the electrodes to recombine. Once the excited charge carriers are separated according to their polarity and reach the terminals, they can be used in an external circuit flowing from the anode to the cathode along the technical current direction. This current flow will lower the concentrations of electrons in the conduction band and holes in the valence band, thus lower ε_{FC} at the anode and raise ε_{FV} at the cathode, thereby decreasing the voltage present at the terminals. At short circuit

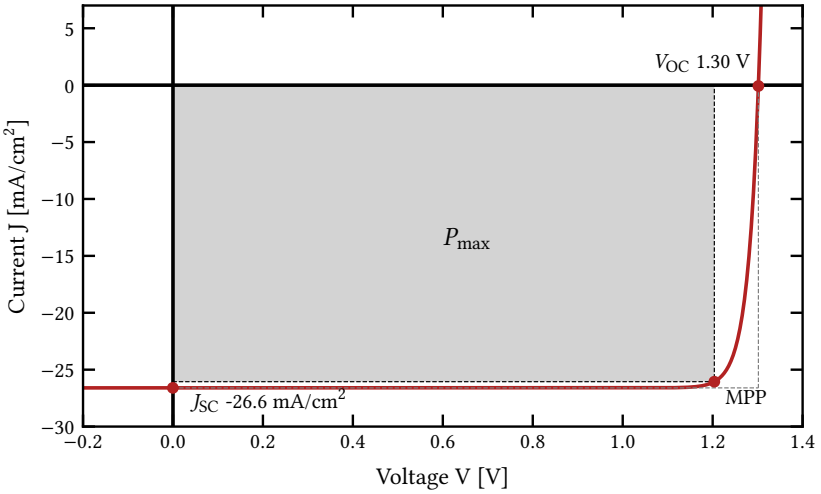

Figure 4.3.: Ideal solar cell JV-curve with a marking of the J_{SC}, V_{OC} and MPP points as well as a grey shaded rectangle indicating the maximum power (and a dashed-lined transparent rectangle indicating the product of V_{OC} and J_{SC} as used in the calculation of the FF).

conditions, ε_{FV} and ε_{FC} align at the terminals just as in the dark case (whereas the Quasi Fermi level splitting is still present in the absorber). Contrarily, at open circuit conditions, the voltage $\Delta\eta/e$ at the terminals is at a maximum. However, certain non-radiative (surface) recombination mechanisms at the terminals can still lower the voltage at the electrodes with respect to the the Fermi level Splitting in the absorber, which we will address in the next section.

Interestingly, the current over a *pn*-junction in the dark is not dominated by its transport resistance but by the effective resistance induced via recombination and generation of electrons and holes in the depletion region[25, p.138-142]. Under illumination, we have to consider that additional excited charge carriers are created in the semiconductor (that is, not only within the depletion region) which contribute to the total current. When calculating the radiative charge carrier generation and recombination rates, G and R, of a homogeneously illuminated *pn*-junction (or a structure shown in Figure 4.2b), the continuity

equation, $\nabla \cdot \vec{j} = G - R$, can be rewritten to yield the ideal current density-voltage characteristics of an illuminated *pn*-junction [25, p.138-142],

$$J_Q = J_S \left[\exp\left(\frac{eV}{kT}\right) - 1 \right] + J_{SC}, \tag{4.25}$$

plotted in Figure 4.3 where V is the terminal voltage, J_S is the dark saturation current of the diode and

$$J_{SC} = -e \int_0^\infty a(\nu) dj_{\gamma,\text{in}}(\nu) \tag{4.26}$$

is the so-called *short circuit current density* obtained by integrating over the absorptance, $a(\nu)$, multiplied with the incident solar irradiation element, $dj_{\gamma,\text{in}}(\nu)$ (see J_{SC} point in Figure 4.3). We note that the typically used reference spectrum is the solar spectrum after the transition through 1.5 times the thickness (or mass) of the atmosphere (AM1.5). With this data at hand, the above equation can be used to calculate the idealized J_{SC} under the assumption that $a(\nu) = 1$ for all $h\nu > \varepsilon_G$ and $a(\nu) = 0$ otherwise, yielding 26.3 mA cm^{-2} for the bandgap of MAPI of 1.58 eV. It is important to be aware that the spectra of solar simulators differ from the ideal AM1.5 reference, such that the J_{SC} must be corrected by the so-called *spectral mismatch factor* via the external quantum efficiency [109]. (In this work, we will not conduct this correction, which impacts the exact values of PCE values. Since this work is however not about exact absolute device PCEs, but more about comparing different processing method, it is not a major drawback).

Setting $j_Q = 0$ yields the *open circuit voltage* [25, p.143] (see V_{OC} point in Figure 4.3) as

$$V_{OC} = \frac{kT}{e} \ln\left(1 - \frac{J_{SC}}{J_S}\right). \tag{4.27}$$

Since $J_{SC} > J_S$ at solar irradiation, it becomes evident that the J_{SC} and J_Q must have opposite signs for the V_{OC} to be well-defined. The power per irradiated area, $J_Q \cdot V$, of the solar cell can be maximized from equation 4.25 yielding the *maximum-power point voltage*,

$$V_{MP} = V_{OC} - \frac{kT}{e} \ln\left(1 + \frac{eV_{MP}}{kT}\right) \approx V_{OC} - \frac{kT}{e} \ln\left(1 + \frac{eV_{OC}}{kT}\right), \tag{4.28}$$

and the corresponding *maximum power point current density*, $J_{MP} = J_Q(V_{MP})$ (see maximum power point drawn in Figure 4.3) [25, p.171-174]. With the *MPP*, we can calculate the *Fill Factor*

$$FF = \frac{J_{MP}V_{MP}}{J_{SC}V_{SC}} \approx \frac{eV_{OC}/kT - \ln(1 + eV_{OC}/kT)}{1 + eV_{OC}/kT}, \tag{4.29}$$

which is the ratio of the maximum power rectangle (see grey area in Figure 4.3) and the rectangle enclosed by the J_{SC} and the V_{OC} (see grey dashed line in Figure 4.3). We will see in the next section that an ideal MAPI perovskite solar cell has a V_{OC} of around 1.3 V (which is determined by the bandgap energy subtracted the radiative recombination losses). With this value, we obtain an FF of 90% at room temperature. The *power conversion efficiency* [25, p.174] is defined as

$$PCE = \frac{J_{MP}V_{MP}}{\int_0^\infty h\nu \, dj_{\gamma,in}(\nu)} = \frac{FF \cdot V_{OC} \cdot J_{SC}}{P_{in}}, \tag{4.30}$$

which holds also for non-ideal solar cells where Equations 4.29 and do 4.28 not necessarily hold any more. $P_{in} \approx 100\,\mathrm{mW\,cm^{-2}}$ is the average global irradiation power incident on the Earth's surface after the sunlight passed through the atmosphere (for the standardized AM1.5 spectrum of a solar simulator this value might differ). The optimum PCE of a solar cell with one absorber material and no solar light concentration can be determined to be around 33% at $\varepsilon_G = 1.34\,\mathrm{eV}$ (Shockley-Queisser-Limit) [25, p.174-175]. The reasons are that, first, due to thermalization a photon of $h\nu > \varepsilon_G$ can maximally contribute the energy ε_G to the extractable power and, second, all photons with $h\nu < \varepsilon_G$ cannot be absorbed. It must however be noted that this maximum is quite broad around for $1\,\mathrm{eV} < \varepsilon_G < 1.5\,\mathrm{eV}$, which makes hybrid perovskites with a tunable bandgap from 1.2 eV to over 2 eV (most studies use perovskite compositions with bandgaps close the MAPI bandgap of 1.58 eV) a good candidate for photovoltaics. In fact, the PCE of the ideal solar cell shown in Figure 4.3 is at 31.5%, which is very close to the Shockley

Queisser limit of 32% at this bandgap, showing that the assumptions made above were consistent.

4.5. Power generation in real solar cells

As stated above, the current-voltage characteristics introduced in the last section (and in particular the equations for the FF and V_{OC} (4.29 and 4.28) are based on the assumption that the only available recombination mechanism in the solar cell is radiative recombination. In a real solar cell however, non-radiative recombination reduces the Fermi-level splitting and thereby the V_{OC} and FF. The amount of non-radiative recombination (as compared to radiative recombination) can be gauged by determining the external quantum efficiency, EQE_{EL}, that is the number of externally emitted photons per injected electron, as measured by electroluminescense – the luminescence emitted under forward electrical bias of the solar cell. It can be related to the internal quantum efficiency approximately as

$$EQE_{EL} = \frac{IQE \cdot \eta_{OC}}{1 - IQE \cdot (1 - \eta_{OC})}, \tag{4.31}$$

where η_{OC} is the outcoupling efficiency determining how many of the emitted photons can escape before being absorbed by parasitic absorption in the layers sandwiching the absorber [26, p. 13]. With this, it can be shown that

$$eV_{OC} = \varepsilon_G - kT\frac{N_C N_V}{n_h n_e} \approx \varepsilon_G - e\Delta V_{OC,rad} - kT \ln EQE_{EL}^{-1}, \tag{4.32}$$

where $\Delta V_{OC,rad} \approx 0.27\,V$ such that $\varepsilon_G/e - 0.27\,eV$ is the purely radiation limited V_{OC} [26, p.14]. The above equation implies that the higher the luminescence of a forward-biased solar cell, the higher its achievable PCE. We note that, by convention, eV_{OC}/ε_G is calculated as an important figure to estimate the relative magnitude of the V_{OC}. It is crucial to keep in mind that the radiative limit, calculated as above, retains this value to a maximum of about 83% for hybrid perovskites even before non-radiative losses are considered.

Additional to the non-radiative recombination, we have to consider possible shunt passes, introducing a shunt resistance $R_{parallel} < \infty$ and possible series

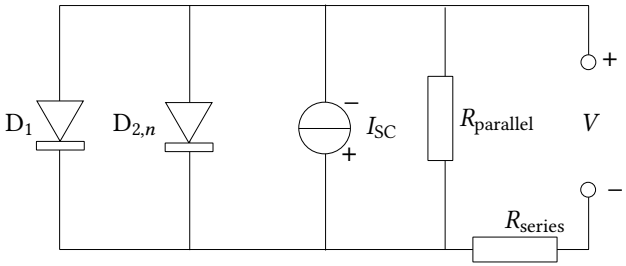

Figure 4.4.: Equivalent circuit of a thin film solar cell with a series resistance $R_{\text{series}} > 0$, a shunt resistance $R_{\text{parallel}} < \infty$ and a second path of recombination diode with ideality factor n.

resistances over the contacts leading to $R_{\text{series}} > 0$. This yields a model equivalent circuit shown in Figure 4.4, whose current flow is described by

$$I = I_{S1}\left[\exp\left(\frac{e(V - I_Q R_S)}{kT}\right) - 1\right] + I_{S2}\left[\exp\left(\frac{e(V - I_Q R_S)}{nkT}\right) - 1\right] + I_{SC} + \frac{V - I_Q R_S}{R_p}, \quad (4.33)$$

where n is the so-called ideality factor of non-radiative recombination and we use the abbreviated notation R_s and R_p for the series and parallel resistance, respectively [25, p. 183-185]. For Shockley-Read-Hall recombination limited by bipolar conduction, the ideality factor takes the value $n = 2$. For Auger recombination it becomes $n = 2/3$ [110].

We will now analyse the effect of the different parameters on simulated JV-curves according to Equation 4.33 (see Figure 4.5). First of all, we start with a variation of the number of impurities available for non-radiative recombination that is an increase in I_{S2} in exponential steps (see Fig. 4.5a). We find that if I_{S2} is low enough it does not influence the JV-curve because Equation 4.33 is dominated by the leading factor I_{S1}. However, if I_{S2} exceeds a certain order of magnitude, it makes the first term almost immediately irrelevant and the altered slope through the changed ideality factor (here $n = 2$) becomes evident. Furthermore, the V_{OC} reduces in linear steps as I_{S2} increases exponentially, while the J_{SC} remains unchanged (so does the FF once I_{S2} has passed the threshold). This is consistent with Equation 4.32.

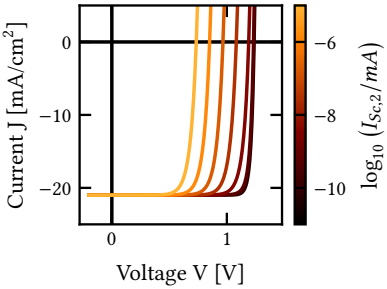

(a) JV-curves for different non-recombination currents

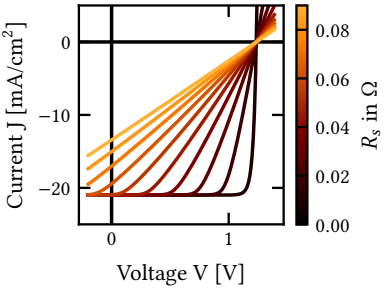

(b) JV-curves for different series resistances R_s

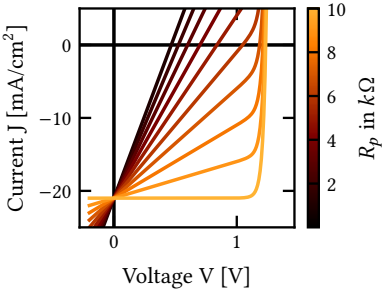

(c) JV-curves for different shunt resistances R_p

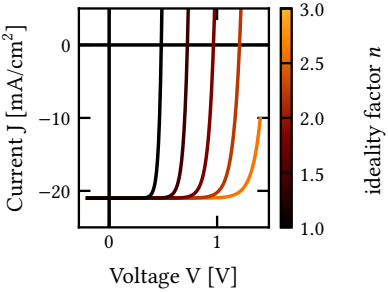

(d) JV-curves for different ideality factors n

Figure 4.5.: Variation of different parameters during the simulation of IV curves based on Eq 4.33

If we increase the series resistance R_s in linear steps, we see that the slope of the JV-curve at the V_{OC} decreases, leaving the V_{OC} and the J_{SC} (until very extreme values) unchanged, while lowering the FF. This is consistent with intuition when keeping in mind that an ohmic resistance in series draws electrical power only when it is available which is not the case at the J_{SC} and V_{OC} (see Figure 4.5b). If a parallel resistance $R_p < \infty$ is added, a slope will be introduced at the J_{SC}, leaving the J_{SC} unchanged, while reducing the V_{OC} slightly (at first) and the FF significantly. In this case, it is clear that the higher the voltage, the more current will flow over the shunt, reducing the

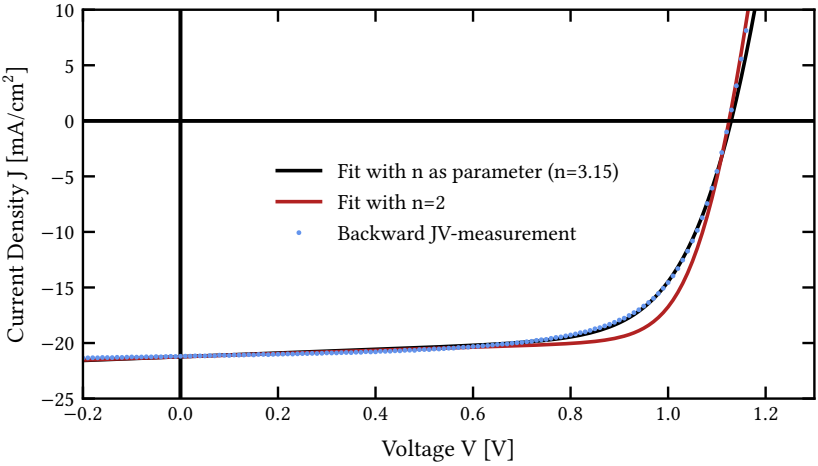

Figure 4.6.: Fit of the simulated JV-curves contained in Equation 4.33 to a measured JV-curve (red with $n = 2$) and (black with $n = 3.15$). Values $n > 2$ do not correspond a model of physical recombination dynamics, but rather show that the equivalent circuit shown in Figure 4.4 is insufficient to explain the charge carrier dynamics in perovskite solar cells.

terminal current and thereby the usable power that the terminals can provide (see Figure 4.5c). Figure 4.5d shows a variation of the ideality factor from 1 to higher values, showing that it affects mainly the FF (it also increases the V_{OC} but this is not a real trend since an increase in non-radiative recombination is most-likely accompanied by a significant increase in I_{S2} reversing the V_{OC} trend). Values above $n = 2$ (that would also decrease the V_{OC}) cannot be identified with a physical charge carrier recombination process (see explanation above). We have included them here just because they would occur when fitting Equation 4.33 to the JV-curves measured within this work at 1 sun, as detailed below.

Figure 4.6 shows the measured JV-curve of one of the best triple cation perovskite solar cells that were fabricated during the work on this thesis by dynamic gas quenching (processing and architecture will be introduced in sections 5.1, 5.3 and 8.3). We note that with the physically sensible ideality

factor for Shockley-Read-Hall recombination $n = 2$ we find ourselves unable to reproduce the measured shape by adjusting R_p, R_S and I_{S2}. Only by choosing $n = 3.15$ we can reproduce the measured data, which clearly cannot be identified with any physical charge carrier recombination process (To potentially obtain the physical ideality factor, n, a proper measurement at varying light intensity can be conducted [108].). This is a clear indication that the model introduced above is incomplete. A more detailed modelling framework is beyond the scope of this thesis. We want however like to refer to a quite recent publication of Uwe Rau and Thomas Kirchartz on the combination of resistive and kinetic models for the accurate simulation of hybrid perovskite solar cell JV-curves [111]. It is also possible that ion drifts and accumulation play role in the deviation of the JV-curve from the above model as detailed in the next section.

4.6. Hysteresis in perovskite solar cells

Another important phenomenon that causes a deviation of the JV-characteristics measured in perovskite solar cells from the model derived above is the *hysteresis* effect. Phenomenologically, hysteresis describes the discrepancy of JV-curves depending on the direction of the scan – in detail if the scan starts at reverse or forward bias and progresses toward forward or reverse bias, respectively. In the MAPI solar cells covered in this thesis, hysteresis is pronounced, while the multi-cation perovskites exhibit less hysteresis (compare Figures 4.7a and 4.7b). However, certain groups reported MAPI solar cells without hysteresis by interface modification at the ETL [112, 113]. This shows that hysteresis is a perovskite-dependent but also an interface dependent phenomenon. Consistently, the perovskite research community has come to the consensus that the hysteresis is mainly caused by the accumulation of mobile ions at the device interfaces potentially altering the charge conduction over these interfaces [114, 113]. This accumulation is the results of ion drifts from the bulk perovskite to the interface when the device is biased. A common addition to the equivalent circuit for modelling this ion drift is depicted in Figure 4.8.

The ion drift is represented by an additional diode and the accumulation on the interface by an additional capacitor. Since the ion drift diffusion coefficients are much smaller than the diffusion coefficients of the electrons

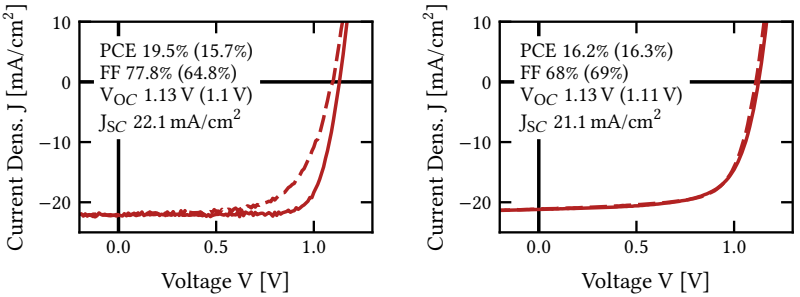

(a) MAPI solar cell fabricated in the laminar air flow exhibiting a strong deviation between backward and forward scans.

(b) TCP solar cell fabricated in dynamic gas quenching showing no clear deviation between backward and forward scans.

Figure 4.7.: Comparison of JV-curves in backward (solid line) and forward JV-scans (dashed line) of best MAPI and TCP solar cells fabricated during the work on this thesis with a scan speed of 1 V s^{-1}.

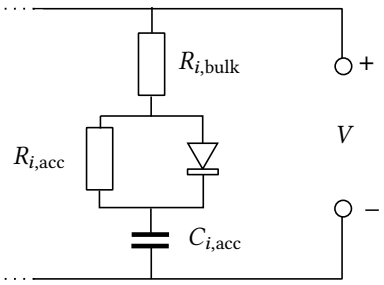

Figure 4.8.: Addition to the equivalent circuit shown in Figure 4.4 modelling the ion drift in the device.

and holes in the device, two resistors are employed – one for the bulk diffusion, R_{bulk}, and one for the transport away from the interface once the bias in reversed $R_{\mathrm{i,acc}}$. As a result, when forward bias is supplied first, the capacitor is slowly charging during the scan decreasing the available current, while in reverse bias, the diode blocks the charging process such that full current is available at the terminals. To eliminate the effect of hysteresis, constant voltage measurements will be conducted for the best devices in this work. During this measurement, the device is constantly biased in one direction

such that the capacitor equivalent circuit comes to an equilibrium state, no longer drawing current from the rest circuit. Of course, it is still possible that this equilibrium accumulation of ions changes the charge transfer over the junction. However, a constant bias is much closer to a real-life application of the solar cell, whereas a rapid JV-scan has only the purpose of quickly determining the approximate PCE of the device.

5. Experimental methods

5.1. Hybrid perovskite solution processes*†‡

In this section, we describe the fabrication processes of the perovskite absorber layer, which were chosen as a reference for the up-scaling (and toxic solvent replacement) efforts explained in more detail chapter 8 according to the respective process. The fabrication of the other functional layers was unaltered (except for the spin coating parameters for different substrate sizes as described in section 5.3) and will be described in the end of the section. The perovskite reference processes rely on the spin coating method on a substrate size of $16 \times 16\,\mathrm{mm}^2$. We will use them with following designation:

- *$MAPbI_3$ (*MAPI*) one-step process[19, 20]:*
  $PbCl_2$:3MAI and $Pb(CH_3COO)_2 \cdot 3H_2O$:3MAI were mixed in a molar ratio of 1:4 and dissolved in DMF with a concentration of 1.05 M [115]. (1 M is defined as 1 mmol of solute per 1 ml of solvent.) The solutions are mixed in separate vials and then one is added to the other, just before the spin coating process. The spin coating is run at 3000 rpm for 30 s and then the sample is left for 9 min of natural drying until the annealing process is started at 110°C for 10 min [116]. For the blade coating precursor, the concentration is lowered to 0.75 M [19].
- *Double cation (*DCP*) two-step process:* The original recipe as developed by Jiang et al. [117] uses DMF as a solvent with an addition of 5% (volume) of DMSO for the deposition of the PbI_2 at a concentration of 1.3 M

*Section reviews Advanced Energy Materials 9 (2019) p. 1901581 by S.T., B.T., J.A.S, I.M.H., T.A., W.M., U.L., P.S., W.S., B.S.R. and U.W.P [19]

†Section reviews Solar RRL 6 (2021) p. 2100353 by S.T., F.L., P.S., W.S., B.S.R., I.A.H. and U.W.P. [20]

‡Section reviews ACS Applied Materials & Interfaces (2022) 14, 9, p. 11300–11312 by S.T., J.M., N.L., H.M.P, M.A., P.S., W.S., B.S.R and U.W.P. [21]

(For the green solvent recipe, this solvent mixture is replaced by DMSO with 10% [volume] of ethylene glycol monobutyl ether [EGBE]). The surfactants (Alpha-LP: L-α-Lecithin, DDAB: Didodecyldimethylammoniumbromide, HD-TMAB: Hexadecyltrimethylammonium bromide) are respectively dissolved in a 0.5 mg ml^{-1} stock solution in DMSO and then 5 volume % of this solution is used instead of the pure DMSO. The PbI_2 layers are spin coated at 1500 rpm for 30 s and annealed for 1 min at 70°C. For the second step, a solution of FAI:MABr:MACl dissolved in Isopropanol (60 mg : 6 mg : 6 mg in 1 ml) is spin coated at 1500 rpm for 30 s and annealed at 150°C for 15 min in ambient air. For the blade coating, the PbI_2 concentration is optimized to be 1 M and the concentration of the cations is decreased by a factor of two (60 mg : 6 mg : 6 mg in 2 ml). The final perovskite has the stoichiometry $(FAPbI_3)_{1-x}(MAPbBr_3)_x$ where $x \approx 0.03$ [118].

- *Triple cation (*TCP*) one-step process[21]:*
  PbI_2 (1.1 M) is mixed with FAI (1 M), $PbBr_2$ (0.2 M), MABr (0.2 M) in DMF and DMSO (v:v ratio 4:1) [119]. Subsequently, 89 μl of CsI (1.5 M) dissolved in DMSO are added. For the green solvent precursor, DMF and DMSO are replaced by DMSO and 5% (volume) of EGBE. The perovskite composition is $Cs_{0.1}(FA_{0.83}FA_{0.17})_{0.9}Pb(I_{0.83}Br_{0.17})_3$. The spin coating is conducted by a first step at 1000 rpm for 10 s and a second step at 6000 rpm for 20 s. 10 s before the end of the second step, 100 μl of Chlorobenzene is poured onto the still spinning substrate in a time of about 2 s. The blade coating is performed with the very same perovskite solution.

Besides the perovskite solution processes, we also process the ETL and HTL interlayers. For these we make the following dispersion and solution:

- *Dispersion of SnO_2 nanoparticles*:
  The nano-particle colloidal dispersion was purchased from Alfa Aeser (15%) and is diluted to 2% with deionized water. The spin coating is then performed at 4000 rpm for 30 s in ambient air and the samples are annealed at 250°C [19] for 1 h. (For the spin coating on larger substrates the spin coating parameters are varied as described in section 5.3)

- *Spiro OMeTAD-solution:*
  80 mg of Spiro OMeTAD purchased from Luminescence Technology is dissolved in 1 ml of Chlorobenzene and doped with 28.5 μl ml^{-1} of 4-*tert* butylpyridine and with 17.5 μl of Lithium bis[trifluoromethanesulfonyl]

imide from a stock solution of 520 mg ml^{-1} in Acetonitrile [120]. The spin coating is performed at 4000 rpm for 30 s in an inert N_2 environment. The spiro-coated substrates are doped with oxygen for about 12 − 15 h at 30% humidity.

5.2. Blade coating of hybrid perovskite thin-films*†‡

Blade coating is a common trial fabrication method for scaling solution processing. The method involves a blade with exactly defined height, h_0, that is dragged or pushed over a substrate with velocity v. In this process, the solution, deposited before the blade, is dragged with the blade leaving behind a liquid film of defined thickness controlled by the above parameters and the sheer forces in the solution (see Figure 5.1). According to rheology, the deposited film has the wet film thickness [121].

$$h_\infty \approx h_0/2, \tag{5.1}$$

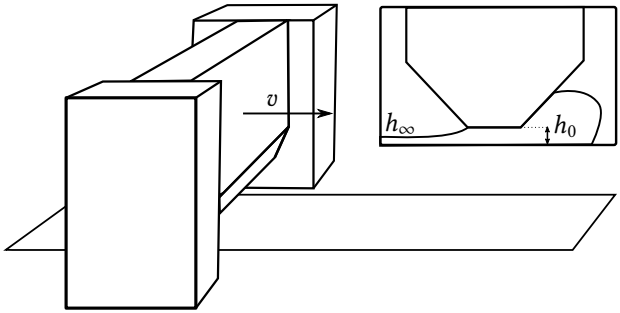

Figure 5.1.: Schematic of blade coating process with the blade coating speed, v, (sometimes called web speed) and the blade gap, h_0.

*Section reviews Advanced Energy Materials 9 (2019) p. 1901581 by S.T., B.T., J.A.S, I.M.H., T.A., W.M., U.L., P.S., W.S., B.S.R. and U.W.P [19]

†Section reviews Solar RRL 6 (2021) p. 2100353 by S.T., F.L., P.S., W.S., B.S.R., I.A.H. and U.W.P. [20]

‡Section reviews ACS Applied Materials & Interfaces (2022) 14, 9, p. 11300–11312 by S.T., J.M., N.L., H.M.P, M.A., P.S., W.S., B.S.R and U.W.P. [21]

However, there are other reports stating that, at high enough velocities, the thickness of a dry phospholipid film, h, follows the relation $h_\infty \propto v^{0.76}$ [122]. In our experiments, we obtain values much lower than $h_0/2$. (The total volume of solution per substrate area used is less and the interferometry measurements introduced in section 7.1 suggest smaller wet film thicknesses). The reason for this could be that we are indeed in a regime where $h_\infty \propto v^{0.76}$ or similar holds. Other possible reasons are that Equation 5.1 describes a long-term static case, which is not reached yet with the substrate sizes we use, or that we simply do not use enough solution for Equation 5.1 to be valid. Afterall, we conclude that a quantitative determination of the wet film thickness just from rheological parameters is challenging. It is crucial to note that wet film thicknesses much smaller $h_0/2$ are favourable for the fabrication of hybrid perovskite absorbers. The reason is that for a concentration of 1.3 M and a targeted final perovskite film thickness of 0.8 μm, we need to deposit a wet film thickness of 4.8 μm as calculated by $0.8\,\mu\text{m}\left[1+\tilde{\rho}_\text{p}/1.3\,\text{M}\right]$ (lowering the perovskite concentration too much is usually not a useful mitigation strategy because it enhances drying related inhomogeneities and subsequently causes an inhomogeneous nucleation). Using a blade gap of 10 μm would however not be feasible due to the tolerances of the substrate, the surface holding the substrate and the blade sliding over the same surface (instead, we use $100\,\mu\text{m} - 200\,\mu\text{m}$ in our experiments).

In conclusion, because we cannot calculate the wet film thickness from rheological parameters, we always estimate it from measuring the dry film thickness, d_p, using the relation[21]

$$d_0 \approx d_\text{p}\left[1+\tilde{\rho}_\text{p}/\tilde{m}_\text{p}\right] \tag{5.2}$$

where $\tilde{m}_\text{p}$ is the molar mass of perovskite per solvent and $\tilde{\rho}_\text{p}$ is the molar mass of the perovskite as calculated from the size of the unit cell [31].

Lastly, let us shortly motivate why blade coating is chosen as the principal deposition technique in this work. Blade coating is the ideal pre-experiment to establish pre-metered slot-die coating, in which new solution is continuously supplied through a small slot [121]. As compared to blade coating, this has the advantage that stabilized coating is possible on arbitrary substrate lengths that is to say even in roll-to-roll coating machines where kilometres of flexible substrates can be coated ('stabilized' means in this context that a video of the coating process would show a constant image). From a practical point

of view, slot-die coating is more challenging to use on a small substrates because a long run-in length is needed until coating and solution supply rate equilibrate, achieving stabilized coating. Furthermore, the technique has a comparatively high 'dead volume', that is an amount of solution on the order of ml needs to be supplied just to fill the feed-in pipes and the nozzle before reaching the substrate. In blade coating, this is not the case. For the average substrate size of $6 \times 3\,\mathrm{cm}^2$ used in this thesis, the amount of solution was on the order of 20 μl [19], which is less than is needed in spin coating for a square substrate of the size $16 \times 16\,\mathrm{mm}^2$. This advantage makes blade coating the ideal candidate for trial experiments bridging the gap between spin coating and slot-die coating.

5.3. Fabrication and characterization of solar cells*†‡

For all the devices covered in this thesis, the *n-i-p* architecture is chosen. The devices are fabricated in the following way [19, 20, 21]: An indium tin oxide (ITO)-coated pre-patterned substrate ($64 \times 64\,\mathrm{mm}^2$) is spin coated with the aqueous SnO_2 nano-particle dispersion for forming the ETL layer (details about the dispersion were provided in section 5.1) using 2000 rpm and 30 s (see step 1 in Figure 5.2) and annealed at 250°C for 60 min thereafter. Then, the substrate is broken in two $32 \times 64\,\mathrm{mm}^2$ parts and the perovskite absorber layer is deposited by blade coating with the respective solution process (see step 2 in Figure 5.2; details follow in chapter 8; for the spin coating as described in section 5.1 the substrates are broken in 16 small $16 \times 16\,\mathrm{mm}^2$ samples.). Subsequently, each such substrate part is broken again into 8 smaller $16 \times 16\,\mathrm{mm}^2$ patches and these are spin coated with a Spiro-OMeTAD layer (see step 3 in Figure 5.2 and details in section 5.1). Finally, Au is thermally evaporated to complete the device stack. Each substrate contains

*Section reviews Advanced Energy Materials 9 (2019) p. 1901581 by S.T., B.T., J.A.S, I.M.H., T.A., W.M., U.L., P.S., W.S., B.S.R. and U.W.P [19]

†Section reviews Solar RRL 6 (2021) p. 2100353 by S.T., F.L., P.S., W.S., B.S.R., I.A.H. and U.W.P. [20]

‡Section reviews ACS Applied Materials & Interfaces (2022) 14, 9, p. 11300–11312 by S.T., J.M., N.L., H.M.P, M.A., P.S., W.S., B.S.R and U.W.P. [21]

four pixels of the size of roughly 0.1 cm^2 (see schematic of the device stack in Figure 5.3).

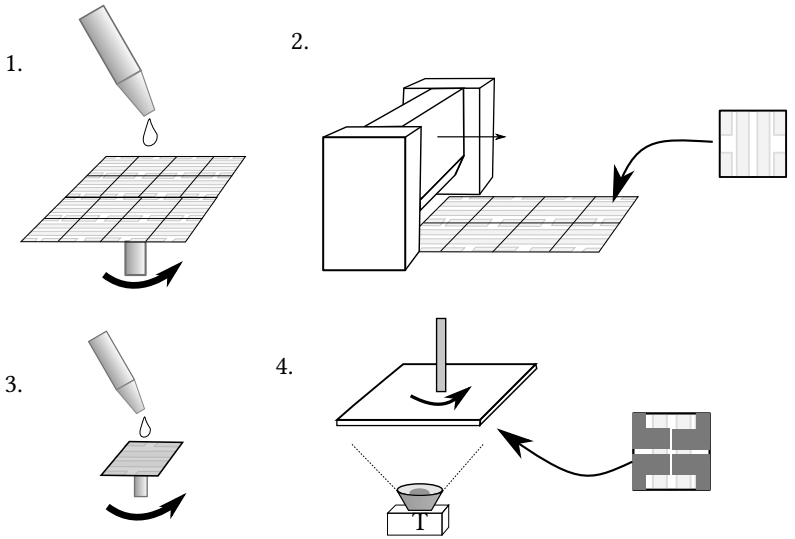

Figure 5.2.: Schematic of perovskite device fabrication in four steps: SnO_2 nano-particle spin coating (1), blade coating of perovskite thin-film (2), spin coating of Spiro OMeTAD (3) and thermal evaporation of Au back contacts (4). Pre-patterned substrates are pre-cut on the bottom side before the first step such that they can be easily broken for the respective next step.

This fabrication process and device architecture are chosen for multiple reasons. First of all, the spin coating of SnO_2 nano-particles and Spiro OMeTAD solution is a fast and already precisely optimized solution process. Second, residual PbI_2 as produced by the two-step process (details follow in section 8.1.2) works as an n-type conductor [123]. Because residual PbI_2 is preferentially present at the bottom contact as the cation solution is deposited from the top, this contact must be an ETL for the respective devices to work. Third, because the work on this thesis started with this architecture, the fabrication process was kept unaltered for the comparability of all differently fabricated perovskite layers. This has, of course, an impact on the maximum achievable PCE, but the advantage is that differences in the JV-parameters can be traced back to differences in the perovskite with almost absolute certainty. (This will be covered in more detail in the analysis of device performances, section

8.4). Trial experiments show however that other architectures are mostly compatible with the methods explained herein, which is beyond the scope of this work.

The devices are characterized by a standard AAA class solar simulator (Newport Oriel Sol3A or Wavelabs Solar Metrology Systems Sinus-70) under an AM1.5G spectrum by JV-sweeps with $1\,\mathrm{V\,s^{-1}}$ [19]. Evidently, the impact of hysteresis needs to be considered when performing such an analysis. For this reason, we always provide backward and forward scans as well as JV-parameter values for both (in some plots in the analysis of device performances, section 8.4, the average of the backward and forward values will be used). Furthermore, measurements under constant voltage of the best solar cells are performed because this simulates better a real application and is less affected by hysteresis as explained in section 4.6. As detailed above, the emphasis of this work is rather on comparing the PCEs between different perovskite deposition methods than on the optimization of devices toward highest, absolute PCE. Therefore, the quick measurement of a large number of small devices and their comparison is preferred to a very exact characterization of individual devices.

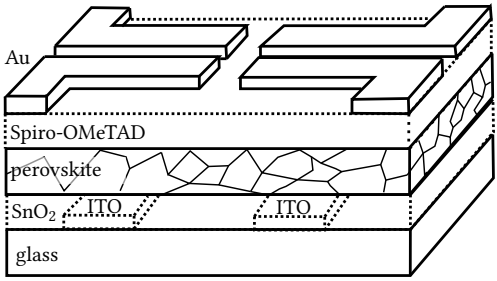

Figure 5.3.: Magnified device stack on a $16 \times 16\,\mathrm{mm^2}$ substrate. The layer thicknesses are not to scale (For the real layer thickness see Figure 5.5 in the next section).

One might ask the question why the device active area is not increased during this work, especially with regard to the topic of up-scaling perovskite solution printing. One part of the answer is that multiple probing of the laterally distributed device performance is preferred to an up-scaled large-area performance, which we would expect to perform, in the ideal case, as an average over all small device performances, and in the worst case, as the weakest of these devices, thereby potentially removing valuable statistical

information. Another part is that, as we will see in chapter 8, although there are individual substrates with almost flaw-less morphology on the lateral area, their appearance is still a statistical outlier. It would have therefore needed many tries to make a large area device, which is valuable work time that was invested instead in the the question if drying and crystallization can be analysed and understood with the goal to avoid the statistical variation in the first place (which is necessary for industrial scale fabrication in the future). In future works, when the lateral device homogeneity as well as the reproducibility of these absorbers is sufficient, larger devices can be fabricated.

5.4. Ex situ thin-film imaging and scanning*†‡

Scanning or imaging methods are crucial to determine homogeneity and morphology of processed perovskite absorber thin-films. '*Ex situ*' refers in this context to techniques that are applied after the annealing process, that is after the fabrication of perovskite thin-films is completed. Because these methods are a well-known standard in the research community, we do not explain their working principle in great detail. Instead, we focus on the question which pieces of information can be acquired by the respective method and give a typical example of a decisive measurement, which was used to analyse perovskite drying and crystallization in this thesis.

- *Optical microscopy*
  is a fast and very common imaging technique. Because the wavelengths of visible light range from about 380 nm to 750 nm, the resolution of smallest structures is also of that order of magnitude (Rayleigh criterion). This implies that typical perovskite grain sizes ($\approx$ 10 nm – 100 nm) and the layer thicknesses ($\approx$ 500 nm – 1000 nm) are mostly below the resolution limit of optical microscopy[19, 21]. However, in case macroscopic crystalline structures such as ribbons, dendrites

*Section reviews Advanced Energy Materials 9 (2019) p. 1901581 by S.T., B.T., J.A.S, I.M.H., T.A., W.M., U.L., P.S., W.S., B.S.R. and U.W.P [19]

†Section reviews Solar RRL 6 (2021) p. 2100353 by S.T., F.L., P.S., W.S., B.S.R., I.A.H. and U.W.P. [20]

‡Section reviews ACS Applied Materials & Interfaces (2022) 14, 9, p. 11300–11312 by S.T., J.M., N.L., H.M.P, M.A., P.S., W.S., B.S.R and U.W.P. [21]

or cracks form in a thin-film, these can be detected easily by optical microscopy. The ideal perovskite film does not have any of these features detectable by optical microscopy (with few exceptions such as textures that can help light in-coupling [124].). The microscope image in Figure 5.4 shows the transition from a growth-dominated to a nucleation-dominated morphology[21] as will be explained in detail in section 8.3. While the dendrites of crystallites forming on the substrate (which are detrimental for the device performance) are clearly visible, the perovskite film with many very small nuclei (as used in efficient perovskite solar cells) appears transparent under the microscope (bottom of the picture). To access structures below the resolution limit of optical microscopy, other microscopic methods explained in the following two bullet points need to be used.

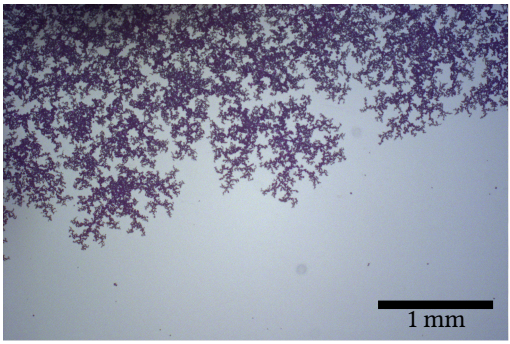

Figure 5.4.: Optical microscope picture of a TCP thin-film fabricated by dynamic coating under a slot nozzle (details follow in section 8.3). The transparent area is a perfectly nucleation-dominated perovskite morphology, while the dendrite structures form due to early heterogeneous nucleation at the substrate surface under non-ideal conditions.

- *Scanning electron microscopy* (SEM)
  is a microscopic technique where an electron beam is scanned over the probe and backscattered electrons are detected [125] (these can be primary backscattered electrons of the beam or secondary electrons ejected from the investigated material). SEM enables the resolution of structures with down to 1 nm due to the small de-Brogly wavelength of the electron at the used energies of several keV. In the commonly

used secondary electron channel, SEM is very surface sensitive (several nano-meters) because the secondary electrons are emitted from a small interaction volume. When operated laterally over the perovskite film surface, SEM can resolve the micro-structure of the polycrystalline perovksite thin-film morphology (some examples follow in section 8.1.1.). However, it can also be used to study the vertical morphology of a solar cell that was sliced or broken[19] as visible in Figure 5.5. Due to the different interaction cross-sections of different materials, the individual layers of the device stack can be distinguished by contrast and their vertical profile can be analysed. It has to be noted that, for a better conductivity, 5 nm of Au was sputtered on the stack before the measurement. So, the difference in contrast could also originate from different gold adhesion on the materials (high conductivities of the investigated specimen are crucial to prevent charging/degradation of the material which would impact the measurement).

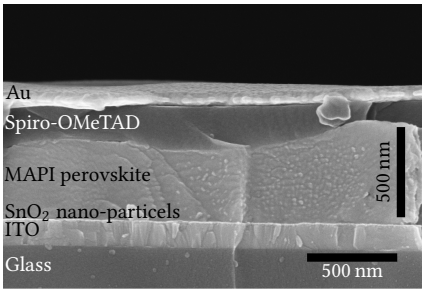

Figure 5.5.: Cross section of a MAPI perovskite solar cell fabricated within the work on the first publication [19]. The difference in scattered intensity (or cross section) indicates the different materials building up the device stack.

- *Atomic force microscopy (AFM)* or *scanning force microscopy* (SFM) is a microscopy technique where a cantilever with a sharp tip is scanned over a probe, while the cantilever vibrates with certain vibrational amplitude and frequency (in the most commonly used operation mode). The atomic forces close to the vibrating tip, impact the vibration frequency and/or amplitude, which are measured by a laser reflected from the back of the cantilever on a photo detector. The image is then created as a function on the cantilever position which is scanned

over the surface in back and forth movements using piezo-crystals. AFM reaches resolutions below 1 nm and can reach down to the size of individual atoms [126]. In the work on this thesis, it was used to investigate the polycrystalline morphology of perovskite thin-films[19, 21]. As compared to SEM, it has the advantage that it also yields height (and thereby roughness) information which can be handy when comparing different samples. Its disadvantage are the comparatively long acquisition times. An often used variation of AFM is profilometry (usually performed by a Bruker Dektak XT system [127] for example in section 8.1.2). In this case, the tip is in direct contact with the sample and scanned just along one line reading the force on the tip with an Inertia Sensor. This is a fast and easy method to determine film thicknesses (as difference between a reference surface and the film surface) and (1D) film roughness. Figure 5.6 shows an AFM measurement of a nucleation-dominated triple cation thin film (details follow in 8.3). It is visible that the micro-grain structure is overlaid by a wavy macro-structure. This wave-structure is often observed in rapidly quenched triple cation perovskites and is attributed to the release of stress[128]. It is further reported to improve the light in-coupling into these layers and enhance overall absorption [124].

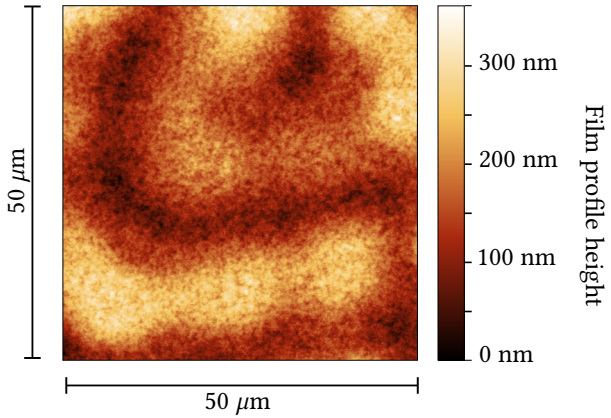

Figure 5.6.: Morphology of a nucleation-dominated triple cation perovskite film as measured by AFM. The morphology is an overlay of two structures: A rougher wave structure, which is reported to be caused by internal stress upon quenching [129], and a fine structure, which are the crystalline grains (that would not be visible in optical microscopy).

- *Whitelight interferometry (WLI)*
  is a profilometric technique just as AFM. However, the profile of the investigated sample is imaged by a Michelson-Morley interferometer whose one arm is fixed and the other one is given by the reflected light from the surface. The whole interferometer is driven up and down while imaging the interference fringes on a 2D camera sensor. From these 2D interference image series, the height at each measurement point (that is pixel on the camera) can be estimated [130, 131]. The advantages of WLI are the exceptionally fast acquisition times, in particular with large-area field of view systems like the Isravision netGAGE3D used in this thesis [132]. Figure 5.7 shows a typical sample as characterized with WLI for the second publication [20]. The magnified image extracts show typical morphological features that can appear during perovskite solution processing. (They will be correlated with device performances in section 7.2). This image can be acquired in less than 5 s, which is at least two order of magnitudes faster than AFM measurements. The disadvantage is however a comparably poor lateral resolution. As a consequence, roughness values will differ significantly from AFM measurements.

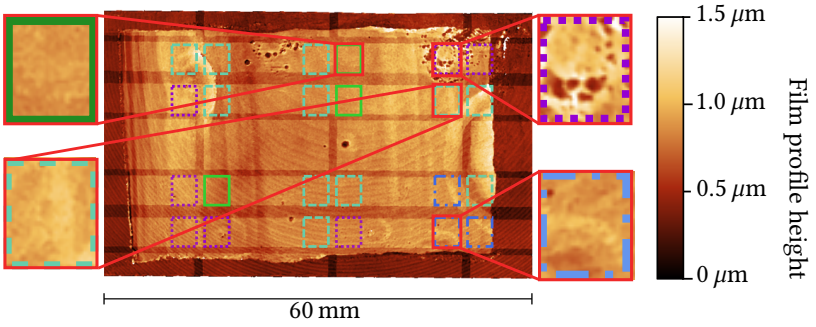

Figure 5.7.: Whitelight Interferometer measurement as conducted for the correlation with IMI data (details follow in section 7.2) [20]. Different morphological defects become apparent in the perovskite film morphology (the bright stripes are the patterned ITO on glass). The borders of the sample were swiped to remove the perovskite. This frame is used for levelling and removing drifts in the data and can also be used to estimate the thickness of the film. Reproduced with permission from [20].

Part III.

Results and discussion

6. Modelling and simulation

This chapter presents modelling toolkits motivated by standard literature on drying and crystallization processes[22, 24] and subsequently adapted to hybrid perovskite precursor solutions (a detailed list of the involved quantities and an order of magnitude estimation of their typical values can be found in the appendix in section A4). The convergence of the model predictions with the experiments is tested by interferometric measurements of drying dynamics in the laminar air flow as well as AFM images of polycrystalline perovskite films produced with different drying speeds (details on interferometry follow in section 7.1 and AFM was introduced in section 5.4). As the first main result, a gas phase controlled drying model is obtained that quantitatively reproduces the drying of MAPI and TCP solution films for $\mathrm{Bi}_d^{\mathrm{an.}}$ up to 10^3 (which will be demonstrated in section A1.5). As the second result, a qualitative simulation of crystal nucleation and growth in a perovskite solution is presented. The two resulting models can be connected yielding a criterion for successful drying/quenching of homogeneous perovskite thin-films. This can be seen as an answer to research questions 1. and 2. as introduced in section 3.3.

6.1. Description of perovskite solution film drying dynamics

6.1.1. Mass transfer and phase boundary equations

Drying is a mass transfer process in which a volatile component evaporates from a liquid, a solid or a mixture of compounds. In this work, we will focus on the drying process of solutions, that is a mixture of a solvent and solute — assumed to be homogeneous on the molecular scale. The drying of a liquid solution film can be described by three sub-processes:

1. The diffusion of the liquid solvent inside of the film to the film surface
2. The phase transition from liquid to gaseous solvent
3. The transport of gaseous solvent away from the film surface by gas-gas diffusion and convection

Figure 6.1 shows the involved, physical quantities. We will explain in the following the fundamental laws governing these sub-processes.

The transport of liquid solvent to the surface is described by Fick's first law of diffusion [133]. It reads

$$j_{i\mathrm{p}} = -D_i^V \frac{\partial \tilde{c}_i^V}{\partial z}, \tag{6.1}$$

where $j_{i\mathrm{p}}$ is the molar flux of solvent molecules $\left[\mathrm{mol\,m^{-2}s^{-1}}\right]$ in the solute material p (which stands traditionally for **p**olymer but can be understood as **p**erovksite herein), D_i^V is the diffusion coefficient or diffusivity $\left[\mathrm{m^2\,s^{-1}}\right]$ and $\tilde{c}_i^V$ is the concentration of the liquid solvent $\left[\mathrm{mol\,m^{-3}}\right]$ in the film. (The 'V' stands for the fact that $\tilde{c}_1^V$ and D_i^V are measured in reference to a volume element in Cartesian coordinates [134]). It is crucial to note that Equation 6.1 holds true at every position z in the film, such that $j_{i\mathrm{p}}(z)$ describes the local net flux from $z - dz$ to $z + dz$. At this point, it is necessary to make

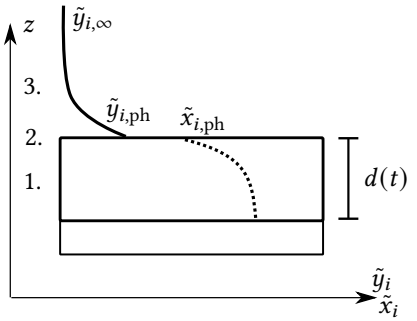

Figure 6.1.: Depiction of a drying thin-film with an indication of the sub-processes 1-3, the molar ratio of liquid solvent in the film $\tilde{x}_i$ (dotted line) and the molar ratio of gaseous solvent over the film surface $\tilde{y}_i$ (solid line). The values on the surface, that is the phase boundary, are indexed by ph and the [asymptotic] value of $\tilde{y}_i$ in the drying gas is indexed by ∞.

a short side note on the definition and order of magnitude of the diffusion coefficients covered in this work. The reader should keep in mind that instead of using the notation D_i^V, we would technically have to write D_{ip}^V to express that the diffusion coefficient depends on both the solvent i and the solute p. However, in literature the first notation is preferred for convenience. Analogously, in a two-solvent solution, the simpler notation D_{ij}^V is preferred to D_{ipj}^V (or similar). In such a two-solvent system, D_{ii}^V denotes the diffusion of solvent i within itself in the solute p, which is sometimes called *self diffusion coefficient* whereas D_{ij}^V is called *interdiffusion coefficient* (in general $D_{ij}^V \neq D_{ji}^V$ for mixtures of unequal amounts) [135]. In dilute, ionic aqueous solutions the diffusivity of water, D_i^V, is on the order of $10^{-9}\,\mathrm{m^2\,s^{-1}}$ [136]. For perovskite solutions, there is no extensive data on diffusion coefficients available (to the knowledge of the author). However, since the initial molar fraction of perovskite unit cells to solvent in most solutions is about 3%, a sensible estimation is given by the self-diffusion coefficient of the pure solvent (or the interdiffusion coefficient of the pure solvent mixture). Typical values are $1.4 \cdot 10^{-9}\,\mathrm{m^2\,s^{-1}}$, $6.6 \cdot 10^{-10}\,\mathrm{m^2\,s^{-1}}$ and $1.0 \cdot 10^{-9}\,\mathrm{m^2\,s^{-1}}$ for DMF, DMSO and DMF:DMSO (volume ratio 4:1) respectively [22, p. Da28-Da29] (the empirical correlations for the estimation of these values and additional information on the concentration dependence of the diffusion coefficient can be found in the section A1.1). Further, Tan *et al.* determined an expression for the diffusion coefficient of DMSO in a (nearly) dry MAPI perovskite film as a function of the temperature, yielding $10^{-26}\,\mathrm{m^2\,s^{-1}}$ at room temperature [137] (details in section A1.1). This comparison of extreme values demonstrates that the diffusion coefficient is not only temperature-dependent but, in most cases, strongly concentration-dependent and solute phase-dependent (it changes over 17 orders of magnitude from the solution to the readily crystallized film!). For this reason, Equation 6.1 is often solved numerically in literature (analytical solutions are mostly available for constant diffusion coefficients only [135]).

It is important to note that in all subsequent sections of this work (in particular for the gas-phase controlled drying model derived in section 6.1.5), we will completely avoid solving Equation 6.1 by assuming that concentration gradients inside the film can be neglected at all times. This assumption is equivalent to the hypothesis that the film thickness is so thin that diffusion inside the film is, at all times, fast enough to mix the individual components. It is understandable that an educated reader might strongly question this hypothesis given the exceptionally low diffusion coefficient in the crystallized

perovskite measured by Tan *et al.*. However, as we will see in section 6.2, the nucleation process naturally segregates the crystalline phase from the remaining solution by creating many small crystalline nuclei. For this reason, the effective diffusion coefficient limiting the drying dynamics will not be the one of the crystal phase but the one of the remaining solution surrounding the nucleated crystals (unless a crystalline crust completely covers the film surface or we investigate very small amounts of residual solvent in the crystal). Further, we will see that the solvent concentration of this remaining solution approaches an equilibrium until the end of the crystallization process. Nevertheless, the author is aware that the hypothesis of a vanishing concentration gradient is strong. Therefore, a detailed analysis of the validity of this hypothesis will follow in section 6.1.5 (more precisely, we will investigate the two individual hypotheses of a negligible concentration gradient between the solvents DMF and DMSO as well as the solute with the solvent). Furthermore, the interested reader will find a description and application of the numerical toolkits for solving Equation 6.1 in the appendix (section A1) to investigate the contrary case of diffusion-limited drying in perovskite solution films. This model based on diffusion-limited drying could become increasingly important for thicker solution films (with the film thickness increases the probability that a capping layer of crystallized perovskite forms of on the film surface during the drying process effectively trapping the solvent in the bulk solution due to the low diffusion coefficient of the crystal).

Now, let us focus on the second sub-process, which is the liquid-gas phase transition. Raoult's law states that

$$\tilde{y}_{i,\mathrm{ph}}\phi_{p,i}p = \tilde{x}_{i,\mathrm{ph}}\gamma_i p_i^*, \tag{6.2}$$

where $\tilde{y}_{i,\mathrm{ph}}$ is the molar ratio of gaseous solvent i just above the film surface $\left[\mathrm{mol\,mol^{-1}}\right]$, $\tilde{x}_{i,\mathrm{ph}}$ is the molar ratio of liquid solvent i just below the film surface $\left[\mathrm{mol\,mol^{-1}}\right]$, p is the pressure of the gas phase [Pa], p_i^* is the vapour pressure of the solvent [Pa], $\phi_{p,i}$ is the fugacity coefficient [no unit] and γ_i is the activity [no unit] [138]. While $\phi_{p,i}$ accounts for deviations of the gas phase from the ideal gas law, γ_i expresses the chemical interaction between the solvent and the solute, altering the effective vapour pressure over the solution. For simplicity, we will assume an ideal gas in the following ($\phi_{p,i} = 1$). In works of Schabel *et al.* covering sorption and diffusion in solvent-polymer mixtures, it was assumed that the activity can be described with a modified Flory-Huggins and free volume solution theory[139]. In the perovskite precursor

solution, which is essentially an ion-solvent mixture, we make the simple assumption of constant activity. While an ideal mixture ($\gamma_i = 1$) is assumed in most cases, we will see that in the TCP precursor solution, the hypothesis of a drying regime of reduced solvent activity is needed, which is likely caused by the formation of a semi-stable intermediate solute-solvent phase with a substantially lowered vapour pressure[140]. The reason for the deliberately simple working hypothesis of constant solvent activity is, first, that to the knowledge of the author no fundamental theory on the activity of perovskite precursor solutions is available and, second, that the experimental evidence affected by the error of the interferometric measurement technique does not encourage introducing more model parameters (details follow in sections 7.1, 6.1.6 and 6.1.7). A similar consideration applies to the question of the interaction between the solvents DMF and DMSO, where the interferometry measurements of the pure mixture did not show any evidence for a deviation from the ideal mixture ($\gamma_i = 1$) within its error of measurement. Indeed, this is consistent with literature suggesting that large deviations from $\gamma_i = 1$ in the gas phase equilibrium of DMF:DMSO mixtures are not to be expected[141].

Now, we come to the last process, the transport of gaseous solvent away from the surface, which is governed by a Fick-type diffusion equation just as the first sub-process:

$$j_{i\mathrm{g}} = -\delta_{i\mathrm{g}} \tilde{\rho}_{\mathrm{g}} \frac{\partial \tilde{y}_i}{\partial z}, \tag{6.3}$$

where $j_{i\mathrm{g}}$ is the molar flux of gaseous solvent $\left[\mathrm{mol\,m^{-2}s^{-1}}\right]$, $\delta_{i\mathrm{g}}$ is the diffusivity of the gaseous solvent i in the drying gas g $\left[\mathrm{m^2\,s^{-1}}\right]$, and $\tilde{\rho}_g$ is the gaseous molar density of the solvent determined by the ideal gas law $\left[\mathrm{mol\,m^{-3}}\right]$. (We assume that the diffusion of gaseous solvent i into another gaseous solvent j can be neglected because the concentration of solvents above the film is very low – the ratio of DMF in the drying gas is typically smaller 1% as estimated in section A4). In contrast to the diffusion in the liquid film, convection is a non-negligible process in the gas phase. In fact, in most applications forced convection (rather than natural convection) is an important method used to control the drying rate [93] (There are reports about convection cells possibly initiated by Marangoni convection inside of liquid perovskite precursor films at higher temperatures[142]. However, we use moderate temperatures for drying and therefore assume no convection inside of the liquid films.). Commonly, the effect of forced convection is approximated by boundary layer

correlations rather than exactly calculated from flow-diffusion equations (see following section).

6.1.2. Boundary layers and transfer coefficients

By convention, the region in which the molar ratio of gaseous solvent on the film surface, $\tilde{y}_{i,\mathrm{ph}}$, decreases to the molar ratio of solvent in the ambient gas, $\tilde{y}_{i,\infty}$, defines the so-called *concentration boundary layer*, which is fully characterized by its thickness ΔS_{C} (called *concentration boundary layer thickness*). We note that, in fluid dynamics, the term 'boundary layer' is more often used to describe the hydrodynamic boundary layer, enclosed by the velocity field gradient from $v = 0$ on the surface to $v = v_0$ in the surrounding air stream [143] (see Figure 6.2). In fact, the two quantities are, in most cases, interrelated by the approximate relation $\Delta S_{\mathrm{hydr}}/\Delta S_{\mathrm{C}} = \mathrm{Sc}^{1/3}$ where Sc is the Schmidt number as defined in the next section [144]. Similarly, the thermal boundary layer, defined by the distance from the temperature of the surface T_{ph} to the temperature of the ambient gas T_∞ is proportional to the concentration boundary layer (see again Figure 6.2). This is a special implication of the general concept of the mass and heat transfer analogy [22, p. Bc 1- Bc 3], as explained later.

Assuming we know ΔS_C, the *mass transfer coefficient* is defined as

$$\beta_{\mathrm{ig}} = \delta_{\mathrm{ig}}/\Delta S_C \tag{6.4}$$

in units of $\left[\mathrm{m\,s^{-1}}\right]$. With this definition, we can approximate the total flux of solvent molecules away from the film surface, j_{ig} $\left[\mathrm{mol\,m^{-2}s^{-1}}\right]$, by the average difference quotient as

$$j_{\mathrm{ig}} = \beta_{\mathrm{ig}}\tilde{\rho}_{\mathrm{g}}\left(\tilde{y}_{i,\mathrm{ph}} - \tilde{y}_{i,\infty}\right). \tag{6.5}$$

This 'linear approach' is valid if the concentration of gaseous solvent in the gas above the film is low enough [22, p. A19]. Indeed, the ratio of DMF in the drying gas is typically smaller 1% for our experimental parameters as estimated in section A4. If this was not the case, for example if a very volatile solvent, very high temperature or a low ambient pressure was used, we would have to use the so called 'logarithmic approach' or 'Stefan-Ansatz' (see [22, p. A19] for more detail).

The *heat transfer coefficient* α $\left[\mathrm{W\,m^{-2}K^{-1}}\right]$ can be defined analogously to the mass transfer coefficient for convective cooling of a plate resulting in the rate equation

$$\dot{q} = \alpha(T_{\mathrm{ph}} - T_{\infty}), \tag{6.6}$$

where T_{ph} is the temperature of the plate surface, T_{∞} is the temperature of the ambient gas and $\dot{q}$ $\left[\mathrm{W\,m^{-2}}\right]$ is the heat flux out of the surface (see again Figure 6.2). It is crucial to note that the transfer coefficients can vary in time (in addition to spatial variations) whenever the convective air stream over the surface changes. However, this still does not change the fact that the *Lewis mass and heat transfer analogy*,

$$\alpha(t) \propto \beta_{\mathrm{ig}}(t), \tag{6.7}$$

holds at all times and positions (explicit formulation follows in the next section) [22, p. Bc 1- Bc 3]. To avoid misunderstanding, it is crucial to mention that there are situations where either heat or mass transfer can be neglected such that we do not need to consider both transfer processes simultaneously. For instance, in an isothermal environment, heat transfer can be neglected (if the evaporative cooling is balanced by heat conduction through the substrate). Analogously, if an inert material plate is heated and subsequently cooled, only heat transfer (and no mass transfer) is apparent because no molecules evaporate from the plate (there are even intermediate cases where the boundary layers are not proportional any more because the film is 'half-dry' and the onset of the concentration boundary layer shifts with time [93]).

In conclusion, the mass and heat transfer analogy should be seen as a resemblance and not as a fundamental law. In one expressive sentence, the analogy could be written as

> The transfer of heat into an air flow field progressively increasing the temperature of the air along the flow direction is analogous to the transfer of mass into the same air flow field progressively increasing the saturation of the air with solvent vapour along the flow direction.

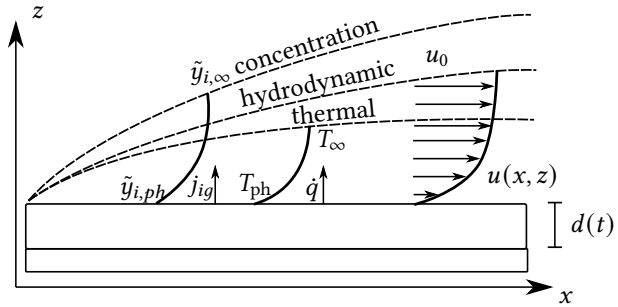

Figure 6.2.: Schematic of hydrodynamic, thermal and concentration boundary layer thickness over a drying liquid thin-film (the absolute heights of the boundary layers are not to scale).

A convenient consequence of this analogy is that the experimenters only need to measure one of the transfer coefficients to determine the other. In this work, we describe the measurement of $\alpha(x)$ by thermochromic liquid crystal (TLC) measurements and $\beta(x)$ by interferometry measurements (compare sections 7.1 and 7.3). However, we will see that the unique TLC measurement of α developed by Cavadini *et al.*[145] is more accurate than the rather indirect measurement of β via drying rates by interferometry. Additionally, the TLC measurement offers a two-dimensional, high spatial resolution, while the interferometry technique only probes one point.

6.1.3. Dimensionless numbers

In engineering, dimensionless number are used to express the fact that many fluid dynamic effects do not depend on the absolute value of dimensions but rather on the ratio of certain dimensions[22, p. Bc 1- Bc 3]. By convention, air flows around certain objects are characterized using the dimensionless *Reynolds number*, Re_x, defined as

$$\mathrm{Re}_x = \frac{u_0 \cdot x}{\nu}, \tag{6.8}$$

where u_0 is the gas velocity $\left[\mathrm{m\,s^{-1}}\right]$, x is a characteristic length [m] and ν is the kinematic viscosity $\left[\mathrm{m^2\,s^{-1}}\right]$. Problems involving the diffusion of one species i into another j are characterized by the *Schmidt number*

$$\mathrm{Sc} = \frac{\nu}{\delta_{ij}}, \tag{6.9}$$

where δ_{ij} is the inter-diffusion coefficient of i in j. As detailed above, we will usually set $j = \mathrm{g}$ to indicate that we are interested in the diffusion of a species i into the drying gas. Further, the *Sherwood number*, Sh_x, used in problems involving a mass transfer with coefficient β_{ig} is a function of the two numbers introduced above. It is defined as

$$\mathrm{Sh}_x = \frac{\beta_{ig} \cdot x}{\delta_{ig}} = f\left(\mathrm{Sc}, \mathrm{Re_x}\right) \tag{6.10}$$

and measures the ratio of *convective mass transfer* to *diffusive mass transfer*. Analogously, for heat conduction, we can define the Nusselt number

$$\mathrm{Nu}_x = \frac{\alpha \cdot x}{k} = f\left(\mathrm{Pr}, \mathrm{Re_x}\right), \tag{6.11}$$

where k is the thermal conductivity $[\mathrm{Wm^{-1}K^{-1}}]$ and $\mathrm{Pr} = \nu/k$ is the Prantl number. As stated above, there is an analogy between mass and heat transfer. In practice, we can translate the equations of heat to mass transfer (or vice versa) simply by exchanging $\mathrm{Nu} \leftrightarrow \mathrm{Sh}$ and $\mathrm{Pr} \leftrightarrow \mathrm{Sc}$ [23, p.374-376]. This can be written as Lewis'law in an explicit form

$$\alpha = \tilde{\rho}_\mathrm{g} \cdot \tilde{c}_\mathrm{p} \cdot \mathrm{Le}^{1-n} \cdot \beta_{\mathrm{ig}}, \tag{6.12}$$

where the Lewis number is defined as $\mathrm{Le} = \mathrm{Pr}/\mathrm{Sc}$, $\tilde{c}_\mathrm{p}$ is the isobaric heat capacity (not a concentration) of the gas mixture and n is the exponent used in the correlations to express turbulent ($n = 0.42$) or laminar flow ($n = 0.33$) [23, p.374-376]. In order to gauge the ratio of evaporation to diffusion in a drying thin-film the Biot-Number for mass transfer is commonly defined as

$$\mathrm{Bi}_d = \frac{\beta_{ig} d}{D_i^V}, \tag{6.13}$$

with the film thickness d [23, p.374]. We will show in the following that this definition used in traditional literature is not ideal. According to the heat/mass transfer analogy, the Biot number for mass transfer should be a useful figure of merit to estimate whether a concentration gradient will build up in the film due to the evaporation of species i on the film surface. In heat transfer calculations, a Biot number smaller 0.1 implies that heat conduction through the film so fast that temperature gradients inside of the film can be neglected[23, p.260-261]. However, mass transfer is distinct from heat transfer in one particular aspect: This is the phase transition at the film surface as described by Equation 6.2 and visible in Figure 6.1 as the discrete difference between $\tilde{x}_{i,\mathrm{ph}}$ and $\tilde{y}_{i,\mathrm{ph}}$. Let us demonstrate in a quick estimation which implication this phase transition has regarding the formation of a concentration gradient. We start by assuming a stable concentration gradient in the film. In this case, the flux of solvent out of the film due to evaporation must approximately equal the flux of solvent from the bulk to the film surface. We further assume, for simplicity, that a single solvent is used in the solution film and that we have at the film surface $\tilde{x}_{\mathrm{i,ph}} \approx \tilde{x}_{\mathrm{p,ph}} = 0.5$, while we have in the bulk solution $\tilde{x}_{\mathrm{i,bulk}} \approx 1$ due to the diffusive limitation. Writing this down, we get for an unloaded ambient gas

$$D_i^V \cdot \bar{\tilde{\rho}}_l \frac{\tilde{x}_{i,\mathrm{bulk}} - \tilde{x}_{i,\mathrm{ph}}}{\delta s} \approx \beta_{i,\mathrm{g}} \tilde{\rho}_g \frac{\gamma_i p_\mathrm{i}^*}{p} \tilde{x}_{i,\mathrm{ph}}, \tag{6.14}$$

where $\bar{\tilde{\rho}}_\mathrm{l} \approx (1.5 \cdot \tilde{\rho}_{\mathrm{i,l}} + 0.5 \cdot \tilde{\rho}_\mathrm{p})/2$ is the (approximate) average molar density of the liquid solution in the concentration gradient region. For the example of an ideal mixture ($\gamma_i = 1$) of DMF with a solute material, this yields $D_i^V \leq \delta s \beta_{i,\mathrm{g}} \cdot 10^{-3}$ and accordingly $\mathrm{Bi}_{\delta \mathrm{s}} > 10^3$, which is a much higher threshold than in the case of heat transport.

To re-establish the analogy between heat and mass transfer, Buss *et al.* modified the definition of the Biot number for mass transfer to account for the liquid-gas phase transition[146]

$$\mathrm{Bi}_d^{\mathrm{an.}} = \mathrm{Bi}_d \frac{\tilde{\rho}_g}{\bar{\tilde{\rho}}_l} \frac{\gamma_i p_\mathrm{i}^*}{p}. \tag{6.15}$$

This is a particular representation of the *analogous mass transfer Biot number* introduced by Parti *et al.*[147]. Indeed, when using this adjustment, concentration gradients can be neglected if $\mathrm{Bi}_d^{\mathrm{an.}} < 0.1$, in analogy to heat transfer.

However, it is important to keep in mind that this modified Biot number is strongly dependent on the choice of solvent (Bi_d, of course, also depends on the solvent, but not that strongly because mostly $D_i^V \approx D_j^V$ and $\beta_{i\mathrm{g}} \approx \beta_{j\mathrm{g}}$). Further, it is not intuitively clear how this definition should be adjusted for multi-solvent systems. As a conservative estimation, it is sensible using the solvent with highest vapour pressure in $\mathrm{Bi}_d^{\mathrm{an.}}$ to judge whether a concentration gradient can build up in the film (which is DMF in this work).

For our typical experimental parameters, we obtain Bi_d on the order of $10^0 - 10^3$ or $\mathrm{Bi}_d^{\mathrm{an.}}$ on the order of $10^{-4} - 10^{-1}$ (with D_i on the order of $10^{-9}\,\mathrm{m^2\,s^{-1}}$) depending on the film thickness and the apparent mass transfer coefficient (see section A4 for typical experimental parameters). This estimation justifies the hypothesis of negligible concentration gradients between solute and solvent (it is true that, occasionally, $\mathrm{Bi}_d^{\mathrm{an.}}$ can exceed 0.1, but this just for a very short time, directly under the nozzle centre as will be shown in the next sections). Fortunately, will show in the appendix in section A1.5 by numerical simulation that the hypothesis of negligible concentration gradients converges with the exact solution of Equation 6.1 for $\mathrm{Bi}_d^{\mathrm{an.}}$ up to 10^3. This constraint is definitely satisfied under the assumption that the diffusion coefficients remain on the order of $10^{-9}\,\mathrm{m^2\,s^{-1}}$, which is plausible given that the crystal phase segregates from the remaining solution upon nucleation. However, assuming the diffusion coefficient measured by Tan *et al.* ($10^{-26}\,\mathrm{m^2\,s^{-1}}$) would apply to the whole film at the end of the drying process, $\mathrm{Bi}_d^{\mathrm{an.}}$ would exceed 10^3 by several orders of magnitude. This could become a problem in case a capping layer of crystallized perovskite forms on the film surface, trapping the remaining solvent inside. Modelling and simulation concepts that can be used in such a case will also be investigated in the appendix in section A1.

6.1.4. Empirical correlations for mass and heat transfer in different air flows*†‡

Empirical correlations are used in different situations involving typically used air flow geometries. In this work, we use mainly two geometries: a laminar air flow over a flat plate and an (oblique impinging) slot-jet. Drying in the laminar air flow is a good reference process for studying the drying dynamics of thin-films in a controlled environment of convective mass transfer that is nearly constant over a large area (see Figure 6.3). The mass transfer still varies because, as stated earlier, the air saturates with solvent as it travels over the substrate. This is reflected in the Sherwood number correlation

$$\mathrm{Sh}_x = \frac{0.332 \cdot \mathrm{Sc}^{1/3} \cdot \mathrm{Re}_x^{1/2}}{\left[1 - (x_0/x)^{3/4}\right]^{1/3}}, \tag{6.16}$$

where x_0 designates the starting point of the concentration boundary layer where $\mathrm{Sh}_{x \to x_0} \to \infty$ (this is not a physically sensible value, however the integral over the correlation starting from x_0 is finite such that the average amount of evaporating solvent for any given area can be accurately calculated) [148]. It is worth mentioning that x_0 can depend on time as the drying front moves over the substrate. In all three journal articles that were published during the work on this thesis[19, 20, 21], this laminar flow geometry is used as an important reference, while *in situ* characterization is performed simultaneously to study the drying and crystallization dynamics (details follow in chapters 7 and 8).

While the laminar air flow is highly interesting for an academic investigation of drying processes, industry almost exclusively uses slot or round jets for convective drying, since these require no channel to achieve laminar flow [149].

*Section reviews Advanced Energy Materials 9 (2019) p. 1901581 by S.T., B.T., J.A.S, I.M.H., T.A., W.M., U.L., P.S., W.S., B.S.R. and U.W.P [19]

†Section reviews Solar RRL 6 (2021) p. 2100353 by S.T., F.L., P.S., W.S., B.S.R., I.A.H. and U.W.P. [20]

‡Section reviews ACS Applied Materials & Interfaces (2022) 14, 9, p. 11300–11312 by S.T., J.M., N.L., H.M.P, M.A., P.S., W.S., B.S.R and U.W.P. [21]

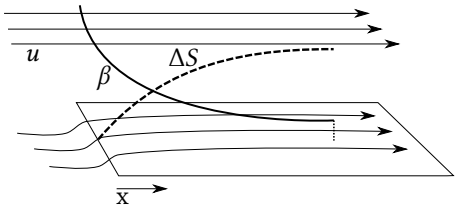

Figure 6.3.: Mass transfer coefficient, β, and boundary layer thickness, ΔS, for a laminar flow with speed u over a flat surface.

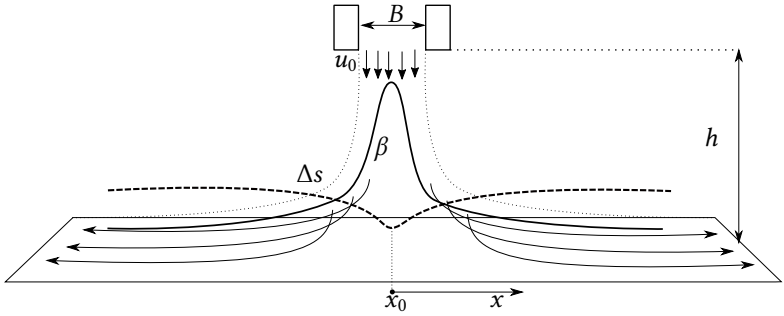

Figure 6.4.: Mass transfer coefficient, β, and boundary layer thickness, ΔS, and stagnation point x_0 for a perpendicularly impinging slot jet of high-pressure gas.

In contrast to laminar air flow geometries, linear slot-jets are characterized by a highly non-uniform mass transfer[21] (see Figure 6.4). This sounds like a disadvantage at first, but we will see in section 8.3 that the exceptionally high mass transfer just below a slot-jet is needed for some perovskite precursors to produce a nucleation-dominated morphology (details about the crystallization follow in section 6.2). Accordingly, in many state-of-the-art publications on the upscaling of perovskite solution printing, (titled) slot-jets are used to induce crystallization [86, 150, 151]. Martin describes the (integrated) Sherwood number in a single slot-jet as

$$\overline{\mathrm{Sh}} = \frac{1.53 \cdot \mathrm{Re}^{m}}{x/D + h/D + 1.39} \mathrm{Sc}^{0.42}, \tag{6.17}$$

$$m = 0.695 - \frac{1}{x/D + (h/D)^{1.33} + 3.06}, \tag{6.18}$$

which is valid under the condition that

$$2 \leq |x/D| \leq 25, \tag{6.19}$$

$$2 \leq h/D \leq 10, \tag{6.20}$$

$$3000 \leq \mathrm{Re}_D \leq 90,000, \tag{6.21}$$

where x is the distance from, x_0, the stagnation point, h is the height of the nozzle over the sample, and $D = 2B$ is the hydrodynamic width of the slot [152] (see symbols in Figure 6.4). In our application, we have $h/D = 2.5$ and $1500 \leq \mathrm{Re_D} \leq 6000$ meaning that we exceed the lower boundary for the validity of the correlation due to the small slot widths $B = 0.3\,\mathrm{mm}$ (details about the parameters follow in section 8.3). Further, we differentiate the expression ($d\overline{\mathrm{Sh}}/dx$) and apply a cubic interpolation in the centre region under the nozzle ($|x/D| \leq 2$) to bridge the definition gap. The so-obtained values for $\beta_{\mathrm{DMSO}}(x)$ (and $\alpha(x)$) are plotted in Figure 6.5a against a typical local heat transfer TLC measurement (experimental details follow in section 7.3). This plot shows that the correlation (red solid line) does not reproduce the data very accurately. This is due to the fact that the correlation was derived for describing the integrated heat and mass transfer, which is relevant when driving the material to be dried or cooled under the jet. It was however not designed to describe the local mass transfer under the nozzle centre of very narrow jets at high Reynolds numbers, which is also reflected the exceeding of its domain of definition. The question arises whether other correlations found in literature perform better at reproducing the data. The correlation formulated by Hofmann *et al.* (equations can be found in [153]) has the advantage that it approximates better the data in intermediate distance to the nozzle centre, but is less accurate in the prediction of the peak mass transfer in the centre. As mentioned earlier, an accurate modelling of the centre region is important for some perovskite precursors, which is why the Hofmann *et al.* is not well-suited for this case.

Chin/Agarwal describe the mass transfer from an oblique impinging slot jet with the formula

$$\mathrm{Sh} = \mathrm{a} \cdot \mathrm{Sc}^{1/3} \cdot \mathrm{Re}_{\mathrm{B}}^{\alpha} \cdot (\mathrm{h/B})^{\gamma} \tag{6.22}$$

at the stagnation point ($-1 < x/B < 1$) and

$$\mathrm{Sh_x} = \mathrm{a} \cdot \mathrm{Sc}^{1/3} \cdot \mathrm{Re_B^{\alpha}} \cdot (\mathrm{x/B})^{\beta} \cdot (\mathrm{h/B})^{\gamma} \tag{6.23}$$

in the laminar-boundary layer ($1 < |x/B| < 4$) and wall-jet regimes ($8 < |x/B|$)[154]. The exponents a, α, β and γ are parametrized as polynomials of the impinging angle θ (for details see [154]). As in the earlier case, the flow transition regime $4 < |x/B| < 8$ has to be interpolated because the correlation is not defined for this regime. When plotting the Chin/Agarwal correlation it does not yield a better accordance with the data than the other correlations (see again Figure 6.5a). Particularly in the off-centre regions, it systematically overestimates the apparent mass transfer. However, due to the explicit definition of the laminar-boundary layer and the stagnation point, the correlation shows a more precise estimation for the region of high mass transfer in the nozzle centre than the other two correlations. Because none of the correlations reproduces the data accurately, we re-fit the correlations globally to 15 such TLC measurements[21], leaving the numerical parameters open and varying the nozzle height, h, and the output air velocity u_0 (for the Chin/Agarwal correlation we removed the stagnation point to avoid over-fitting, more details follow in section 7.3). The result can be seen in Figure 6.5b. Evidently, both the Martin and the Hofmann *et al.* correlation still do not reproduce the experimental data accurately in the centre region. The re-fitted Chin/Agarwal correlation is not only more accurate in the centre region but also in the off-centre region (it still does not perfectly reproduce the two data points in the centre, but these also have a high uncertainty due to the measurements principle as described in section 7.3). Furthermore, neither Martin nor Hofmann *et al.* provide a method to consider tilted air flow geometries, while a corresponding parametrization of the tilting angle exists in the Chin/Agarwal correlation, as mentioned above. For these reasons, we will use the re-fitted Chin/Agarwal correlation for the prediction of the local mass transfer in all future models (the re-fitting comprises in this case additional 27 TLC measurements at the tilting angles 82.5°,75° and 67.5°).

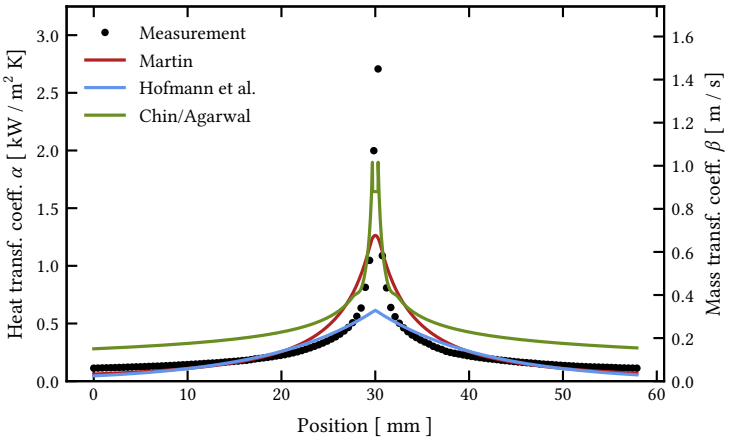

(a) Predicted local heat transfer coefficient, α, and local mass transfer coefficient β (for DMSO) calculated from correlations by Martin, Hofmann *et al.* and Chin/Agarwal with typical local heat transfer measurement

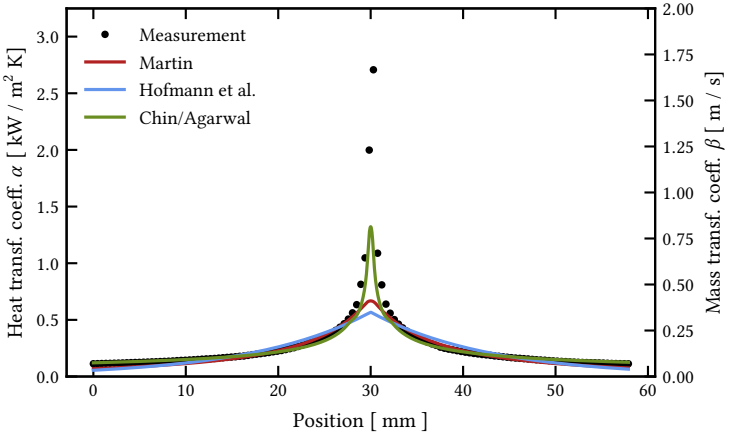

(b) The same plot as above but with (globally) re-fitted parameters of the correlations by Martin, Hofmann *et al.* and Chin/Agarwal

Figure 6.5.: Comparison of empirical correlations for the prediction of heat/mass transfer before and after re-fitting for a perpendicularly mounted slot-nozzle. The parameters are $u_0 = 79\,\mathrm{m\,s^{-1}}$, $h = 3\,\mathrm{mm}$ and $B = 0.3\,\mathrm{mm}$.

6.1.5. Gas phase controlled drying at sufficiently low Biot numbers*‡

Let us now derive a simple gas phase controlled drying model for perovskite precursor solution films[19, 21]. First of all, we assume an isothermal environment at temperature, T, where evaporative cooling is balanced directly by heat transfer through the substrate due to the small film thickness (that is to say we can neglect heat transfer and only consider mass transfer). Furthermore, as stated earlier, we will make the assumption that the diffusion inside of the solution thin-film removes the concentration gradient caused by the evaporation quickly at all times. This is equivalent to stating that all components in the film remain mixed at all times, that is c_i^V and $\tilde{x_i}$ are constant along the vertical axis, z. Therefore, we can write the molar fraction of solvent on the film surface (as well as everywhere else) as

$$\tilde{x}_{1,\mathrm{ph}} = \tilde{x}_{1,\mathrm{tot}} \approx \frac{N_1}{N_1 + N_\mathrm{p}}, \tag{6.24}$$

where N_1 total number of molecules [mol] of solvent 1 and the N_p is total number of perovskite unit cells [mol] in the film. Using Raoult's law (Equation 6.2), the linear approach of drying (Equation 6.5) and the ideal gas law $p = \tilde{\rho}_g RT$, we write $j_{1\mathrm{g}}$ as $-dN/(dt\delta A)$ and get

$$\frac{\mathrm{dN_1}}{\mathrm{dt}} = -\delta A \frac{p_1^*}{RT} \beta_{1g}(t) \cdot \frac{N_1}{N_\mathrm{p} + N_1} \tag{6.25}$$

,

where δA is a small area element in which β_{1g} is constant. In perovskite precursor solutions, we often have a mixture of two (or more) different solvents, 1 and 2 (details follow in section 5.1). In this case, we obtain a system of coupled differential equations. To simplify the problem, we can make use of the fact that the mass transfer coefficients at the same time and place are proportional (this is a consequence of the heat and mass transfer analogy discussed earlier). This proportionality allows us to define a constant

*Section reviews Advanced Energy Materials 9 (2019) p. 1901581 by S.T., B.T., J.A.S, I.M.H., T.A., W.M., U.L., P.S., W.S., B.S.R. and U.W.P [19]

‡Section reviews ACS Applied Materials & Interfaces (2022) 14, 9, p. 11300–11312 by S.T., J.M., N.L., H.M.P, M.A., P.S., W.S., B.S.R and U.W.P. [21]

K_{12} such that $p_1^* \beta_{1g}(t) = K_{12} p_2^* \beta_{2g}(t)$ is true at all times. Furthermore, we assume that solvent-solvent inter-diffusion in the gas phase can be neglected due to the low concentrations of solvent molecules in the drying gas, as mentioned earlier. In total, we get

$$\begin{aligned} \frac{\mathrm{dN_1}}{\mathrm{dt}} &= -\delta A \frac{p_1^*}{RT} \beta_{1g}(t) \cdot \frac{N_1}{N_\mathrm{p} + N_1 + N_2}, \\ \frac{\mathrm{dN_2}}{\mathrm{dt}} &= -\frac{\delta A}{K_{12}} \frac{p_1^*}{RT} \beta_{1g}(t) \cdot \frac{N_2}{N_\mathrm{p} + N_1 + N_2}. \end{aligned} \tag{6.26}$$

This system of equations can be solved analytically[21], yielding

$$N_\mathrm{p} \ln(N_1) + N_1 + K_{12} N_2 = C - \delta A \frac{p_1^*}{RT} \int_0^t \beta_{1g}(t') dt', \tag{6.27}$$

where

$$N_2 = D\,(N_1)^{1/K_{12}}. \tag{6.28}$$

The free constants C and D are chosen such that the initial conditions $N_1(t = 0)$ and $N_2(t = 0)$ are fulfilled. Equation 6.27 can be solved efficiently by numerical root finding[21]. Once $N_1(t)$ is known, we simply get N_2 using Equation 6.28. The total thickness of the film can then be calculated as

$$d = d_\mathrm{p} + d_1 + d_2 = \frac{N_\mathrm{p}}{\tilde{\rho}_\mathrm{p} \delta A} + \frac{N_1}{\tilde{\rho}_{1,\mathrm{l}} \delta A} + \frac{N_2}{\tilde{\rho}_{2,\mathrm{l}} \delta A}, \tag{6.29}$$

where $\tilde{\rho}_\mathrm{p}$ is the molar density of the perovskite, and $\tilde{\rho}_{i,\mathrm{l}}$ is the respective molar density of the liquid solvent. We note that Equations 6.26 can easily be extended to add one more solvent. However, a solution must then be calculated by a time-stepping algorithm since an analytical solution is challenging. Inversely, if we want to get back to a one-solvent system, we simply set ($N_2 = 0$ always). Equations 6.27 - 6.29 can then be written as

$$d(t) = d_\mathrm{p} + d_s \cdot W\left(\exp\left[-\frac{p_1^*}{d_s \tilde{\rho}_1 RT} \int_0^t \beta_{1\mathrm{g}}(t') dt' + C'\right]\right), \tag{6.30}$$

where $C' = C/N_{\mathrm{pvk}} - \ln(N_{\mathrm{pvk}})$, $d_s = d_{\mathrm{p}}\tilde{\rho}_{\mathrm{p}}/\tilde{\rho}_{i,l}$ and W is the Lambert W-function satisfying $z = W(ze^z)$ for all (complex) numbers z. We note that for large enough $x = ze^z$, we have $x \approx e^z$. Therefore, in the beginning of the drying process Equation 6.30 can be nicely approximated by $W(x) \approx \ln(x)$ yielding

$$d(t) \approx d_0 - r_1 \int_0^t \beta_{1\mathrm{g}}(t')dt', \tag{6.31}$$

where $d_0 = d_{\mathrm{p}} + C' \cdot d_s$ was assumed to be the thickness of film at $t = 0$ and $r_1 = p_1^*/\tilde{\rho}_{1,\mathrm{l}}RT$. However, for small x just before the film is dry, we will have $x \approx z$, implying $W(x) \approx x$ and therefore

$$d(t) \approx d_{\mathrm{p}} + d_s \exp\left[-\frac{r_1}{d_s}\int_0^t \beta_{1\mathrm{g}}(t')dt' + C'\right]. \tag{6.32}$$

We now want to discuss different cases for time dependencies of $\beta_{12}(t)$ and thus the integral in the above Equations. In case of a constant mass transfer coefficient, that we have (in approximation) in the laminar air flow, we get simply

$$\int_0^t \beta_{1g}(t')dt' = \beta_{1g} \cdot t. \tag{6.33}$$

Inserting this into Equation 6.30 yields Eq (4) from the first publication [19]. Figure 6.6 shows a plot of Equation 6.27 (and Equations 6.28 and 6.29) under these constant mass transfer conditions for a perovskite precursor film with different DMF and DMSO ratios, but the same wet film and dry film ratios. Evidently, for the common mixture of DMF:DMSO in the volume ratio 4:1, the drying rate in the beginning is almost the same as in the case of pure DMF, while in the end of the drying process, the drying dynamics are almost only governed by the DMSO, meaning that all DMF has evaporated.

For the one-solvent precursors, the asymptotic case of Equation 6.31 leads, in combination with Equation 6.33, to a linear thickness decrease in the beginning of the drying process (see black and yellow lines in Figure 6.6). For a pure film of one solvent (without solute), we would further have $d_s \to 0$ everywhere and this linear decrease would continue until all solvent have

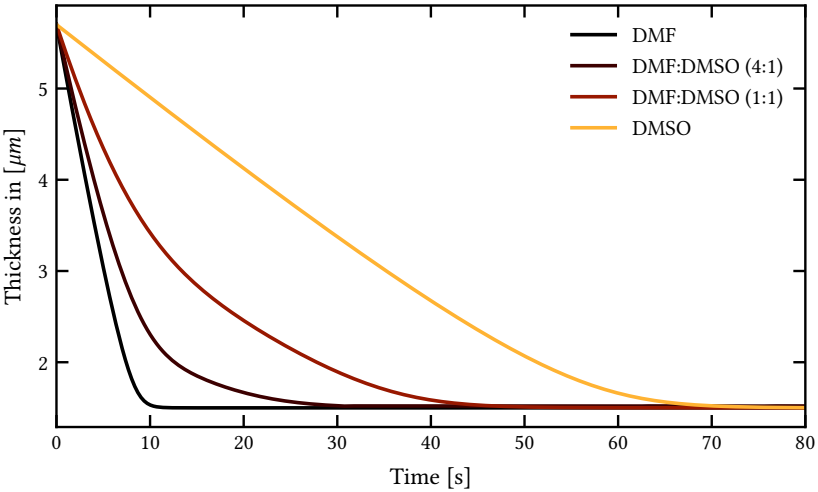

Figure 6.6.: Drying dynamics of a 5.8 μm perovskite precursor film with different DMF:DMSO ratios according to Equation 6.27. The case of pure DMF or DMSO is a representation of Equation 6.30. For the calculation a dry film of 1.3 μm was assumed.

evaporated (in the real laminar air flow drying, we still have to factor in possible changes in the mass transfer coefficient, once the concentration boundary layer onset, x_0, shifts with the drying front over the substrate, which speeds up the drying process slightly in the end. For more detail see reports by Schmidt-Hansberg *et al.* [93] and the example of pure DMF will in the next section in Figure 6.7). As we see in Figure 6.6, at low solvent concentrations, Equation 6.32 will become valid, exponentially decreasing the drying rate before the dry film is reached (At high enough concentrations, this effect is much stronger than the acceleration due to the movement of the drying front, which is why we neglected the drying front movement in the following).

In case of a roll-to-roll coating machine moving with a constant web speed, v, under an air nozzle with the position dependent, constant mass transfer $\beta_{1g}(x)$ we would obtain

$$\int_0^t \beta_{1g}(t')dt' = \frac{1}{v}\int_{L_0}^{L} \beta_{1g}(x)dx \equiv \frac{B(L,L_0)}{v}, \tag{6.34}$$

where $B(L, L_0)$ is the mass transfer coefficient integrated along the coating web from the position of the coater, L_0 to the end of the web L. We note that, of course, in the beginning of the coating process, when the web accelerates, this equation does not hold any more. Furthermore, in an unstable drying process, the concentration boundary layer can shift because fully dried parts of the film do not release any more solvent molecules. Therefore, the relations above only apply for 'stabilized coating and coating', meaning that the concentration boundary layer onset is stable.

Finally, we can ask the question how low the Biot number must be for the model to still remain accurate. As mentioned earlier, the initial hypothesis of negligible concentration gradients in the film can be decomposed into two individual hypotheses for a two-solvent TCP solution. The first hypothesis is that the solvents DMF and DMSO remain mixed during the drying process (evidently, in a one-solvent solution, such as the MAPI solution, this hypothesis is not needed). To investigate the validity of the hypothesis, we start by assuming the contrary for a 4:1 volume-to-volume ratio of DMF to DMSO as used in the TCP precursor solution (see again section 5.1 for details). In this case, the ratio of the solvents on the film surface would be fully controlled by the equilibrium of the evaporative fluxes of the individual solvent molecules out of the surface and the diffusive flux of solvent molecules from the bulk to the surface. The bulk solution (assumed to be much thicker than the surface diffusion gradient) would remain with the initial solvent ratio for a long time. It can be shown that, with these assumptions (in a pure DMF:DMSO film without solute), the molar DMF ratio on the film surface, $\tilde{x}_{\mathrm{DMF,ph}}$, would fall down to 0.12 (as opposed to 0.78 in the bulk) and that the concentration gradient would require $\mathrm{Bi}_d^{\mathrm{an.}}$ greater 1 (the detailed calculation can be found in the appendix in section A1.3). The second hypothesis, which is the absence of a concentration gradient of the solute and the solvent, is false only if the $\mathrm{Bi}_d^{\mathrm{an.}}$ is significantly greater 0.1 as already discussed in section 6.1.3. In the same section we already stated that, for our typical experimental parameters, we obtain $\mathrm{Bi}_d^{\mathrm{an.}}$ on the order of $10^{-4} - 10^{-1}$ (with D_i on the order of $10^{-9}\,\mathrm{m^2\,s^{-1}}$) depending on the film thickness and the apparent mass transfer coefficient (see section A4 for typical experimental parameters). It must be noted that values greater 10^{-1} are possible under the nozzle centre (mostly

where $\beta > 1\,\mathrm{m\,s^{-1}}$), but these values are only apparent for very short times, leaving the film not enough time to form a diffusion gradient.

Beyond the above estimation, a numerical investigation considering only self-diffusion in a DMSO:DMF solution with solute (just as in TCP) shows, that for films with $\mathrm{Bi}_d^{\mathrm{an.}}$ smaller or equal 10^3, the deviations from the gas phase controlled drying model are non-significantly small (see section A1.5 for more details). The reason for the difference in the order of magnitude of $\mathrm{Bi}_d^{\mathrm{an.}}$ from the above estimations is, most likely, that the estimations already assume the existence of an equilibrium state concentration gradient. In reality, this state however needs a certain time to form. In other words, the components in the film need a certain time for the evaporation and diffusion to the reach the equilibrium state. If the drying process finishes faster than this equilibration time, the hypothesis of negligible concentration gradients (and with it the analytical model) still describes the reality well enough. In this context, it is important to remember that, as we showed above, at the end of the drying process, the drying rate decreases exponentially as the total molar ratio of solvent decreases (even in the case of fully gas phased controlled drying). This exponential decrease of the flux of solvent out of the film gives the diffusion more time to equilibrate the evaporation at the film surface. Furthermore, independent of the simulation, it is noteworthy that, as we will show in section 6.2.4, the onset of the nucleation process will segregate the crystal grains from the remaining solution, thereby increasing the solvent concentration at the film surface again (unless crystallization forms a covering film on the surface rather than only loosely connected crystal grains). This mechanism counteracts the trapping of solvent inside of the film due to diffusion limitations and makes the resemblance of the model to the real perovskite solution drying more likely.

6.1.6. Drying of a one-solvent methylammonium lead iodide solution*

For the case of methylammonium lead iodide, MAPI, a special solution of different lead salts is used (explained later in section 5.1 in detail) [19]. In this solution, there are several components which evaporate before the MAPI is

*Section reviews Advanced Energy Materials 9 (2019) p. 1901581 by S.T., B.T., J.A.S, I.M.H., T.A., W.M., U.L., P.S., W.S., B.S.R. and U.W.P [19]

readily crystallized. These are excessive MAI, Cl_2 and $(CH_3COO)_2 \cdot 3H_2O$ (possibly also as as MACl or MA CH_3COO) contained in the lead salts. Therefore, it is unclear whether these volatile components influence the drying dynamics. Further, it is proposed in literature that intermediate phases could alter the drying dynamics by binding the solvent in the film caused by solute-solvent interactions[155, 156]. The main solvent used is DMF. With the help of interferometry (discussed later in section 7.1), we measure the actual thickness evolution of pure DMF as well as different MAPI precursors in the laminar air flow with (almost) constant mass transfer coefficient. The results are depicted in Figure 6.7.

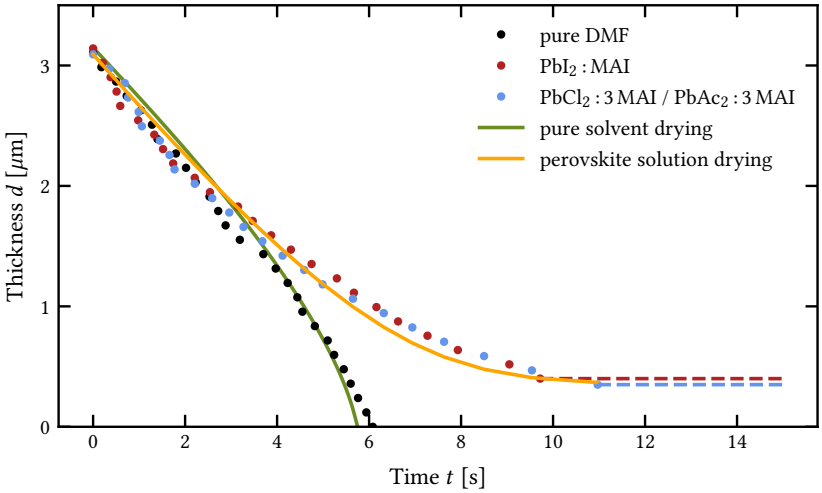

Figure 6.7.: Drying dynamics of different MAPI precursors (all dissolved in pure DMF) as measured by interferometry (blue dots for optimized precursor described in section 5.1 and dark red dots for classical stoichiometric precursor) along with the same measurement for a pure DMF film (black dots). The solid lines represent the drying dynamics according to Equation 6.30 (yellow line) and the dynamics with moving drying front according to Schmidt-Hansberg *et al.* [93] (dark green line). The drying dynamics of the different perovskite precursor solutions do not show any significant deviation.

We find that, indeed, a pure DMF film follows the model that was proposed by Schmidt-Hansberg *et al.* before (black dots and green solid line) [93],

which includes the moving of the drying front as explained above. However, at the end of the drying process the dynamics of the perovskite solutions deviate significantly from the pure solvent film, which was to be expected as the drying transitions from Equation 6.31 at high solvent contents to Equation 6.32 at low solvent contents. To check this correspondence between the experimental data and the model, we fit Equation 6.30 to the drying dynamics of the MAPI precursors (the only free parameter is the initial wet film thickness). The result is also depicted in Figure 6.7 (orange line). (This experiment was repeated in more than 25 measurements at a variety of different drying parameters, which are the laminar air flow velocity and the temperature.) As a result, we find no significant deviation of the thickness evolution from Equation 6.30 just as shown in Figure 6.7. (For estimating the accuracy of the fit, the weighted sums of squared residuals χ^2 are calculated for different parameters, resulting in an average around 1). This observation is further underlined by the fact that a classical MAPI precursor, where PbI_2 and MAI are mixed with a 1:1 stoichiometry does not show a deviation from the investigated precursor (compare blue dots and dark red dots in Figure 6.7.). We conclude that neither solute-solvent interaction nor the retarded evaporation of residuals is observable within the errors of the used interferometric technique. This does however not imply that these do not exist, but rather that the effects are negligible for the drying dynamics with the error of the measurement (see section 7.1 for details). In the next section, we will show that this may not be true for different perovskite precursor systems.

6.1.7. Drying of a two-solvent triple cation perovskite solution[‡]

The drying dynamics of the triple cation precursor are investigated in the third main publication [21]. The major difference to the MAPI precursor discussed in the last section is that a 4:1 volume mixture of DMF and DMSO is used for this precursor system (and a mixture of cations as detailed in section 5.1). Therefore, we use Equation 6.27 for fitting the precursor drying dynamics. When comparing the predicted thickness dynamics against the

[‡]Section reviews ACS Applied Materials & Interfaces (2022) 14, 9, p. 11300–11312 by S.T., J.M., N.L., H.M.P, M.A., P.S., W.S., B.S.R and U.W.P. [21]

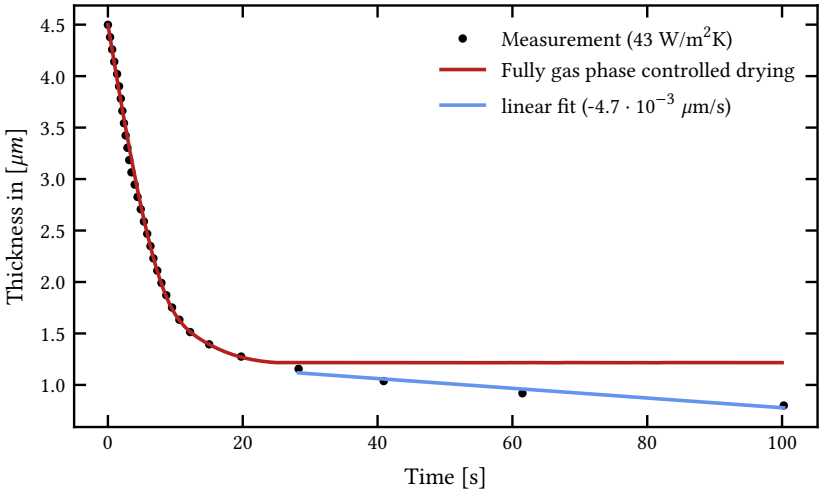

Figure 6.8.: Interferometric data of the drying rate of a DMSO:DMF triple cation perovskite precursor along with the analytical model described by Equation 6.27. At the end of the drying process, the measurement deviates from the prediction, which we suspect to be caused by an intermediate phase reducing the vapour pressure of the remaining solvent. The slope is estimated by a linear fit (blue line).

interferometry measurement in the laminar air flow, we find a significant deviation of the prediction (see Figure 6.8).

We suspect that the deviation between the model assuming ideal mixture ($\gamma_i = 1$) is caused by the formation of an intermediate phase. Thermodynamically, this could be described by a reduction in the activity, γ_i, and thus the effective vapour pressure of the solvent over the thin-film. As mentioned before, for polymer-solvent systems extensive theory exists on how the activity of solvents over solution films reduces with the solvent concentration [139]. However, for hybrid perovskite systems no such relation is available to the knowledge of the author. The simplest assumption is that the activity is just a constant $\gamma_i < 1$. This adjustment modifies the pre-factor in the integral in Equation 6.27. To simplify further, we assume that the bound solvent behaves like a single species (which is most likely DMSO as discussed above). From these assumptions, we get the empirical equation

$$d(t) = d_{0,\text{crit.}} - \frac{m_{\text{ref}}}{\beta_{\text{ref}}} \int_{t_{0,\text{crit.}}}^{t} \beta(t)dt. \tag{6.35}$$

This equation is, in effect, a representation of Equation 6.31, which is a good enough approximation given that we only have a small number of data points in this region. In the laminar air flow, we would expect a linear thickness decrease as the integration becomes $\beta_{1g} \cdot t$, as explained above. Accordingly, we can fit a linear function to the data, estimating the constant, m_{ref}, by the slope of the fit (see blue line in Figure 6.8). In the publication, we perform this fit for 15 such measurements and determine $< m_{\text{ref}}/\beta_{\text{ref}} >= (2.81 \pm 0.03) \cdot 10^{-7}$. We note that, with this value at hand, Equation 6.35 can also be used in dynamic coating with an inhomogeneous $\beta(x)$ in combination with Equation 6.34, later. It is possible to calculate the associated vapour pressure, which is about 10 Pa, corresponding to an activity of 0.05 for DMSO and 0.007 for DMF (in other words, the vapour pressure of the suspected intermediate phase is below 1% of the vapour pressure of DMF at our experimental parameters, see section A4 for parameter values).

We note that an alternative hypothesis to explain the deviation of the data from the gas phase controlled drying is the formation of a diffusion limited drying regime. This hypothesis will be discussed further in section 8.3. However, we can already state that a diffusion limitation in the end of the drying process is not very likely. First of all, this is due to the fact that, in our experiments, we mostly have $\text{Bi}_d^{\text{an.}}$ of $10^{-4} - 10^{-1}$. We estimated earlier that the hypothesis of negligible concentration gradients is approximately valid in this regime (see last section and typical experimental parameters in section A4) and we will show in the appendix that simulations confirm a good approximation up to $\text{Bi}_d^{\text{an.}}$ of about 10^3 (see section A1.5). Beyond these considerations, we will determine a critical mass transfer coefficient for the perovskite morphology formation in section 8.3. If a diffusion limited drying was the case, we would however expect the drying and crystallization process to be (nearly) independent on the convection over the film. Lastly, we will also show in section A1.5 that even simulations with concentration dependent diffusion coefficient fail to reproduce the particular shape of the measured drying dynamics.

6.2. Description of crystallization dynamics in drying perovskite solution films

6.2.1. Basic concepts of crystallization from solution

Crystallization is a thermodynamic transition from one phase – vapour, gel, melt or solute – into the crystalline phase, a solid state with a highly ordered micro-structure. In this work, we focus on crystallization from a solution – a mixture of a solvent and a solute material that is homogeneous on the molecular scale (or the solute complexes are at least not bigger than a small number of molecules) [24, 157]. Due to the stoichiometry of hybrid perovskite (details were explained in section 5.1), all solutions treated later have different solute molecules and ions present at the same time. However, assuming these are always perfectly mixed, we simplify our models in this chapter to one species of solute particles. We designate the mass of these 'solute particles' per unit volume of solution $\left[\mathrm{kg\,m^{-3}}\right]$ as the concentration c_p^V and the number of 'solute particles' per unit volume $\left[\mathrm{mol\,m^{-3}}\right]$ as the molar concentration $\tilde{c}_\mathrm{p}^V$.

If c_p^V exceeds a certain value, the so-called *critical concentration*, $c_\mathrm{p,c}^V$, the solution will no longer be homogeneous, but solid state material precipitates as crystalline grains [24, p.115-116]. The forming of these grains encompasses the separate processes of *heterogeneous* and *homogeneous nucleation* as well as *crystal growth*, which we will treat in detail in the following sections. Whenever we use the term *crystallization*, we refer to both of these processes (it is discussed in recent literature that also the *agglomeration* that is coalescence of existing clusters should be seen as important process during crystallization[158]). Further, we define the concentration, at which a continuously stirred solution in contact with a powder of arbitrarily shaped crystal grains neither grows in solute mass due to dissolution nor diminishes in solute mass due to crystal growth, as the *equilibrium concentration* $c_\mathrm{p,0}^V$ (all powder particles are assumed to be larger than the critical nucleus size) [24, p.6]. It is important to be aware that $c_\mathrm{p,c}^V$ can be significantly higher than $c_\mathrm{p,0}^V$ because the nucleation of crystal seeds is limited by the surface-energy of the forming grains [24, p.82-83], as explained in the next section.

Let us now assume, we drive a system with a homogeneous solution from an initial concentration below $c_\mathrm{p,c}^V$ to a new concentration, $c_\mathrm{p}^V > c_\mathrm{p,c}^V$. We

expect that there is a net force as created by the particle-particle interactions favouring the agglomeration of particles such that the crystalline phase is formed. In thermodynamics, this driving force is represented by a difference in the chemical potentials, $\Delta\mu$, between the solute phase and the crystalline phase (the chemical potential is defined as the energy required or obtained when one particle is added to the respective phase). This chemical potential difference is defined as the *supersaturation* [24, p.4-6]

$$\Delta\mu = \mu_{\text{cryst.}} - \mu_{\text{solute}} = kT \ln\left(\frac{c_{\text{p}}^{V}}{c_{\text{p,0}}^{V}}\right) = kT \ln\left(\frac{\tilde{c}_{\text{p}}^{V}}{\tilde{c}_{\text{p,0}}^{V}}\right), \tag{6.36}$$

where $\mu_{\text{cryst.}}$ is the chemical potential of the crystalline phase, μ_{solute} is the chemical potential of the solute phase, k is the Boltzmann constant and T is the absolute temperature. (Depending on the concentration, c_{p}^{V}, the supersaturation can be negative or positive, thus favouring dissolution or crystallization. As stated above, we assume herein that $c_{\text{p}}^{V} > c_{\text{p,c}}^{V}$, implying $\Delta\mu > 0$.). In certain literature, we find the term supersaturation [24, p.197] alternatively defined as

$$\sigma = \frac{1}{kT}\Delta\mu = \ln\left(\frac{c_{\text{p}}^{V}}{c_{\text{p,0}}^{V}}\right). \tag{6.37}$$

Herein, we will use the term supersaturation synonymously for both quantities and distinguish in text and formulas by using the respective symbol σ or $\Delta\mu$.

6.2.2. Nucleation dynamics

Nucleation is the precipitation of at least one nucleus (or multiple nuclei) of n particles (or n_i particles for each nucleus i) in crystalline phase from the solution [24, p.77-79]. We distinguish between *homogeneous nucleation*, which describes the formation of nuclei of the pure solute phase, and *heterogeneous nucleation*, which designates the formation of nuclei on top of the surface of another material or a phase boundary, which are typically the substrate and film surfaces in thin-film processing (it is however also possible that suspended or dissolved impurities in the solution act as heterogeneous

nucleation centres, thus providing a critical mechanism for perovskite morphology formation). For now, we focus on homogeneous nucleation and later discuss how the equations need to be modified in case of heterogeneous nucleation.

There are two important quantities involved in formation of each nucleus – first, the supersaturation, $\Delta\mu$, as defined above, second, the surface energy of all the crystal facets of the nucleus. The latter can be calculated by the sum of all surface energy densities, f_i, multiplied with the respective area, A_i, of the crystal facet. The energy that is needed for the formation of a nucleus of n particles is then written as a difference of Gibbs free energy [24, p.84],

$$\Delta G = \sum_i f_i A_i - n\Delta\mu. \tag{6.38}$$

For a low number of particles, n, the surface energy term is commonly larger than the supersaturation term. However, as the particle number increases, the ratio of surface area to volume decreases such that a maximum value, ΔG^*, is reached at the so-called critical nucleus size, n^*. Consequently, all nuclei with $n < n^*$ will tend to decrease in size, while all nuclei $n > n^*$ will start growing as they follow the gradient to lowest energy. In other words, ΔG^* is the energy barrier that needs to be overcome for nucleation to take place [24, p.82-83]. This is the thermodynamic energy balance of classical nucleation theory (CNT), which is the only theory presented herein for the sake of simplicity. However, recent advances in nucleation theory show that random fluctuations alone are insufficient for describing nucleation in most real-world material systems[159]. In fact, the popular CNT assumption of nucleation by random fluctuations leads to a systematic overestimation of critical nucleus sizes. In many material systems, the much smaller 'kinetically effective nucleus' (KEN) as defined by only several molecular agglomeration processes governs nucleation instead[160]. Accordingly, it was demonstrated that substantial non-classical nucleation pathways exist in these material systems, which must be computed by considering the detailed molecular mechanisms involved in the formation of nuclei[161] (the high potential for misinterpretation of data arises from the fact that typical in situ characterization used for measuring nucleation rates have a detection limit of smallest particle size. Therefore, measurements of nucleation rates start only with 'first observable clusters', which may be significantly larger than elementary nuclei[160]).

For a large number of particles, each occupying the volume v_p, we can approximate the form of the nucleus as a sphere with radius, r. The number of particles is then given as $n \approx \frac{4}{3}\pi r^3/v_p$ and the area of the nucleus is $A \approx 4\pi r^2$. We define the average surface energy density, $\bar{f}$, such that $\sum_i f_i A_i = \bar{f}A$ and get [24, p.83]

$$\Delta G^* \approx \frac{16\pi}{3}\frac{\bar{f}^3 v_p^2}{\Delta\mu^2} \tag{6.39}$$

at the critical radius $r^* = 2\bar{f}v_p/\Delta\mu$ and the critical nucleus size [24, p.91]

$$n^* = 2\Delta G^*/\Delta\mu. \tag{6.40}$$

In case of heterogeneous nucleation, the critical nucleus size decreases because the surface energy density between the crystalline material and the substrate surface is lower than at least one f_i (if this inequality was not true, heterogeneous nucleation would be very unlikely because the bulk nucleation would cost less energy). Consequently, the energy barrier for heterogeneous nucleation, ΔG^*_{het}, is lowered as compared to the one for homogeneous nucleation ΔG^*_{hom} — proportional to the ratio of the volumes of the nucleus on the substrate, V^*, and the free floating nucleus, V_0 as shown in Figure 6.9. This adjustment yields the equation [24, p.90]

$$\Delta G^*_{\text{het}} = \Delta G^*_{\text{hom}} \cdot \frac{V^*}{V_0}. \tag{6.41}$$

This equation clearly demonstrates that solution impurities and/or the substrate surface can have a significant impact on nucleation dynamics by decreasing the effective critical nucleus size and thus the energy barrier for nucleation. This issue becomes increasingly important for solutions involving multiple, potentially impure precursor chemicals such as the perovksite solutions analysed in this work. The reason is that the space of possible chemical mechanics increases with the solution complexity opening up multiple nucleation pathways that all compete for lowest energy usage. Due to this reasoning, it is very probable that the nucleation in these solutions is governed by heterogeneous nucleation effects (at this point, the question arises of how the terms ‘heterogeneous’ and ‘homogeneous’ are defined properly. If impurities

are considered part of the solution or possibly the suspension, it is tempting to identify nucleation involving these impurities as 'homogeneous' because one commonly associates 'heterogeneous' with nucleation on surfaces or phase boundaries. These issues can only be resolved by acknowledging that nucleation truly consists of [multiple combinations of] elementary mechanisms of agglomeration. An accurate description of nucleation, including a definition of the terms 'heterogeneous' and 'homogeneous', must therefore start from an accurate analysis of these elementary mechanisms and classify them according to the involvement of 'foreign' species as demonstrated for example by Handwerk *et al.*[162, 163], which is however beyond the scope of this work).

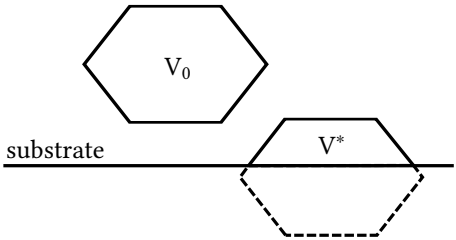

Figure 6.9.: A free floating nucleus with volume V_0 as formed by homogeneous nucleation and a smaller nucleus with volume V^* forming on the substrate surface by heterogeneous nucleation.

The rate of nucleation, J_0, is the number of nuclei forming in the solution per volume and per time [$cm^{-3}s^{-1}$]. In this work, we treat only stabilized nucleation rates, J_0. The real nucleation rate may however lag behind a change in supersaturation due to the time that the nuclei need to form from random fluctuations [24, p.143-154].

We can write the equilibrium nucleation rate [24, p.114] as

$$J_0 = \omega^* \Gamma N^*, \tag{6.42}$$

where ω^* is the frequency of attachment of particles [s^{-1}], Γ is the Zeldovich factor [no unit] and N^* is the equilibrium concentration of critical nuclei [cm^{-3}]. These can be found in literature:

- The Zeldovich factor [24, p.113] is given as

$$\Gamma = \left(\frac{\Delta G^*}{3\pi k T n^{*2}} \right)^{1/2}. \tag{6.43}$$

- The equilibrium concentration of critical nuclei [24, p.113]

$$N^* = \tilde{c}_\mathrm{p}^V N_A \exp\left(-\frac{\Delta G^*}{kT} \right), \tag{6.44}$$

  where N_A is Avogadro's number.

- For nucleation from solution, the frequency factor [24, p.118] is given as

$$\omega^* = 4\pi r^{*2} c_\mathrm{p}^V \nu \lambda \exp\left(-\frac{\Delta U}{kT} \right), \tag{6.45}$$

  where ν is another frequency factor $\left[\mathrm{s}^{-1}\right]$, λ is the mean free path of the particles [cm] and ΔU is the energy barrier of desolvation as caused by the interaction between solvent and solute.

In conclusion, because the exponential terms have the largest contribution, we find the approximate dependency [24, p.119]

$$J_0 \propto \exp\left(-\frac{K/\sigma^2 + \Delta U}{kT} \right), \tag{6.46}$$

where K is a constant depending on the surface energy of the crystal grains. When we plot this relation (see black curve in Figure 6.10), we find that the nucleation rate is very close to zero until a certain threshold of supersaturation, σ_c, is reached (as marked by the intersection of the dashed blue line with the x-axis). This threshold is the critical supersaturation that defines the critical concentration $c_{\mathrm{p,c}}^V = c_{\mathrm{p},0}^V \exp\left(\sigma_\mathrm{c}\right)$.

6.2.3. Crystal growth dynamics

The rate of step advance [cm/s] of a crystal face growing by spirals in a solution [24, p.229] is given as

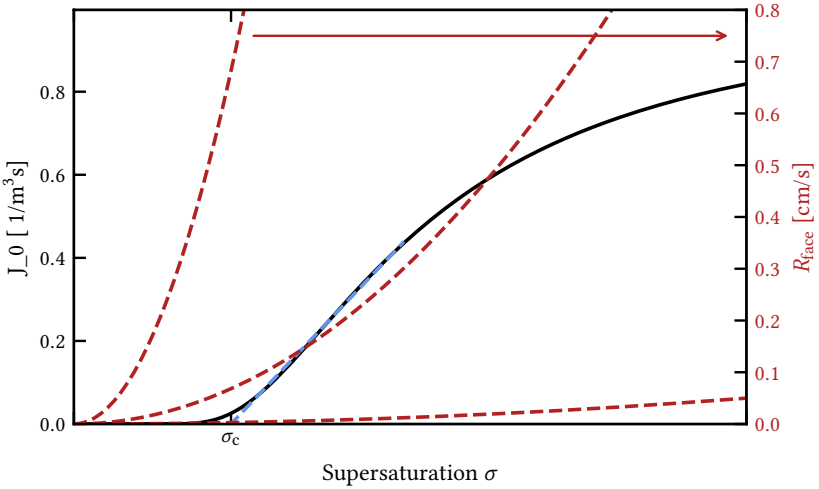

Figure 6.10.: Nucleation and growth rates according to Equations 6.46 (black solid line) and 6.48 (dark red dashed line). In the case of Equations 6.48 different proportionality constants are plotted. The critical supersaturation, σ_c, is obtained from a linear fit to the initial rise in nucleation rate (dashed blue line).

$$R_{\text{face}} = \frac{D_{\text{p,surf.}} c^V_{\text{p},0} v_p}{d} \frac{\sigma^2}{\sigma_{\text{ch}}} \ln\left[\frac{d}{\pi a}\frac{\sigma_{\text{ch}}}{\sigma}\sinh\left(\frac{\sigma}{\sigma_{\text{ch}}}\right)\right]^{-1}, \tag{6.47}$$

where σ_{ch} a characteristic supersaturation ($\neq \sigma_c$), a is the height of one growth step, d is the stagnant boundary layer thickness over the growing crystal facet and $D_{\text{p,surf.}}$ is the diffusion coefficient of solute particles on the crystal facet. Hence, for low supersaturation $\sigma \approx \sigma_{\text{ch}}$, we have [24, p.230]

$$R_{\text{face}} \propto \frac{\sigma^2}{\sigma_{\text{ch}}} \tag{6.48}$$

and for high supersaturation $\sigma \gg \sigma_{\text{ch}}$

$$R_{\text{face}} \propto \sigma. \tag{6.49}$$

Although used in some works on perovskite crystallization [164, 165, 166], it is crucial to note that the above relations are only true under the assumption, that it is very unlikely that new (2D)-nucleation occurs on the growing surface. If the supersaturation is high enough, this will no longer hold and 2D nuclei will form on the growing facet, potentially accelerating the growth [24, p.231-237]. Since the 2D-nucleation rate is proportional to $\exp\left[-K/kT\sigma - \Delta U/kT\right]$, we can then have for example

$$R_{\text{face,layer}} \propto \sigma^{(1/2)} \cdot \exp\left(-\frac{K_{\text{mono}}/\sigma + \Delta U}{kT}\right) \tag{6.50}$$

for mono-nuclear layer-by-layer growth [24, p.233] or

$$R_{\text{face,poly}} \propto \sigma^{(5/6)} \cdot \exp\left(-\frac{K_{\text{poly}}/\sigma^2 + \Delta U}{kT}\right) \tag{6.51}$$

for poly-nuclear layer-by-layer growth [24, p.231-237]. As a side note, we want to mention that many works [164, 165, 167] use a relation from Burton-Cabrera-Frank (BCF) theory (first introduced by Li *et al.* [168]) to determine the number of grains per unit area $[1/\text{cm}^2]$ as given by

$$< n >= 1.1 \left(\frac{J_0}{R}\right)^{1/2}. \tag{6.52}$$

It is often argued that, at high σ, the exponential relation in J_0 will dominate over the quadratic term in Equation 6.48, which would explain the significantly higher grain density in perovskite thin-films that were rapidly dried (driving the supersaturation up quickly). However, this argument is questionable given that the proportionality constants in Equations 6.48 and 6.46 are not known. Therefore, a comparison of magnitudes can produce arbitrary results as we show in Figure 6.10 by plotting R_{face} with different pre-factors. Besides, there is no certainty as to which of the growth mechanism takes place in dependence on the environmental parameters. To complete the picture further, we must consider that, during a drying process, the concentration and thus the supersaturation are not constant. This questions whether Equation 6.52, even if it was quantifiable, would determine the correct value for the grain size measured in the resulting polycrystalline thin-film. Concluding, Equation 6.52 could, in the optimal case, only determine the average size of

currently nucleating crystals and a more general, dynamic model is needed to predict the final grain size distribution as will be treated in the next section.

6.2.4. Predicting grain size distributions with LaMer's model‡

LaMer's model[169], introduced by Prof. Victor LaMer in 1950, is still widely cited to explain the precipitation of (close-to) mono-disperse particles from a supersaturated solution. Likewise, in perovskite research, it is often cited to explain how the crystal grain formation depends on the temporal evolution of the supersaturation[142, 170, 72, 165]. However, this practice must be seen with caution considering recent reviews by Whitehead *et al.*[159, 160]. They elaborate that LaMer's pioneering work is mostly 'inappropriately-cited' because it is often applied in its 'words-only form' to explain 'burst nucleation', while the original model is actually a growth-model and 'burst nucleation' is merely an assumption of the model rather than a consequence [158]. Arguably, considering the title of this section, we have to take a standpoint on this issue. The mathematical model we are going to elaborate herein is not identical to LaMer's original model, but a refined version according to the interpretations of Sugimoto *et al.*[171] and Chu *et al.*[172]. In that sense, nucleation is not any more assumed instantaneous (or 'burst') from the start (we rather assume a stabilized nucleation rate J_0 as a function of the current supersaturation, which is most likely incorrect, but good enough for our qualitative line of arguments). One could still argue that there is not enough experimental evidence for using this model and that models based on disprove-hardened two to four step molecular mechanisms should be preferred[159, 160]. However, at the state of this work, the author did not find enough evidence in literature to decide on a concrete mechanism (which may change in the future) and neither quantitative measurements of crystal growth nor nucleation rates are performed in this work. In this sphere of missing evidence, the (modified) LaMer model can be applied in a qualitative explanatory sense until disproved by quantitative measurements in the future.

According to LaMer's model as interpreted by Chu *et al.* [172], the solute concentration increase upon a nucleation is given by the simple rate equation

‡Section reviews ACS Applied Materials & Interfaces (2022) 14, 9, p. 11300–11312 by S.T., J.M., N.L., H.M.P, M.A., P.S., W.S., B.S.R and U.W.P. [21]

$$\frac{d\tilde{c}_{\mathrm{p}}^{V}}{dt} = Q_0 - e_1 n^* J_0 - e_2 R p_T, \tag{6.53}$$

where we added $e_1 = N_A^{-1}$ and $e_2 = \tilde{\rho}_{\mathrm{p}}^{1/3} N_A^{-2/3}$ to translate the equation to molar concentrations and harmonize the units, Q_0 is the rate of the increase of the concentration of perovskite due to drying $\left[\mathrm{mol\,m^{-3}s^{-1}}\right]$, J_0 is the equilibrium rate of nucleation $\left[\mathrm{m^{-3}s^{-1}}\right]$ (as introduced in section 6.2.2), n^* is the critical nucleus size [no unit], R is the rate of crystal face advance $\left[\mathrm{m\,s^{-1}}\right]$ (as introduced in the last section) and p_T is the number of already existing nuclei per volume $\left[\mathrm{m^{-3}}\right]$. Evidently, the number of existing nuclei must increase with the nucleation rate [172] as

$$\frac{dp_T}{dt} = J_0. \tag{6.54}$$

We assume further that the $n_i = J_0 dt$ new grains that nucleate at time t_i within the time span dt per volume are of critical nucleus size, n^*, and grow with time as

$$\frac{dr(n_i)}{dt} = R_{\mathrm{face}}, \tag{6.55}$$

where $r(n_i)$ is the radius of these nuclei (to be precise, this should change the last term in Equation 6.53 to $e_2' R \Sigma_i A(n_i) n_i$ or similar because the material used for crystal growth should increase with the areas of the existing nuclei, but we assumed for simplicity that the number of nuclei is very high and the nuclei are very small. We further note that state-of-the-art models of crystal growth of dispersions often come to the contrary conclusion that smaller nuclei grow faster than bigger ones[160]). As a last step, we need to specify Q_0, which we calculate from the film thickness evolution $d(t)$ determined as described before in section 6.1.5 (this is an approximation because a change in solute concentration also changes the concentration of solvent on the film surface, directly impacting the drying dynamics. However, since we assume that, in the ideal case, nucleation and crystal growth are induced very rapidly, the approximation is valid for our modelling concept.). We obtain Q_0 by the mean change in the concentration of solute molecules as

$$Q_0 = \frac{\mathrm{d}}{\mathrm{d}t}\left(\frac{n_\mathrm{p}}{d}\right) = -\frac{n_\mathrm{p}}{d^2}\cdot\frac{\mathrm{d}d}{\mathrm{d}t}, \tag{6.56}$$

where $n_p = \tilde{c}_p^V d\Big|_{t=0}$ is the number of solute particles per unit area $\left[\mathrm{mol\,cm^{-2}}\right]$. With all the above background information at hand, Equation 6.53 can be solved numerically using Euler steps (we assume for simplicity a constant thickness change $\mathrm{d}d/\mathrm{d}t$ and that the nucleation density is given by Equation 6.46 and the crystal growth rate by Equation 6.48).

As a result we obtain a qualitative model of the temporal evolution of $\tilde{c}_\mathrm{p}^V$ and J_0 in Figure 6.11 (the simulation cannot be quantitative because the quantitative nucleation and growth rates, as well as the critical supersaturation are not known). It is apparent that a higher drying rate leads to a narrower, higher peak in concentration/supersaturation and thus nucleation rate than a lower drying rate. Hence, the faster the film drying, the faster the concentration falls off and converges toward $\tilde{c}_{\mathrm{p},0}^V$ (or a supersaturation, σ, of 1), leaving the existing nuclei less time to grow. Figure 6.12 shows the corresponding simulated crystal grain size distributions. As a result, we find that a faster drying leads to a narrower grain size distribution with smaller grains than at lower drying rates.

Figure 6.13 shows AFM images of TCP thin-films as obtained by different drying rates[21] (details follow in section 8.3 and details on the perovskite follow in section 5.1). In Figure 6.13a, we find a morphology where individual nuclei grew to crystal domains with a diameter of almost 10 μm as produced by a relatively slowly dried perovskite solution film. Because the crystal growth depletes solute from the solution, the domains leave large spaces between them. In the following, we will call this morphology *growth-dominated* because the crystal growth mainly influences where the material will agglomerate and the nucleation density is low. In contrast, Figure 6.13b shows a morphology where the nucleation density is very high as produced by rapid drying of the same precursor solution. As a result, the examined area is densely packed by small nuclei, leaving the growth less time to influence the morphology, which is why we will call the morphology *nucleation-dominated*. We conclude that the predictions of LaMer's model are in line with the experimental observation that faster dried perovskite thin-films will have a higher grain density (details follow in section 8.1 and 8.3). (We use the term 'grain' synonymously with the crystalline domains that can be spotted in AFM and SEM, even if this definition is known to be problematic [173]. However, it

is still plausible that the formation of these domains follows LaMer's model even if one domain can contain multiple pure crystalline grains.).

At the end of this section, it has to be stressed again that the outcome of LaMer's model depends heavily on the (currently unknown) dependencies of nucleation and crystal growth on the supersaturation - probably affected by heterogeneous nucleation due to impurities. However, even when leaving aside these issues in addition to the above-mentioned problems with inappropriate citation and sparse quantitative evidence, LaMer's model is still a strong simplification. The reason is that locations of grains are not considered and the model represents only an average balance over the whole reaction volume instead. This description might be appropriate for the case of a stirred solution volume, which the model was developed for. However, in a drying solution film covered in this work, we do not expect the growing nuclei to move laterally by a significant amount and their positions might be crucial for the resulting morphology. The reason is that, as we showed before, each nucleus depletes the solute concentration in a halo around them, which is partially equilibrated by diffusion of solute from the surrounding solution [24, 165, p.161]. Furthermore, the nuclei might have preferential directions of growth, potentially as a function of their (heterogeneous) nucleation mechanism [24, p.14-32]. All these effects can produce characteristic shapes and morphologies, which are not included in the simple balance equation model derived above. More detailed treatments can be found, for example, in the works of Liu *et al.* [164] and Michels *et al.* [174]. In this work, we consider only the qualitative trend that different grain size distributions are the result of different drying rates as demonstrated above. For this purpose, LaMer's model yields enough detail, given that a more detailed prediction would require accurate *in situ* characterization to test these predictions, rather than just the distinction of *ex situ* SEM, AFM, photographs and/or WLI measurements as we use in our studies (see chapter 5 for more details). Once, more detailed nucleation and growth kinetics are determined, the modelling concepts introduced in this section can be refined in the future, which will most likely narrow down the number of possible models.

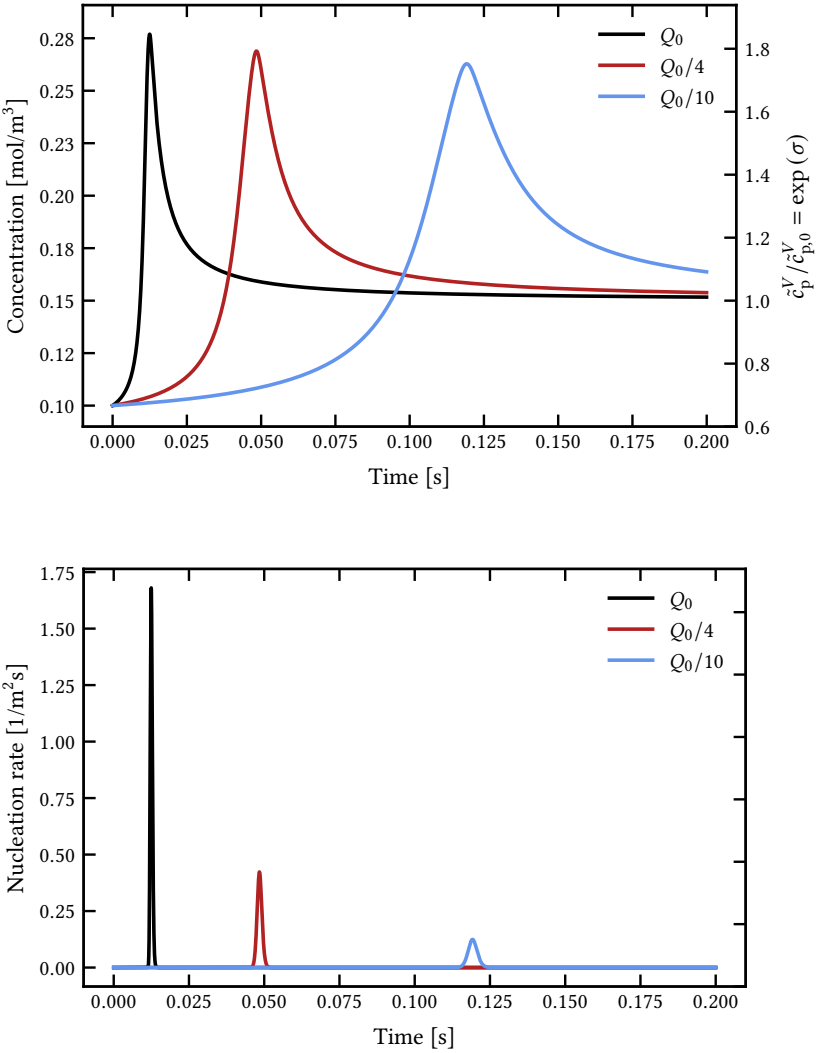

Figure 6.11.: Simulation of solute concentration $\tilde{c}_p^V$, or exponential of supersaturation $\exp(\sigma)$ and nucleation rate, J_0, according to Equations 6.53 - 6.55 for different drying rates, that is mass transfer coefficients, as represented by the constants Q_0, $Q_0/4$ abd $Q_0/10$. The units are not quantitative.

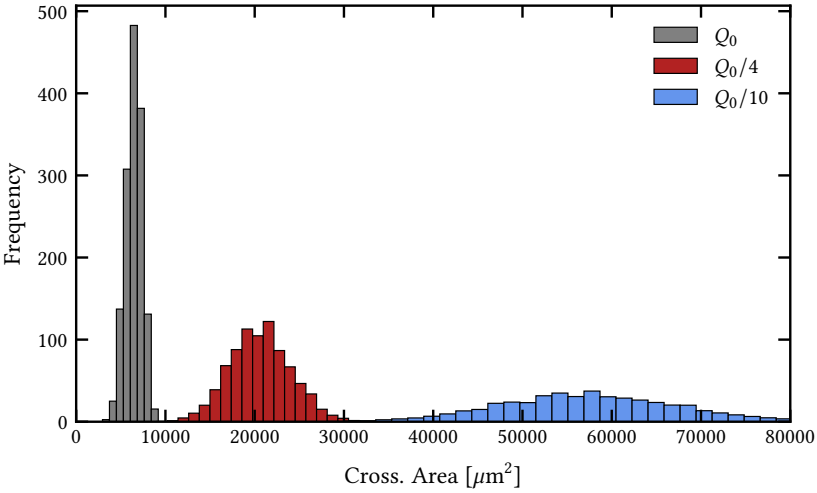

Figure 6.12.: Histogram of simulated grain size distribution for scenarios in Figure 6.11.

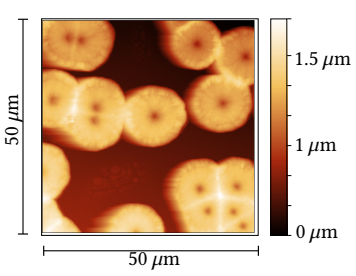

(a) AFM measurement of morphology of a slowly dried TCP thin-film

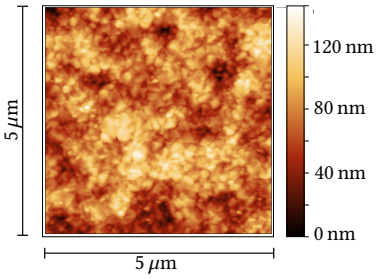

(b) AFM measurement of morphology of a rapidly dried TCP thin-film

Figure 6.13.: Growth and nucleation-dominated morphology due to different drying[21].

6.3. Final assessment of drying and crystallization models for hybrid perovskites

It is crucial to note that there is never a perfectly accurate, 'true' model. Only comparative falsification, that is the distinction between more and less suitable models, is within the reach of experimental science[175]. In this spirit, we can classify the models/equations according to their logical rigidity, on the one side, and empirical prediction power on the other side. While we derived some models from logically solid principles (that is deductively), they do not (yet) enable the prediction of relevant experimental results, mostly because important parameters are unknown, we do not have the necessary characterization tools to test them or the resulting dynamics are too complicated to calculate. Examples for this kind of models are the equations of crystal growth and nucleation rates. In this case, it is not sensible to provide more detailed theories beyond the standard ones, here classical nucleation and fluctuation theory, because there is no way of distinguishing from quantitative data which model applies. Instead, we used hypothetical parameters or simplified numerical models to enable at least a qualitative idea of the involved dynamics in extreme cases, as for example nucleation-dominated or growth-dominated areas. Other models derived herein may be subject to controversy because only motivated by empirical observation (that is inductively) and not (yet) by logical foundation, but predict quantitative, experimental data astonishingly well. Therefore, they are very useful working hypotheses that however need further testing. These are for example the Chin/Agarwal correlation that was used for fitting the mass transfer and/or the reduction of the vapour pressure due to suspected intermediate phases resulting in Equation 6.35. The optimal case, which are models that are derived from fundamental principles and enable high empirical prediction power are, of course, what we aim for. The fewer degrees of freedom a model has, while still consistent with the experiment, the higher is its prediction power. This makes the models simpler and easier to falsify, which is a scientific advantage[175]. In this context, the reduction of free parameters by making suitable approximations is very important, such as the hypothesis of negligible concentration gradients we apply in section 6.1.5. Furthermore, the reduction of free parameters mostly simplifies calculations. For example, simplified differential equations that can be solved analytically are, if still consistent with the measured data, preferential equations that only have numerical solutions. Equations 6.27 and 6.28 modelling the drying dynamics in a two-solvent film are a good example

of a such a simplified model based on fundamental principles that still has a high predictive power and essentially no free parameters, except the initial concentration of molecules N_1 and N_2. Of course, as mentioned above, this model lasts on the very strong assumption of negligible concentration gradients of all components at all times. However, it is still astonishingly successful as we showed in Figures 6.7 and 6.8, which can be explained by the fact that $\mathrm{Bi}_d^{\mathrm{an.}}$ used in our experiments are (most of the time) below 0.1 hindering the formation of diffusion gradients inside of the film. In the case of higher $\mathrm{Bi}_d^{\mathrm{an.}}$, we have to use solvers for partial differential equations. This will be elaborated in the appendix for readers who are interested in a more rigorous treatment (see section A1.2), yielding the result that the hypothesis of negligible concentration gradients is a good approximation even until $\mathrm{Bi}_d^{\mathrm{an.}}$ of 10^3 (The simulation further shows that the observed drying dynamics cannot be reproduced by film limited drying even with a concentration-dependent diffusion coefficient). Another possibility to extend the capability of the model would be the addition of another solvent. In this case, the differential equations would need to be solved by a time-stepping algorithm, which is a standard numerical method. We did not include any further information in this thesis for keeping it concise, but further information can be found for example in [176].

Let us now recapitulate quickly the content of this chapter. An easy-to-use modelling framework is provided for the quantitative description of the drying dynamics of perovskite precursor solutions with up to two solvents and temporally or spatially varying mass transfer coefficient. The model is well defined if the mass transfer coefficient (or heat transfer coefficient) is known (and $\mathrm{Bi}_d^{\mathrm{an.}}$ is below 10^3). For the TCP solution, the model needs an additional measurement of the reduced activity and onset thickness of the intermediate phase drying regime. In the future, model extensions for more solvents or other quenching methods (beyond gas quenching) are imaginable. This is the answer to research question 1 (see section 3.3). What concerns the crystallization, LaMer's model combined with fundamental equations of nucleation and crystal growth provides a qualitative way of predicting the crystal grain size distribution. It is however very likely that LaMer's model will be replaced in the future by a disprove-hardened, more detailed mechanistic model consistent with dynamic measurements of crystal growth and nucleation. This could also allow a more detailed understanding of the impact of other process parameters, as for example the temperature. We conclude that we answered research question 2 (see section 3.3), as well.

7. Advancing characterization techniques for perovskite solution printing

In order to assess whether the drying or crystallization models discussed in the last chapter are accurate, characterization techniques are needed. Herein, we distinguish between *ex situ* techniques that are applied after the annealing process of the readily crystallized perovskite films and *in situ* techniques that are applied during the drying or the crystallization process. We note that both are equally important and should be seen as complementary rather than contradictory. In chapter 5, we already described the *ex situ* microscopic techniques used in this work. Here, we will discuss the adoption of one-point *in situ* interferometry to perovskite solutions, which was originally developed for a previous work on organic PV by Schmidt-Hansberg *et al.* [93]. Furthermore, we will discuss the design of *in situ* multichannel imaging, which addresses the question whether *in situ* characterization can be extended to record large areas and to have the capability of (spectral) photoluminescence measurements at the same time. Additionally, the adapting of thermochromic liquid crystal measurements to very narrow slots and fitting of mass transfer correlations to these measurements is discussed (the corresponding setup used was designed by Cavadini *et al.* to determine the localized heat-transfer of large-area nozzle arrays[145]). The gathered analytical measurement methods discussed in this chapter are an answer to research question 3 (see section 3.3).

7.1. In situ interferometry* ‡

Interferometry relies on the effect of thin-film interference. In the configuration used in this work, the reflected light of five consecutive points (along the air flow direction in the drying channel discussed later in section 8.1) is probed by five red laser diodes (660 nm) and respective photodiodes (see Figure 7.1) [19, 21, 93]. As the monochromatic light impinges on a thin-film under a certain angle α, it splits into two partial light waves. One light wave is directly reflected on the top film surface. The other passes through the film, is reflected on the bottom surface and then leaves the film, being diffracted in the same direction as the first wave (see Figure 7.1). As a result, the two light waves superpose with the geometric optical path difference

$$\Delta(d, n_f) = 2d\sqrt{n_f^2 - \sin\alpha^2}, \tag{7.1}$$

where d is the film thickness and n_f is the refractive index of the film. The reflected light waves interfere constructively if $\Delta = m\lambda$ and destructively if $\Delta = (2m + 1)\lambda/2$, where m is an integer (see typical interference signal in Figure 7.2).

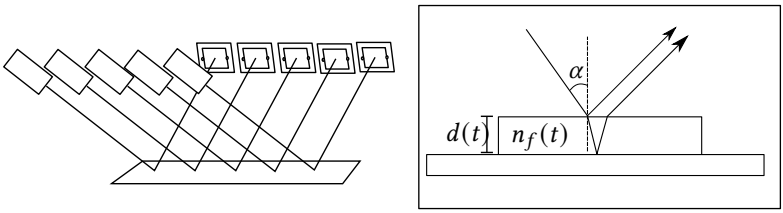

Figure 7.1.: Schematic of the reflectometric setup used on top of the drying channel described later in Figure 8.1. Five lasers probe the reflection on the thin-film in five positions along the air flow direction and the reflected light intensities are measured by respective photodiodes. Each laser beam is split into two partial light beams that superpose again on the photodiode.

*Section reviews Advanced Energy Materials 9 (2019) p. 1901581 by S.T., B.T., J.A.S, I.M.H., T.A., W.M., U.L., P.S., W.S., B.S.R. and U.W.P [19]

‡Section reviews ACS Applied Materials & Interfaces (2022) 14, 9, p. 11300–11312 by S.T., J.M., N.L., H.M.P, M.A., P.S., W.S., B.S.R and U.W.P. [21]

It follows that, in a drying film of solvent with refractive index n_i where d varies from $d = d_0$ to $d = 0$, we will see $n = \text{int}\,[\Delta(d_0, n_i)/\lambda]$ full (and $2n$ peak-to-peak) oscillations, where 'int []' is the integer function that cuts off the decimal part of the number (instead of rounding). If we now introduce a solute, the drying process will stop at a certain thin-film thickness d_p where the film consists entirely of solid (details were explained in the analytical drying model in section 6.1.5). Furthermore, we will have in this state $n_f = n_p$. Hence, the process stops at the offset $\Delta(d_p, n_p)$ of optical path difference. We note that, in this case, we cannot simply calculate the number of oscillations as above because the refractive index of the film, n_f, will change with the thickness as the film dries. Schmidt-Hansberg *et al.* have used a very simple interpolation formula to estimate the evolution of the refractive index, n_f [177]. They set

$$n_f = \phi_p n_p + \phi_i n_i = \frac{d_p}{d} n_p + \left(1 - \frac{d_p}{d}\right) n_i. \tag{7.2}$$

where ϕ_p and ϕ_i are the volume fractions of the solute and the solvent respectively. Inserting this into Equation 7.1, we obtain a quadratic equation in d that can be solved (not shown here, see [177]). We count the extrema (peak-to-peak) backwards in time from the dry film (see Figure 7.2), set $\Delta = \Delta(d_p, n_p) + n\lambda/2$ (which is called *backtracking algorithm*) and insert this into the quadratic equation. We then plot the obtained thicknesses d_n against the time signatures of the extrema t_n (that is the positions of the maxima visible in Figure 7.2) and obtain the drying curves treated earlier in Figures 6.7 and 6.8. We note that Equation 7.2 was not tested experimentally. However, the refractive index of perovskite at the laser wavelength, being 2.48 [178], and 1.43 of the DMF (or 1.47 of DMSO), limit the possible error on the measurement of d [179]. (This is not enough to yield any significant deviations from the thickness evolution used for validating the drying models in Figures 6.7 and 6.8.)

As a last remark, we want to elaborate the case, where we use mixtures of the two solvents DMF and DMSO with the interferometry technique. The above described calculation method becomes more difficult in this case, because the molar mixing ratio of DMF to DMSO would need to be known at any point in time to calculate the resulting refractive index in the film. This could be done by starting from the wet film as calculated from the concentration of the solution (which is an alternative to starting from the dry film thickness)

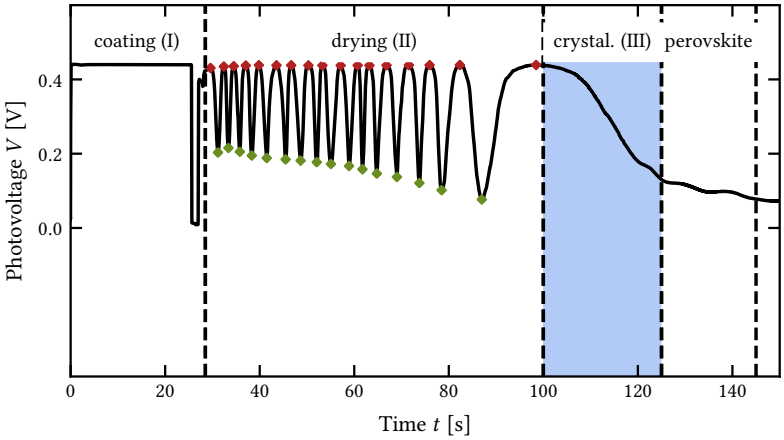

Figure 7.2.: Typical interference signal as measured by a single interferometer (solid black line) on a drying MAPI solution thin-film [19]. The red and green diamonds mark the positions of the respective interference maxima and minima. The different perovskite formation stages can be distinguished from the signal shape. Before the coating, the signal is just the reflection on the substrate, then the drying thin-film causes the oscillations as explained in the main text and finally the crystallization decreases the reflected light as more and more light is getting absorbed by the forming perovskite and reaches a semi-stable final state of (pre-annealed) MAPI.

with a known DMF:DMSO ratio and then, at the next data point, assume the ratio of evaporated DMF to DMSO is proportional to the ratio of vapour pressures and mass transfer coefficients. However, as stated above, the true difference in refractive index from DMSO to DMF is 0.05, implying that the error introduced by simply using the mean refractive index of the two solvents (as weighted with the initial volume ratio of solvents) is below the accuracy of the measurement technique.

7.2. In situ multichannel imaging[†]

In situ multichannel imaging (IMI) is a novel characterization technique that was developed in close cooperation with Felix Laufer[20]. The need to develop a new *in situ* technique became evident regarding two design limits of the interferometry setup (see last section). First, laser interferometry only resolves the drying process at five distinct points on the sample. Instead, a large-area detection would be suitable to monitor industrial scale fabrication. Second, after the onset of the crystallization process (as shown before in Figure 7.2), the interferometry cannot extract any further information (except changes in the reflectivity of the film surface at the probed wavelength). Instead, a method that is able to assess thin-film transformation after nucleation is preferable. With the goal in mind to create a highly-scalable, facile and easy-to-use technique compatible with industrial fabrication, we designed IMI according to the following principles:

- A large-area detection window
- High spatial resolution
- The capability to monitor reflectance, PL intensity and emission wavelength (that is three different channels)
- Fast acquisition times
- Non-invasiveness

The resulting system is depicted in Figure 7.3 (and is part of the second publication [20]). A scientific camera purchased from Thorlabs (CS2100M Quantalux) is mounted on a rack (compatible with the laminar flow channel discussed later in section 8.1) over a high power LED ring (HPR2-100BL) used for excitation. Under the camera, a quickly rotating filter wheel is mounted that is synchronized with the camera by an arduino UNO REV3 equipped with both a stepper motor driver board (MOTOR SHIELD REV3) and a thorlabs trigger board (TSI- IOBOB2). The filter wheel is loaded with different filters. These are:

1. A neutral density filter consisting of two rotatable polarisers

[†]Section reviews Solar RRL 6 (2021) p. 2100353 by S.T., F.L., P.S., W.S., B.S.R., I.A.H. and U.W.P. [20]

2. A longpass filter at a wavelength around the centre emission wavelength of the PL (780 nm in the publication)
3. A second longpass filter that is slightly off-centre but still within the Full Width Half Maximum (FWHM)-range of the PL (760 nm in the publication)
4. A shortpass filter at a wavelength around the centre emission wavelength of the PL combined with another longpass filter to block the excitation light. (775 nm, combined with a 660 nm long pass in the publication)

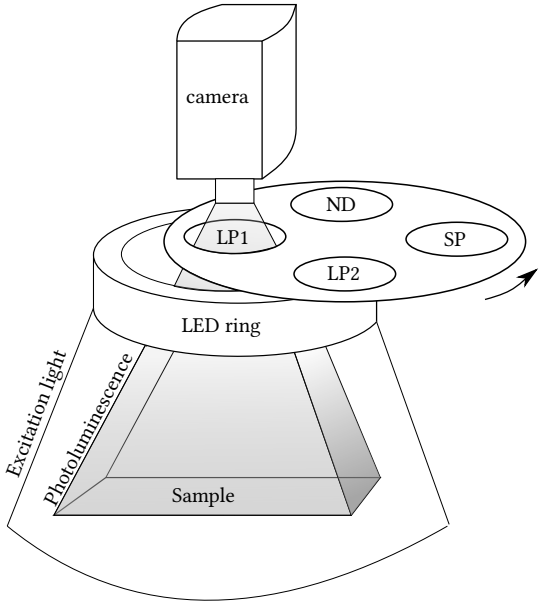

Figure 7.3.: Schematic of the IMI system. A high power LED ring excites the sample. The PL response / reflected light is recorded through a respective filter with a camera. The spinning filter wheel is synchronized with the camera trigger such that the next image is taken through the successive filter until the measurement is stopped (see section A2 for a photograph of the setup mounted on the laminar drying channel).

The images taken by the camera are sorted in different folders corresponding to the filter they were taken through. These folders are then used for the further image processing with Python. Four images at a specific time make up

a complete image set. From such an image set we can calculate the following 'channelled' images:

- The reflectance channel by simply choosing the ND images. These can optionally be normalized by a reference image of the substrate before the coating was applied.
- The PL intensity channel by simply adding up the images of the first longpass filter and the shortpass filter. These do, in approximation, yield the full PL intensity.
- The central emission wavelength channel by using all three images taken through the bandpass filters according to the method introduced by Chen *et al.* [180]. The longpass filtered images are divided by the short pass filter image, yielding images of two ratios. These ratios are then searched for every pixel in two lookup tables with the dimensions FWHM and centre emission wavelength, λ_0. The look-up tables are generated by calculating the ratios I_2/I_4 and I_2/I_4. The intensities are predicted using a simple Gaussian PL emission model, transmission measurements of the respective filter(s), $T_{i,\mathrm{filters}}(\lambda)$, as well as the cameras lenses, T_{lens}, and the spectral response of the detector $R_{\mathrm{det}}(\lambda)$ according to the formula

$$I_i = A \times \int \mathrm{Gaussian}_{\lambda_0,\mathrm{FWHM}}(\lambda) \times R_{\mathrm{det}}(\lambda) \times T_{\mathrm{lens}} \times T_{i,\mathrm{filters}}(\lambda) d\lambda \quad (7.3)$$

  where A is a calibration factor that can account for systematic offsets in the measurements (see [20] or [180] for details).

We note that the IMI technique is not restricted to the coating method. It could be used with slot-die coating, spray coating or inkjet printing. The only constraint is a free view on the drying thin-film from a minimal distance of around 5 cm. The setup is fully scalable and cost-efficient such that it could be replicated several times in an industrial production line to monitor large areas. Some transients of reflectance, PL intensity and emission wavelength acquired by IMI during MAPI fabrication will be described in section 8.1.1. For now, we just want to point out that the results are consistent with knowledge obtained by other works on *in situ* characterization [181, 182, 183].

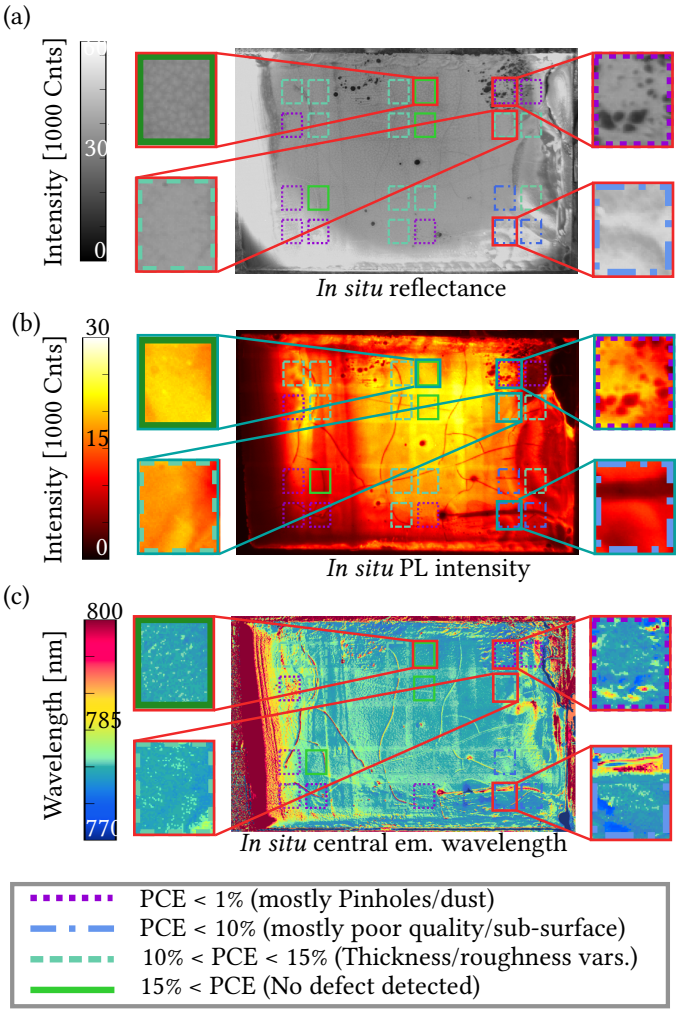

Figure 7.4.: Exemplary image set of the three channels of IMI during the drying of a blade coated MAPI film in the drying channel ($T = 40\,^{\circ}\mathrm{C}, v = 2\,\mathrm{m\,s^{-1}}$). The rectangles magnify extracts of the image where the active areas of the solar cells are situated later. The colours and line styles indicate which performance the respective solar cell exhibits later. These PCEs mostly correlate with active areas where IMI can detect a corresponding morphological defect. Reproduced with permission from [20].

Due to the large-area detection of IMI, it can be used to localize morphological defects (see Figure 7.4). These defects can be classified according to their occurrence in either channel [20]. Pinholes/dust (see magnified rectangle in the top right of each image) are visible in all three channels, semiconductor quality/subsurface defects are only visible in the PL channels (see magnified rectangles in the bottom right) but not in the reflection channel. The same is true for thickness/roughness variations (see magnified rectangles in the bottom left), which are indicated by slight variations in PL intensity and PL emission wavelength. It can be demonstrated that the defect classes correlate with the performance of PSCs incorporating the absorber layers with the respective defect (see Figure 7.5). The small rectangles in Figure 7.4 indicate the PCE of the respective device that was built incorporating the examined perovskite layer. In most cases, a PCE over 15% correlates with a device area where no defect is detected (see green solid line rectangles and magnified rectangles in the top left in Figure 7.4 and solid green JV-curves in Figure 7.5). Small thickness/roughness variations mostly cause the PCE to lie between 10% and 15% (see turquoise dashed rectangles in Figure 7.4 and turquoise dashed JV-curves in Figure 7.5), semiconductor quality defects let the PCE decay to under 10% (see blue dash-dotted rectangles in Figure 7.4 and blue dash-dotted JV-curves in Figure 7.5) and pinholes/dust prevent the functionality of the device completely (see purple dashed rectangles in Figure 7.4 and purple dashed JV-curves in Figure 7.5). However, when analysing the image extracts in Figure 7.4, we find that the correlation is not always confirmed.

Table 7.2 depicting the identical data from the second publication [20] contains a more detailed statistical analysis of the statements made above, in particular a count of devices below 10% of PCE. If IMI is seen as a tool to detect coating problems affecting the PCE, we can derive rates of false negatives or false positives. Clearly, the 38% of devices (9) that exhibited no defect, but still have a device performances below 10% can be counted to false negatives. (It is important to mention that a PCE drop is not necessarily caused by a problem with the perovskite absorber. Also during the deposition of the ETL/HTL layers as well as the sample handling, errors might affect the PCE which might explain these false negatives.) The false positives, on the other side, need to be analysed according to the category of the detected defect. In case pinholes/dust are detected, all examined devices exhibit an inferior PCE. With the semiconductor/quality detected in the PL response, this is the case for almost all devices (83%). However, the thickness/roughness variations exhibit almost equally many devices over 10% PCE as below 10%

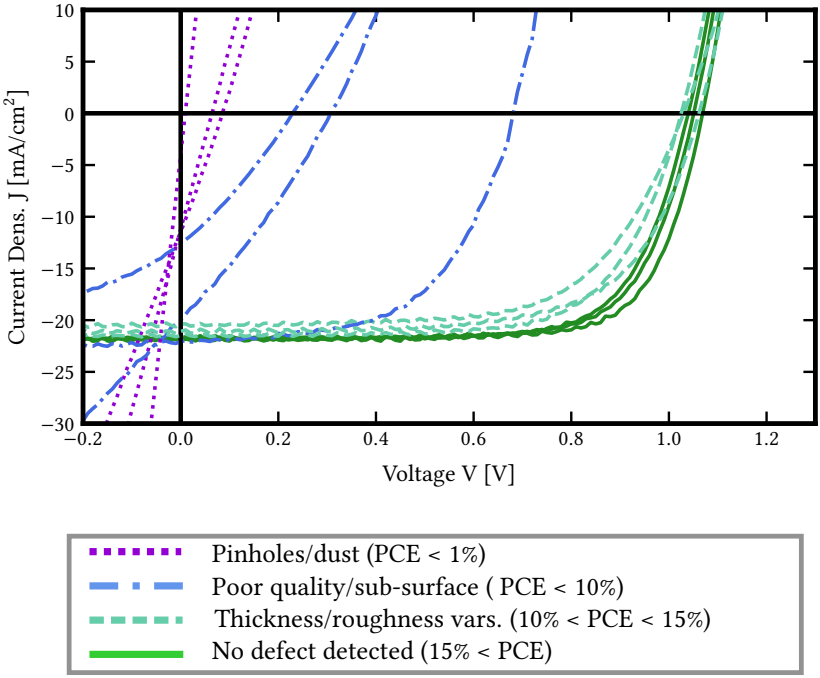

Figure 7.5.: Typical device performances (as measured by backward JV-sweep) for MAPI devices fabricated on the active areas shown in Figure 7.4. Reproduced with permission from [20].

PCE. This is, of course, partially because the chosen threshold of 10% lies within the range of most PCEs for this category. However, it also points to the fact that this category of defects does not yield enough information to decide whether the respective devices will be performant or not. For this category, it is probably necessary to conduct more sophisticated data analysis, in the future. Afterall, we conclude that IMI succeeds in localizing a large fraction of defects that lead with almost certainty to non-functional devices (which is 63% of the faulty devices) with a false positive rate of 4% (as given by the two devices in the category of semiconductor/quality exhibiting still a PCE above 10%). Furthermore, the additional PL channels help identify more defects than would be visible solely by a reflection measurement. Due to the fast and large-area acquisition, IMI could be used for in-line direct

	Thickness variations	**Absorber quality**	**Pinholes/dust**	**No defect detected**
Best detection	PL, WLI	PL, Em. Wl.	All, preferably ND, WLI	None
Impact	FF, R_s	V_{OC}, FF, R_s, R_p	FF,V_{OC}, J_{SC}, R_s	-
Performance of most devices	10% < PCE < 15%	PCE < 10%	PCE < 1% or n.a.	15% < PCE
# times detected (/# samples)	53(40%)	12(9%)	43(33%)	24(18%)
# devices with PCE < 10% in this category	24	10	43	9
# devices PCE < 10% / # times detected	45%	83%	100%	38%

Table 7.2.: Table of the different defect categories detected by IMI and a statistical evaluation of their correlation with 132 n-i-p device PCEs [20]. The WLI image in Figure 5.7 was additionally correlated with the images in Figure 7.4 for comparison.

feedback optimization. The feedback signal could be, for example, the density of defects or characteristic transients in reflectance, PL intensity or emission wavelength (as will be shown in section 8.1.1). In this way, differences in the production as for example the air humidity of the solution concentration could be detected instantly and corrected by the coating or drying parameters. This could be an efficient way to mitigate the problem of reproduction, which is imminent in almost all perovskite solution processes[184].

7.3. Thermochromic liquid crystal measurements ‡

Spatially resolved thermochromic liquid crystal (TLC) measurements were introduced by Cavadini *et al.* [145]. A plate of perspex with known heat capacity, $c_{p,w}$ $\left[\mathrm{J\,kg^{-1}K^{-1}}\right]$, heat conductivity, λ_w $\left[\mathrm{W\,m^{-1}K^{-1}}\right]$, and mass density, ρ_w $\left[\mathrm{kg\,m^{-3}}\right]$, is stabilized at a pre-set temperature, T_0. Then, the plate is quickly moved under the air stream to be investigated and the air stream cools the plate by a heat transfer process. The bottom side of the plate is coated with a temperature sensitive liquid crystal which is imaged during the experiment by a commercial camera (see Figure 7.6a) [21].

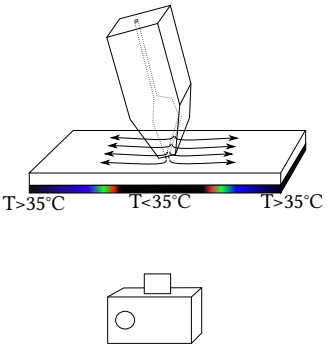

(a) Sketch of the TLC measurment setup. A plate of perspex coated with TLCs recorded by a camera is cooled by the air stream to be investigated.

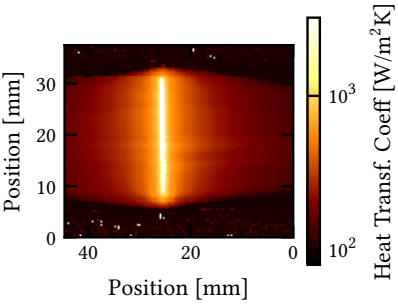

(b) Measured (2D) heat transfer coefficient as measured with the setup on the left.

Figure 7.6.: Schematic of a TLC measurement: As the temperature gradually changes, the colour of the TLCs changes as imaged by a camera. From these colour changes the 2D Heat Transfer Coefficient can be calculated.

‡Section reviews ACS Applied Materials & Interfaces (2022) 14, 9, p. 11300–11312 by S.T., J.M., N.L., H.M.P, M.A., P.S., W.S., B.S.R and U.W.P. [21]

The recorded colour change over time in the foil can be correlated with a temperature-change of the plate by tracking the green intensity maximum. The temperature over time, $T(t)$, is then fitted to the step function solution of the heat equation

$$\frac{T_w(t) - T_0}{T_\infty - T_0} = 1 - \exp\left(\alpha^2 \frac{t}{\rho_w c_{p,w} \lambda_w}\right) \operatorname{erf}\left(\alpha \sqrt{\frac{t}{\rho_w c_{p,w} \lambda_w}}\right) \tag{7.4}$$

where T_0 is the initial temperature, T_∞ is the temperature of the environment and α is the heat transfer coefficient to be determined as defined in Equation 6.1.3. A typical result of such a measurement is depicted in Figure 7.6b. If such a measurement is averaged over horizontal lines in the centre of the nozzle, the data shown before in Figure 6.5b and 6.5a are obtained. As stated before in section 6.1.4, we perform many of these measurements at different parameters to get a good estimation of the mass transfer of the used slot-nozzle (details follow in section 8.3 for different parameters). In these experiments, we vary the gas velocity, v, from $15.8\,\mathrm{m\,s^{-1}}$ to $79.4\,\mathrm{m\,s^{-1}}$ in steps of $15.8\,\mathrm{m\,s^{-1}}$, the distance of the plate, H, from 3 mm, 4 mm to 5 mm and the angle, θ, from $90°, 82.5°, 75°$ to $62.5°$. These measurements are fitted globally against the correlations introduced before (see section 6.1.4). For the fit, the appended sum of squared residuals, χ^2, are minimized by variation of the parameters $p_1, \ldots, p_n$ of the respective correlation. That is to say, we calculate for all measurements

$$\chi^2(p_1, \ldots, p_n) = \sum_k \sum_i \frac{\left[\alpha_{\mathrm{corr}}\left(x_i, u_{0,k}, H_k, \theta_k, p_1, \ldots p_n\right) - \alpha_{\mathrm{meas,k}}\left(x_i\right)\right]^2}{\left[\Delta\alpha_{\mathrm{meas,k}}\left(x_i\right)\right]^2} \tag{7.5}$$

where $\alpha_{\mathrm{meas,k}}\left(x_i\right)$ is calculated by averaging all regular horizontal rows of the 2D distribution and $u_{0,k}, H_k, \theta_k$ are the respective gas velocity, nozzle height and impinging angle. The resulting parameters are used for predicting $\beta(x)$ (as plotted before for exemplary u_0, H and θ in Figure 6.5b) when modelling the drying process of dynamically moved substrates under the slot jet later (see section 8.3). An overview of the full datasets and resulting parameter values can be found in [21].

7.4. Prospects and limitations of in situ characterization

The importance of *in situ* characterization is demonstrated with two main setups in this work, the one-probe interferometry (at five points) and the *in situ* multichannel imaging (IMI). Both methods should be seen complementary and one does not replace the other. While one-probe interferometry has a very high sampling rate (up to 100 kHz) and is successful at probing thin-film interference and thereby drying dynamics in the laminar air flow, the time resolution of IMI is limited by the frame rate of the camera such that it can detect some oscillations in reflectance but the oscillation period saturates at 100 Hz. However, IMI offers instead a high spatial resolution and multiple detection channels, which makes it the perfect candidate for surveillance of process homogeneity on large scales. *In situ* characterization is always a trade between temporal or spectral resolution on the one hand and the information content in the detection channels on the other hand. For example, if one wanted get more precise spectral information or highly time-resolved photoluminescence data, one would need to sacrifice one spatial dimension (since detector areas are mostly 2D) or slow down the acquisition rate substantially. IMI is, seen from this perspective, a design compromise to obtain a fairly high information content and time resolution on large areas. In future designs, one could indeed investigate the exact spectra at some sample points in depth or make a spectrally sensitive system that images only a line of points. In this way, the information of IMI could be correlated more accurately and understood. It would be possible as well to use x-ray diffraction in combination with the system. The hope would be that IMI records enough information in the detection channels to predict the success or failure of principal formation dynamics such as nucleation density, intermediate phase formation, crystal growth rate or direction. Another viable way to filter the information out of IMI's detection channels would be a more sophisticated data analysis methods such as artificial intelligence.

For attempting an answer to research question 3 (see section 3.3), we could state that both *in situ* interferometry as well as *in situ* multi-channel imaging can yield crucial information on the perovskite drying and crystallization dynamics in large-scale coating systems. If this information is combined with the modelling frameworks discussed in chapter 6 and additional exact measurements of heat/mass transfer coefficients by thermochromic liquid

crystal measurements described in the last section, the current state of drying and crystallization can be assessed very early in the fabrication process, which can possibly be used to directly correct coating parameters without the need to finish device fabrication (or even annealing), first. In the future, the level of data evaluation as well as automation can be increased to profit from these advantages at full scale.

8. Drying and crystallization in blade coated perovskite solution films

The vast majority of state-of-the-art perovskite solar cells is fabricated by in-glovebox spin coating, rinsing the still-spinning substrate with an anti-solvent – a process called anti-solvent quenching – to induce a fast and homogeneous nucleation of the perovskite film by rapid supersaturation (this is analogous to a very fast drying as explained in section 6.2.4). However, both the spin coating process and the anti-solvent quenching by pipetting on a spinning substrate are non-scalable. The reason is that the substrate breaks at too high rotational force and that the centrifugal spreading of the liquid film is radius dependent. Therefore, a transfer of this process to scalable deposition methods is required. In this chapter, we transfer typical spin coating recipes to blade coating of the perovskite precursor with additional processing steps to achieve the quenching: The application of a laminar air flow on a static sample, the anti-solvent spray quenching on a static sample and a dynamically moving sample moving past a narrow-slot high-pressure gas jet. In every section, the optimization of the respective process parameters in terms of thin-film morphology and device performances is presented. Whenever possible, the outcomes are correlated with *in situ* characterization methods as well as drying and crystallization models to fundamentally explain the interrelation of the processing steps and the perovskite formation stages. In the two final sections, we compare the resulting device performances in terms of magnitude as well as repeatability and attempt a comparative assessment of suitability of the different methods for large-scale perovskite printing, which is essential an answer to research question 4 (see section 3.3). Finally, also the impact of using green solvents as compared to conventional solvents is discussed, providing an answer to research question 5.

8.1. Drying (or quenching) in a laminar air flow channel

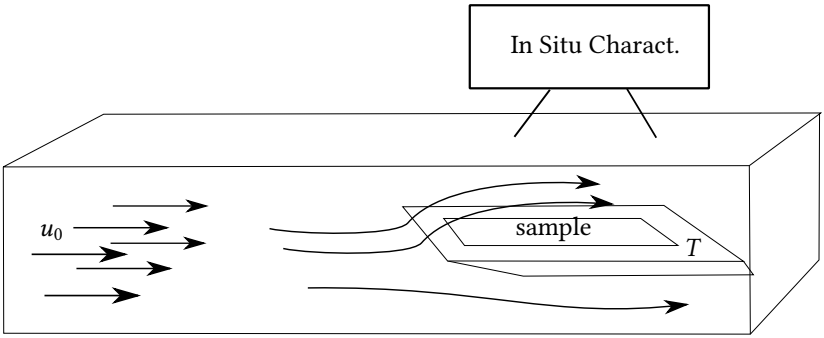

Figure 8.1.: Schematic of laminar air flow channel as applied in all main publications [19, 20, 21] (photos of the setup can be found in the appendix in section A2). After a run-in distance of 48 cm the air flows over a wing-shaped table holding the substrate with the blade-coated perovksite solution film. The temperature, T, of the whole system (air, table, walls) can be stabilized and the air flow, u_0, is controlled by a mass flow controller (and measured by a hot-wire anemometer).

.

The laminar air flow channel drawn in Figure 8.1 was developed and applied on the fabrication of organic solar cell devices by Schmidt Hansberg *et al.*[177]. The purpose of the system is to investigate drying processes of blade coated solution thin-films in a highly controlled environment of a constant air flow velocity, u_0, and temperature, T. In the same time, *in situ* characterization such as reflectometry (see section 7.1) or IMI (see section 7.2) can be applied to study the drying dynamics and/or the structural morphology evolution upon crystallization. For example, the drying rate or the photoluminescence response in dependence on u_0 and T can be assessed. Finally, the obtained thin-film morphology as well as the device performances can be correlated with such *in situ* data. In the following, we will summarize the results of this methodology for different perovskite precursors.

8.1.1. One-step deposition of methylammonium lead iodide*†

Methylammonium lead iodide, $CH_3NH_3PbI_3$ (short: MAPI) has the advantage that, in the reference spin coating process, natural drying is sufficient for the formation of a nucleation-dominated morphology [115] (see Figure 8.2a and section 5.1 for details on the used solution), leading to a high device performance as shown in Figure 8.2b. With this finding in mind, one could expect that the corresponding up-scaled blade coating process should require only natural drying to obtain a favourable thin film morphology. However, when investigating thin-films blade coated from the same precursor, they appear diffusely reflecting to the naked eye (not shown), which is correlated with a non-covering morphology on the micro-scale as measured by SEM (see Figure 8.2c). We attribute this to the higher wet film thickness (and correspondingly lower concentration) of the blade coated perovskite solution films, altering the preconditions for the crystallization due to different drying dynamics. Correspondingly, devices incorporating these layers will exhibit significant losses in performance, most of which is in FF and V_{OC}, indicating that significant non-radiative recombination and/or series resistance are present due to the direct contact of the the ETL and HTL layers (compare Figures 8.2b and 8.2d as well as Figures 4.5a and 4.5b). Additionally, a slight decrease in J_{SC} indicates that less area is covered by perovskite generating current (which is most likely a small effect due to light scattering and reflection on the back electrode). Fortunately, when increasing convection over the substrate by the laminar flow during the drying process, we obtain a nucleation-dominated morphology as in spin coating (see Figure 8.2e), leading to a comparable PCE [19] (compare Figures 8.2b and 8.2f). We note that the blade coated device exhibits less hysteresis, but that the average PCE of forward and backward JV-sweeps and the PCE at constant voltage are comparable (not shown here, see [19]).

*Section reviews Advanced Energy Materials 9 (2019) p. 1901581 by S.T., B.T., J.A.S, I.M.H., T.A., W.M., U.L., P.S., W.S., B.S.R. and U.W.P [19]

†Section reviews Solar RRL 6 (2021) p. 2100353 by S.T., F.L., P.S., W.S., B.S.R., I.A.H. and U.W.P. [20]

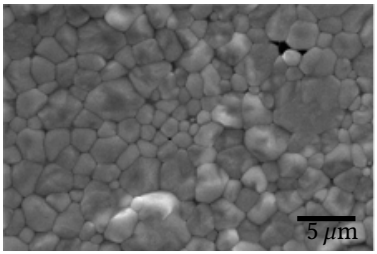

(a) SEM image of a MAPI film processed by spin coating

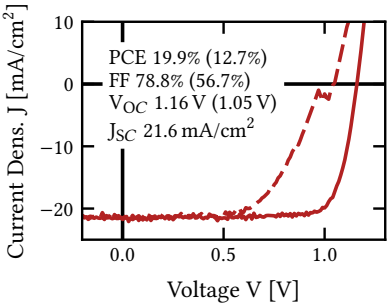

(b) JV-swipe characterization of a MAPI device fabricated by spin coating

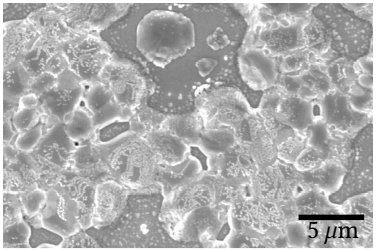

(c) SEM image of a MAPI film blade-coated with $u_0 = 0.02\,\mathrm{m\,s^{-1}}$ and $T = 55°\mathrm{C}$

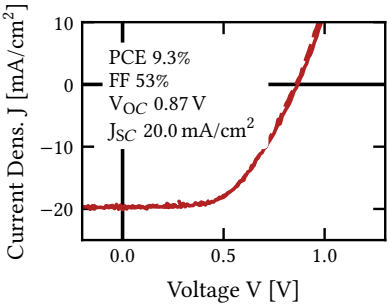

(d) JV-swipe of a MAPI device fabricated with the morphology shown on the left

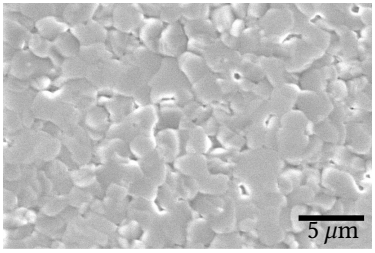

(e) SEM image of a MAPI film blade-coated with $u_0 = 2\,\mathrm{m\,s^{-1}}$ and $T = 55°\mathrm{C}$

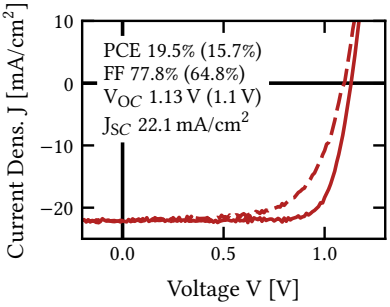

(f) JV-swipe of a MAPI device fabricated with the morphology shown on the left

Figure 8.2.: Transfer from spin- to blade coating and optimization of MAPI deposition by application of laminar convection with different air flow velocities.

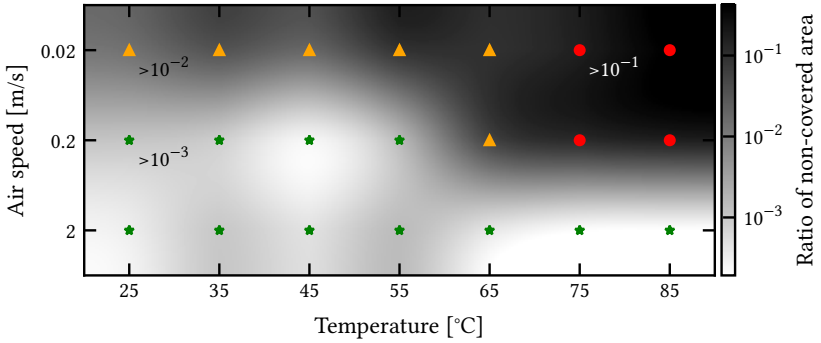

(a) Coating window characterized by the ratio of non-covered area (pinholes, etc.) to the total investigated area determined by SEM and AFM.

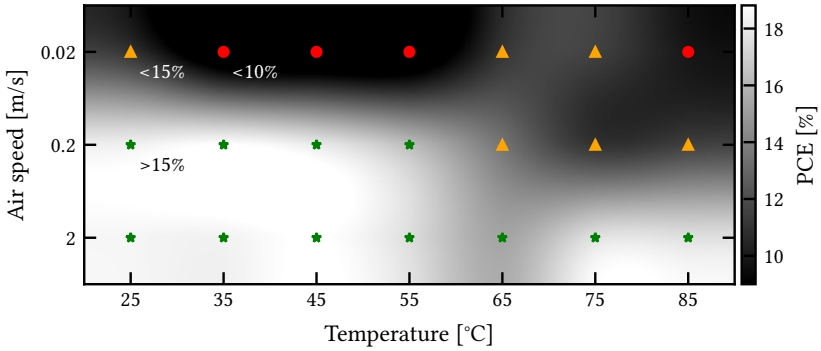

(b) Coating window characterized by the average, backward JV-sweep PCE of devices incorporating the respective thin-film.

Figure 8.3.: 2D coating windows of MAPI thin-films blade coated in the laminar air flow according to SEM/AFM analysis and device performances.

To investigate the drying of MAPI thin-films in detail, we conduct an extensive study correlating the obtained perovksite morphology with the device performances in dependence on the parameters T and u_0 [19]. While the temperature, T, is varied in linear steps of 10 K from 25°C to 85°C , the air speed, u_0, is varied in logarithmic steps from 0.02 m/s to 0.2 m/s and 2 m/s.

The perovskite morphology (after annealing) was characterized by SEM and AFM in correlation. From these experiments, we obtain the ratio of the area not covered by perovskite (that is the 'pinhole-area') to the total investigated area as well as the PCE measured by the backward JV-sweeps (the 'stabilised' PCE under constant voltage, which falls below the PCE measured by backward JV-sweep due to hysteresis, was also measured but not used in the plot due to the higher sampling number of the JV-sweeps). Consequently, the experiment yields a 2D coating window as depicted in Figure 8.3, which can be expressed in non-covered substrate area ratio (see Figure 8.3a) or in PCE (see Figure8.3b) because these properties anti-correlate just as one might expect (the differences in PCE are mainly caused by a decrease in FF and V_{OC} just as shown before in Figure 8.2). These coating windows are the main result of the first publication, demonstrating how the difficulties in up-scaling the MAPI spin coating to a blade coating process can be overcome by applying sufficient convection over the substrate [19].

An explanation of the empirically determined coating window can be attempted by investigating the impact of T and u_0 in the corresponding models for drying and crystallization [19]. As shown before, the chosen MAPI precursor exhibits a regular gas phase controlled drying without a large contribution of intermediate phases (see section 6.1.6). The gas flow velocity, u_0, determines the laminar boundary layer thickness and thereby the mass transfer coefficient, β, as well as the drying rate, dd/dt, and thereby the coefficient Q_0 in LaMer's model according to Equation 6.56. The temperature, T, mainly impacts the vapour pressure of the solvent (and only slightly the mass transfer coefficient), thereby altering the drying rate and Q_0, as well. As we showed earlier in section 6.2.4, obtaining a covering, nucleation-dominated morphology is potentially achieved by a high Q_0. This implies that we should choose T and u_0 as high as possible (in practice, T is limited by the degradation temperature of the perovskite and u_0 by the volume flow of high pressure gas and by solution waves forming at too high u_0 as explained later.) For u_0, this is perfectly in line with the experimental observation. However, for T this is not the case. The reason is that an increase in T not only changes Q_0 but also impacts the other two terms in LaMer's model (see Equation 6.53), namely nucleation and crystal growth dynamics (see exponential dependencies in Equation 6.46 and Equations 6.50-6.51). Since we do not have quantitative knowledge on nucleation and crystal growth rates, a change in temperature can change the crystal morphology in a multitude of unpredictable ways, making it a potentially problematic parameter for our study. Experimentally,

in the coating window, we observe a detrimental effect of too high temperatures in the 0.2 m/s data set. We obtain a covering, nucleation-dominated morphology at temperatures equal or less than 55°C, while higher temperatures alter the crystal growth in a way that larger crystalline domains are formed in a growth-dominated morphology and the surface-coverage decreases significantly. By increasing u_0 by a factor of 10 however, we can mitigate this problem and obtain nucleation dominated morphology for all temperatures.

To investigate further the crystallization dynamics as present in this precursor system, we characterize three samples at different T and/or u_0 with *in situ* IMI [20] (equally contributing co-author Felix Laufer, see section 2 details on contributions). These are designated by their processing temperature and air flow as (40°C, 2 m/s), (20°C, 2 m/s) and (30°C, 0.02 m/s). Exemplary full videos can be found in the supplementary material of the publication [20]. In order to extract statistically reliable transients from these image series, we average the data of the three image channels over multiple substrates and multiple points on each substrate, obtaining the results shown in Figure 8.4. Examining the reflectance channel at first, we find significant differences between the three sample categories. The (40°C, 2 m/s) samples exhibit an increase and stabilization of the reflectance after the onset of crystallization. The reason is that after the nucleation, which decreases the reflectance due to the emerging absorption in the perovskite (not shown), the crystal domains start coalescing and build up a new thin-film with higher specular and diffuse reflection. The (20°C, 2 m/s) samples show the very same trend, but with a delayed onset due to the lower temperature slowing down the crystallization dynamics. Furthermore, the reflection does not reach the same magnitude because solution droplets, as pushed by the air flow, cause irregularities in the thin-film morphology (a more detailed explanation follows later, based on Figure 8.5). In case of the (30°C, 0.02 m/s) samples, the reflection transients are completely different. The reason is the formation of large individual crystallites from the thin-film that do not coalesce. As a result, after an initial increase the reflectance falls off again stabilizing at a similar value as the initial reflectance of the plain sample because the space between the crystalline domains dominates the reflection.

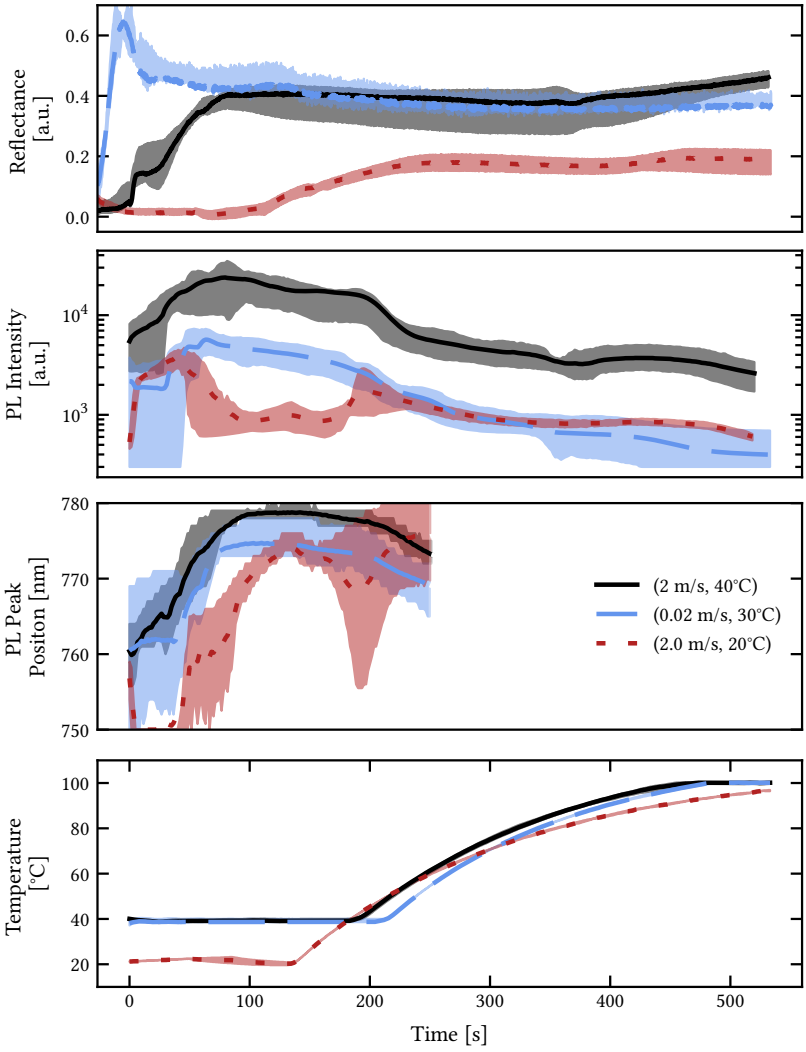

Figure 8.4.: Transients of reflectance, PL intensity, PL emission wavelength and temperature as monitored by IMI (and the peltier module) in the drying channel. All data was shifted to the PL onset time and averaged over multiple spots on multiple samples (solid line). The shaded area lies between the first and third quartiles.

In the PL intensity channel, we observe significant differences between the sample categories once more. The (40°C, 2 m/s) samples exhibit, first, an increase in the PL intensity, then a semi-stable (that is slowly decaying) maximum and, finally, upon the increase in temperature a steep decay in the PL intensity. The first increase could be correlated with progressing perovskite thin-film growth from the solution as consistent with the simultaneous increase in reflectance. The slow, initial decay of the PL intensity could be caused either by increasing re-absorption, that is more and more PL trapped in the thin-film due to internal reflection on the top film surface[102], or by increased charge carrier diffusion length, enabling more and more excited charge carriers to reach non-radiative recombination centres at the substrate interface or crystal facets[185]. The last, steep decrease, upon the increasing temperature, is most probably caused by the increase in non-radiative recombination due to increased thermal energy of the excited charge carriers [120]. Interestingly, the (30°C, 0.02 m/s) samples exhibit exactly the same trend, just about one order of magnitude lower in intensity. This resemblance confirms the assumptions made above, while hinting in the same time on to lower surface coverage/semiconductor quality of these films produced without the assistance of the air stream. (It is commonly known that pinhole-free films of high nucleation density have preferential optoelectric properties and thus an increased IQE_{PL} according to Equation 4.24 [115, 186]). The (20°C, 2 m/s) samples exhibit a different transient that overlays almost with the (30°C, 0.02 m/s) samples except in the region from about 50 s to 250 s. This difference in PL intensity evolution indicates a difference in crystallization kinetics as compared to the other two samples due to the lower temperature. The reason could be the influence of residuals from the lead salts, Methylammonium cations or humidity, impeding the crystallization until they are ejected from the crystal. At higher temperatures, these residuals presumably leave the precursor much earlier.

The PL emmission wavelength transient of the (40°C, 2 m/s) samples is characterized by a red-shift of the emission wavelength after the onset of crystallization. This effect is well-known and could be attributed to quantum confinement in the nucleating perovskite crystal seeds, which decreases the energy of emitted photons with increasing crystal domain sizes[187]. However, it is also possible that the fraction of re-absorped photons increases as the top film surface forms, effectively red-shifting these photons due to additional thermalization[102]. Once more, the (40°C, 2 m/s) and (30°C, 0.02 m/s) samples exhibit almost the same transient behaviour. The only difference is

that the transients have a constant offset. A streight-forward explanation for this is, consistent with the effect of re-absorption, that the surface of the (40°C, 2 m/s) samples is overall smoother and therefore internal reflection (and thus re-absorption) is increased, red-shifting the PL to a larger extent. This can be confirmed when gauging the homogeneity of the PL intensity responses (explained later in Figure 8.5). In case of the (20°C, 2 m/s) samples, we observe a much slower red-shifting indicating once more the delayed crystallization kinetics. We further find that the two peaks in the PL intensity formation correspond to two local extrema in the PL wavelength, strongly suggesting that a semi-stable PL active perovksite phase forms at the time of the first peak, that is then redissolved and formed again when the residuals leave the wet film.

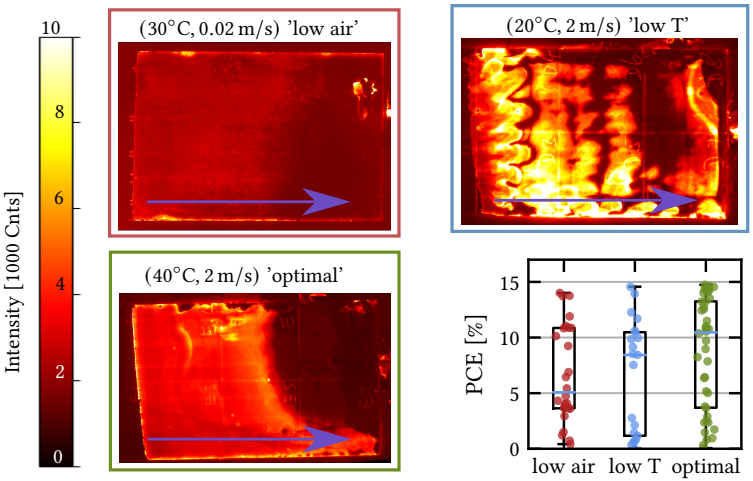

Figure 8.5.: PL images of the three sample categories (40°C, 2 m/s), (20°C, 2 m/s) and (30°C, 0.02 m/s) recorded at one point in time during the drying with purple air flow indicating the air flow direction as well as PCE distribution of the devices fabricated incorporating segments of the active layers examined by IMI. The (30°C, 0.02 m/s) samples ('low air', red frame and points) have a low granular PL response, while the (20°C, 2 m/s) samples ('low T', blue frame and points) show a high but inhomogeneous response and the (40°C, 2 m/s) samples ('optimal', green frame and points) show a homogeneous and high PL response.

Figure 8.5 depicts the PL intensity images of each sample category at a half-dried state along with an exemplary batch of solar cell PCEs (as measured by backward JV-sweep) incorporating these layers. In the (30°C, 0.02 m/s) sample, the overall PL response is lower and small grains are visible in correlation with the rough crystalline islands we saw earlier for this parameter range (see Figure 8.2c). Devices incorporating such layer will mostly exhibit a PCE smaller 10%. In the image of the (20°C, 2 m/s) sample, we can clearly see the inhomogeneity caused by waves of solution pushed by the air flow over the substrate (the purple arrow depicts the direction of air flow). There are regions of very high and quite homogeneous PL and other regions of low very inhomogeneous PL. Accordingly, the PCEs are clustered in two categories – one where the pixels is accidentally placed on a region of high layer quality and one where the pixel is placed on a region of low layer quality. For the (40°C, 2 m/s) sample, the PL response is homogeneous and high everywhere (except for certain morphological defects which we analysed in section 7.2). Consistently, the device performances are mostly over 15%, which is higher than in the other two cases (occasional morphological defects still decrease the PCE however as described before in section 7.2).

8.1.2. Sequential two-step deposition of double cation perovskite films

In the last section, we showed how the one-step deposition of MAPI can be migrated from spin coating to blade coating by a laminar air flow. However, the hybrid perovskite research community nowadays investigates mostly multi-cation perovskites due to their improved optoelectronic properties and stability [188, 189]. One possibility to fabricate double cation (DCP), that is $(FAPbI_3)_{1-x}(MAPbBr_3)_x$, solar cells is to employ a two-step deposition process. For the scale-up of this respective process, we set the additional constraint to exclusively rely on green solvents (see section 5.1 for details) to potentially avoid the application of DMF in industrial scale production. During the Master's thesis of Kristina Geistert co-supervised with Fabian Schackmar (see section 2 for detailed contributions), a precursor of PbI_2 dissolved in DMSO and EGBE (10 volume %) is examined for the first step of deposition, while the second step is still performed by spin coating. To manipulate the surface energy of the solution, different surfactants (that is Alpha-LP, DDAB, HD-TMAB, see section 5.1 for details) are added in very small amounts to the solution [190]. The goal is to avoid de-wetting and

pin the solution film to the substrate (see Figure 8.5). Wetting (or Pinning) describes a state where the solution 'sticks' to the substrate due to a beneficial ratio of surface energy of the solution-gas interface and the solution-substrate interface [191], which is a precondition for solution processing of homogeneous thin-films. Other optimized parameters are, just as in the last section, the temperature T and the gas flow velocity u_0 as well as the blade coating parameters (the blading speed v, the blade gap h_0 and the volume of solution on the substrate V_0), the drying time and the annealing time. A result is that the pin-down effect and homogeneity can be enhanced by using a medium flow rate of $u_0 = 0.2\,\mathrm{m/s}$ and $T = 60°\mathrm{C}$. The other parameters are optimized as $v = 25\,\mathrm{mm/s}$, $h_0 = 150\,\mu\mathrm{m}$, $V_0 = 35\,\mu\mathrm{l}$ with a drying time of 10 min and an annealing time of 2 min (not shown here). The spin coating of the cation solution is then performed at 1500 rpm and 30 s, followed by an annealing at 150°C for 15 min, which is consistent with the original recipe [117]. The results can be seen in Figure 8.5, showing the respective PbI_2 film (and a Dektak profile measurement of the same) along with the best device fabricated using the same layer in dependence on the type of surfactant. Comparing Figures 8.6a, 8.6c and 8.5e, we find that the PbI_2 film processed with Alpha-LP exhibits the smoothest morphology with the strongest absorption (as indicated by the visibility of the ITO patterning), which could be due to a more homogeneous surface morphology with less pinholes (this can be verified by SEM measurements not shown here). Correspondingly, we would expect that after the cation solution is deposited, the Alpha-LP perovskite thin films would outperform the films fabricated from the other PbI_2 layers. However, despite a slightly higher shunt resistance in the Alpha-LP sample, we observe that decent device performances can be achieved with all tested surfactants. This is probably due to the complex transition of PbI_2 to the DCP, which can 'correct' some morphological features of the PbI_2. We note that the average PCEs achieved herein are comparable with those achieved with MAPI (and triple cation later) but completely without the usage of DMF. The only remaining task is the migration of the recipe toward a scalable deposition of the cation solution.

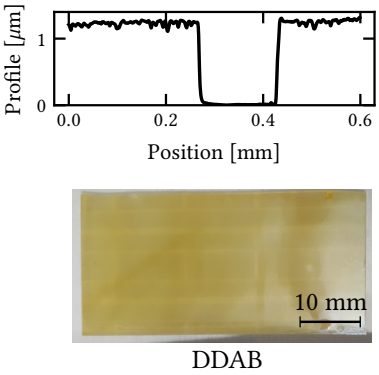

(a) PbI_2 coated sample with DDAB surfactant and Dektak XT measurement over a scratch in the sample.

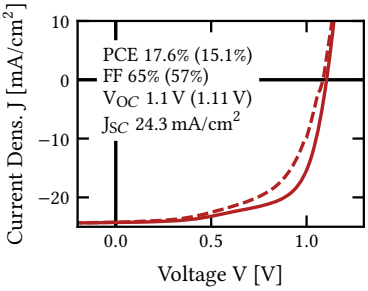

(b) Champion device JV-performance of samples processed with the layer on the left.

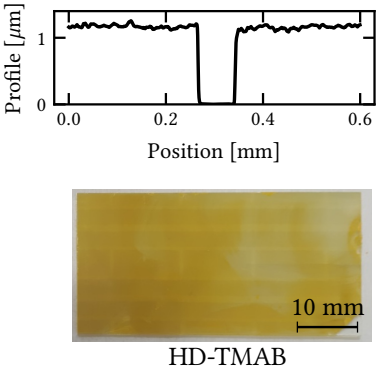

(c) PbI_2 coated sample with TMAB surfactant and Dektak XT measurement over a scratch in the sample.

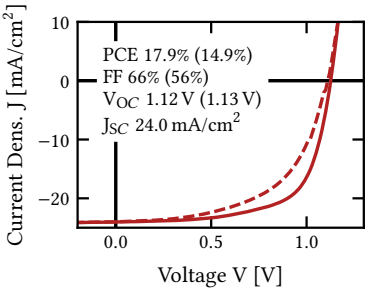

(d) Champion device JV-performance of samples processed with the layer on the left.

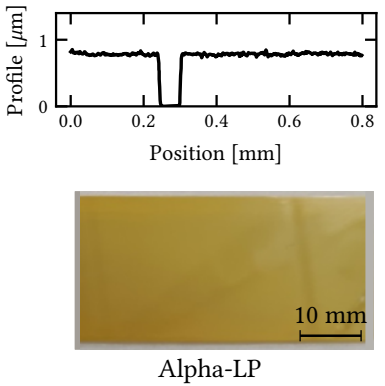

(e) PbI_2 coated sample with TMAB surfactant and Dektak XT measurement over a scratch in the sample.

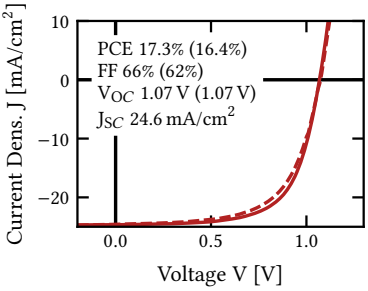

(f) Champion device JV-performance of samples processed with the layer on the left.

Figure 8.5.: PbI_2 films deposited with small amounts of different surfactants in a DMSO:EGBE solution (details in section 5.1).

In a consecutive Master's thesis of Vashu Kamboj (see section 2 for details on contributions), the recipe is further developed to up-scale the cation deposition by blade coating. During her work, it is found that the air flow does not impact the conversion to the perovksite after the blade coating of the cation solution significantly. This finding makes sense when taking into account that this process is mainly limited by the diffusion of the cations from the solute phase in isopropanol into the PbI_2 and the subsequent phase transition to the perovskite phase. Consistent with intuition, this process should not depend on the drying rate as long as contact interface stays unchanged. Further, the blading parameters, the temperature and the cation concentration are optimized, yielding a blade gap of 250 μm, a temperature of 40°C, a concentration of 0.18 M : 0.027 M : 0.044 M (FAI:MABr:MACl), which is half of the original recipe, a blading speed of 60 mm/s and an annealing temperature of 150°C at 15 min. Remarkably, one of the resulting blade coated samples exhibits a very homogeneous coating and lateral distribution of PCEs of test devices averaging around 14% (see Figure 8.6a). The best performing device exhibits almost the same PCE as the device with spin-coated cation deposition and the PCE stabilizes at around 15% under constant voltage (see Figure 8.6b). This result can be seen as proof of concept of the scalability

of this process with the perspective to use larger active areas, in the future. We note once more that the whole fabrication is done only be using green solvents.

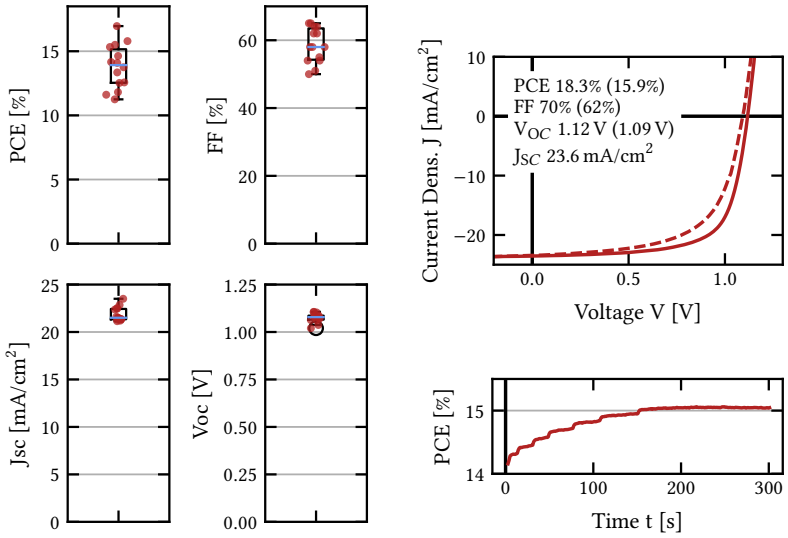

(a) Box plot of JV-parameters measured by backward JV-scans of all devices fabricated from the same blade coated perovskite substrate.

(b) JV-curve and constant voltage measurement for champion device

Figure 8.6.: Devices built with the same blade coated perovskite film fabricated by green solvent 2-step DCP process entirely by blade coating.

From a modelling perspective, the two-step process has a much higher degree of complexity than the one-step MAPI process described in the last section. While the PbI_2 deposition could be modelled with LaMer's model just as the one-step perovskite deposition, the second step would need to be modelled by a diffusion of cations (possibly mediated by the liquid solvent) and a simultaneous crystalline phase transition. This would require very complex modelling concepts, which we omitted for the sake of simplicity (a more advanced theory on diffusion processes can be found however in the appendix in section A1). As we will detailed before in section 6.2.4, the use of such a model would need to be justified with an advanced *in situ* characterization

technique capable of resolving the diffusion and perovskite conversion process to test the developed modelling concepts. Since such *in situ* technique was not available in the worktime on this process, there is no need to develop an advanced model because it cannot be tested experimentally.

8.1.3. One-step deposition of triple cation perovskite films

Beyond the two experiments described above, we also conducted a study using the DMF:DMSO (4:1) triple cation precursor (see section 5.1) in the laminar air flow. This investigation was crucial for understanding the drying dynamics of this precursor, which are characterized by a decelerated drying that we attribute to the formation of an intermediate phase (see section 6.1.7). However, the obtained morphology was in all cases not nucleation-dominated because the drying channel could not reach the necessary mass transfer coefficient for this precursor (will be shown later in Figure 8.8a). In the next two sections, we will elaborate two different quenching methods for overcoming this issue.

8.2. Anti-solvent spray quenching (in laminar air flow)

8.2.1. Triple cation perovskite with conventional solvents

The anti-solvent process is one of the most popular methods to fabricate high-PCE perovksite solar cells from solution by spin coating [192, 184]. However, the scaling of this method is very challenging since the flow of anti-solvent must occur at a precise time and with a precise flow rate [186]. Additionally, the formation of the anti-solvent layer, which occurs in dynamic spin coating (that is the immersion of solvent on an already spinning substrate), is hard to replicate in scalable coating methods because these methods typically apply a less regular, thicker wet film. Spraying anti-solvent was proposed as a method to homogenize the anti-solvent quenching [193, 194]. Therefore, we test the possibility of scaling the anti-solvent quenching process by employing a commercial airbrush nozzle to spray the anti-solvent onto the perovskite solution film (see Figure 8.7), while the film is still drying in the laminar

air flow (as explained in the last section) until the quenching is performed. To obtain a proper reference to this methodology, we compare it with the application of an anti-solvent bath, where the whole substrate is dipped in anti-solvent after the drying. Analogous to section 8.1.2, we put an emphasis on the incentive to replace toxic solvents with green solvents. This replacement is particularly important because anti-solvent spray vaporizes quickly due to the high surface area ratio of the droplets. In the first step, which is the Bachelor's thesis of Louis Kressibuch (as reflected in Figure 8.8a-8.7j) the DMF:DMSO (4:1 volume:volume) triple cation (TCP) precursor is used (see section 5.1 for details), while for the spraying process, we use Anisole, which is relatively non-toxic [195] (and Diethlyether for an anti-solvent bath). Later we will describe the effort to replace DMF, as well, just as described in section 8.1.2.

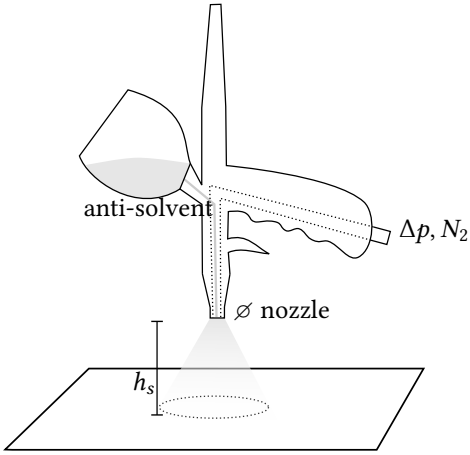

Figure 8.7.: Schematic of a spray quenching setup with the relevant parameters. These are the kind of anti-solvent, the differential N_2 pressure, the nozzle diameter and the height h_s.

Figure 8.7 highlights the important parameters of the employed spray quenching process. The most critical one is the choice of the used anti-solvent. For the initial experiments, we used Diethyl ether (DEE) which is relatively non-toxic, as well, however anaesthetic when inhaled at concentrations higher 3% [196]. By dipping the sample in a bath of DEE just before the onset of crystallization, a rough but homogeneous morphology of perovskite thin-films

is formed (see Figure 8.8c) as compared with the clearly growth-dominated morphology obtained by just drying the thin film in the laminar air flow (see Figure 8.8a). However, the PCE achieved by incorporating this layer into a device is still poor and not much better than in the sample which was not quenched (compare Figures 8.8b and 8.8d). The reason could be that the excess amount of anti-solvent leads to the dissolution or washing out of some of the cations in the perovskite. Interestingly, dip-coating in the completely non-toxic Anisole yields a very rough morphology leading to no functional device (see Figures 8.8e and 8.8f). However, when the Anisole is sprayed, a completely different morphology is formed (see Figure 8.7g). This morphology, which contains domains and 'cracks', was observed by other groups[197] and leads to a decent device functionality (see Figure 8.7h). Optimizing the temperature (yielding 18°C by cooling below room temperature), the air flow velocity (yielding 0.2 m s^{-1} and 2 m s^{-1}), the drying time before the quenching (yielding 70 s) and the perovskite film thickness (yielding 480 nm, by adjusting the blade parameters h_0 and v), we can reduce the crack density and obtain an overall more regular morphology (see Figure 8.7i) yielding an overall higher device performance see (Figure 8.7j), which is, remarkably, quasi on the same level as spin-coated perovskite solar cells with the same device stack. More detailed device statistics will follow in section 8.4.3.

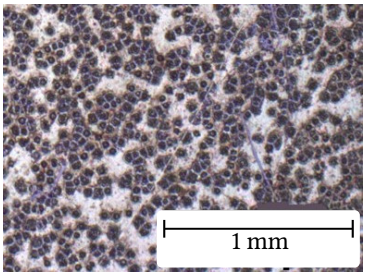

(a) Triple cation perovskite film dried in the laminar air flow without additional quenching.

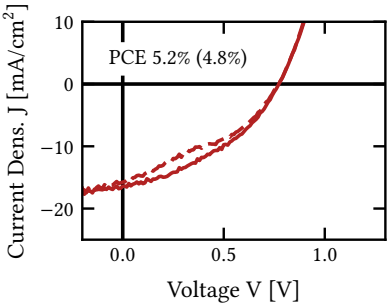

(b) JV-sweep of typical PSC fabricated with the film morphology shown in 8.8a.

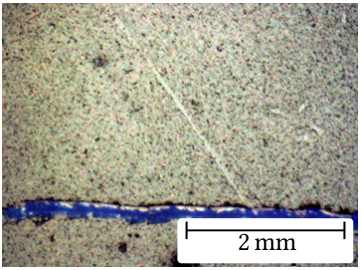

(c) Triple cation film dipped in Diethylether after a certain drying time

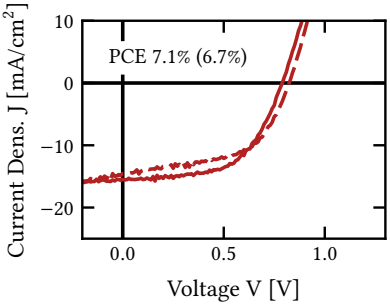

(d) JV-sweep of typical PSC fabricated with the film morphology shown in 8.8c

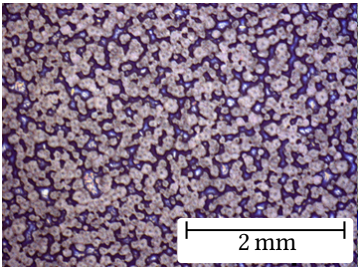

(e) Triple cation perovskite film dipped in Anisole after a certain drying time.

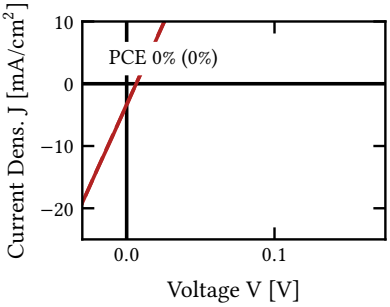

(f) JV-sweep of typical PSC fabricated with the film morphology shown in 8.8e

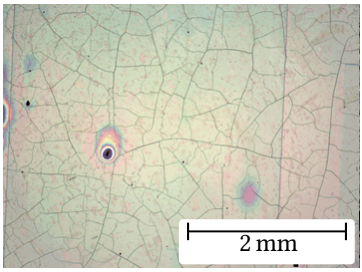

(g) Triple cation perovskite film spray quenched in Anisole.

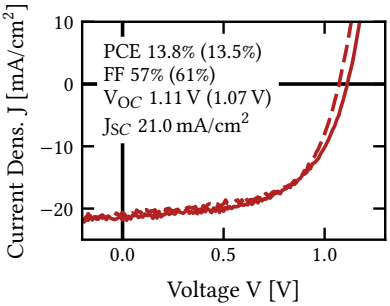

(h) JV-sweep of typical PSC fabricated with the film morphology shown in 8.7g.

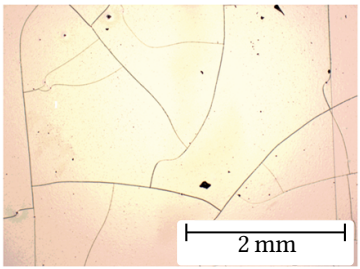

(i) TCP film spray quenched in Anisole with optimized parameters (see main text).

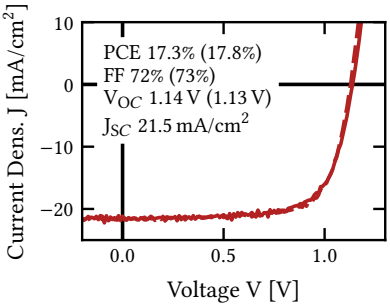

(j) JV-sweep of typical PSC fabricated with the film morphology shown in 8.7i

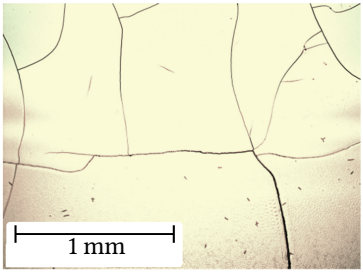

(k) TCP film from DMSO:EGBE green solvent precursor spray quenched in Anisole.

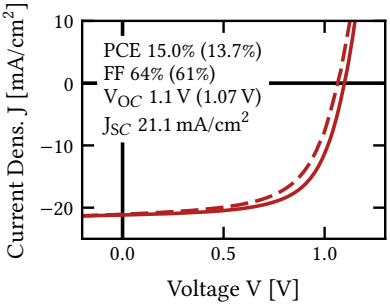

(l) JV-sweep of typical PSC fabricated with the film morphology shown in 8.7k

Figure 8.7.: Corner stone optimization results of (green solvent) spray quenching on blade coated perovskite films.

8.2.2. Triple cation perovskite with green solvents

As announced above, in the following Master's thesis of Virajini Palakonda, the DMF in the precursor is replaced by a mixture of DMSO and EGBE. (No beneficial effect of surfactants on the device PCE are observed in this case). The amount of EGBE is 5% of the total solution volume (see section 5.1 for details). As a result, we obtain a similar (but slightly more inhomgeneous) morphology (see Figure 8.7k) with a slightly lower PCE. Additional to the drying time (15 min), temperature (18°C) and film thickness (d_p = 500 nm) we optimize the open parameters, which is the distance to the film and also the nozzle diameter by employing different spray guns. The results are depicted in Figure 8.8. Unfortunately, even if we can observe a trend that the 0.3 mm⌀ nozzle at a distance of 1 − 3 cm yields the best results, the variance remained always high, making an up-scaled usage of this fabrication method not recommendable. The PCE differences were visible in all JV-parameters, but the biggest deviations are observed in FF, indicating that shunt and series resistances play an important role. Interestingly, the J_{SC}s show significant deviation, as well, indicating that there might be extraction problems of the charge carriers (or severe series resistance).

Nevertheless, the results described above can be seen as a proof of concept that green solvent spray quenching is a possible fabrication route. It could one day become important with a different precursor mixture and/or quenching solvent. Another possibility would be the dissolution of certain amounts of cations in the anti-solvent [197]. In this way, a continuous transition between two step fabrication (as described in section 8.1.2) and one step spray quenching could be established, which could combine the advantages of both processing methods.

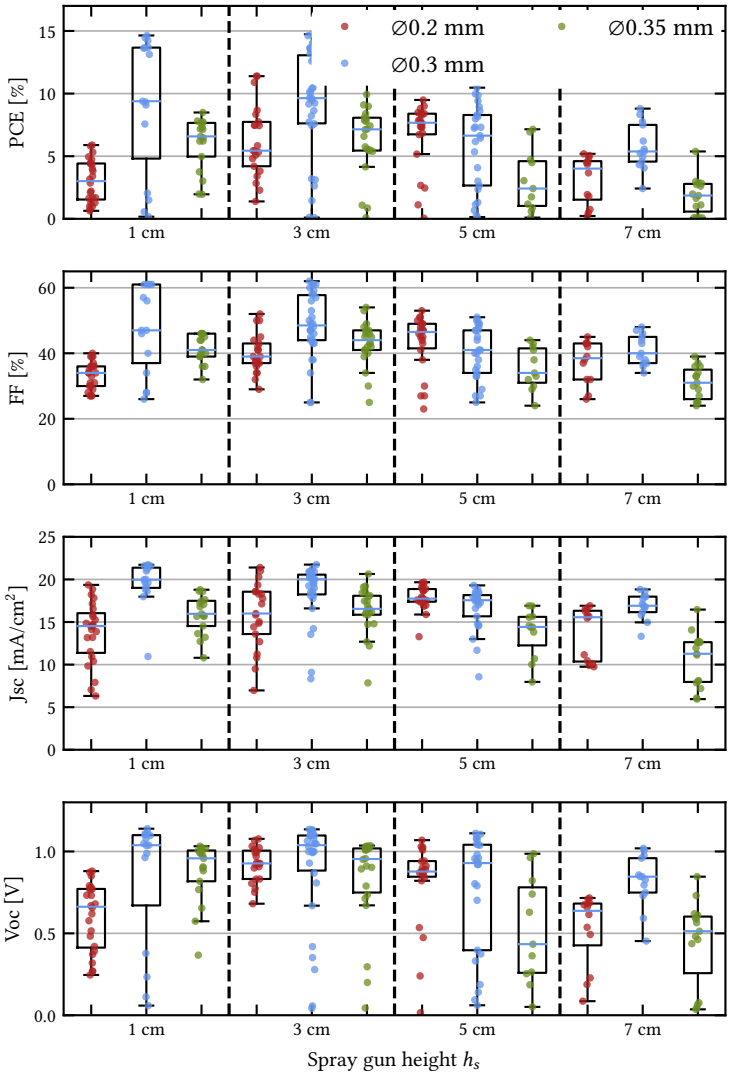

Figure 8.8.: Overview of JV-parameters of devices resulting from the optimization of Anisole spray quenching of perovskite films blade coated with the DMSO:EGBE solvent system.

8.3. Dynamic coating under a slot dryer

Fast drying under a focused, high-pressure jet of impinging air, commonly known as 'gas quenching', was established as one of the most facile and effective methods for scaling perovskite deposition[150]. With this method, perovskite solar cells with >20% of PCE and perovskite tandem devices with >26% of PCE can be fabricated[86]. In order to mimic large-scale solution processing with gas quenching, we use a model setup as depicted in Figure 8.9. A long glass substrate blade coated with a wet perovskite precursor film (not shown) is moved by a rubber roll with coating speed, v, under a linear air slot nozzle over a table stabilized at temperature T. The nozzle has the output gas velocity, u_0, slot width, B, height over the substrate, H, and oblique angle θ. We note that u_0 is measured by an MKS mass flow controller (by the volume flow rate divided by the nozzle aperture area) and that the pressure of the air entering the nozzle is not a necessary parameter for the mass transfer correlations (the pressure drop across the nozzle is a complex function of the exact nozzle geometry and therefore not very useful for reproducing the results).

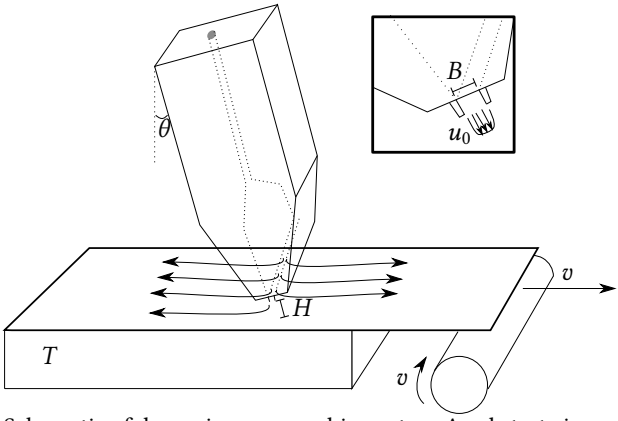

Figure 8.9.: Schematic of dynamic gas quenching setup. A substrate is moved over a table at temperature T by a rubber roll with velocity v. A nozzle with slot width B ejecting high-pressure gas with velocity u_0 is mounted at the height H and with the angle θ over the substrate (see section A2 for a photograph of the setup).

8.3.1. Dynamic drying of triple cation perovskite films‡

Before we treat the dynamic coating of the TCP solution thin-films (see section 5.1 for details), we would like to mention which thin-film morphology forms if a substrate coated with this solution is placed under the slot nozzle without movement. The result is depicted in Figure 8.10a, which shows a photograph (from top) of the perovskite film coated on a glass/ITO substrate marked with two sample extracts[21]. Far from the nozzle centre (extract 1), the film appears grey and diffusely reflecting, while under the centre (extract 2), a different texture forms, which appears dark brown and specularly reflecting. Further investigation with AFM shows that these macroscopic, optical properties are an indication for growth- and nucleation dominated morphologies, respectively, as shown in Figures 8.10b and 8.10c (identical to Figures 6.13b and 6.13a), which is in accordance with LaMer's model [21](for details see section 6.2.4). Consistently, the PCE of perovskite solar cells is only decent if the pixel is situated at a region comparable to extract 2 (compare Figures 8.10d and 8.10e). When correlating this finding with 2D TLC measurement (see section 7.3), we learn that the morphology changes at a heat transfer coefficient threshold, α, of around $500\,\mathrm{W/m^2K}$. As compared to industrial standards, this is quite a high value that can only be reached using slot widths of about 1 mm (see again section 7.3). It is also much higher than the threshold value reachable in the drying channel described in section 8.1, which is around $25\,\mathrm{W/m^2K}$. When reconsidering the models derived in sections 6.1 and 6.2, we understand that the threshold value must originate from a minimum drying rate $\mathrm{d}d/\mathrm{d}t$ and thus a minimum solute concentration increase Q_0. In particular, when comparing the drying dynamics of MAPI with the TCP drying dynamics, we find that the suspected formation of the intermediate phase decelerates the drying dynamics of the TCP according to Equation 6.35. (A simple calculation shows that the vapour pressure of this intermediate phase would be below 1% of the vapour pressure of DMF; see section A4 for typical experimental parameters). This explains why the threshold value for TCP is much higher than for MAPI – we need a mass transfer coefficient that is at least 100 times higher to obtain the same Q_0 as for the MAPI. Furthermore, when studying the LaMer's model, we come to the conclusion that the high drying rate is needed exactly when (and only when)

‡Section reviews ACS Applied Materials & Interfaces (2022) 14, 9, p. 11300–11312 by S.T., J.M., N.L., H.M.P, M.A., P.S., W.S., B.S.R and U.W.P. [21]

the concentration of solute crossed critical concentration. (Before this instant, the solution concentration simply increases by drying without influencing the crystal morphology. Afterwards, under the assumption that the crystal nucleation and growth happen very quickly, the high mass transfer is not needed any more because the film has already crystallized.) We summarize this as a criterion for the quenching of TCP [21]:

> *"The mass and heat transfer coefficient must exceed a certain threshold ($\beta_{\mathrm{DMSO}} > 0.3\,\mathrm{m/s}$ or $\alpha > 500\,\mathrm{W/m^2K}$ for the* TCP *precursor system) exactly when the concentration of solute crosses critical concentration/supersaturation".*

If the above criterion is correct, it must also apply when drying the perovskite dynamically, that is driving the substrate under the slot nozzle with velocity, v. To apply the criterion to dynamic drying in inhomogeneous mass transfer, we consider the dynamic drying model we derived and tested before in sections 6.1.5 and 6.1.7. The model implies that the crystallization onset is crossed at different positions relative to the nozzle, depending on the web speed, v. Figure 8.11a depicts a plot of the simulated drying dynamics depending on the position of the web for a sweep in coating velocity from $0.5\,\mathrm{mm\,s^{-1}}$ to $6.5\,\mathrm{mm\,s^{-1}}$ in steps of $1\,\mathrm{mm\,s^{-1}}$ (while $u_0 = 70\,\mathrm{m\,s^{-1}}$) based on Equations 6.27 - 6.29, 6.34 and 6.35. We find that, as predicted, the film reaches critical supersaturation (here assumed at $0.9\,\mu$m as indicated by the dashed black line) at different positions. When the web speed is too low ($v < 2\,\mathrm{m\,s^{-1}}$), the film reaches critical supersaturation before the nozzle (black and dark brown lines). When the web speed is too high ($v > 4\,\mathrm{m\,s^{-1}}$), the film reaches critical supersaturation behind the nozzle (lines from dark orange to yellow). In both cases, we do not expect a nucleation-dominated film morphology according to the criterion. However, in case of an optimal web speed, the film reaches critical supersaturation just below the nozzle, that is in the region of high enough mass transfer. Indeed, the thin-film morphologies show the same optimum web speed, which was omitted here for the sake of simplicity. (see [21] for more detail).

(a) Photograph of statically quenched TCP film at $u_0 = 79\,\mathrm{m\,s^{-1}}$, $B = 3\,\mathrm{mm}$ and $H = 3\,\mathrm{mm}$.

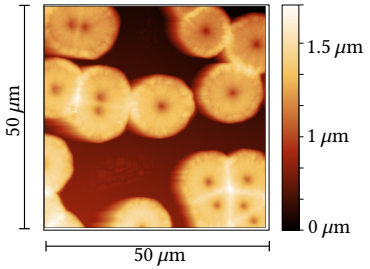

(b) AFM measurement of perovskite thin-film morphology off-centre (region 1 in Figure 8.10a)

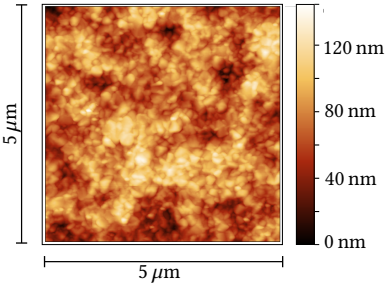

(c) AFM measurement of perovskite thin-film morphology under the nozzle (region 2 in Figure 8.10a)

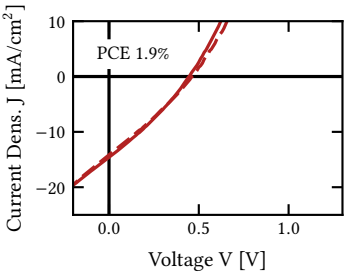

(d) JV-sweep of device built on morphology in Figure 8.10b (extract 1)

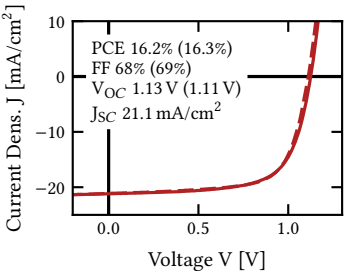

(e) JV-sweep of device built on morphology in Figure 8.10c (extract 2)

Figure 8.10.: Thin film morphology forming on a (statically) gas-quenched blade coated TCP perovskite thin film investigated in two representative area segments with typical solar cell JV-sweeps incorporating these morphologies.

Instead of varying the web speed, v, with a fixed gas velocity, u_0 it is also a valid approach to vary u_0 with a fixed web speed. (This could have advantages in industrial fabrication because a change in the web speed would also alter the coating process.). A simulated sweep of u_0 is depicted in Figure 8.11b where u_0 is varied from $20\,\mathrm{m\,s^{-1}}$ to $100\,\mathrm{m\,s^{-1}}$ in steps of $10\,\mathrm{m\,s^{-1}}$ (while $v = 2\,\mathrm{mm\,s^{-1}}$). In this scenario, the film reaches the onset of crystallization behind the nozzle if the gas velocity is insufficient ($u_0 < 50\,\mathrm{m\,s^{-1}}$), and (slightly) before the nozzle if the gas velocity is too high ($u_0 > 80\,\mathrm{m\,s^{-1}}$). When examining TCP thin films with these parameters, we find the optimum as predicted: In case of a low air velocity, we obtain a growth-dominated morphology everywhere (see Figures 8.12a and 8.12b). As the air speed increases, we find that a larger part of the substrate is covered with nucleation-dominated morphology because the crystallization takes place nearly under the nozzle (a little after the nozzle for 8.12c and a little before the nozzle for 8.12d). In case of a high air speed, we observe a greyish stripe in the middle of the substrate (see Figure 8.12e) that expands when the air speed is increased further (see Figure 8.12f). This is caused by too early nucleation before the nozzle, which starts in the middle of the film because the mass transfer is highest there (visible in Figure 7.6b in section 7.3). We note that a greyish appearance in Figures 8.12e and 8.12f does not necessarily imply that the film is growth-dominated along its vertical profile. Instead, heterogeneous nucleation can start at the substrate surface, while the nucleation onset for homogeneous nucleation is not yet met. Then the film is driven into the nozzle opening, where the bulk nucleation is induced by rapid drying. Accordingly, we found that the film shows dendrite structures on the bottom of the substrate (as shown before in Figure 5.4), but has a homogeneous top surface, as surface sensitive WLI analysis confirms (not included here, see [21]).

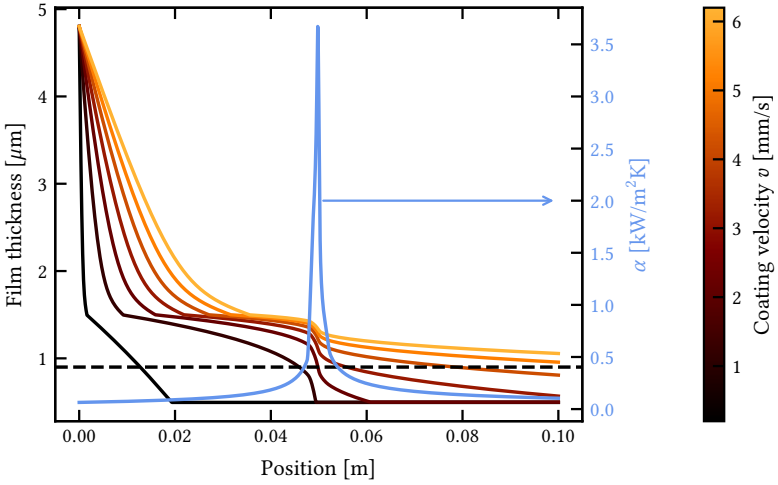

(a) Drying dynamics of TCP with a sweep in coating velocity, v (and $u_0 = 70\,\mathrm{m\,s^{-1}}$)

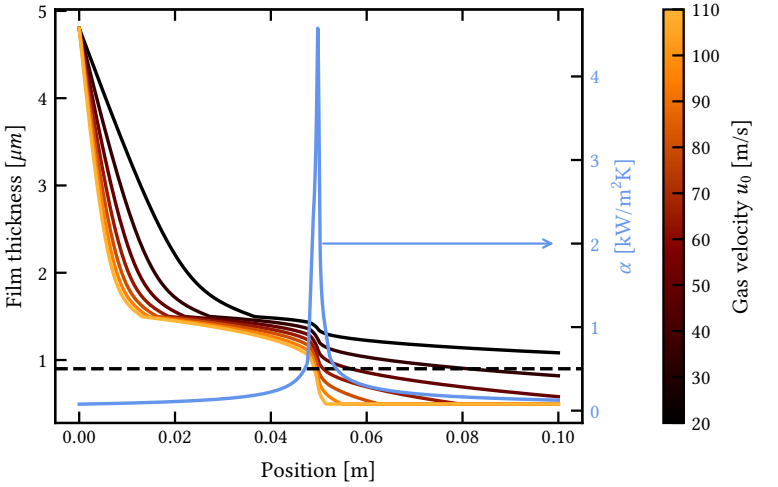

(b) Drying dynamics of TCP precursor with a sweep in gas velocity, u_0 (and $v = 2\,\mathrm{mm\,s^{-1}}$). Figure 8.12 shows the corresponding processes thin-films.

Figure 8.11.: Drying dynamics of a DMF:DMSO TCP solution film as predicted by Equations 6.27 and 6.35 for varying coating velocity, v, and gas velocity u_0. The black dashed line indicates the crystallization onset (which is not equal the dry thickness). The blue line is the apparent mass/heat transfer exerted by the slot-jet centred at 0.05 m.

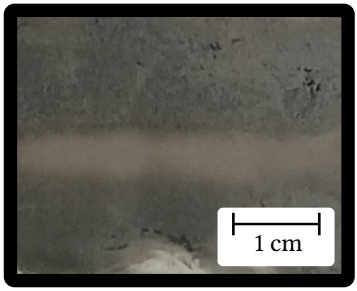

(a) $u_0 = 20\,\mathrm{m/s}$

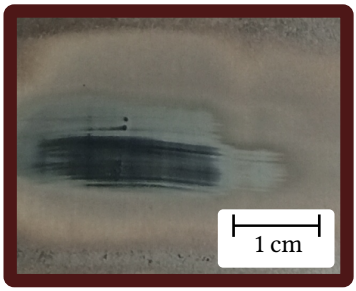

(b) $u_0 = 30\,\mathrm{m/s}$

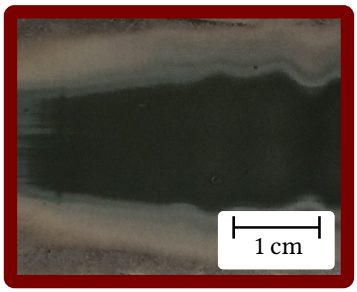

(c) $u_0 = 40\,\mathrm{m/s}$

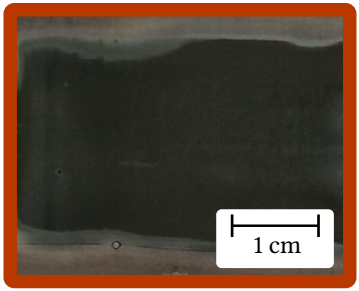

(d) $u_0 = 50\,\mathrm{m/s}$

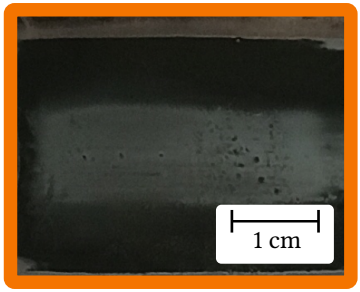

(e) $u_0 = 70\,\mathrm{m/s}$

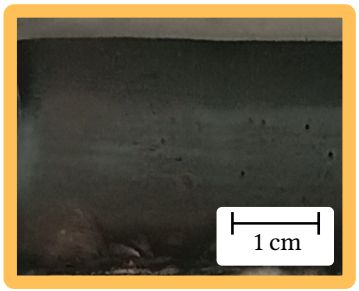

(f) $u_0 = 100\,\mathrm{m/s}$

Figure 8.12.: Dynamically coated triple cation perovskite thin films at $v = 2\,\mathrm{mm/s}, T = 40°\mathrm{C}, \theta = 75°, D = 0.3\,\mathrm{mm}, H = 1.5\,\mathrm{mm} and u_0 = 20 - 100\,\mathrm{m\,s^{-1}}$

Generalizing the insights above, we expect that for every air velocity, u_0, there is an optimal web speed, v, such that critical thickness is reached just under nozzle opening (or, more precisely, at the stagnation point where the mass transfer is at its maximum.). We performed coating experiments to verify this model prediction. To analyse the coated TCP films (such as those shown in Figure 8.12), we measure the film's surface roughness by WLI which enables the distinction of growth or nucleation-dominated properties on the film surface (extensive data can be found in [21]). For simplification, in the further analysis, we only take these WLI measurements as a foundation to rule out the additional complexity of heterogeneous nucleation (to account for the presence of heterogeneous nucleation, all optima would shift to higher air speeds or lower gas speeds.). In this way, we obtain a 2D coating window for this precursor (see Figure 8.13).

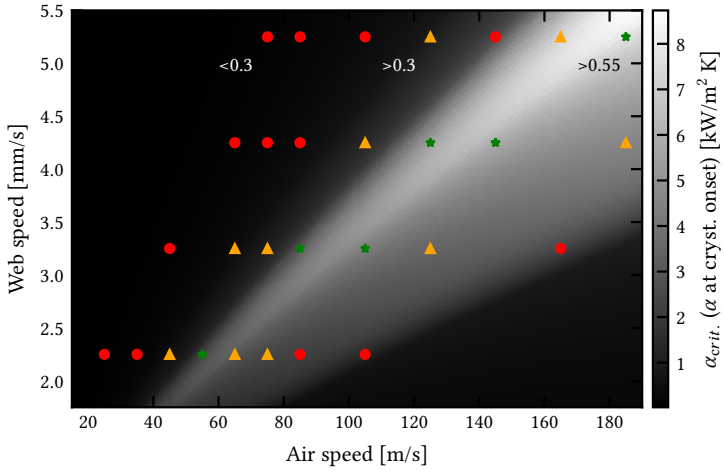

Figure 8.13.: Processing window of the triple cation perovskite precursor as determined by coating experiments and calculating the fraction of nucleation-dominated areas to the total area (red dots: fraction <0.3, orange triangles 0.3 < fraction < 0.55, green stars 0.55 < fraction). In the background the simulated critical heat transport coefficient on nucleation onset is plotted that is decisive for the forming thin-film morphology as defined in the criterion above. Constant parameters are $T = 40°C$, $d_p = 0.8\,\mu m$, $H = 1.5\,mm$, $B = 0.3\,mm$, $\theta = 75°$.

The boundaries of the depicted air velocity and web speed in Figure 8.13 are given by the maximum gas speed at which the solution starts skidding over the

substrate. The symbols are chosen according to the fraction of the examined sample area that is covered with nucleation-dominated area (a green star for a fraction greater 0.55, a yellow triangle for a fraction greater 0.3 but smaller 0.55 and a red dots for a fraction smaller 0.3). The reason why we cannot reach more than a fraction of 60% is the inhomogeneity of the applied mass transfer in the direction along the nozzle length of 2.7 cm as compared to the substrate width of 3.2 cm (see again heat transfer measurement in Figure 7.6b). In the future, a longer nozzle can be used to mitigate this problem. The heatmap in the background of Figure 8.13 shows the critical α, that is α at the position where the solution transitions critical concentration (at a thickness of 0.9 μm) on the substrate according to the drying model shown in Figure 8.11. The experimental fractions of nucleation-dominated areas data correspond well with the model's prediction. This correspondence is outstanding when taking into account that the model does not have any free parameters (the dry film thickness was measured, the wet film thickness calculated from the concentration and the used heat transfer was predicted according to the re-fitted Chin/Agarwal correlation. Details about the re-fitting were explained in section 6.1.4). We note that the success of the above described methodology in predicting the perovskite thin-film morphology strongly suggests that the hypothesis of reduced solvent activity due to intermediate phase formation (described in section 6.1.7) is correct (if, contrarily, a film diffusion limitation caused the decrease in the drying rate, we would expect a divergence of the model from the thin-film morphologies).

8.3.2. Dynamic drying of methylammonium lead iodide films‡

To cross-check the results discussed in the last section, we investigate dynamic MAPI coating, as well[21]. For MAPI, we use only the solvent DMF and did not find any deviation from the gas phase controlled drying (see section 6.1.6).

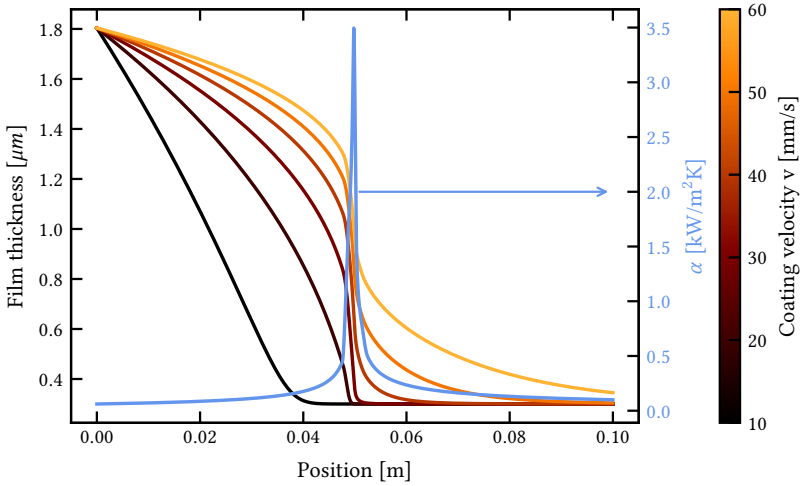

Figure 8.14.: Drying dynamics of MAPI precursor driven into an inhomogeneous mass transfer as produced by a narrow slot nozzle ($D = 0.3\,\mathrm{mm}, H = 3\,\mathrm{mm}$) described by the refitted Chin/Agarwal correlation. The colour gradient from black to yellow indicates a gradient in the coating velocity from $10\,\mathrm{mm\,s^{-1}}$ to $60\,\mathrm{mm\,s^{-1}}$ (constant parameters $u_0 = 60\,\mathrm{m\,s^{-1}}$, $T = 20°\mathrm{C}$, $d_\mathrm{p} = 0.3\,\mu\mathrm{m}$). The blue line is the apparent mass/heat transfer exerted by the slot-jet centred at 0.05 m.

Figure 8.14 shows a sweep of v from $10\,\mathrm{mm\,s^{-1}}$ to $60\,\mathrm{mm\,s^{-1}}$ in steps of $10\,\mathrm{mm\,s^{-1}}$ (while $u_0 = 70\,\mathrm{m\,s^{-1}}$) for MAPI. Because the drying process in MAPI is much faster than in the TCP precursor (due to the absence of the intermediate phase deceleration described by Equation 6.35), we expect that the coating velocity, v, should be higher at the same u_0. Comparing Figures

‡Section reviews ACS Applied Materials & Interfaces (2022) 14, 9, p. 11300–11312 by S.T., J.M., N.L., H.M.P, M.A., P.S., W.S., B.S.R and U.W.P. [21]

8.11a and 8.14 shows that this is indeed the case. The coating velocities for MAPI are almost one order of magnitude higher than for the TCP precursor. Furthermore, consistent with Figure 8.14 and the discussion above, we expect to find an optimal v for every u_0 (or vice versa) when coating MAPI perovskite thin-films dynamically. (This is $v = 30\,\mathrm{m\,s^{-1}}$ in Figure 8.14 where the film reaches critical supersaturation under the nozzle centre). Figure 8.15 shows the coating window of MAPI with the exact same notation as used in Figure 8.13. For the prediction of the critical α-values, we used the gas phase controlled drying model with one solvent (DMF) in accordance with the drying dynamics shown in Figure 8.14.

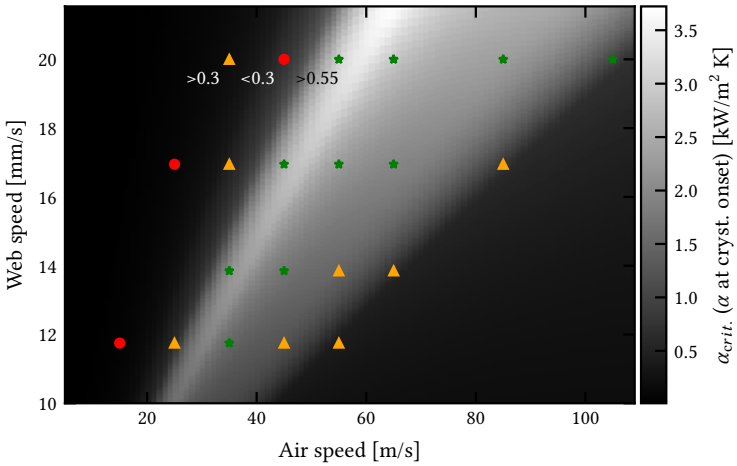

Figure 8.15.: Processing window of the MAPI perovskite precursor as determined by coating experiments and calculating the fraction of nucleation-dominated areas to the total area (red dots: fraction < 0.3, orange triangles 0.3 < fraction < 0.55, green stars 0.55 < fraction). In the background the simulated critical heat transport coefficient on the nucleation onset is plotted. Constant parameters are $T = 20°\mathrm{C}$, $d_\mathrm{p} = 0.3\,\mu\mathrm{m}$, $H = 1.5\,\mathrm{mm}$, $D = 0.3\,\mathrm{mm}$ and $\theta = 75°$

Consistently, we find that the coating window depicted in Figure 8.15 is shifted to faster coating velocities. This is a clear demonstration that the derived models as tested with interferometry are able to predict coating windows in a quantitative manner for completely different precursor systems. The general convergence between the model predictions and the experiments

shows that the methodological framework presented in this thesis is of high value for the dynamic processing of functional thin-films from solution. One could ask the question why the MAPI thin-film morphology is not nucleation-dominated everywhere given the low threshold in heat transfer for MAPI of $25\,W\,m^{-2}K^{-1}$. However, the distinction between morphologies in Figure 8.15 is done on the basis of a much narrower distinction in roughness, such that we got high-performing devices at all places on the substrate. Still, the least rough layers are obtained with the highest critical mass transfer.

8.4. Analysis of device performances

8.4.1. Device comparability

Because the solar cells fabricated during the work on this thesis have all the same active area and device stack, comparability between different processing methods is possible (details of the device fabrication were listed in section 5.3). In fact, comparability between the properties of the processed perovskite absorbers is the reason why the stack was unaltered (An alternative state-of-the-art device stack could have increases stability and maximum PCE [198]). Furthermore, all hybrid perovskite layers are deposited by blade coating (with the exception of the spin coated reference solar cells and the cation layer in the incomplete two-step green solvent process [see section 8.1.2].). This narrows down the main differences between the investigated processes to either the perovksite composition (that is MAPI, TCP and DCP perovskite), the solvents and additives in the precursor solution (that is pure DMF with salt residuals, DMF:DMSO and green solvent formulations EGBE:DMSO optionally with surfactants) as well as the quenching/drying method (laminar air flow, anti-solvent spray and dynamic slot jet). As explained in the last chapter, not all combinations were tested but merely those who were in a logical succession. The following lines of process development were pursued.

- MAPI spin coating was transferred to blade coating by quenching in the laminar air flow (section 8.1.1).
- Two-step double cation spin coating process was transferred to blade coating PbI_2 in the laminar air flow with green solvents. First, with subsequent spin coating and, later, blade coating of the cation solution in Isopropanol (section 8.1.2).

- Triple cation spin coating with anti-solvent quenching was transferred to blade coating in combination with spray quenching using Anisole. First with DMF:DMSO precursor and later with an EGBE:DMSO mixture (section 8.2).
- Triple cation spin coating with anti-solvent quenching was transferred to dynamic triple cation blade coating under a slot nozzle. The same was tested for MAPI as a reference. (sections 8.3.1 and 8.3.2).

The common goal was the principal investigation of process transfer from spin- to blade coating, while the active areas were kept constant.

8.4.2. Champion perovskite solar cell performances

In order to assess the success of the process transfer summarized above, we compare the champion device of each fabrication method with a typical high-performance spin-coated sample in Figure 8.16 in terms of PCE, V_{OC}, J_{SC}, FF as well as series and parallel resistances as measured from fits of the JV-curves close to the axes. The devices fabricated only with green solvent precursor are marked in green. Analysing the depicted data, we find a proof-of-concept demonstration of how successful the process transfer to blade coating can be – using the respective processing method. Furthermore, the impact of green solvent fabrication is visible. (The statistical distribution of fabricated devices will be analysed in detail later.) Let us take a look at the PCEs first (see Figure 8.16a depicting the backward PCE in dots, the forward PCE in triangles and the PCE after 300 s under constant voltage operation in squares). In order to judge the process transfer success, we compare the grey reference with their red and green counter parts. Both for MAPI and for TCP, the backward PCE and stabilized PCE after 300 s of blade coated cells fall shortly behind their spin coated counterparts. The use of green solvents in the precursor however introduces another PCE drop, which is expected from state-of-the-art literature (see Figure 3.5). While both MAPI devices exhibit a high hysteresis, as indicated by a large gap between forward and backward PCE, the DCP and TCP devices show considerably less hysteresis. This confirms the expectation that double and triple cation perovskites are less affected by ion migration than MAPI [199]. However, upon the introduction of green solvents the hysteresis increases again. In this context it must be repeated that hysteresis is not only a property of the bulk perovskite but also of the HTL and ETL interfaces with the perovskite

(see section 4.6). The higher hysteresis in green solvent devices might be an indication for an incomplete morphology formation causing more defect sites in the bulk and/or at these interfaces. Furthermore, we notice that the PCE of the gas-quenched TCP falls behind the anti-solvent counterpart. This is probably caused by the higher thickness of 0.8 μm that was a consequence of the choice of experimental parameters. It also is an indication that further optimization is needed for this process.

The FF similarly reflects the hysteresis behaviour mentioned above (see Figure 8.16b). But, interestingly, it does not always correlate with the PCE. While it is true that the green solvent devices show a significantly decreased FF, the FF of blade coated and spin-coated devices seems to be roughly the same. The MAPI backward scans show the best fill factor. However, this fill factor is probably "artificially" enhanced by mobile ions that accumulate at an interface (see section 4.6). When investigating the series resistance (see Figure 8.16c), we find that it has an anti-correlation with the FF. This indicates that the FF difference are (at least partially) caused by resistive losses in the perovskite or over the perovskite/ETL and perovskite/HTL junctions. On the other side, the shunt resistances are comparable for all devices, indicating that the magnitude of shunt conduction does not vary that much between the champion devices (see Figure 8.16d, there are two outliers which show about double the average value. However, since these are champion devices without any statistical reliability, they could be measurement artefacts and should not be overinterpreted.).

To compare the V_{OC} between different perovskites (see Figure 8.16e), we must normalize with the bandgap of the respective perovskite (From literature, we got $\varepsilon_G = 1.58$ eV for MAPI, $\varepsilon_G = 1.51$ eV for the DCP and $\varepsilon_G = 1.54$ eV for the TCP). Astonishingly, we find that the V_{OC}s of all champion solar cells are comparable. This indicates that the amount of non-radiative recombination in the perovskite as well as at the perovskite HTL/ETL junctions is not significantly different between the champion devices (with an exception of the anti-solvent green-solvent process). This might be a consequence of using the same stack for all devices.

For analysing the J_{SC}s (see Figure 8.16e), we normalized the data with the idealized J_{SC} obtained from integrating the AM1.5 spectrum starting from the bandgap (see Equation 4.26 and statements below it). Here, we find that all J_{SC}s are scattered around a ratio of about 0.83. The absolute values of J_{SC} should however not be over-interpreted since they are susceptible to the active

area of the devices, which may vary slightly in the gold evaporation with shadow masks. Furthermore, the cells were measured without a mask under the solar simulator such that excited charge carriers outside generated outside the electrodes may contribute to the J_{SC} such that it can be overestimated. For a proper J_{SC} measurement, the active area should be exactly measured and a shadow mask should be used in the solar simulator (furthermore, spectral mismatch must be corrected by a measurement of the integrated external quantum efficiency). Given the hypothesis that the differences in J_{SC} would be only caused by the effects listed above and the real J_{SC}s would be all the same (which is an extreme hypothesis), we could 'renormalize' the PCE data from Figure 8.16a. This would cause the MAPI blade coated sample to corrected down in PCE with respect to the reference. However, the double cation 2-step process would be much closer to its reference device PCE. The same is true for the triple cation processes (with the exception of the green solvent route).

In conclusion, we find that the process transfer from spin- to blade coating could be demonstrated as a proof-of-concept – that is in champion devices – with almost no loss in performance. However, when introducing green solvents, a significant drop in performance is observed that is mainly attributed to a degradation in the FF (and in case of the one-step TCP process also the V_{OC}).

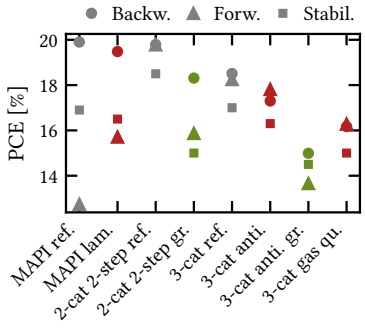

(a) Champion PCE measured by JV-scans and 300 s of constant voltage

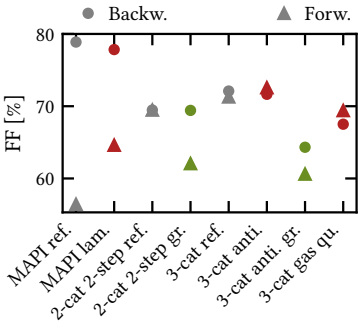

(b) Fill Factor measured by backw./forw. JV-scans

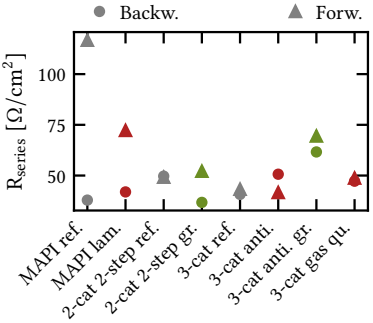

(c) R_{series} measured by backw./forw. JV-scans

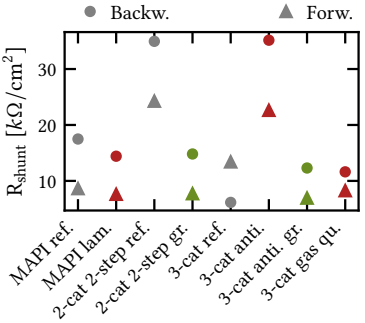

(d) R_{shunt} measured by backw./forw. JV-scans

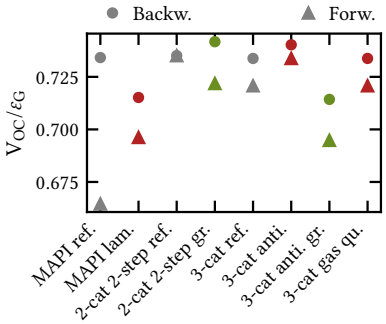

(e) V_{OC} measured by backw./forw. JV-scans

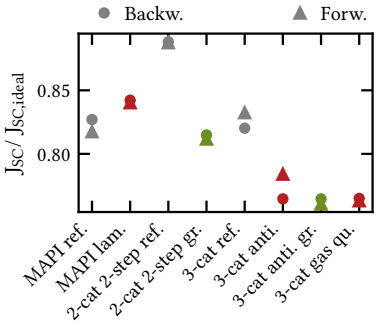

(f) J_{SC} measured by backw./forw. JV-scans

Figure 8.16.: Comparison of JV-parameters and resistances for the champion devices

8.4.3. Comparison of all perovskite solar cell performances

Figures 8.17 - 8.20 provide an overview of the JV-parameters (in detail, the average of the parameters obtained from forward and backward JV-scans) of all devices fabricated during the work on this thesis plotted in a chronological order. The reason for the chronological plotting is twofold. For one thing, it is a simple way to depict all device performances in only one graph per JV-parameter. For another thing, it enables the comparison of the development of either process with optimization time. For every batch, we omit 33% of low-performing devices and then plot the remaining respective data as transparent points (see Figures 8.17 - 8.20). This is done to account for the fact that the fabrication of individual devices is prone to many sources of error, which are not necessarily due to the defects in the perovskite (for example the sample handling, dust particles or an imperfect coating of the HTL and ELT layers). Additionally, we average the respective property over the remaining cells of each batch and plot the mean value by the bold symbols over the same date. Finally, we perform a linear regression through these mean values to test the hypothesis (H_1) that the average device performance should increase due to the optimization effort. For the regression we use the standard error of the mean to estimate the individual weights of the data points. (As a result, the fit will lie closer to batches with lower spread in their data). This picture of the entire device data provides a complete overview to avoid an artificial overestimation of the reliability and yield of the respective fabrication method (of course, selecting single data points with specific parameters can still yield interesting trends as we showed in the preceding section.) In this self-critical view, the counter hypothesis (H_0) is that the increase in PCE over time is merely caused by a random statistical variation or a parameter drift effect and not by the optimization itself. By analysing the data carefully, we test this contrary hypothesis and qualitatively estimate the likelihood of H_1 as compared to H_0 at the end of this section. Indeed, we find an overall increase in the average PCE over time for all investigated processes. Further, for all investigated processes, this PCE-increase can be correlated with an increase in all individual JV-parameters (the V_{OC} of the MAPI process is an exception. This V_{OC} problem with the *n-i-p* architecture was observed by other group members, as well, but remained unidentified. It is possible that it influenced as well the V_{OC} of the TCP solar cells fabricated at the same time.) In the following, we will analyse the extensive plotted data under certain criteria, which are relevant for the scaling of the respective solution process.

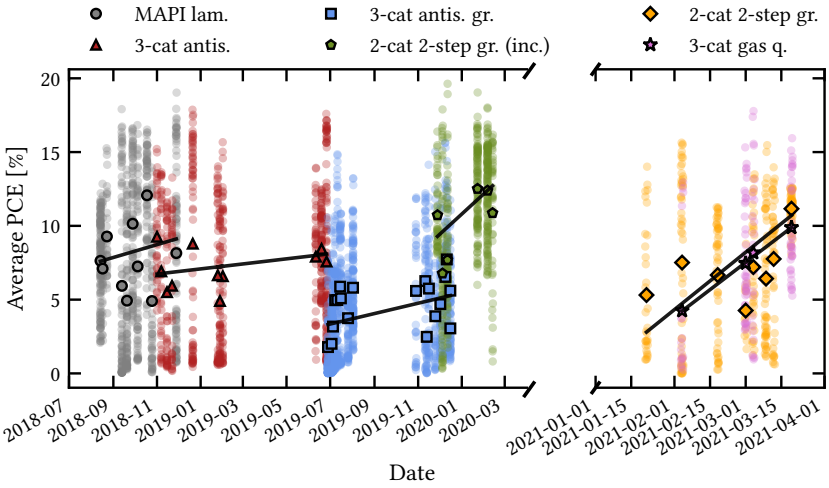

Figure 8.17.: Average PCE over fabrication date. The bold symbols are the means of each batch and the solid lines are a linear fit to these means ('inc.' = incomplete).

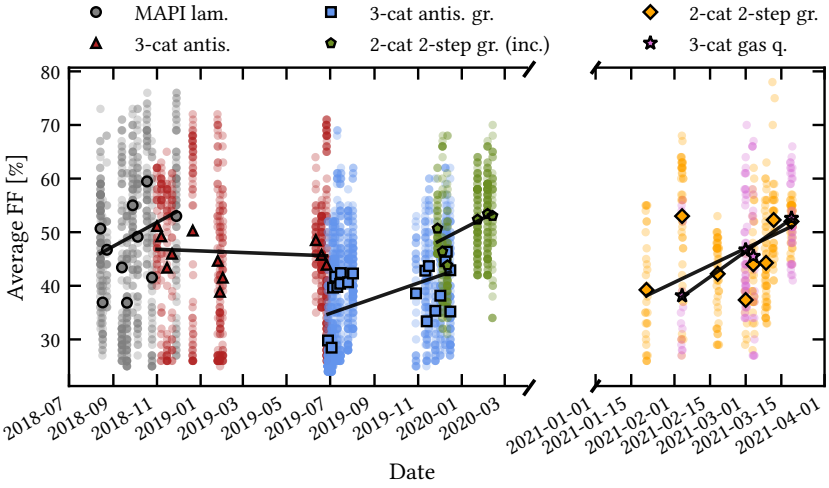

Figure 8.18.: Average Fill Factor over fabrication date. The bold symbols are the means of each batch and the solid lines are linear fits to these means ('inc.' = incomplete).

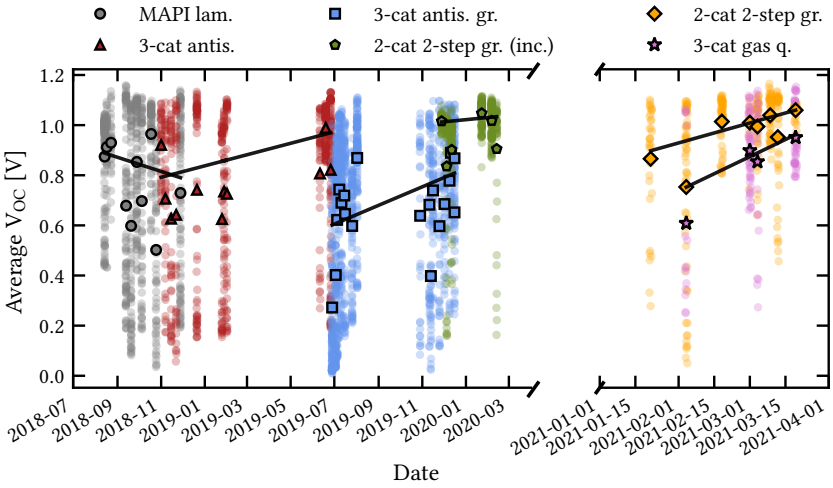

Figure 8.19.: Average V_{OC} over fabrication date. The bold symbols are the means of each batch and the solid lines are a linear fit to these means ('inc.' = incomplete).

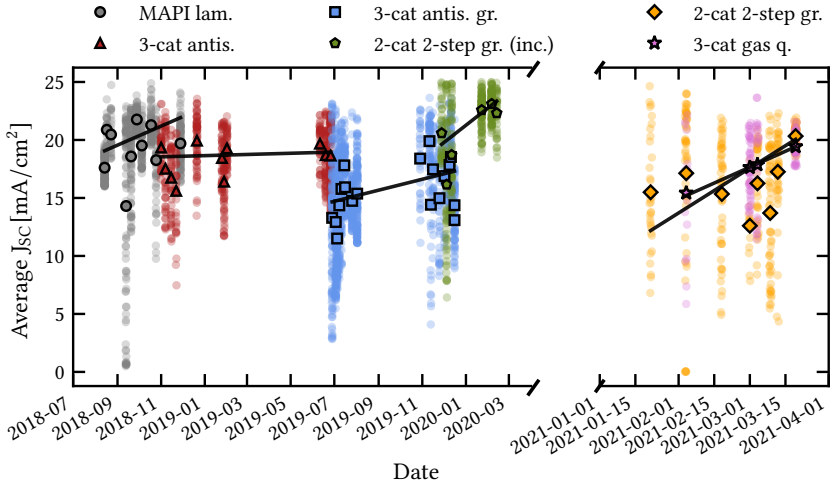

Figure 8.20.: Average J_{SC} over fabrication date. The bold symbols are the means of each batch and the solid lines are a linear fit to these means ('inc.' = incomplete).

Overall, the MAPI and the TCP anti-solvent processes show only a slight learning rate. It has to be noted that, during the optimization, many parameters were varied in each batch (sometimes even deliberately tuned to sub-optimal values) and that the gathered data shows the global optimization effort. However, in the respective last batches, the optimization was mostly stopped and the repeatability was tested. In this context it must be noted that, occasionally, clusters of high-performant devices that leave the average values can be spotted. These clusters are often identified with a single 32 mm × 64 mm blade coated layer. We conclude that the repeatability of the blade coating process is still a major concern for the scaling of solution processes. Further, the introduction of the green solvent in the precursors leads to a noticeable PCE offset. The two-step process is however an exceptional case. When the PbI_2 is blade coated and the cation layer is spin-coated afterwards on top, a higher reproducibility and PCE is achieved than in all other processes (which is a results of Ms. Geistert's optimization efforts of the PbI_2 deposition). However, if the cation layer is blade coated instead of spin coated, the PCEs drop and the reliability decreases. Perhaps, a future investigation could be done to answer the question how the cations could be deposited more uniformly on the PbI_2 layer by spray coating or inkjet printing. The gas quenching might further be a promising process, but not enough samples were processed so far to study its reliability in detail.

Let us take a look at the other JV-parameters. The FFs show the highest variability and correlate almost directly with the observed PCE statistics. An exception is the triple cation anti-solvent process, showing a slight decrease in FF. This puts the optimization efforts of this process in question because, as described above, there is high probability that the V_{OC} increase was not caused by the process optimization, but by an unidentified effect, artificially lowering the V_{OC} initially, instead. This encourages the H_0 hypothesis. We note that for the anti-solvent triple cation process using green solvents, we find that except for two batches in the very beginning that show almost only shunted devices, the FF stayed almost constant, which is in favour of the H_0 hypothesis, as well. When analysing the V_{OC}, we find a clear clustering of values to V_{OC}s around 1 V for all processes (except the TCP green solvent process). This is in line with the fact that the V_{OC} is a more stable parameter than the FF with respect to variations in the perovskite morphology. While the FF reacts very sensitively to shunt and series resistances, the V_{OC} stays unchanged unless non-radiative recombination is significantly increased (explained in detail in section 4.5). We conclude that the amount of non-radiative recombination is not different

for the devices that cluster around 1 V. However, significant deviations in the V_{OC} from these clusters can be observed in all processes, indicating difficulties with scaling and/or reproduction. The distribution of the V_{OC}s of the 2-step DCP processes as well as the TCP gas quenching process is much narrower than for the other processes. This indicates that these processes have superior repeatability and scalability as compared to the other processes (more details follow in the next section). Comparing J_{SC}s, we find a confirmation of the fact that the J_{SC} should be an even more stable parameter than the V_{OC}. The reason is that the J_{SC} is 'immune' to non-radiative recombination in the two-diode model (see section 4.5). While the J_{SC} improves for all observed processes during the development, the improvements in the TCP anti-solvent processes are only marginal, again supporting the H_0 hypotheses here. Once more, the introduction of the green solvent offsets the J_{SC} (as well as the V_{OC}) from their conventional counterparts (with the exception of some individual batches). The best J_{SC}s with the highest repeatability are obtained for the two-step process with a spin coated cation layer. After the cation layer is blade coated, the J_{SC}s are lower and their spread is wider. This might indicate that the crystallization of PbI_2 to perovskite did not succeed equally well in this process. Although the TCP gas quenching process looks promising, more data would be needed to compare the process reliably with the others. We conclude that the H_1 hypothesis ('optimization increases device performance') is probable for all investigated processes except the triple cation anti-solvent processes which puts the controllability, repeatability and scalability of these processes into question.

8.4.4. In-batch and batch-to-batch variation of perovskite solar cell performance

As we saw in the last section, scattering of JV-parameters, that is a broad statistical distribution of these parameters, remained an issue for all investigated processes. Therefore, we want to address the topic of reproducibility in the next two sections, which is one of the greatest challenges for the production of perovskite solar cells. It can be understood in two fundamental ways. For one thing, the batch-to-batch variation is a decisive variable that affects the reproducibility. For another thing, in-batch reproducibility between subsequent samples but also between different areas on the same sample are to be considered. Let us look at the in-batch variation at first, which is partially a measure for the scalability of each process (performance variation between

pixels on each substrate) and the repeatability of several blade coating processes (variation of cells between substrates). In this context, we note that, as described in section 5.3, blade coating includes only 6-12 $64 \times 32\,mm^2$ samples per batch. As mentioned above, this may introduce a statistical correlation of all respective cells stemming from one such large substrate causing clustering in the data, which we do not investigate separably herein. Moreover, as stated above as well, we do not explicitly exclude low performing samples as caused by the variation of process parameters during optimization. However, the obtained measures are still a figure-of-merit of the 'robustness' of the processes and the corresponding device performances to these parameter variations. To quantify the mean variations of the JV-parameters within each batch, we calculate the standard deviation, σ_i, and the standard error on the mean $\Delta\mu_i = \sigma_i/\sqrt{N}$ for every batch and average over all batches. In order to compare the standard deviation and standard errors of all JV-parameter, we divide them by the respective mean over all batches of the processing method for comparability. The results are shown in Figure 8.21. We find, as expected, that the relative standard deviation and standard error of the PCE is high compared to the other JV-parameters because the PCE is a product of all other JV-parameters. We find further that the two-step processes mostly have the lowest in-batch variation (an exception is the J_{SC} variation in the complete two-step process.), while the anti-solvent processes have the highest in-batch variability. Consequently, the anti-solvent spraying (at the current state with the used air brush guns) has the lowest repeatability and scalability. We note that the variations of this process are mainly introduced in the V_{OC}, which could indicate that non-radiative recombination (at defect sites/or interfaces) plays a bigger role in this process. The gas quenching process has, in comparison, an average in-batch variability comparable to MAPI dried in the laminar air flow. However, the standard error is comparatively high because the number of processed sample, N, was still low compared to the other processes. Additionally, we need to take into account that the batches also include cells which were not in a spot of nucleation-dominated morphology as explained in section 8.3 (although many of these are filtered out by the 33% of omitted data). We conclude that, although the in-batch variation is high for all processes, the DCP two-step process as well as the TCP gas quenching process are the most promising ones for future scalable perovskite deposition.

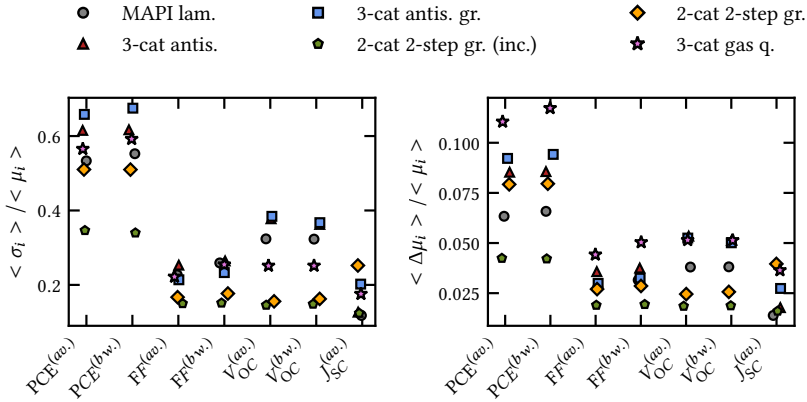

(a) The standard deviation averaged over all batches divided by the mean value of all batches for all JV-parameters

(b) The standard error averaged over all batches divided by the mean value of all batches for all JV-parameters

Figure 8.21.: Comparison of standard deviation and standard error averaged over all batches of the respective processing method for all JV-parameters. The superscripts '(av.)' and '(bw.)' indicate that the average of backward and forward JV-scans or the backward scan values are used for the calculation, respectively ('inc.' = incomplete process with blade coating of the PbI_2 and spin coating of cation deposition).

Considering Figures 8.17 - 8.20 again, we find that batch-to-batch variation, as represented by the deviation of the batch mean values from the linear fitting line, remains high for all processes. This can be quantified by calculating the sum of squared residuals r^2/N per data point. In order to compare the relative magnitude of this value for different JV-parameters, we divide its square-root by the mean value of all data points of the respective processing method (see Figure 8.22a). We find that the relative batch-to-batch variation in PCE is lowest for the gas quenching process. However, we note that for this process yet (see next section for more details). The other processes are in a comparable regime of batch-to-batch repeatability. Interestingly, the relatively largest issues with reproduction from batch-to-batch is the V_{OC}. This could imply that non-radiative recombination at the interfaces (that is partially independent of the perovskite) is causing this high batch-to-batch variation (see section 4.5 for an explanation), since these interfaces are also influenced by environment parameters during the fabrication of the

ETL/HTL layers. The two-step processes have the highest repeatability in V_{OC} (subtracting the gas quenching process due to low sample count). This could be due to the fact that an incomplete conversion of PbI_2 to perovskite can act as a passivating layer on the ETL side and thus stabilizing the V_{OC} [200] (while it negatively affects the other JV-parameters). However, it is questionable whether the differences are statistically reliable enough to draw any specific conclusions as this one.

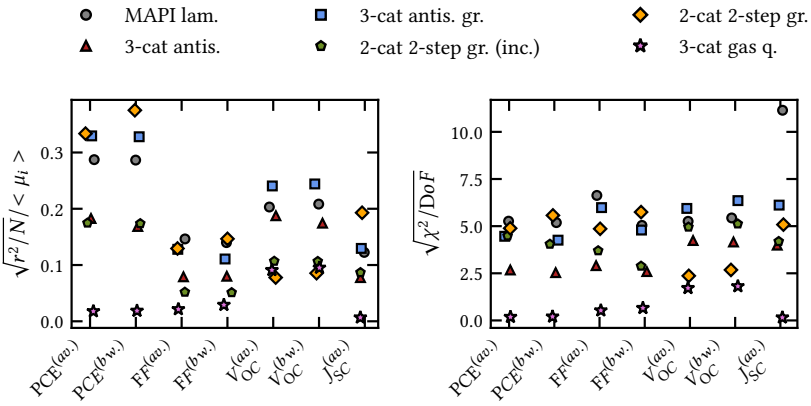

(a) Square root of squared residuals per data point divided by the mean of the respective processing method for different JV-parameters

(b) Square root of reduced χ^2 statistic using the standard errors on the means as uncertainty processing method for different JV-parameters

Figure 8.22.: Quantification of batch-to-batch variation by the square root of the squared residuals per data point divided by the mean of the respective JV-parameter and the reduced χ^2 statistic of the respective JV-parameter. The superscripts '(av.)' and '(bw.)' indicate that the average of backward and forward JV-scans or the backward scan values are used for the calculation, respectively ('inc.' = incomplete process with blade coating of the PbI_2 and spin coating of cation deposition).

Evidently, high batch-to-batch variation is correlated statistically with a high sample-to-sample variation. If the performance of individual samples varies by a large amount, the average performance of each batch varies. This effect should, theoretically, be eliminated by the law of high numbers. To account for the uncertainty of the mean values due to the in-batch variation, we can calculate the reduced χ^2-values, dividing each individual residual by the standard error of the mean. The total χ^2 value is then divided by the

degrees of freedom, $N - 2$, to obtain a contribution per free fitting point. In this corrected batch-to-batch variation, we find mostly values much greater than 1 (except for the gas quenching process, which is probably due to the low sample number.). This implies that the batch-to-batch variation is, on average, larger than the respective standard errors would allow, from which we draw the conclusion that the batch-to-batch variation is not only caused by sample-to-sample variation but also other influential parameters (such as the ambient humidity, differences in the precursor solutions, etcetera). Except for some outliers the batch-to-batch repeatability of all processes is comparable.

8.5. Final assessment of process transfer methods

In the analyses above, we included the comparison of different methods for scaling three original spin coating recipes: The one-step spin coating of methylammonium lead iodide, the two-step spin coating of double cation perovskite and the one-step deposition of triple cation perovskite. The scaling was done by three main methods of transferring the quenching (or drying) step. First, by applying a laminar air flow, second by applying an anti-solvent spray and third by using a high-pressure gas jet and dynamic coating. Remarkably, with all presented quenching methods, the fabrication of individual performant perovskite solar cells is possible. In case of the MAPI deposition and the laminar one-step TCP deposition by anti-solvent, these devices only fall slightly behind their spin coated counter parts in terms of PCE. However, the methods using green solvents further reduce the achievable PCE as will be detailed below. Furthermore, the PCE achieved by dynamic gas quenching still has an offset from this spin coated sample. (This can most probably be attributed to the too high layer thickness and still incomplete optimization).

In terms of reproducibility and yield, the two-step and dynamic gas quenching processes were clearly superior to the anti-solvent and laminar one-step samples (although the sample number in the dynamic gas quenching is still insufficient to provide high enough statistical reliability). We must further take note of the fact that the statistical variation in all fabrication methods is substantial and yet insufficient for industrial large scale processing. However, the fundamental lessons learnt from the conditions required for scaling these processes could be used for the development of more reliable processes in the

future. Furthermore, the level of control could be enhanced by measuring *in situ* transients and controlling the coating with the help of these parameters during the perovskite deposition process. These findings, in summary, can be seen as an answer to research question 4 (see section 3.3 for details).

Let us now answer research question 5 on the impact of green solvents (these are mainly mixtures of EGBE with DMSO potentially with small amounts of surfactants) and conventional solvents (these are mainly mixtures of DMF and DMSO). According to Figures 8.17 - 8.20, the introduction of green solvents to the triple cation anti-solvent process leads to a PCE offset that is correlated with an offset in all JV-parameters. Unfortunately, the PCE offset could not be corrected by extensive optimization. However, when switching to the two-step double cation process, devices with a decent PCE and reproducibly could be fabricated. This indicates that the pathway toward green solvent fabrication is probably through the processing of PbI_2 separately from the cations. This has the advantage that the solution formulation is simplified and must fulfil fewer constraints. The disadvantage is however the complexity of the cation diffusion and perovskite conversion in the second step. In practice, this manifests in the experimental observation, that the cation layer cannot be deposited as homogeneously with blade coating as with spin coating, again leading to a PCE offset. Even if, through optimization of process parameters this offset could be partially overcome and a whole blade coated substrate with high and uniform PCE was produced (shown in 8.6), other ways of depositing the cation solution should be investigated in the future. Ultrasonic spray coating[201], chemical vapour deposition[202] or inkjet printing[203] could be some that might allow for a better control of the dosage of cations such that the PbI_2 layer could be transformed to perovskite more successfully.

Part IV.

Conclusion

9. Summary

We summarize the main findings of this work as follows. The drying of two typical perovskite precursor solutions, methylammonium lead iodide (MAPI) and triple cation perovskite (TCP), was investigated by interferometry in the laminar air flow channel. The involved drying dynamics could be modelled quantitatively with a simple and extensible fully gas phase controlled drying model, which is estimated to be valid for sufficiently low Biot numbers. For the TCP precursor, the assumption of a second regime of reduced activity was needed. A criterion for producing nucleation-dominated perovskite layers – having a homogeneous polycrystalline thin-film morphology with high surface coverage — is identified by a critical mass/heat transfer coefficient threshold exactly when the solution crosses critical concentration. By applying this criterion, the MAPI deposition can be transferred from spin coating to blade coating by means of a laminar air flow channel without a significant loss in performance of perovskite solar cells incorporating these layers. Furthermore, a two-step double cation perovskite (DCP) process can be scaled with the help of the same linear air flow from spin to blade coating by entirely using green solvents, reaching decent device performance and reproducibility (while the second step of blade coating the cation solution should be replaced by a different processing method in the future). Additionally, the TCP one-step deposition could be scaled up, in principle, by spray solvent quenching, however still showing a lack in reproducibility and scalability after extensive optimization (and with a significant PCE loss when using green solvents). A better device performance/reproducibility could be reached by moving a substrate dynamically under a slot nozzle of high-pressure gas. While yield and reproducibility must still be demonstrated with higher sample numbers, this process is very promising for industry because it is comparatively simple, compatible with high-throughput operation and the drying dynamics can be completely determined by the drying models introduced herein (using localized heat transfer measurements).

One main achievement of this work is the insight that coating windows in terms of different coating parameters (like for example air or coating speed) can be derived from the introduced modelling concepts. In this way, the formation of the perovskite thin-film morphology can be predicted from simple principles, which decouples the design of perovskite coating machines from extensive pilot line testing. This became possible by shedding light on the perovskite formation stages of drying by using *in situ* interferometry and adapting modelling concepts from literature. The other main achievement is the advancement of *in situ* characterization capabilities from one-probe interferometry toward *in situ* multi-channel imaging for large-areas. In this way, not only the classification and localization of defects can be quickly performed but also the transients of these optoelectronic properties can be monitored in two dimensions. This could be used for direct feedback fabrication, in the future.

After this general summery, we will now give concise answers to the research questions providing all technical parameters:

- *"How can the drying dynamics of perovskite solutions films be quantitatively modelled and measured?"*

  The measurement of drying dynamics is performed by *in situ* interferometry as introduced in section 7.1 in the laminar air flow channel at five points along the coating direction. (As described in section 7.2, the IMI setup can also measure the drying dynamics resolved in 2D as long as these are slower than about $0.5\,\mu\mathrm{m\,s^{-1}}$). The gas phase controlled drying model introduced in section 6.1.5 is a powerful and versatile tool for modelling the drying dynamics of the perovskite precursors quantitatively. It is estimated to stay valid at least up to Biot numbers of 10^3 or even 10^7 as demonstrated by numerical simulation. The model accurately describes the MAPI drying dynamics as measured by *in situ* interferometry independent of the tested additional residual components (see section 6.1.6). For the TCP however, the model needs to be adjusted by a second drying regime of reduced solvent activity, $\gamma_i < 1$, which is measured in the flow channel at a known mass transfer coefficent as described in section 6.1.7. We attribute this change in activity to the formation of an intermediate phase, whose partial pressure is about 1% of the vapour pressure of DMF at the investigated temperature of 40°C (parameters are detailed in section A4).

- *What necessary conditions need to be met for the crystal growth and nucleation to yield a homogeneous polycrystalline morphology and what does this imply for the fabrication of decent perovskite solar cells in large-scale solution printing lines?*

  LaMer's model as introduced in section 6.2.4 implies that the solute concentration must be increased rapidly exactly when and only when the solution crosses critical concentration (see criterion in section 8.3). This, in turn, defines a minimum threshold of mass/heat transfer coefficient that must be reached at exactly at this moment in time. For MAPI we found that this threshold can be as low as $25\,\mathrm{W\,m^{-2}K^{-1}}$ ($\beta_{\mathrm{DMSO}} > 0.015\,\mathrm{m\,s^{-1}}$), while for TCP we determined $500\,\mathrm{W\,m^{-2}K^{-1}}$ ($\beta_{\mathrm{DMSO}} > 0.3\,\mathrm{m\,s^{-1}}$). This difference is the consequence of the reduced activity before the crystallization in the TCP precursor as described above.

  With the knowledge of the drying dynamics and thermochromic local heat/mass transfer measurements of the used air stream at hand, we can predict whether the threshold is met or not in a certain parameter space, defining a coating window. This is not only possible for constant mass transfer but also for the case of temporally varying mass transfer as in the case where the substrate moves dynamically past a nozzle with highly inhomogeneous mass transfer. In this way, coating windows for MAPI as well as for TCP in terms of gas velocity and web speed can be determined without any free parameter. The ability of morphology prediction can help in a variety of up-scaled deposition setups with different coating as well as drying methods, effectively avoiding trial-and-error fabrication.

- *"How can knowledge about the drying and crystallization dynamics be obtained during large-scale perovskite solution printing?"*

  The two main methods for obtaining knowledge of the drying and crystallization dynamics presented in this work are *in situ* interferometry and *in situ* multi-channel imaging (IMI). In *in situ* interferometry, the reflectivity is probed by a laser (and a photodiode) during the drying process, enabling the determination of the wet film thickness over time by using an accurate backtracking algorithm until the onset of the nucleation process. The advantage of the technique is the fast sampling rate ($\approx 100\,\mathrm{kHz}$). While *in situ* interferometry was used for studies on organic PV before, IMI was completely designed from scratch. It

comprises of a scientific CMOS camera and a filter wheel with different bandpass filters (and an ND filter) that the camera is synchronized with. IMI can record reflection images, photoluminescence (PL) and PL emission wavelength images at the same time with a rate of about 100 Hz. The advantages of IMI are the large-area detection window on the one side and the ability to obtain valuable information on the optoelectronic quality of the perovskite thin-film after the nucleation on the other side. IMI can be used to monitor the transients of the above-mentioned optoelectronic film properties during the drying and crystallization. In addition, it can be used for identifying about 62% of faulty devices (as counted by absorber quality defects and pinholes) with almost certainty before the device fabrication is completed (with a false positive rate of 4%).

- *"How do different drying and quenching methods influence the homogeneity of the thin-film morphology and the achievable* PCE*, yield and repeatability in perovskite solar cells processed by blade coating?"*

  In section 8.4.2, we demonstrated that decent perovskite solar cells can be fabricated with a variety of different quenching methods. First, we showed that the difference between spin coating and blade coating can be effectively annihilated for MAPI perovskite solar cells by using a laminar air flow. However, for multi-cation perovskites, the mass transfer achieved in this channel is insufficient and the method is not suitable industrial fabrication either. The TCP anti-solvent process by spray quenching is feasible, in principle, but shows poor reproducibility, scalability and optimization reward. In contrast, the two-step DCP deposition process yields a fabrication route for perovskite solar cells with rather reproducible and decent PCE (as detailed below this is also a fully green solvent process). An open challenge is however the scaling of the second step because blade coating the cation solution reduces the reproducibility drastically. The gas-quenching process up-scaled by a slot nozzle and dynamic coating exhibits a promising scaling behaviour, as well. The advantage compared to the two-step process for industry could be the much simpler process, the usability of the same process in p-i-n architecture (which is important for tandem devices) and the fact that drying models with additional heat transfer measurements can very accurately predict this process. A disadvantage is its reliance on the conventional, toxic solvent N,N-Dimethylformamide (at the current state of this work).

- *"How do the measures discussed above change when toxic solvents are replaced by entirely green alternatives?"*

  The two-step DCP process was developed entirely based on the green solvents Dimethylsulfoxide and ethylene glycol monobutyl ether (+ additional surfactants). The results are promising, although the deposition of the cations in the second step by blade coating could be improved or replaced by a different deposition method. Trying to use green solvents in the anti-solvent spray coating process leads, unfortunately, to a significant PCE offset that could not be overcome by additional optimization effort.

Despite these concise answers to the initially posed research questions, additional questions remain open for future work. For example, one could investigate the derivation and experimental testing of a more exact model of the perovskite thin-film morphology formation when crystallizing, a more detailed prediction of the PCE or a precise model for the activity changes in perovskite precursor. These ideas for future research will be discussed (among others) in the next chapter.

10. Outlook

Large-scale perovskite solution processing is one prominent route for fabricating perovskite photovoltaics in the future. The other route is thermal co-evaporation of the precursors. Assuming that hybrid perovskites will play a role in the future renewable energy production, it is still an open question which fabrication method will dominate commercial production in the future. The advantage of evaporation is its comparably simple scalability and the possibility to process on a variety of different substrates with different textures. The advantages of solution processing is the more cost-effective production (which becomes increasingly important with scale) and the fast optimization of process parameters. However, the main disadvantage are difficulties to control the morphology on large scales as well as the susceptibility to environment parameters such as for example the humidity or the temperature. These issues became apparent as well in the in-batch and batch-to-batch reproducibility of PCEs of perovskite solar cells fabricated during the work on this thesis. It is possible that these disadvantages are the reason why evaporation might promise a less risky business plan to enter the PV market.

However, the advantages of solution processing prevail and can potentially be used to mitigate its problems in future works. First of all, because the throughput of a solution processing line can be increased more easily, promising cost-effective production, the reward of such cheap and fast production might justify the additional research effort to mitigate scaling issues. In this context, this work can be seen as a first step to understanding the formation dynamics involved in scalable perovskite solution processing on a fundamental level. In particular, the criterion for successful gas quenching can be used in industrial-scale projects to predict the produced perovksite thin-film morphology and design large-scale drying machines from scratch without the need to launch extensive coating experiments. Furthermore, by making use of the second advantage of solution processing, the fast optimization of parameters, the reproducibility issues (as caused for example by the susceptibility to

the environment conditions) could be corrected using fast feedback. In a first step, this feedback could come from known drifts and dependencies identified by the operators (as for example caused by weather or seasonal differences in the environment). In a consecutive step, an electronic feedback system could be implemented, in which a quality monitoring technique assesses the fabricated perovskite layer quality and the feedback is provided by a control loop directly manipulating the coating parameters such as the quenching air velocity or the wet film thickness, etcetera. In this context, it is important to mention that we introduced extensive *in situ* characterization methods (first of all, *in situ* multichannel imaging) in this work that can be used to assess the perovskite layer quality early on in the fabrication process.

Another considerable issue in perovskite solution processing is the use of green solvents that are environmentally friendly and have a low toxicity. As we showed in this work, the use of green solvents however limits the achievable device performances. We demonstrated, as well, that the transition to two-step processes could be a possible mitigation strategy because this reduces the requirement to satisfy all constraints at once (solubility, wettablity, stability, ...). It is however still to be shown if and how the second step of spin coating the cation solution can be transferred effectively to a larger scale deposition technique. Afterall, it is very likely that an enhanced understanding of drying and crystallization processes as well as a feedback line involving *in situ* characterization could help mitigating the issues with green solvent fabrication, in the future.

Let us now discuss possible future advancements in the modelling and simulation presented in this work. Modelling drying and crystallization dynamics is a methodology for providing a fundamental understanding of large-scale perovskite solution processing in this work. It has to be noted that the presented drying models are quantitative in a sense that the predictions are compared to quantitative measurements of the evolution of the film thickness over time. This is not true for the LaMer's model framework on crystallization, where only qualitative predictions of the grain sizes depending on the applied drying rates are presented. This is a major potential for improving modelling concepts, in the future. However, it must be noted that a quantitative description of perovskite crystallization is only possible by using tools for the quantitative determination of nucleation and growth rates [204, 205] (Unfortunately, the *in situ* techniques presented herein are insufficient for this task because they measure only macroscopic optical properties such as the reflectance or photoluminescence). However, in all these considerations, the question

must be assessed whether a detailed study is already sensible given the fast evolution within the field by empirical testing of processes. To date, it is still fully unclear which precursor composition and/or solvents will be used in a potential commercial application. Concerning the presented modelling of drying dynamics, some straight-forward extensions would be the adding of another solvent. A more detailed model extension could also encompass the role of individual components and solvents on possible activity reductions by intermediate phase formation. Furthermore, it is an open question whether the presented modelling framework can be extended to other quenching processes as for example vacuum quenching, infra-red flash annealing or anti-solvent quenching. However, again, it is crucial to remember that the field advances fast and an accurate investigation might take too long for the results to impact state-of-the-art works. In comparison with the tools needed to answer questions of this type, the modelling presented in this work relies on very simple measurement and analytical methods. This enables a very quick rough testing of the methodology, possibly with more state-of-the-art precursors. For this reason, the methods were chosen for this work in the first place.

In summary, all future modelling concepts have to be seen critically as to how they can impact the concrete fabrication of perovskite devices. Of course, in some years, the development speed of state-of-the-art perovskite solution processes might decrease as the technology approaches its radiative limitations[26]. This would make more fundamental investigation of drying and crystallization dynamics rewarding. Additionally, sophisticated methods of data analysis can be used in situations where an explicit analysis by differential equations are not possible due to a high degree of complexity. For example, Artificial Intelligence methods are on the rise in Material Sciences. Precondition for the application of these methods is a large dataset of repeated data. These can be acquired preferentially by automatic image or scan data of a certain measurement quantity. In this context, *in situ* multi-channel imaging presented in this work is a potentially viable candidate for performing this task.

Bibliography

[1] *Climate change | 21st Century Challenges*. URL: https://21stcenturychallenges.org/climate-change-2/ (visited on 04/07/2022).

[2] James Hansen et al. "Climate Change: Earth's energy imbalance: Confirmation and implications". In: *Science* 308.5727 (June 2005), pp. 1431–1435. ISSN: 00368075. DOI: 10.1126/SCIENCE.1110252/SUPPL_FILE/PAPV2.PDF. URL: https://www.science.org/doi/full/10.1126/science.1110252.

[3] M. Ades et al. "Global Climate". In: *Bulletin of the American Meteorological Society* 101.8 (Aug. 2020), S9–S128. ISSN: 0003-0007. DOI: 10.1175/BAMS-D-20-0104.1. URL: https://journals.ametsoc.org/view/journals/bams/101/8/bamsD200104.xml.

[4] *Sixth Assessment Report — IPCC*. URL: https://www.ipcc.ch/assessment-report/ar6/ (visited on 04/07/2022).

[5] *Global Warming of 1.5 ˚C —*. URL: https://www.ipcc.ch/sr15/ (visited on 04/08/2022).

[6] Claudia Tebaldi et al. "Climate model projections from the Scenario Model Intercomparison Project (ScenarioMIP) of CMIP6". In: *Earth System Dynamics* 12.1 (Mar. 2021), pp. 253–293. ISSN: 21904987. DOI: 10.5194/ESD-12-253-2021. URL: https://esd.copernicus.org/articles/12/253/2021/.

[7] *Creative Commons — Attribution 4.0 International — CC BY 4.0*. URL: https://creativecommons.org/licenses/by/4.0/ (visited on 08/12/2022).

[8] Malte Meinshausen et al. "The shared socio-economic pathway (SSP) greenhouse gas concentrations and their extensions to 2500". In: *Geosci. Model Dev* 13 (2020), pp. 3571–3605. DOI: 10.5194/gmd-13-3571-2020. URL: https://doi.org/10.5194/gmd-13-3571-2020.

[9] Nico Bauer et al. “Shared Socio-Economic Pathways of the Energy Sector – Quantifying the Narratives”. In: *Global Environmental Change* 42 (Jan. 2017), pp. 316–330. ISSN: 0959-3780. DOI: 10.1016/J.GLOENVCHA.2016.07.006. URL: https://www.sciencedirect.com/science/article/pii/S0959378016301224.

[10] *SSP Database*. URL: https://tntcat.iiasa.ac.at/SspDb/dsd?Action=htmlpage%7B%5C&%7Dpage=welcome (visited on 03/23/2022).

[11] *Renewables 2021 – Analysis - IEA*. URL: https://www.iea.org/reports/renewables-2021 (visited on 03/30/2022).

[12] *Aktuelle Fakten zur Photovoltaik in Deutschland - Fraunhofer ISE*. URL: https://www.ise.fraunhofer.de/de/veroeffentlichungen/studien/aktuelle-fakten-zur-photovoltaik-in-deutschland.html (visited on 07/19/2022).

[13] *BloombergNEF says global solar will cross 200 GW mark for first time this year, expects lower panel prices – pv magazine International*. URL: https://www.pv-magazine.com/2022/02/01/bloombergnef-says-global-solar-will-cross-200-gw-mark-for-first-time-this-year-expects-lower-panel-prices/ (visited on 07/19/2022).

[14] *How the Renewable Energy Sector is Growing so Rapidly | World Resources Institute*. URL: https://www.wri.org/insights/growth-renewable-energy-sector-explained (visited on 04/29/2022).

[15] P Ringler et al. *Decentralized Energy Systems, Market Integration, Optimization*. KIT Scientific Publishing, 2016, pp. 1–96. ISBN: 978-3-7315-0505-1. DOI: 10.5445/KSP/1000053596. URL: https://publikationen.bibliothek.kit.edu/1000053596.

[16] *Photovoltaics Report - Fraunhofer ISE*. URL: https://www.ise.fraunhofer.de/en/publications/studies/photovoltaics-report.html (visited on 01/05/2022).

[17] Marios Theristis et al. *Energy Yield in Photovoltaic Systems*. Ed. by Soteris A. Kalogirou. Third Edit. Academic Press, Jan. 2018, pp. 671–713. ISBN: 9780128103975. DOI: 10.1016/B978-0-12-809921-6.00017-3. URL: https://www.sciencedirect.com/science/article/pii/B9780128099216000173.

[18] Liz Allen, Alison O'Connell, and Veronique Kiermer. "How can we ensure visibility and diversity in research contributions? How the Contributor Role Taxonomy (CRediT) is helping the shift from authorship to contributorship". In: *Learned Publishing* 32.1 (Jan. 2019), pp. 71–74. ISSN: 17414857. DOI: 10.1002/LEAP.1210. URL: https://onlinelibrary.wiley.com/doi/10.1002/leap.1210.

[19] Simon Ternes et al. "Drying Dynamics of Solution-Processed Perovskite Thin-Film Photovoltaics: In Situ Characterization, Modeling, and Process Control". In: *Advanced Energy Materials* 9 (2019), p. 1901581. ISSN: 1614-6832. DOI: 10.1002/aenm.201901581. URL: https://onlinelibrary.wiley.com/doi/abs/10.1002/aenm.201901581.

[20] Simon Ternes et al. "Correlative In Situ Multichannel Imaging for Large-Area Monitoring of Morphology Formation in Solution-Processed Perovskite Layers". In: *Solar RRL* 6 (Sept. 2021), p. 2100353. ISSN: 2367198X. DOI: 10.1002/solr.202100353. URL: https://onlinelibrary.wiley.com/doi/10.1002/solr.202100353.

[21] Simon Ternes et al. "Drying and Coating of Perovskite Thin Films: How to Control the Thin Film Morphology in Scalable Dynamic Coating Systems". In: *ACS Applied Materials & Interfaces* 14, 9, (Feb. 2022), pp. 11300–11312. ISSN: 1944-8244. DOI: 10.1021/acsami.1c22363. URL: https://pubs.acs.org/doi/10.1021/acsami.1c22363.

[22] Verein Deutscher Ingenieure VDI-Gesellschaft Verfahrenstechnik und Chemieingenieurwesen (GVC), ed. *VDI Heat Atlas*. Springer-Verlag Berlin Heidelberg, 2006. ISBN: 978-3-540-25504-8. DOI: 10.1007/978-3-540-32218-4.

[23] Frank P. Incropera et al. *Fundamentals of Heat and Mass Transfer 6th-Edition*. New York: John Wiley and Sons Inc., 2006. ISBN: 9780471457282.

[24] Ivan V Markov. *Crystal Growth for Beginners. Fundamentals of Nucleation, Crystal Growth and Epitaxy*. 3rd editio. World Scientific Publishing Co. Pte. Ltd., Dec. 2017. ISBN: 978-981-3143-42-5. URL: https://doi.org/10.1107/S2052520619014999.

[25] Uli Würfel Peter Würfel. *Physics of Solar Cells From Basic Principles to Advanced Concepts*. 3rd. Wiley-VCH Verlag, 2016. ISBN: 978-3-527-41312-6. URL: https://www.wiley-vch.de/de/fachgebiete/naturwissenschaften/physik-11ph/festkoerperphysik-11ph6/physics-of-solar-cells-978-3-527-41312-6.

[26] Wolfgang Tress. “Perovskite Solar Cells on the Way to Their Radiative Efficiency Limit - Insights Into a Success Story of High Open-Circuit Voltage and Low Recombination”. In: *Advanced Energy Materials* (2017), p. 1602358. ISSN: 16146832. DOI: 10.1002/aenm.201602358. URL: http://doi.wiley.com/10.1002/aenm.201602358.

[27] Henry J. Snaith. “Perovskites: The emergence of a new era for low-cost, high-efficiency solar cells”. In: *Journal of Physical Chemistry Letters* 4.21 (2013), pp. 3623–3630. ISSN: 19487185. DOI: 10.1021/jz4020162. arXiv: nn504795v [10.1021]. URL: https://pubs.acs.org/doi/10.1021/jz4020162.

[28] Martin A. Green et al. “The emergence of perovskite solar cells”. In: *Nat. Photonics* 8.7 (2014), p. 506. ISSN: 1749-4885. DOI: 10.1038/nphoton.2014.134. URL: https://www.nature.com/articles/nphoton.2014.134.

[29] Ian A. Howard et al. “Coated and Printed Perovskites for Photovoltaic Applications”. In: *Advanced Materials* 31.26 (Apr. 2019), p. 1806702. ISSN: 15214095. DOI: 10.1002/adma.201806702. URL: https://onlinelibrary.wiley.com/doi/abs/10.1002/adma.201806702.

[30] C.N.R. Rao. “Perovskites”. In: *Encyclopedia of Physical Science and Technology (Third Edition)*. Elsevier, Jan. 2003, pp. 707–714. DOI: 10.1016/b0-12-227410-5/00554-8. URL: https://www.sciencedirect.com/science/article/pii/B0122274105005548.

[31] P. S. Whitfield et al. “Structures, Phase Transitions and Tricritical Behavior of the Hybrid Perovskite Methyl Ammonium Lead Iodide”. In: *Scientific Reports* 6.October (2016), p. 35685. ISSN: 2045-2322. DOI: 10.1038/srep35685. URL: http://www.nature.com/articles/srep35685.

[32] Julian A. Steele et al. “Phase Transitions and Anion Exchange in All-Inorganic Halide Perovskites”. In: *Accounts of Materials Research* 1.1 (Oct. 2020), pp. 3–15. ISSN: 2643-6728. DOI: 10.1021/accountsmr.0c00009. URL: https://dx.doi.org/10.1021/accountsmr.0c00009.

[33] Shahab Ahmad et al. “In Situ Intercalation Dynamics in Inorganic - Organic Layered Perovskite Thin Films”. In: *Appl. Mater. Interfaces* 6,13 (2014), pp. 10238–10247. DOI: 10.1021/am501568j. URL: https://pubs.acs.org/doi/10.1021/am501568j.

[34] Qin Hu et al. "In situ dynamic observations of perovskite crystallisation and microstructure evolution intermediated from [PbI 6]4-cage nanoparticles". In: *Nature Communications* 8.June (2017), p. 15688. ISSN: 20411723. DOI: 10.1038/ncomms15688. URL: http://www.nature.com/doifinder/10.1038/ncomms15688.

[35] D. B. Mitzi et al. "Conducting layered organic-inorganic halides containing <110>-oriented perovskite sheets". In: *Science* 267.5203 (Mar. 1995), pp. 1473–1476. ISSN: 00368075. DOI: 10.1126/science.267.5203.1473. URL: https://www.science.org/doi/10.1126/science.267.5203.1473.

[36] Akihiro Kojima et al. "Novel Photoelectrochemical Cell with Mesoscopic Electrodes Sensitized by Lead-halide Compounds (5)". In: *ECS Meeting Abstracts* MA2007-02.8 (Sept. 2007), p. 352. DOI: 10.1149/ma2007-02/8/352. URL: https://iopscience.iop.org/article/10.1149/MA2007-02/8/352%20https://iopscience.iop.org/article/10.1149/MA2007-02/8/352/meta.

[37] Roberto Brenes et al. "Metal Halide Perovskite Polycrystalline Films Exhibiting Properties of Single Crystals". In: *Joule* 1.1 (Sept. 2017), pp. 155–167. ISSN: 25424351. DOI: 10.1016/j.joule.2017.08.006. URL: https://www.sciencedirect.com/science/article/pii/S2542435117300314.

[38] Stefaan De Wolf et al. "Organometallic halide perovskites: Sharp optical absorption edge and its relation to photovoltaic performance". In: *Journal of Physical Chemistry Letters* 5.6 (Mar. 2014), pp. 1035–1039. ISSN: 19487185. DOI: 10.1021/jz500279b. URL: https://pubs.acs.org/sharingguidelines.

[39] Valerio D'Innocenzo et al. "Excitons versus free charges in organo-lead tri-halide perovskites." In: *Nature communications* 5 (2014), p. 3586. ISSN: 2041-1723. DOI: 10.1038/ncomms4586. URL: http://www.ncbi.nlm.nih.gov/pubmed/24710005.

[40] Y. Chen et al. "Extended carrier lifetimes and diffusion in hybrid perovskites revealed by Hall effect and photoconductivity measurements". In: *Nature Communications* 7.1 (Aug. 2016), pp. 1–9. ISSN: 20411723. DOI: 10.1038/ncomms12253.

[41] K. Xerxes Steirer et al. “Defect Tolerance in Methylammonium Lead Triiodide Perovskite”. In: *ACS Energy Letters* 1.2 (Aug. 2016), pp. 360–366. ISSN: 23808195. DOI: 10.1021/acsenergylett.6b00196. URL: http://pubs.acs.org/journal/aelccp.

[42] Jun Kang and Lin Wang Wang. “High Defect Tolerance in Lead Halide Perovskite CsPbBr3”. In: *Journal of Physical Chemistry Letters* 8.2 (Jan. 2017), pp. 489–493. ISSN: 19487185. DOI: 10.1021/acs.jpclett.6b02800. URL: https://pubs.acs.org/sharingguidelines.

[43] Terry Chien Jen Yang et al. “High-Bandgap Perovskite Materials for Multijunction Solar Cells”. In: *Joule* 2.8 (Aug. 2018), pp. 1421–1436. ISSN: 25424351. DOI: 10.1016/j.joule.2018.05.008. URL: https://www.sciencedirect.com/science/article/pii/S2542435118302277.

[44] Molang Cai et al. “Cost-Performance Analysis of Perovskite Solar Modules”. In: *Advanced Science* 4.1 (Jan. 2017), p. 1600269. ISSN: 2198-3844. DOI: 10.1002/ADVS.201600269. URL: https://onlinelibrary.wiley.com/doi/full/10.1002/advs.201600269%20https://onlinelibrary.wiley.com/doi/abs/10.1002/advs.201600269%20https://onlinelibrary.wiley.com/doi/10.1002/advs.201600269.

[45] Zongqi Li et al. “Cost Analysis of Perovskite Tandem Photovoltaics”. In: *Joule* 2.8 (2018), pp. 1559–1572. ISSN: 25424351. DOI: 10.1016/j.joule.2018.05.001. URL: https://www.sciencedirect.com/science/article/pii/S2542435118301910.

[46] Prashant V. Kamat. “Evolution of perovskite photovoltaics and decrease in energy payback time”. In: *Journal of Physical Chemistry Letters* 4.21 (Nov. 2013), pp. 3733–3734. ISSN: 19487185. DOI: 10.1021/jz402141s. URL: https://pubs.acs.org/sharingguidelines.

[47] Xueyu Tian, Samuel D. Stranks, and Fengqi You. “Life cycle energy use and environmental implications of high-performance perovskite tandem solar cells”. In: *Science Advances* 6.31 (July 2020). ISSN: 23752548. DOI: 10.1126/sciadv.abb0055. URL: https://www.science.org/doi/10.1126/sciadv.abb0055.

[48] Yana Vaynzof. “The Future of Perovskite Photovoltaics—Thermal Evaporation or Solution Processing?” In: *Advanced Energy Materials* 10.48 (Dec. 2020), p. 2003073. ISSN: 1614-6832. DOI: 10.1002/aenm.202003073. URL: https://onlinelibrary.wiley.com/doi/10.1002/aenm.202003073.

[49] Haotong Wei et al. “Sensitive X-ray detectors made of methylammonium lead tribromide perovskite single crystals”. In: *Nature Photonics* 10.5 (2016), pp. 333–339. ISSN: 1749-4885. DOI: 10.1038/nphoton.2016.41. URL: http://www.nature.com/doifinder/10.1038/nphoton.2016.41.

[50] Henning Mescher et al. “Flexible Inkjet-Printed Triple Cation Perovskite X-ray Detectors”. In: *ACS Applied Materials and Interfaces* 12.13 (Apr. 2020), pp. 15774–15784. ISSN: 19448252. DOI: 10.1021/acsami.9b14649. URL: https://dx.doi.org/10.1021/acsami.9b14649.

[51] Kun Mu Lee et al. “Selection of anti-solvent and optimization of dropping volume for the preparation of large area sub-module perovskite solar cells”. In: *Solar Energy Materials and Solar Cells* 172.August (2017), pp. 368–375. ISSN: 09270248. DOI: 10.1016/j.solmat.2017.08.010. URL: http://dx.doi.org/10.1016/j.solmat.2017.08.010.

[52] Xiao Ke Liu et al. “Metal halide perovskites for light-emitting diodes”. In: *Nature Materials 2020 20:1* 20.1 (Sept. 2020), pp. 10–21. ISSN: 1476-4660. DOI: 10.1038/s41563-020-0784-7. URL: https://www.nature.com/articles/s41563-020-0784-7.

[53] Haiming Zhu et al. “Lead halide perovskite nanowire lasers with low lasing thresholds and high quality factors.” In: *Nature materials* 14.6 (2015), pp. 636–642. ISSN: 1476-1122. DOI: 10.1038/nmat4271. URL: http://www.nature.com/nmat/journal/v14/n6/full/nmat4271.html%7B%5C#%7Dmethods.

[54] Philipp Brenner et al. “Triple cation mixed-halide perovskites for tunable lasers”. In: *Optical Materials Express* 7.11 (Nov. 2017), p. 4082. ISSN: 2159-3930. DOI: 10.1364/OME.7.004082. URL: https://www.osapublishing.org/abstract.cfm?URI=ome-7-11-4082.

[55] Ajay Kumar Jena, Ashish Kulkarni, and Tsutomu Miyasaka. “Halide Perovskite Photovoltaics: Background, Status, and Future Prospects”. In: *Chemical Reviews* 119.5 (Mar. 2019), pp. 3036–3103. ISSN: 15206890. DOI: 10.1021/acs.chemrev.8b00539. URL: https://www.nrel.gov/pv/assets/pdfs/pv-efficiency-.

[56] NREL National Renewable Energy Laboratory. *NREL Efficiency chart*. 2021. URL: https://www.nrel.gov/pv/cell-efficiency.html (visited on 01/12/2021).

[57] Tianhao Wu et al. “The Main Progress of Perovskite Solar Cells in 2020–2021”. In: *Nano-Micro Letters* 13.1 (Dec. 2021), pp. 1–18. ISSN: 21505551. DOI: 10.1007/S40820-021-00672-W/TABLES/1. URL: https://link.springer.com/article/10.1007/s40820-021-00672-w.

[58] Yang Zhao et al. “Research progress in large-area perovskite solar cells”. In: *Photonics Research, Vol. 8, Issue 7, pp. A1-A15* 8.7 (July 2020), A1–A15. ISSN: 2327-9125. DOI: 10.1364/PRJ.392996. URL: https://opg.optica.org/viewmedia.cfm?uri=prj-8-7-A1%7B%5C&%7Dseq=0%7B%5C&%7Dhtml=true%20https://opg.optica.org/abstract.cfm?uri=prj-8-7-A1%20https://opg.optica.org/prj/abstract.cfm?uri=prj-8-7-A1.

[59] *News Release:21.4%! Microquanta Sets New Efficiency World Record for Perovskite Minimodule*. URL: http://www.microquanta.com/en/newsinfo/80D096B5B598F211/ (visited on 01/05/2022).

[60] *Champion Photovoltaic Module Efficiency Chart | Photovoltaic Research | NREL*. URL: https://www.nrel.gov/pv/module-efficiency.html (visited on 01/05/2022).

[61] *Why perovskite photovoltaics? | Oxford PV*. URL: https://www.oxfordpv.com/perovskite-pv-transform-global-solar-market (visited on 01/05/2022).

[62] *Swift Solar - Next generation lightweight and efficient solar technology*. URL: https://www.swiftsolar.com/tech/ (visited on 01/05/2022).

[63] Axel F. Palmstrom et al. “Enabling Flexible All-Perovskite Tandem Solar Cells”. In: *Joule* 3.9 (Sept. 2019), pp. 2193–2204. ISSN: 2542-4351. DOI: 10.1016/J.JOULE.2019.05.009. URL: https://www.sciencedirect.com/science/article/pii/S2542435119302521.

[64] S. Akhil et al. “Review on perovskite silicon tandem solar cells: Status and prospects 2T, 3T and 4T for real world conditions”. In: *Materials & Design* 211 (Dec. 2021), p. 110138. ISSN: 0264-1275. DOI: 10.1016/J.MATDES.2021.110138. URL: https://www.sciencedirect.com/science/article/pii/S0264127521006936.

[65] *Swift Solar - Next generation lightweight and efficient solar technology*. URL: https://www.swiftsolar.com/applications/ (visited on 01/05/2022).

[66] *Products – Saule Technologies*. URL: https://sauletech.com/product/ (visited on 01/05/2022).

[67] *German-led consortium aims for 33% efficient perovskite-silicon solar cell – pv magazine International*. URL: https://www.pv-magazine.com/2020/08/24/german-led-consortium-aims-for-27-efficient-perovskite-silicon-solar-cell/ (visited on 01/05/2022).

[68] Nikhil Shrivastav et al. "Investigations aimed at producing 33% efficient perovskite-silicon tandem solar cells through device simulations". In: *RSC Advances* 11.59 (Nov. 2021), pp. 37366–37374. ISSN: 20462069. DOI: 10.1039/d1ra06250f. URL: https://pubs.rsc.org/en/content/articlehtml/2021/ra/d1ra06250f%20https://pubs.rsc.org/en/content/articlelanding/2021/ra/d1ra06250f.

[69] Enbing Bi et al. "Efficient Perovskite Solar Cell Modules with High Stability Enabled by Iodide Diffusion Barriers". In: *Joule* 3.11 (Nov. 2019), pp. 2748–2760. ISSN: 25424351. DOI: 10.1016/j.joule.2019.07.030.

[70] *Microquanta demonstrates high stability beyond IEC standards*. URL: http://www.microquanta.com/en/newsinfo/112E5B4ABC180F9D/ (visited on 01/05/2022).

[71] *IEC 61215-1:2021 | IEC Webstore*. URL: https://webstore.iec.ch/publication/61345 (visited on 01/05/2022).

[72] Zhichun Yang et al. "Slot-die coating large-area formamidinium-cesium perovskite film for efficient and stable parallel solar module". In: *Science Advances* 7.18 (Apr. 2021), p. 3749. ISSN: 23752548. DOI: 10.1126/sciadv.abg3749. URL: https://www.science.org.

[73] *Microquanta claims 20.2% efficiency on small perovskite module – pv magazine International*. URL: https://www.pv-magazine.com/2021/05/17/microquanta-claims-20-2-efficiency-on-small-perovskite-module/ (visited on 01/06/2022).

[74] *Microquanta achieves 14.24% efficiency with large-area perovskite solar module – pv magazine International*. URL: https://www.pv-magazine.com/2019/10/24/microquanta-achieves-14-24-efficiency-with-large-area-perovskite-solar-module/ (visited on 01/06/2022).

[75] *Large-area perovskite solar module with 18% efficiency – pv magazine International*. URL: https://www.pv-magazine.com/2021/04/28/large-area-perovskite-solar-module-with-18-efficiency/ (visited on 01/06/2022).

[76] *Toshiba claims 15.1% efficiency for polymer film-based large-area perovskite solar module – pv magazine International*. URL: https://www.pv-magazine.com/2021/09/09/toshiba-achieves-efficiency/ (visited on 01/06/2022).

[77] Aslihan Babayigit et al. "Toxicity of organometal halide perovskite solar cells". In: *Nature Materials 2016 15:3* 15.3 (Feb. 2016), pp. 247–251. ISSN: 1476-4660. DOI: 10.1038/nmat4572. URL: https://www.nature.com/articles/nmat4572.

[78] Endre Horváth et al. "Fighting Health Hazards in Lead Halide Perovskite Optoelectronic Devices with Transparent Phosphate Salts". In: *ACS Applied Materials and Interfaces* 13.29 (July 2021), pp. 33995–34002. ISSN: 19448252. DOI: 10.1021/acsami.0c21137. URL: https://doi.org/10.1021/acsami.0c21137.

[79] Xun Li et al. "On-device lead sequestration for perovskite solar cells". In: *Nature* 578.7796 (Feb. 2020), pp. 555–558. ISSN: 14764687. DOI: 10.1038/s41586-020-2001-x. URL: https://doi.org/10.1038/s41586-020-2001-x.

[80] Andreas Binek et al. "Recycling Perovskite Solar Cells to Avoid Lead Waste". In: *ACS Applied Materials and Interfaces* 8.20 (May 2016), pp. 12881–12886. ISSN: 19448252. DOI: 10.1021/acsami.6b03767. URL: https://pubs.acs.org/doi/10.1021/acsami.6b03767.

[81] Rosario Vidal et al. "Assessing health and environmental impacts of solvents for producing perovskite solar cells". In: *Nature Sustainability* 4.3 (Mar. 2021), pp. 277–285. ISSN: 23989629. DOI: 10.1038/s41893-020-00645-8. URL: https://www.nature.com/articles/s41893-020-00645-8.

[82] Gerald L. Kennedy. "Acute and subchronic toxicity of dimethylformam ide and dimethylacetamide following various routes of administration". In: *Drug and Chemical Toxicology* 9.2 (1986), pp. 147–170. ISSN: 01480545. DOI: 10.3109/01480548608998272. URL: https://www.tandfonline.com/action/journalInformation?journalCode=idct20.

[83] Tae Hyun Kim and Sang Geon Kim. "Clinical Outcomes of Occupational Exposure to N,N-Dimethylformamide: Perspectives from Experimental Toxicology". In: *Safety and Health at Work* 2.2 (June 2011), pp. 97–104. ISSN: 2093-7911. DOI: 10.5491/SHAW.2011.2.2.97.

URL: https://www.sciencedirect.com/science/article/pii/S209379111122002X.

[84] *The MAK-Collection for Occupational Health and Safety*. Wiley, Nov. 2002. ISBN: 9783527600410. DOI: 10.1002/3527600418. URL: https://onlinelibrary.wiley.com/doi/book/10.1002/3527600418.

[85] K LEE. "Toxicity of N-methyl-2-pyrrolidone (NMP): Teratogenic, subchronic, and two-year inhalation studies". In: *Fundamental and Applied Toxicology* 9.2 (Aug. 1987), pp. 222–235. ISSN: 02720590. DOI: 10.1016/0272-0590(87)90045-5. URL: https://pubmed.ncbi.nlm.nih.gov/3653566/.

[86] Jinzhao Li et al. "20.8% Slot-Die Coated MAPbI3 Perovskite Solar Cells by Optimal DMSO-Content and Age of 2-ME Based Precursor Inks". In: *Advanced Energy Materials* 11.10 (Mar. 2021), p. 2003460. ISSN: 1614-6832. DOI: 10.1002/aenm.202003460. URL: https://onlinelibrary.wiley.com/doi/10.1002/aenm.202003460.

[87] Michael P Dieter. *National Toxicology Program Toxicity Report Series Number 26 NTP Technical Report on Toxicity Studies of Ethylene Glycol Ethers Administered in Drinking Water to F344/N Rats and B6C3F X Mice*. Tech. rep. 1993, pp. 111–76.

[88] T Jesper Jacobsson et al. "An open-access database and analysis tool for perovskite solar cells based on the FAIR data principles". In: *Nature Energy* (Dec. 2021), pp. 1–9. ISSN: 2058-7546. DOI: 10.1038/s41560-021-00941-3. URL: https://doi.org/10.1038/s41560-021-00941-3.

[89] José Danglad-Flores, Stephan Eickelmann, and Hans Riegler. "Deposition of polymer films by spin casting: A quantitative analysis". In: *Chemical Engineering Science* 179 (Apr. 2018), pp. 257–264. ISSN: 00092509. DOI: 10.1016/j.ces.2018.01.012. URL: https://www.sciencedirect.com/science/article/pii/S0009250918300125.

[90] Jennifer A. Baker et al. "From spin coating to roll-to-roll: investigating the challenge of upscaling lead halide perovskite solar cells". In: *IET Renewable Power Generation* 11.5 (Apr. 2017), pp. 546–549. ISSN: 1752-1416. DOI: 10.1049/iet-rpg.2016.0683. URL: https://onlinelibrary.wiley.com/doi/10.1049/iet-rpg.2016.0683.

[91] B. Roth, R. R. Søndergaard, and F. C. Krebs. "Roll-to-roll printing and coating techniques for manufacturing large-area flexible organic electronics". In: *Handbook of Flexible Organic Electronics: Materials, Manufacturing and Applications*. Elsevier Inc., Jan. 2015, pp. 171–197. ISBN: 9781782420439. DOI: 10.1016/B978-1-78242-035-4.00007-5. URL: https://www.sciencedirect.com/science/article/pii/B9781782420354000075.

[92] Benjamin Schmidt-Hansberg et al. "Moving Through the Phase Diagram : Morphology Formation in Solution Cast Polymer – Fullerene Blend Films for Organic Solar Cells". In: *ACS Nano* 5.11 (2011), pp. 8579–8590. DOI: 10.1021/nn2036279. URL: https://pubs.acs.org/doi/abs/10.1021/nn2036279.

[93] Benjamin Schmidt-Hansberg et al. "Spatially resolved drying kinetics of multi-component solution cast films for organic electronics". In: *Chemical Engineering and Processing: Process Intensification* 50.5-6 (2011), pp. 509–515. ISSN: 02552701. DOI: 10.1016/j.cep.2010.12.012. URL: http://dx.doi.org/10.1016/j.cep.2010.12.012.

[94] Olivier J.J. Ronsin et al. "A phase-field model for the evaporation of thin film mixtures". In: *Physical Chemistry Chemical Physics* 22.12 (Mar. 2020), pp. 6638–6652. ISSN: 14639076. DOI: 10.1039/d0cp00214c. arXiv: 2001.05160. URL: https://pubs.rsc.org/en/content/articlehtml/2020/cp/d0cp00214c%20https://pubs.rsc.org/en/content/articlelanding/2020/cp/d0cp00214c.

[95] Byungho Lee et al. "Microstructural Evolution of Hybrid Perovskites Promoted by Chlorine and its Impact on the Performance of Solar Cell". In: *Scientific Reports* 9.1 (Dec. 2019), pp. 1–8. ISSN: 20452322. DOI: 10.1038/s41598-019-41328-5. URL: www.nature.com/scientificreports.

[96] Mohammad Ali Akhavan Kazemi, Arash Jamali, and Frédéric Sauvage. "A Holistic Study on the Effect of Annealing Temperature and Time on CH3 NH3PbI3-Based Perovskite Solar Cell Characteristics". In: *Frontiers in Energy Research* 9 (Oct. 2021), p. 702. ISSN: 2296-598X. DOI: 10.3389/fenrg.2021.732886. URL: https://www.frontiersin.org/articles/10.3389/fenrg.2021.732886/full.

[97] Md Arafat Mahmud et al. "Controlled Ostwald ripening mediated grain growth for smooth perovskite morphology and enhanced device performance". In: *Solar Energy Materials and Solar Cells* 167 (Aug.

2017), pp. 87–101. ISSN: 09270248. DOI: 10.1016/j.solmat.2017.03.034.

[98] Peng Cui et al. "Reduced surface defects of organometallic perovskite by thermal annealing for highly efficient perovskite solar cells". In: *RSC Advances* 5.92 (Sept. 2015), pp. 75622–75629. ISSN: 2046-2069. DOI: 10.1039/C5RA16669A. URL: https://pubs.rsc.org/en/content/articlehtml/2015/ra/c5ra16669a%20https://pubs.rsc.org/en/content/articlelanding/2015/ra/c5ra16669a.

[99] Lucija Rakocevic et al. "Loss Analysis in Perovskite Photovoltaic Modules". In: *Solar RRL* 3.12 (2019), p. 1900338. ISSN: 2367198X. DOI: 10.1002/solr.201900338.

[100] Rudolf Gross and Achim Marx. *Festkörperphysik*. 2nd editio. OLDENBOURG WISSENSCHAFTSVERLAG, Aug. 2014. ISBN: 978-3-11-035869-8. DOI: 10.1524/9783110358704.

[101] Hiroyuki Fujiwara et al. "Optical Characteristics and Operational Principles of Hybrid Perovskite Solar Cells". In: *physica status solidi (a)* 215.12 (June 2018), p. 1700730. ISSN: 18626300. DOI: 10.1002/pssa.201700730. URL: https://onlinelibrary.wiley.com/doi/10.1002/pssa.201700730.

[102] Paul Fassl et al. "Revealing the internal luminescence quantum efficiency of perovskite films via accurate quantification of photon recycling". In: *Matter* 4.4 (Feb. 2021), pp. 1391–1412. ISSN: 25902385. DOI: 10.1016/j.matt.2021.01.019. arXiv: 2010.12950. URL: https://linkinghub.elsevier.com/retrieve/pii/S2590238521000199.

[103] Martin Stolterfoht et al. "The perovskite/transport layer interfaces dominate non-radiative recombination in efficient perovskite solar cells". In: *Energy and Environmental Science* 12.9 (Oct. 2018), pp. 2778–2788. DOI: 10.1039/c9ee02020a. arXiv: 1810.01333. URL: http://arxiv.org/abs/1810.01333%20http://dx.doi.org/10.1039/c9ee02020a.

[104] Christian M. Wolff et al. "Nonradiative Recombination in Perovskite Solar Cells: The Role of Interfaces". In: *Advanced Materials* 31.52 (Dec. 2019), p. 1902762. ISSN: 0935-9648. DOI: 10.1002/adma.201902762. URL: https://onlinelibrary.wiley.com/doi/10.1002/adma.201902762.

[105] Ranbir Singh and B. Jayant Baliga. "P-I-N Diode". In: *Cryogenic Operation of Silicon Power Devices*. Springer US, 1998, pp. 37–48. DOI: 10.1007/978-1-4615-5751-7_4. URL: https://link.springer.com/chapter/10.1007/978-1-4615-5751-7%7B%5C_%7D4.

[106] Mehmet Copuroglu et al. "Location and Visualization of Working p-n and/or n-p Junctions by XPS". In: *Scientific Reports* 6.1 (Sept. 2016), pp. 1–9. ISSN: 20452322. DOI: 10.1038/srep32482. URL: www.nature.com/scientificreports.

[107] Hui Xia et al. "Nanoscale imaging of the photoresponse in PN junctions of InGaAs infrared detector". In: *Scientific Reports* 6.1 (Feb. 2016), pp. 1–8. ISSN: 20452322. DOI: 10.1038/srep21544. URL: www.nature.com/scientificreports.

[108] Tomonori Nakamura et al. "Surface potential imaging and characterizations of a GaN p-n junction with Kelvin probe force microscopy". In: *AIP Advances* 10.8 (Aug. 2020), p. 085010. ISSN: 21583226. DOI: 10.1063/5.0007524. URL: http://aip.scitation.org/doi/10.1063/5.0007524.

[109] Harald Müllejans et al. "Spectral mismatch in calibration of photovoltaic reference devices by global sunlight method". In: *Measurement Science and Technology* 16.6 (2005), pp. 1250–1254. ISSN: 0957-0233. DOI: 10.1088/0957-0233/16/6/002. URL: https://iopscience.iop.org/article/10.1088/0957-0233/16/6/002.

[110] W. Shockley and W. T. Read. "Statistics of the recombinations of holes and electrons". In: *Physical Review* 87.5 (Sept. 1952), pp. 835–842. ISSN: 0031899X. DOI: 10.1103/PhysRev.87.835. URL: https://journals.aps.org/pr/abstract/10.1103/PhysRev.87.835.

[111] Uwe Rau and Thomas Kirchartz. "Charge Carrier Collection and Contact Selectivity in Solar Cells". In: *Advanced Materials Interfaces* 6.20 (Oct. 2019), p. 1900252. ISSN: 2196-7350. DOI: 10.1002/admi.201900252. URL: https://onlinelibrary.wiley.com/doi/10.1002/admi.201900252.

[112] Yi Hou et al. "Suppression of Hysteresis Effects in Organohalide Perovskite Solar Cells". In: *Advanced Materials Interfaces* 4.11 (June 2017), p. 1700007. ISSN: 21967350. DOI: 10.1002/admi.201700007. URL: https://onlinelibrary.wiley.com/doi/10.1002/admi.201700007.

[113] Dong-Ho Kang and Nam-Gyu Park. "On the Current–Voltage Hysteresis in Perovskite Solar Cells: Dependence on Perovskite Composition and Methods to Remove Hysteresis". In: *Advanced Materials* 31.34 (Aug. 2019), p. 1805214. ISSN: 0935-9648. DOI: 10.1002/adma.201805214. URL: https://onlinelibrary.wiley.com/doi/10.1002/adma.201805214.

[114] Bo Chen et al. "Origin of J-V Hysteresis in Perovskite Solar Cells". In: *Journal of Physical Chemistry Letters* 7.5 (Mar. 2016), pp. 905–917. ISSN: 19487185. DOI: 10.1021/ACS.JPCLETT.6B00215/ASSET/IMAGES/LARGE/JZ-2016-00215A_0011.JPEG. URL: https://pubs.acs.org/doi/full/10.1021/acs.jpclett.6b00215.

[115] Weiming Qiu et al. "Pinhole-Free Perovskite Films for Efficient Solar Modules". In: *Energy Environ. Sci.* 9 (2016), pp. 484–489. ISSN: 1754-5692. DOI: 10.1039/C5EE03703D. URL: http://pubs.rsc.org/en/Content/ArticleLanding/2016/EE/C5EE03703D.

[116] Ihteaz M. Hossain et al. "Scalable processing of low-temperature TiO2 nanoparticles for high-efficiency perovskite solar cells". In: *ACS Applied Energy Materials* 2.1 (Jan. 2019), pp. 47–58. ISSN: 25740962. DOI: 10.1021/acsaem.8b01567. URL: https://pubs.acs.org/doi/10.1021/acsaem.8b01567.

[117] Qi Jiang et al. "Planar-Structure Perovskite Solar Cells with Efficiency beyond 21%". In: *Advanced Materials* 29.46 (Dec. 2017), p. 1703852. ISSN: 09359648. DOI: 10.1002/adma.201703852. URL: http://doi.wiley.com/10.1002/adma.201703852.

[118] Mahdi Malekshahi Byranvand et al. "Chemical vapor deposited polymer layer for efficient passivation of planar perovskite solar cells". In: *Journal of Materials Chemistry A* 8.38 (Oct. 2020), pp. 20122–20132. ISSN: 20507496. DOI: 10.1039/d0ta06646j. URL: https://pubs.rsc.org/en/content/articlehtml/2020/ta/d0ta06646j%20https://pubs.rsc.org/en/content/articlelanding/2020/ta/d0ta06646j.

[119] Somayeh Moghadamzadeh et al. "Spontaneous enhancement of the stable power conversion efficiency in perovskite solar cells". In: *Journal of Materials Chemistry A* 8.2 (Jan. 2020), pp. 670–682. ISSN: 20507496. DOI: 10.1039/c9ta09584e. URL: https://pubs.rsc.org/en/content/articlehtml/2020/ta/c9ta09584e%20https://pubs.rsc.org/en/content/articlelanding/2020/ta/c9ta09584e.

[120] Jonas A. Schwenzer et al. “Temperature Variation-Induced Performance Decline of Perovskite Solar Cells”. In: *ACS Applied Materials and Interfaces* 10.19 (May 2018), pp. 16390–16399. ISSN: 19448252. DOI: 10.1021/acsami.8b01033. URL: https://pubs.acs.org/doi/10.1021/acsami.8b01033.

[121] Lukas Wengeler et al. “Comparison of large scale coating techniques for organic and hybrid films in polymer based solar cells”. In: *Chemical Engineering and Processing: Process Intensification* 68 (June 2013), pp. 38–44. ISSN: 02552701. DOI: 10.1016/j.cep.2012.03.004. URL: https://www.sciencedirect.com/science/article/pii/S0255270112000645.

[122] Maël Le Berre, Yong Chen, and Damien Baigl. “From convective assembly to landau - Levich deposition of multilayered phospholipid films of controlled thickness”. In: *Langmuir* 25.5 (Mar. 2009), pp. 2554–2557. ISSN: 07437463. DOI: 10.1021/la803646e. URL: https://pubs.acs.org/doi/10.1021/la803646e.

[123] Qi Wang et al. “Qualifying composition dependent p and n self-doping in CH3NH3PbI3”. In: *Applied Physics Letters* 105.16 (Oct. 2014), p. 163508. ISSN: 00036951. DOI: 10.1063/1.4899051. URL: http://aip.scitation.org/doi/10.1063/1.4899051.

[124] Steffen Braunger et al. “Cs x FA1- xPb(I1- yBr y)3 Perovskite Compositions: The Appearance of Wrinkled Morphology and its Impact on Solar Cell Performance”. In: *Journal of Physical Chemistry C* 122.30 (2018), pp. 17123–17135. ISSN: 19327455. DOI: 10.1021/acs.jpcc.8b06459. URL: https://pubs.acs.org/doi/abs/10.1021/acs.jpcc.8b06459.

[125] D. McMullan. “Scanning electron microscopy 1928-1965”. In: *Scanning* 17.3 (Dec. 2006), pp. 175–185. ISSN: 01610457. DOI: 10.1002/sca.4950170309. URL: https://onlinelibrary.wiley.com/doi/10.1002/sca.4950170309.

[126] F. Ohnesorge and G. Binnig. “True atomic resolution by atomic force microscopy through repulsive and attractive f.” In: *Science* 260.5113 (June 1993), pp. 1451–1456. ISSN: 00368075. DOI: 10.1126/science.260.5113.1451. URL: https://www.science.org/doi/10.1126/science.260.5113.1451.

[127] *DektakXT | Bruker*. URL: https://www.bruker.com/de/products-and-solutions/test-and-measurement/stylus-profilometers/dektakxt.html (visited on 03/22/2022).

[128] Adrien Bercegol et al. "Spatial Inhomogeneity Analysis of Cesium-Rich Wrinkles in Triple-Cation Perovskite". In: *Journal of Physical Chemistry C* 122.41 (2018), pp. 23345–23351. ISSN: 19327455. DOI: 10.1021/acs.jpcc.8b07436. URL: https://pubs.acs.org/doi/10.1021/acs.jpcc.8b07436.

[129] Kevin A. Bush et al. "Controlling Thin-Film Stress and Wrinkling during Perovskite Film Formation". In: *ACS Energy Letters* 3.6 (2018), pp. 1225–1232. ISSN: 23808195. DOI: 10.1021/acsenergylett.8b00544.

[130] A. P. Kovács et al. "Group-delay measurement on laser mirrors by spectrally resolved white-light interferometry". In: *Optics Letters* 20.7 (Apr. 1995), p. 788. ISSN: 0146-9592. DOI: 10.1364/ol.20.000788. URL: https://opg.optica.org/viewmedia.cfm?uri=ol-20-7-788%7B%5C&%7Dseq=0%7B%5C&%7Dhtml=true%20https://opg.optica.org/abstract.cfm?uri=ol-20-7-788%20https://opg.optica.org/ol/abstract.cfm?uri=ol-20-7-788.

[131] Tatiana V. Amotchkina et al. "Measurement of group delay of dispersive mirrors with white-light interferometer". In: *Applied Optics* 48.5 (Feb. 2009), pp. 949–956. ISSN: 15394522. DOI: 10.1364/AO.48.000949. URL: https://opg.optica.org/viewmedia.cfm?uri=ao-48-5-949%7B%5C&%7Dseq=0%7B%5C&%7Dhtml=true%20https://opg.optica.org/abstract.cfm?uri=ao-48-5-949%20https://opg.optica.org/ao/abstract.cfm?uri=ao-48-5-949.

[132] *High precision 3D surface inspection with white light interferometry by ISRA VISION*. URL: https://www.isravision.com/en/ready-to-use/high-precision-3d-metrology/product-line-netgage3d/ (visited on 03/22/2022).

[133] Adolf Fick. "Ueber Diffusion". In: *Annalen der Physik und Chemie* 170.1 (Jan. 1855), pp. 59–86. ISSN: 00033804. DOI: 10.1002/andp.18551700105. URL: https://onlinelibrary.wiley.com/doi/10.1002/andp.18551700105.

[134] R. Saure, G. R. Wagner, and E. U. Schlünder. "Drying of solvent-borne polymeric coatings: I. Modeling the drying process". In: *Surface and Coatings Technology* 99.3 (1998), pp. 253–256. ISSN: 02578972. DOI: 10.1016/S0257-8972(97)00564-1. URL: https://www.sciencedirect.com/science/article/pii/S0257897297005641.

[135] J. W. Westwater and H. G. Drickamer. "The Mathematics of Diffusion". In: *Journal of the American Chemical Society* 79.5 (1957), pp. 1267–1268. ISSN: 15205126. DOI: 10.1021/ja01562a072.

[136] Kenneth R. Applin. "The diffusion of dissolved silica in dilute aqueous solution". In: *Geochimica et Cosmochimica Acta* 51.8 (Aug. 1987), pp. 2147–2151. ISSN: 00167037. DOI: 10.1016/0016-7037(87)90263-8.

[137] Qin Tan et al. "Temperature Dependent Diffusion of DMSO in CH3 NH3PbI3 Precursor Films during Layer Formation and Impact on Solar Cells". In: *ACS Applied Energy Materials* 2.7 (July 2019), pp. 5116–5123. ISSN: 25740962. DOI: 10.1021/acsaem.9b00769. URL: https://pubs.acs.org/doi/10.1021/acsaem.9b00769.

[138] F.-M. Raoult. "Recherches expérimentales sur les tensions de vapeur des dissol." In: *Journal de Physique Théor. et Appl.* 8.1 (1889), pp. 5–20. ISSN: 0368-3893. DOI: 10.1051/jphystap:0188900800500. URL: http://www.edpsciences.org/10.1051/jphystap:0188900800500.

[139] Wilhelm Schabel et al. "Sorption and diffusion measurements in ternary polymer-solvent-solvent systems by means of a magnetic suspension balance-Experimental methods and correlations with a modified Flory-Huggins and free-volume theory". In: *Chemical Engineering Science* 62.8 (Apr. 2007), pp. 2254–2266. ISSN: 00092509. DOI: 10.1016/j.ces.2006.12.062. URL: https://www.sciencedirect.com/science/article/pii/S0009250907000310.

[140] David P. Nenon et al. "Structural and chemical evolution of methylammonium lead halide perovskites during thermal processing from solution". In: *Energy and Environmental Science* 9.6 (2016), pp. 2072–2082. ISSN: 17545706. DOI: 10.1039/c6ee01047d. URL: http://dx.doi.org/10.1039/C6EE01047D%7B%5C%%7D5Cnhttp://xlink.rsc.org/?DOI=C6EE01047D.

[141] Xuemei Zhang et al. "Experimental isobaric (vapor + liquid) equilibrium data for the binary system N, N-dimethyl formamide + dimethyl sulfoxide and the quaternary system sec-butyl alcohol + sec-butyl acetate + N, N-dimethyl formamide + dimethyl sulfoxide at 101.3 kPa".

In: *Fluid Phase Equilibria* 409 (Feb. 2016), pp. 78–83. ISSN: 03783812. DOI: 10.1016/j.fluid.2015.09.039.

[142] Kejun Liao et al. "Hot-Casting Large-Grain Perovskite Film for Efficient Solar Cells: Film Formation and Device Performance". In: *Nano-Micro Letters 2020 12:1* 12.1 (July 2020), pp. 1–22. ISSN: 2150-5551. DOI: 10.1007/S40820-020-00494-2. URL: https://link.springer.com/article/10.1007/s40820-020-00494-2.

[143] L. Prandtl. "Zur Berechnung der Grenzschichten". In: *ZAMM - Zeitschrift für Angewandte Mathematik und Mechanik* 18.1 (Jan. 1938), pp. 77–82. ISSN: 00442267. DOI: 10.1002/zamm.19380180111. URL: https://onlinelibrary.wiley.com/doi/10.1002/zamm.19380180111.

[144] E. Pohlhausen. "Der Wärmeaustausch zwischen festen Körpern und Flüssigkeiten mit kleiner reibung und kleiner Wärmeleitung". In: *ZAMM - Zeitschrift für Angewandte Mathematik und Mechanik* 1.2 (Jan. 1921), pp. 115–121. ISSN: 00442267. DOI: 10.1002/zamm.19210010205. URL: https://onlinelibrary.wiley.com/doi/10.1002/zamm.19210010205.

[145] Philipp Cavadini, Philip Scharfer, and Wilhelm Schabel. "Investigation of heat transfer within an array of impinging jets with local extraction of spent fluid". In: *Proceedings of the 15th International Heat Transfer Conference, IHTC 2014*. Begell House Inc., 2014. DOI: 10.1615/ihtc15.mtr.008875. URL: https://www.ihtcdigitallibrary.com/conferences/ihtc15,1ab275235dc6315e,6b52b6857a9daa5f.html.

[146] Felix Buss. *Zur Lösemitteldiffusion in Polymernanoschichten: Schichtdicken- und Konzentrationsabhängigkeit*. KIT Scientific Publishing, 2017. ISBN: 978-3-7315-0591-4. DOI: 10.5445/KSP/1000060263. URL: https://publikationen.bibliothek.kit.edu/1000060263.

[147] Mihály Parti. "MASS TRANSFER BIOT NUMBERS". In: *Periodica Polytechnica Mechanical Engineering* 38.2-3 (1994), pp. 109–122. URL: https://pp.bme.hu/me/article/view/5519.

[148] Timothy A. Ameel. "Average effects of forced convection over a flat plate with an unheated starting length". In: *International Communications in Heat and Mass Transfer* 24.8 (Dec. 1997), pp. 1113–1120. ISSN: 0735-1933. DOI: 10.1016/S0735-1933(97)00105-X.

[149] Evangelos Tsotsas and Arun S. Mujumdar. *Modern Drying Technology*. Vol. 1-4. Weinheim, Germany: Wiley-VCH Verlag GmbH & Co. KGaA, Feb. 2014, pp. 1–394. ISBN: 9783527631728. DOI: 10.1002/9783527631728. URL: http://doi.wiley.com/10.1002/9783527631728.

[150] Bo Chen et al. "Blade-Coated Perovskites on Textured Silicon for 26 % -Efficient Monolithic Perovskite / Silicon Tandem Solar Cells Blade-Coated Perovskites on Textured Silicon for 26 % -Efficient Monolithic Perovskite / Silicon Tandem Solar Cells". In: *Joule* (2020), pp. 1–15. ISSN: 2542-4351. DOI: 10.1016/j.joule.2020.01.008. URL: https://doi.org/10.1016/j.joule.2020.01.008.

[151] Luigi Vesce et al. "Ambient Air Blade-Coating Fabrication of Stable Triple-Cation Perovskite Solar Modules by Green Solvent Quenching". In: *Solar RRL* 5.8 (Aug. 2021), p. 2100073. ISSN: 2367-198X. DOI: 10.1002/solr.202100073. URL: https://onlinelibrary.wiley.com/doi/10.1002/solr.202100073.

[152] E. U. Schlünder, P. Krötzsch, and Fr.-W. Hennecke. "Gesetzmäßigkeiten der Wärme- und Stoffübertragung bei der Prallströmung aus Rund- und Schlitzdüsen". In: *Chemie Ingenieur Technik* 42.6 (Mar. 1970), pp. 333–338. ISSN: 0009286X. DOI: 10.1002/cite.330420602. URL: https://onlinelibrary.wiley.com/doi/10.1002/cite.330420602.

[153] Herbert Martin Hofmann, Matthias Kind, and Holger Martin. "Measurements on steady state heat transfer and flow structure and new correlations for heat and mass transfer in submerged impinging jets". In: *International Journal of Heat and Mass Transfer* 50.19-20 (2007), pp. 3957–3965. ISSN: 00179310. DOI: 10.1016/j.ijheatmasstransfer.2007.01.023.

[154] D. -T. Chin and M. Agarwal. "Mass Transfer from an Oblique Impinging Slot Jet". In: *Journal of The Electrochemical Society* 138.9 (Sept. 1991), pp. 2643–2650. ISSN: 0013-4651. DOI: 10.1149/1.2086031. URL: https://iopscience.iop.org/article/10.1149/1.2086031%20https://iopscience.iop.org/article/10.1149/1.2086031/meta.

[155] Rahim Munir et al. "Hybrid Perovskite Thin-Film Photovoltaics: In Situ Diagnostics and Importance of the Precursor Solvate Phases". In: *Advanced Materials* 29.2 (2017), p. 1604113. ISSN: 15214095. DOI:

10.1002/adma.201604113. URL: https://onlinelibrary.wiley.com/doi/full/10.1002/adma.201604113.

[156] Oleksandra Shargaieva et al. "Hybrid perovskite crystallization from binary solvent mixtures: interplay of evaporation rate and binding strength of solvents". In: *Materials Advances* 1.9 (Dec. 2020), pp. 3314–3321. DOI: 10.1039/d0ma00815j. URL: https://pubs.rsc.org/en/content/articlehtml/2020/ma/d0ma00815j%20https://pubs.rsc.org/en/content/articlelanding/2020/ma/d0ma00815j.

[157] D. P. Woodruff. "How does your crystal grow? A commentary on Burton, Cabrera and Frank (1951) The growth of crystals and the equilibrium structure of their surfaces". In: *Philosophical Transactions of the Royal Society A: Mathematical, Physical and Engineering Sciences* (2015). DOI: 10.1098/RSTA.2014.0230. URL: https://royalsocietypublishing.org/doi/full/10.1098/rsta.2014.0230.

[158] Murielle A. Watzky and Richard G. Finke. "Transition metal nanocluster formation kinetic and mechanistic studies. A new mechanism when hydrogen is the reductant: Slow, continuous nucleation and fast autocatalytic surface growth". In: *Journal of the American Chemical Society* 119.43 (1997), pp. 10382–10400. ISSN: 00027863. DOI: 10.1021/JA9705102/ASSET/IMAGES/MEDIUM/JA9705102E00022.GIF. URL: https://pubs.acs.org/doi/full/10.1021/ja9705102.

[159] Christopher B. Whitehead, Saim Özkar, and Richard G. Finke. "LaMer's 1950 Model for Particle Formation of Instantaneous Nucleation and Diffusion-Controlled Growth: A Historical Look at the Model's Origins, Assumptions, Equations, and Underlying Sulfur Sol Formation Kinetics Data". In: *Chemistry of Materials* 31.18 (Sept. 2019), pp. 7116–7132. ISSN: 15205002. DOI: 10.1021/ACS.CHEMMATER.9B01273/ASSET/IMAGES/MEDIUM/CM9B01273_M020.GIF. URL: https://pubs.acs.org/doi/full/10.1021/acs.chemmater.9b01273.

[160] Christopher B Whitehead and Richard G Finke. "LaMer's 1950 model of particle formation: a review and critical analysis of its classical nucleation and fluctuation theory basis, of competing models and mechanisms for phase-changes and particle formation, and then of its application to silver halide, s". In: *Cite this: Mater. Adv* 2 (2021), p. 186. DOI: 10.1039/d0ma00439a.

[161] S. Karthika, T. K. Radhakrishnan, and P. Kalaichelvi. "A Review of Classical and Nonclassical Nucleation Theories". In: *Crystal Growth and Design* 16.11 (Nov. 2016), pp. 6663–6681. ISSN: 15287505. DOI: 10.1021/ACS.CGD.6B00794/ASSET/IMAGES/LARGE/CG-2016-00794M_0021.JPEG. URL: https://pubs.acs.org/doi/full/10.1021/acs.cgd.6b00794.

[162] Derek R. Handwerk et al. "Mechanism-Enabled Population Balance Modeling of Particle Formation en Route to Particle Average Size and Size Distribution Understanding and Control". In: *Journal of the American Chemical Society* 141.40 (Oct. 2019), pp. 15827–15839. ISSN: 15205126. DOI: 10.1021/JACS.9B06364/ASSET/IMAGES/MEDIUM/JA9B06364_M006.GIF. URL: https://pubs.acs.org/doi/full/10.1021/jacs.9b06364.

[163] Derek R. Handwerk et al. "Particle Size Distributions via Mechanism-Enabled Population Balance Modeling". In: *Journal of Physical Chemistry C* 124.8 (Feb. 2020), pp. 4852–4880. ISSN: 19327455. DOI: 10.1021/ACS.JPCC.9B11239/ASSET/IMAGES/MEDIUM/JP9B11239_M020.GIF. URL: https://pubs.acs.org/doi/full/10.1021/acs.jpcc.9b11239.

[164] Dong Liu et al. "Supersaturation controlled growth of MAFAPbI3 perovskite film for high efficiency solar cells". In: *Science China Chemistry* 61.10 (Oct. 2018), pp. 1278–1284. ISSN: 1674-7291. DOI: 10.1007/s11426-018-9250-6. URL: http://link.springer.com/10.1007/s11426-018-9250-6.

[165] Hanlin Hu et al. "Room-Temperature Meniscus Coating of >20% Perovskite Solar Cells: A Film Formation Mechanism Investigation". In: *Advanced Functional Materials* (Apr. 2019), p. 1900092. ISSN: 1616-301X. DOI: 10.1002/adfm.201900092. URL: https://onlinelibrary.wiley.com/doi/abs/10.1002/adfm.201900092.

[166] Hanlin Hu et al. "Nucleation and crystal growth control for scalable solution-processed organic-inorganic hybrid perovskite solar cells". In: *Journal of Materials Chemistry A* 8.4 (Jan. 2020), pp. 1578–1603. ISSN: 20507496. DOI: 10.1039/c9ta11245f. URL: https://pubs.rsc.org/en/content/articlehtml/2020/ta/c9ta11245f%20https://pubs.rsc.org/en/content/articlelanding/2020/ta/c9ta11245f.

[167] Kai Zhang et al. "A prenucleation strategy for ambient fabrication of perovskite solar cells with high device performance uniformity". In: *Nature Communications 2020 11:1* 11.1 (Feb. 2020), pp. 1–11. ISSN:

2041-1723. DOI: 10.1038/s41467-020-14715-0. URL: https://www.nature.com/articles/s41467-020-14715-0.

[168] Liang Li et al. "The Additive Coordination Effect on Hybrids Perovskite Crystallization and High-Performance Solar Cell". In: *Advanced Materials* 28.44 (Nov. 2016), pp. 9862–9868. ISSN: 09359648. DOI: 10.1002/adma.201603021. URL: https://onlinelibrary.wiley.com/doi/10.1002/adma.201603021.

[169] Victor K. Lamer and Robert H. Dinegar. "Theory, Production and Mechanism of Formation of Monodispersed Hydrosols". In: *Journal of the American Chemical Society* 72.11 (Nov. 1950), pp. 4847–4854. ISSN: 15205126. DOI: 10.1021/JA01167A001/ASSET/JA01167A001.FP.PNG_V03. URL: https://pubs.acs.org/doi/abs/10.1021/ja01167a001.

[170] Chang Liu, Yi Bing Cheng, and Ziyi Ge. *Understanding of perovskite crystal growth and film formation in scalable deposition processes*. Mar. 2020. DOI: 10.1039/c9cs00711c. URL: https://pubs.rsc.org/en/content/articlehtml/2020/cs/c9cs00711c%20https://pubs.rsc.org/en/content/articlelanding/2020/cs/c9cs00711c.

[171] Tadao Sugimoto et al. "Spontaneous nucleation of monodisperse silver halide particles from homogeneous gelatin solution I: silver chloride". In: *Colloids and Surfaces A: Physicochemical and Engineering Aspects* 164.2-3 (May 2000), pp. 183–203. ISSN: 0927-7757. DOI: 10.1016/S0927-7757(99)00366-0.

[172] Daniel B.K. Chu, Jonathan S. Owen, and Baron Peters. "Nucleation and Growth Kinetics from LaMer Burst Data". In: *Journal of Physical Chemistry A* 121.40 (Oct. 2017), pp. 7511–7517. ISSN: 15205215. DOI: 10.1021/ACS.JPCA.7B08368/ASSET/IMAGES/LARGE/JP-2017-08368U_0004.JPEG. URL: https://pubs.acs.org/doi/full/10.1021/acs.jpca.7b08368.

[173] Mathias Uller Rothmann et al. "Microstructural Characterisations of Perovskite Solar Cells – From Grains to Interfaces: Techniques, Features, and Challenges". In: *Advanced Energy Materials* 7.23 (Dec. 2017), p. 1700912. ISSN: 1614-6832. DOI: 10.1002/aenm.201700912. URL: https://onlinelibrary.wiley.com/doi/10.1002/aenm.201700912.

[174] Jasper J. Michels et al. “Predictive modelling of structure formation in semiconductor films produced by meniscus-guided coating”. In: *Nature Materials* 20 (Aug. 2020), pp. 68–75. ISSN: 14764660. DOI: 10.1038/s41563-020-0760-2. URL: https://doi.org/10.1038/s41563-020-0760-2.

[175] Karl Popper. *The Logic of Scientific Discovery*. 2nd Editio. London and New York: Routledge (Taylor & Francis Group), 1935. ISBN: 9780415278430.

[176] Rubin H. Landau, Manuel J. Páez, and Cristian C. Bordeianu. *Computational Physics*. Wiley, July 2007, pp. 1–593. ISBN: 9783527406265. DOI: 10.1002/9783527618835. URL: https://onlinelibrary.wiley.com/doi/book/10.1002/9783527618835.

[177] B. Schmidt-Hansberg et al. “In situ monitoring the drying kinetics of knife coated polymer-fullerene films for organic solar cells”. In: *Journal of Applied Physics* 106 (2009), p. 124501. ISSN: 00218979. DOI: 10.1063/1.3270402. URL: https://aip.scitation.org/doi/10.1063/1.3270402.

[178] Laurie J. Phillips et al. “Dispersion relation data for methylammonium lead triiodide perovskite deposited on a (100) silicon wafer using a two-step vapour-phase reaction process”. In: *Data in Brief* 5 (Dec. 2015), pp. 926–928. ISSN: 23523409. DOI: 10.1016/j.dib.2015.10.026.

[179] Tejraj M. Aminabhavi and Bindu Gopalakrishna. “Density, Viscosity, Refractive Index, and Speed of Sound in Aqueous Mixtures of N,N-Dimethylformamide, Dimethyl Sulfoxide, N,N-Dimethylacetamide, Acetonitrile, Ethylene Glycol, Diethylene Glycol, 1,4-Dioxane, Tetrahydrofuran, 2-Methoxyethanol, and 2-Ethox”. In: *Journal of Chemical and Engineering Data* 40.4 (July 1995), pp. 856–861. ISSN: 15205134. DOI: 10.1021/je00020a026. URL: https://pubs.acs.org/doi/10.1021/je00020a026.

[180] Boyi Chen et al. “Imaging Spatial Variations of Optical Bandgaps in Perovskite Solar Cells”. In: *Advanced Energy Materials* 9.7 (Dec. 2019), p. 1802790. ISSN: 16146840. DOI: 10.1002/aenm.201802790. URL: https://onlinelibrary.wiley.com/doi/abs/10.1002/aenm.201802790.

[181] Lukas Wagner et al. “Distinguishing crystallization stages and their influence on quantum efficiency during perovskite solar cell formation in real-time”. In: *Scientific Reports* 7 (2017), p. 14899. ISSN: 20452322. DOI: 10.1038/s41598-017-13855-6. URL: https://www.nature.com/articles/s41598-017-13855-6.

[182] Tze Bin Song et al. “Revealing the Dynamics of Hybrid Metal Halide Perovskite Formation via Multimodal In Situ Probes”. In: *Advanced Functional Materials* 30.6 (Dec. 2020), p. 1908337. ISSN: 16163028. DOI: 10.1002/adfm.201908337. URL: https://onlinelibrary.wiley.com/doi/abs/10.1002/adfm.201908337.

[183] Mihirsinh Chauhan et al. “Investigating two-step MAPbI3 thin film formation during spin coating by simultaneous: In situ absorption and photoluminescence spectroscopy”. In: *Journal of Materials Chemistry A* 8.10 (Mar. 2020), pp. 5086–5094. ISSN: 20507496. DOI: 10.1039/c9ta12409h. URL: https://pubs.rsc.org/en/content/articlehtml/2020/ta/c9ta12409h%20https://pubs.rsc.org/en/content/articlelanding/2020/ta/c9ta12409h.

[184] Michael Saliba et al. “How to Make over 20% Efficient Perovskite Solar Cells in Regular (n-i-p) and Inverted (p-i-n) Architectures”. In: *Chemistry of Materials* 30.13 (2018), pp. 4193–4201. ISSN: 15205002. DOI: 10.1021/acs.chemmater.8b00136. arXiv: arXiv:1408.1149. URL: https://pubs.acs.org/doi/abs/10.1021/acs.chemmater.8b00136.

[185] Jacobus J. van Franeker et al. “Monitoring Thermal Annealing of Perovskite Solar Cells with In Situ Photoluminescence”. In: *Advanced Energy Materials* 7.7 (2017), p. 1601822. ISSN: 16146832. DOI: 10.1002/aenm.201601822. URL: http://doi.wiley.com/10.1002/aenm.201601822.

[186] Alexander D. Taylor et al. “A general approach to high-efficiency perovskite solar cells by any antisolvent”. In: *Nature Communications* 12 (Dec. 2021), p. 1878. ISSN: 20411723. DOI: 10.1038/s41467-021-22049-8. arXiv: 2102.02050. URL: https://doi.org/10.1038/s41467-021-22049-8.

[187] Konstantin Schötz and Fabian Panzer. “Using in situ optical spectroscopy to elucidate film formation of metal halide perovskites”. In: *Journal of Physical Chemistry A* 125.11 (Mar. 2021), pp. 2209–2225. ISSN: 15205215. DOI: 10.1021/ACS.JPCA.0C10765/ASSET/IMAGES/

LARGE/JP0C10765_0016.JPEG. URL: https://pubs.acs.org/doi/full/10.1021/acs.jpca.0c10765.

[188] Michael Saliba et al. "Cesium-containing triple cation perovskite solar cells: Improved stability, reproducibility and high efficiency". In: *Energy and Environmental Science* 9.6 (2016), pp. 1989–1997. ISSN: 17545706. DOI: 10.1039/c5ee03874j. arXiv: arXiv:1408.1149. URL: https://pubs.rsc.org/en/content/articlelanding/2016/ee/c5ee03874j.

[189] Makhsud I. Saidaminov et al. "Multi-cation perovskites prevent carrier reflection from grain surfaces". In: *Nature Materials* 19.4 (Apr. 2020), pp. 412–418. ISSN: 14764660. DOI: 10.1038/s41563-019-0602-2. URL: https://doi.org/10.1038/s41563-019-0602-2.

[190] Yehao Deng et al. "Surfactant-controlled ink drying enables high-speed deposition of perovskite films for efficient photovoltaic modules". In: *Nature Energy* 3.7 (July 2018), pp. 560–566. ISSN: 20587546. DOI: 10.1038/s41560-018-0153-9. URL: https://www.nature.com/articles/s41560-018-0153-9.

[191] M. Edalatpour et al. "Managing water on heat transfer surfaces: A critical review of techniques to modify surface wettability for applications with condensation or evaporation". In: *Applied Energy* 222 (July 2018), pp. 967–992. ISSN: 0306-2619. DOI: 10.1016/J.APENERGY.2018.03.178. URL: https://www.sciencedirect.com/science/article/abs/pii/S0306261918305294.

[192] Nam Joong Jeon et al. "Solvent engineering for high-performance inorganic-organic hybrid perovskite solar cells". In: *Nature Materials* 13.9 (July 2014), pp. 897–903. ISSN: 14764660. DOI: 10.1038/nmat4014. URL: https://www.nature.com/articles/nmat4014.

[193] Jincheol Kim et al. "Overcoming the Challenges of Large-Area High-Efficiency Perovskite Solar Cells". In: *ACS Energy Letters* (2017), pp. 1978–1984. ISSN: 2380-8195. DOI: 10.1021/acsenergylett.7b00573. URL: http://pubs.acs.org/doi/abs/10.1021/acsenergylett.7b00573.

[194] Oscar Telschow et al. "Preserving the stoichiometry of triple-cation perovskites by carrier-gas-free antisolvent spraying". In: *Journal of Materials Chemistry A* (2022). ISSN: 2050-7496. DOI: 10.1039/D1TA10566C. arXiv: 2202.02375. URL: https://pubs.rsc.org/en/

content/articlehtml/2022/ta/d1ta10566c%20https://pubs.rsc.org/en/content/articlelanding/2022/ta/d1ta10566c.

[195] Kathie L. Dionisio et al. "Data Descriptor: The Chemical and Products Database, a resource for exposure-relevant data on chemicals in consumer products". In: *Scientific Data* 5 (July 2018), p. 180125. ISSN: 20524463. DOI: 10.1038/sdata.2018.125. URL: https://www.nature.com/articles/sdata2018125.

[196] *Ether effects - Anesthesia General*. URL: https://anesthesiageneral.com/ether-effects/ (visited on 12/01/2021).

[197] Shi Tian et al. "A facile green solvent engineering for up-scaling perovskite solar cell modules". In: *Solar Energy* 183.March (2019), pp. 386–391. ISSN: 0038092X. DOI: 10.1016/j.solener.2019.03.038. URL: https://doi.org/10.1016/j.solener.2019.03.038.

[198] Amran Al-Ashouri et al. "Conformal monolayer contacts with lossless interfaces for perovskite single junction and monolithic tandem solar cells". In: *Energy and Environmental Science* 12.11 (Nov. 2019), pp. 3356–3369. ISSN: 17545706. DOI: 10.1039/c9ee02268f. URL: https://pubs.rsc.org/en/content/articlelanding/2019/ee/c9ee02268f.

[199] Satyaprasad P. Senanayak et al. "A general approach for hysteresis-free, operationally stable metal halide perovskite field-effect transistors". In: *Science Advances* 6.15 (2020), eaaz4948. ISSN: 23752548. DOI: 10.1126/sciadv.aaz4948. URL: https://www.science.org/doi/abs/10.1126/sciadv.aaz4948.

[200] Byung-wook Park et al. "Understanding how excess lead iodide precursor improves halide perovskite solar cell performance". In: *Nature Communications* (2018), pp. 1–8. ISSN: 2041-1723. DOI: 10.1038/s41467-018-05583-w. URL: http://dx.doi.org/10.1038/s41467-018-05583-w.

[201] James E. Bishop et al. "Fully Spray-Coated Triple-Cation Perovskite Solar Cells". In: *Scientific Reports* 10 (Dec. 2020), p. 6610. ISSN: 20452322. DOI: 10.1038/s41598-020-63674-5. URL: https://www.nature.com/articles/s41598-020-63674-5.

[202] James E. Bishop et al. "Spray-cast multilayer perovskite solar cells with an active-area of 1.5 cm2". In: *Scientific Reports* 7.1 (2017), p. 7962. ISSN: 2045-2322. DOI: 10.1038/s41598-017-08642-2. URL: https://www.nature.com/articles/s41598-017-08642-2.

[203] Fabian Schackmar et al. “Perovskite Solar Cells with All-Inkjet-Printed Absorber and Charge Transport Layers”. In: *Advanced Materials Technologies* 6.2 (Feb. 2021), p. 2000271. ISSN: 2365-709X. DOI: 10.1002/admt.202000271. URL: https://onlinelibrary.wiley.com/doi/10.1002/admt.202000271.

[204] Thomas Vetter et al. “Modeling nucleation, growth, and ostwald ripening in crystallization processes: A comparison between population balance and kinetic rate equation”. In: *Crystal Growth and Design* 13.11 (Nov. 2013), pp. 4890–4905. ISSN: 15287483. DOI: 10.1021/CG4010714/SUPPL_FILE/CG4010714_SI_001.PDF. URL: https://pubs.acs.org/doi/abs/10.1021/cg4010714.

[205] Cedric Devos, Tom Van Gerven, and Simon Kuhn. “A Review of Experimental Methods for Nucleation Rate Determination in Large-Volume Batch and Microfluidic Crystallization”. In: *Crystal Growth and Design* 21.4 (Apr. 2021), pp. 2541–2565. ISSN: 15287505. DOI: 10.1021/acs.cgd.0c01606. URL: https://dx.doi.org/10.1021/acs.cgd.0c01606.

[206] Wilhelm Schabel et al. “Sorption and diffusion measurements in ternary polymer–solvent–solvent systems by means of a magnetic suspension balance—Experimental methods and correlations with a modified Flory–Huggins and free-volume theory”. In: *Chemical Engineering Science* 62.8 (Apr. 2007), pp. 2254–2266. ISSN: 00092509. DOI: 10.1016/j.ces.2006.12.062. URL: http://linkinghub.elsevier.com/retrieve/pii/S0009250907000310.

[207] David Siebel, Philip Scharfer, and Wilhelm Schabel. “Determination of Concentration-Dependent Diffusion Coefficients in Polymer-Solvent Systems: Analysis of Concentration Profiles Measured by Raman Spectroscopy during Single Drying Experiments Excluding Boundary Conditions and Phase Equilibrium”. In: *Macromolecules* 48.23 (2015), pp. 8608–8614. ISSN: 15205835. DOI: 10.1021/acs.macromol.5b02144. URL: https://pubs.acs.org/doi/10.1021/acs.macromol.5b02144.

[208] David Siebel, Wilhelm Schabel, and Philip Scharfer. “Diffusion in quaternary polymer solutions—Model development and validation”. In: *Progress in Organic Coatings* 110.December 2016 (2017), pp. 187–194. ISSN: 03009440. DOI: 10.1016/j.porgcoat.2017.05.002. URL: http://dx.doi.org/10.1016/j.porgcoat.2017.05.002.

[209] J. Krenn et al. “Drying of solvent-borne coatings with pre-loaded drying gas: Diffusion controlled skinning - Solvent-solvent-interaction”. In: *European Physical Journal: Special Topics*. Vol. 166. 1. Springer-Verlag, Feb. 2009, pp. 45–48. DOI: 10.1140/epjst/e2009-00876-0. URL: https://link.springer.com/article/10.1140/epjst/e2009-00876-0.

[210] Laura M. Herz. “Charge-Carrier Mobilities in Metal Halide Perovskites: Fundamental Mechanisms and Limits”. In: *ACS Energy Letters* 2.7 (July 2017), pp. 1539–1548. ISSN: 23808195. DOI: 10.1021/ACSENERGYLETT.7B00276/ASSET/IMAGES/LARGE/NZ-2017-00276E_0001.JPEG. URL: https://pubs.acs.org/doi/full/10.1021/acsenergylett.7b00276.

[211] Fengshuo Zu et al. “Constructing the Electronic Structure of CH 3 NH 3 PbI 3 and CH 3 NH 3 PbBr 3 Perovskite Thin Films from Single-Crystal Band Structure Measurements”. In: *Journal of Physical Chemistry Letters* 10.3 (Feb. 2019), pp. 601–609. ISSN: 19487185. DOI: 10.1021/ACS.JPCLETT.8B03728/ASSET/IMAGES/LARGE/JZ-2018-037283_0004.JPEG. URL: https://pubs.acs.org/doi/full/10.1021/acs.jpclett.8b03728.

[212] Min I. Lee et al. “First determination of the valence band dispersion of CH3NH3PbI3 hybrid organic–inorganic perovskite”. In: *Journal of Physics D: Applied Physics* 50.26 (June 2017), 26LT02. ISSN: 0022-3727. DOI: 10.1088/1361-6463/AA71E7. URL: https://iopscience.iop.org/article/10.1088/1361-6463/aa71e7%20https://iopscience.iop.org/article/10.1088/1361-6463/aa71e7/meta.

List of Figures

List of Tables

Part V.

Appendix

A1. Film diffusion limited drying

A1.1. Diffusion coefficients

In general, diffusion coefficients in solution thin films are not constant, but depend on the concentration. Therefore, a solution of Fick's law (Equation 6.1) is non-trivial and can only be accomplished numerically (details follow in section A1.5). We start our consideration with a two-solvent system. In the limiting case where the solute is very low concentrated, we can assume that the solution is merely a mixture of the two solvents. We can then use the equation of Tyn/Calus[22, Da 28] to calculate the diffusion coefficient of a very low concentration of solvent i in solvent j as :

$$\frac{D_{ij}^{\infty,i}}{\mathrm{cm^2/s}} = 8.93 \cdot 10^{-8} \left(\frac{v_j(T_{j,NBP})}{\mathrm{cm^3/mol}}\right)^{-1/3} \left(\frac{v_i(T_{i,NBP})}{\mathrm{cm^3/mol}}\right)^{1/6} \left(\frac{P_j}{P_i}\right)^{0.6} \left(\frac{\eta_j}{\mathrm{mPas}}\right)^{-1} \frac{T}{K}, \tag{A.1}$$

where v_i is the specific volume of the solvent $\left[\mathrm{m^3\,kmol^{-1}}\right]$, η_j [mPa s] is the dynamic viscosity and P_k is the respective parachor that can be calculated as

$$P_k = \frac{v_k(T_{k,NBP})}{\mathrm{cm^3/mol}} \left(\frac{\sigma_i}{\mathrm{mN/m}}\right), \tag{A.2}$$

where σ_i $\left[\mathrm{mN\,m^{-1}}\right]$ are the respective surface tensions (for typical values see section A4). For the self-diffusion coefficient we must have accordingly

$$\frac{D_{ii}^{\infty}}{\mathrm{cm^2/s}} = 8.93 \cdot 10^{-8} \left(\frac{v_i(T_{j,NBP})}{\mathrm{cm^3/mol}}\right)^{-1/6} \left(\frac{\eta_i}{\mathrm{mPas}}\right)^{-1} \frac{T}{K}. \tag{A.3}$$

With the Vignes correlation we can then calculate the concentration dependent diffusion of i within j as

$$D_{ij}^{V} = \left(D_{ij}^{V,i}\right)^{\tilde{x}_i} \left(D_{ji}^{V,j}\right)^{1-\tilde{x}_i} \left(\frac{\partial\left(\tilde{x}_i \gamma_i\right)}{\partial \tilde{x}_i}\right)_{T,p}. \tag{A.4}$$

It is clear that the formulas above provide only the starting point of our consideration for very high solvent loading. As stated in section 6.1.1, they yield the values $1.4 \cdot 10^{-9}\,\mathrm{m^2\,s^{-1}}$, $6.6 \cdot 10^{-10}\,\mathrm{m^2\,s^{-1}}$ and $1.0 \cdot 10^{-9}\,\mathrm{m^2\,s^{-1}}$ for DMF, DMSO and DMF:DMSO (volume ratio 4:1) respectively. These values can however only be an accurate at the beginning of the drying process. As mentioned earlier as well, Tan *et al.* reported that the diffusion coefficient of DMSO in a (nearly) dry MAPI perovskite film is $3.8 \cdot 10^{-26}\,\mathrm{m^2\,s^{-1}}$ at room temperature [137]. This implies that the diffusion coefficient must vary over a large range of orders of magnitude. As already described in section 6.1.1, it is however important to remember that the crystallization segregates naturally the crystalline material containing close to zero concentration of solvent from the solution and that the concentration of solvent in the remaining solution approaches equilibrium concentration until the end of the crystallization process. For the numerical solution of diffusion equations described in the following sections, we will contrarily assume that no such segregation happens but that the solid material is merely of a homogeneous, amorphous form such as a polymer and that the solvent concentration falls down to 0. The purpose is to test if, hypothesizing on these alternative assumptions, we could reproduce the drying dynamics observed in the triple cation perovskite precursor in section 6.1.7 and to test up to which Biot number (as an order of magnitude) the hypothesis of negligible concentration gradients approximates the numerical solution well enough.

To describe the concentration dependence of the diffusion coefficient, Schabel *et al.* used the relationship[206, 207] for the self-diffusion,

$$\frac{D_{ii}^{V}}{\mathrm{m^2/s}} = \exp\left(-\frac{A_i + B_i\left(X_i + X_j\right)}{1 + C_i\left(X_i + X_j\right)}\right), \tag{A.5}$$

where X_i is the solvent content [kg solvent / kg solute] of the respective solvent i. We note that only the self-diffusion is considered because inter-diffusion may cause instabilities in the solution of the diffusion equations as we will see in the next section. In the limiting cases, we must have

$$D_{ii}^{V} \xrightarrow{X_i + X_j \to \infty} D_{ii}^{\infty} = \exp\left(-\frac{B_i}{C_i}\right) \tag{A.6}$$

and

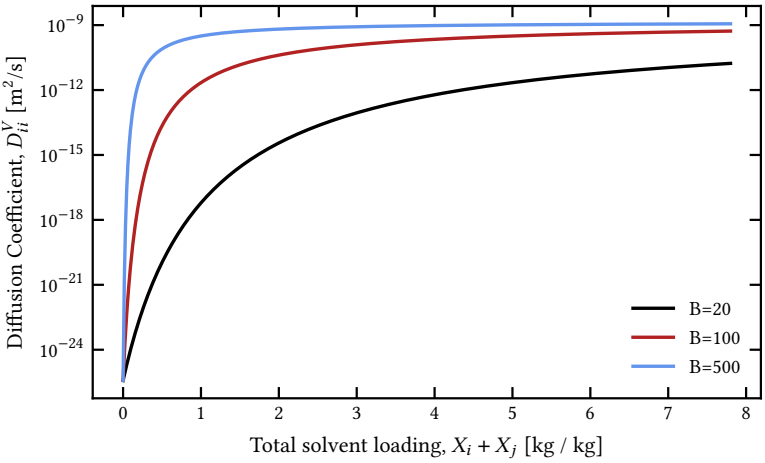

Figure A1.1.: Dependency of the diffusion coefficient according to Equation A.5 with varying constant B.

$$D_{ii}^{V} \xrightarrow{X_i+X_j \to 0} D_{ii}^{0} = \exp\left(-A_i\right) \tag{A.7}$$

where D_{ii}^{0} is the diffusion coefficient applying when nearly no solvent is left in the film. In conclusion, these conditions determine two of the three constants in Equation A.5. In the future, we will use B as a free parameter which describes the steepness of the concentration variation as visible in Figure A1.4. We will however also vary the diffusion at zero solvent content D_{ii}^{0}.

A1.2. Diffusion inside of a liquid film

In order to solve Fick's law as introduced in Equation 6.1, it is transformed to Fick's second law using the equation of continuity $\partial c/\partial t = -\mathrm{div}\, j$, which effectively reduces the problem to one solvable variable. For a one-solvent one-solute system, Fick's second law reads

$$\frac{\partial c_1^V}{\partial t} = \frac{\partial}{\partial z}\left(D_{11}^V \frac{\partial c_1^V}{\partial z}\right) \tag{A.8}$$

However, if we extend to a three component system featuring one solute and two solvents, we get the coupled PDE system

$$\begin{aligned}
\frac{\partial c_1^V}{\partial t} &= \frac{\partial}{\partial z}\left(D_{11}^V \frac{\partial c_1^V}{\partial z} + D_{12}^V \frac{\partial c_2^V}{\partial z}\right) = \frac{\partial}{\partial z}\left(-j_{11}^V - j_{12}^V\right) \equiv -\frac{\partial}{\partial z} j_1^V \\
\frac{\partial c_2^V}{\partial t} &= \frac{\partial}{\partial z}\left(D_{22}^V \frac{\partial c_2^V}{\partial z} + D_{21}^V \frac{\partial c_1^V}{\partial z}\right) = \frac{\partial}{\partial z}\left(-j_{22}^V - j_{21}^V\right) \equiv -\frac{\partial}{\partial z} j_2^V .
\end{aligned} \tag{A.9}$$

We note that in general, we have $D_{12}^V \neq D_{21}^V$, but that mass conservation requires

$$j_1^V \rho_{1,l} + j_2^V \rho_{2,l} + j_p^V \rho_p = 0 \tag{A.10}$$

everywhere. Furthermore, we always have

$$c_1^V / \rho_{1,l} + c_2^V / \rho_{2,l} + c_p^V / \rho_p = \phi_{1,l} + \phi_{2,l} + \phi_p = 1, \tag{A.11}$$

where $\phi_{i,l}$ and ϕ_p are the volume fractions of the solvents and the solute respectively. A similar equation can be written for the molar fractions of solvents and solute in the film as

$$\tilde{x}_1 + \tilde{x}_2 + \tilde{x}_\mathrm{p} = 1. \tag{A.12}$$

A1.3. Estimation of the film thickness for diffusion governed two-solvent drying

Even if there is no diffusion-limitation due to the solute, it is still possible that the drying dynamics are impacted by the limited solvent-solvent diffusion combined with the different evaporation rates of the solvents on the film surface. For estimating the equilibrium solvent ratio on the film surface, let us assume for simplicity that we are dealing with a pure mixture of solvent 1 with solvent 2.

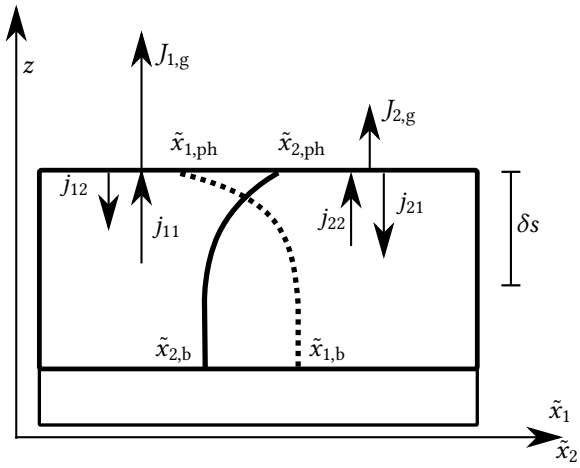

Figure A1.2.: Diffusion and evaporation fluxes in a drying DMF:DMSO film that is thick enough to exhibit a significant diffusion gradient of the two solvents just below the film surface.

Figure A1.2 depicts the solvent flux rates into the drying gas and inside of the film that must be considered in the equation system A1.4. For simplicity, we only consider the film surface and assume that all flux rates are in a steady state there. In this state, the concentration gradient reaches a distance δs into the film, while the molar solvent ratios in the bulk, $\tilde{x}_{1,b}$ and $\tilde{x}_{2,b}$, remain unchanged. Because of the steady state condition, the fluxes of the components 1 and 2 from the bulk to the surface (and back) must equal the respective evaporative fluxes, yielding

$$\frac{p_1^*}{RT}\beta_{1\mathrm{g}}\tilde{x}_{1,\mathrm{ph}} \approx D_{11}^V\bar{\tilde{\rho}}_{\mathrm{l}}\cdot\left(\tilde{x}_{1,\mathrm{ph}}-\tilde{x}_{1,\mathrm{b}}\right)/\delta s + D_{12}^V\bar{\tilde{\rho}}_{l}\cdot\left(\tilde{x}_{2,\mathrm{ph}}-\tilde{x}_{2,\mathrm{b}}\right)/\delta s \quad \text{(A.13)}$$

$$\frac{p_2^*}{RT}\beta_{2\mathrm{g}}\tilde{x}_{2,\mathrm{ph}} \approx D_{22}^V\bar{\tilde{\rho}}_{\mathrm{l}}\cdot\left(\tilde{x}_{2,\mathrm{ph}}-\tilde{x}_{2,\mathrm{b}}\right)/\delta s + D_{21}^V\bar{\tilde{\rho}}_{\mathrm{l}}\cdot\left(\tilde{x}_{1,\mathrm{ph}}-\tilde{x}_{1,\mathrm{b}}\right)/\delta s \quad \text{(A.14)}$$

where $\bar{\tilde{\rho}}_{\mathrm{l}}$ is the mean liquid density of the two solvents. We further use the mass balance equations $\tilde{x}_{1,\mathrm{ph}} + \tilde{x}_{2,\mathrm{ph}} = 1$ and $\tilde{x}_{1,\mathrm{b}} + \tilde{x}_{2,\mathrm{b}} = 1$ yielding

$$\frac{p_1^*}{RT}\beta_{1\mathrm{g}}\tilde{x}_{1,\mathrm{ph}} \approx \left(D_{11}^V - D_{12}^V\right)\bar{\tilde{\rho}}_{\mathrm{l}}\cdot\left(\tilde{x}_{1,\mathrm{ph}}-\tilde{x}_{1,\mathrm{b}}\right)/\delta s \quad \text{(A.15)}$$

$$\frac{p_2^*}{RT}\beta_{2\mathrm{g}}\left(1-\tilde{x}_{1,\mathrm{ph}}\right) \approx \left(D_{21}^V - D_{22}^V\right)\bar{\tilde{\rho}}_{l}\cdot\left(\tilde{x}_{1,\mathrm{ph}}-\tilde{x}_{1,\mathrm{b}}\right)/\delta s \quad \text{(A.16)}$$

Solving for $\tilde{x}_{1,\mathrm{ph}}$ yields the astonishingly simple estimation

$$\tilde{x}_{1,\mathrm{ph}} = \frac{K'_{12}}{K'_{12}+1} \quad \text{(A.17)}$$

with $K'_{12} = K_{12}(D_{11}^V - D_{12}^V)/(D_{21}^V - D_{22}^V)$ and $K_{12} = p_1^*\beta_{1g}/p_2^*\beta_{2g}$ is defined as in section 6.1.5. Let us now consider the example of a 4:1 DMF:DMSO mixture as used in the TCP precursor solution. Using the empirical formulas for the diffusion coefficient in this mixture (as detailed in section A1.1), we get roughly $K'_{12} = 0.14$ and thus $\tilde{x}_{\mathrm{DMF,ph}} = 0.12$. This ratio differs from the initial ratio significantly, which was to be expected due to the higher vapour pressure of the DMF as compared to the DMSO. We can now calculate the necessary film thickness

$$\delta s \approx \frac{D_{11}^V - D_{12}^V}{\beta_{i,\mathrm{g}}}\bar{\tilde{\rho}}_{l}\frac{RT}{p_1^*}\frac{\tilde{x}_{1,\mathrm{ph}}-\tilde{x}_{1,b}}{\tilde{x}_{1,\mathrm{ph}}}. \quad \text{(A.18)}$$

When inserting typical numbers, we get $\delta s = -1.4\cdot 10^5\Delta D/\beta_{i,\mathrm{g}}$. As a conclusion, for a typical value of $\Delta D = 4\cdot 10^{-10}$ m and an extreme $\beta_{ig} = 1\,\mathrm{m\,s^{-1}}$, we get $\delta s \approx 60\,\mu$m, which is about one order of magnitude above the typical film thicknesses of 5 μm. With the estimation $\Delta D \approx 0.1 D_{ii}^V$ we find that, as long as the $\mathrm{Bi}_d < 10^4$ or $\mathrm{Bi}_d^{\mathrm{an.}} < 1$, the formation of a substantial DMF:DMSO concentration gradient is neglectable.

A1.4. Evaporation at the liquid-gas phase boundary

If we want to solve Fick's law for the concentrations c_i^V (or the molar ratios $\tilde{x}_i$) for a drying thin-film, we face a challenge with the boundary conditions. As the film shrinks upon the evaporation of solvent, we have a moving boundary of the film surface. Although there are mathematical methods to deal with such cases [135], a particularly elegant way is to use coordinates, ζ, which are relative to the current film thickness as introduced by Saure *et al.*[134]. The coordinate transformation reads

$$\frac{\partial \zeta}{\partial z} \equiv \frac{V_p}{V(t)} = \frac{d_p}{d(t)} = \Phi_p(t) \tag{A.19}$$

where $V(t)$ is the total volume of the film changing over time and V_p is the (constant) volume of the solute in the solution (see Figure A1.3 for a schematic how the transformation works).

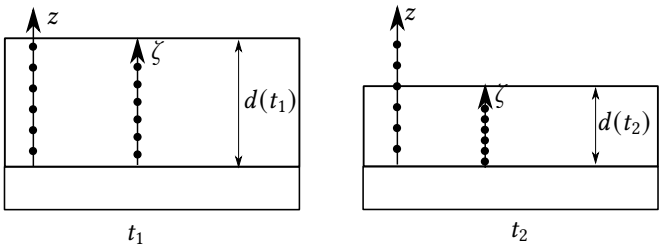

Figure A1.3.: Schematic of the difference between Cartesian coordinates, z, and Polymer coordinates, ζ, with time as the film decreases in thickness upon drying.

Accordingly we define the locally varying concentrations in this reference frame (called in literature as polymer reference frame) as

$$c_i^P \equiv \frac{\delta m_i}{\delta V_p} = \frac{\delta m_i}{\delta m_p} \cdot \frac{\delta m_p}{\delta V_p} \equiv X_i \cdot \rho_p \tag{A.20}$$

where $X_i = c_i^V / c_p^V$ is the so-called solvent content [kg solvent / kg solute]. With these coordinates, one can write Fick's second law as

$$\frac{\partial X_i}{\partial t} = \frac{\partial}{\partial \zeta}\left(D_{ii}^P \frac{\partial X_i}{\partial \zeta}\right) \tag{A.21}$$

It follows that $D_{ii}^P = \Phi_p^2 D_{ii}^V$ for the diffusivity as well as for the solvent fluxes $j_i^P = j_i^V/\Phi_p$. For the extension to two solvents, we follow a similar approach as Siebel *et al.* [208]. We start by using Equation A.12 to calculate

$$c_i^V = \frac{X_i}{X_1/\rho_1 + X_2/\rho_2 + 1/\rho_p} \equiv \frac{X_i}{A_{12}} \tag{A.22}$$

This equation can be seen as a direct transformation from the solvent contents, X_1 and X_2 to the volume concentrations, c_1^V and c_2^V. Differentiating this equation, we obtain

$$\frac{\partial c_i^V}{\partial \zeta} = \frac{\frac{\partial X_i}{\partial \zeta}}{A_{12}} - \frac{X_i}{A_{12}^2}\left(\frac{1}{\rho_1}\frac{\partial X_1}{\partial \zeta} + \frac{1}{\rho_2}\frac{\partial X_2}{\partial \zeta}\right) \tag{A.23}$$

We can now write

$$-j_i^V = D_{ii}^V \phi_p \frac{\partial c_i^V}{\partial \zeta} + D_{ij}^V \phi_p \frac{\partial c_j^V}{\partial \zeta} \equiv B_{ii}\frac{\partial X_i}{\partial \zeta} + B_{ij}\frac{\partial X_j}{\partial \zeta} \tag{A.24}$$

with

$$B_{ii} = D_{ii}^V \frac{\phi_p}{A_{12}}\left(1 - \frac{X_i}{\rho_i A_{12}}\right) - D_{ij}^V \frac{\phi_p X_j}{\rho_i A_{12}^2} \tag{A.25}$$

$$B_{ij} = D_{ij}^V \frac{\phi_p}{A_{12}}\left(1 - \frac{X_j}{\rho_j A_{12}}\right) - D_{ii}^V \frac{\phi_p X_i}{\rho_j A_{12}^2} \tag{A.26}$$

The flux in polymer coordinates is then calculated with $j_i^p = j_i^V - X_i j_P^V$ from [208] using Equation A.10 as

$$j_i^p = j_i^V + X_i\left(j_1^V \frac{\rho_p}{\rho_1} + j_2^V \frac{\rho_p}{\rho_2}\right) \equiv -D_{ii}^P \rho_p \frac{\partial X_i}{\partial \zeta} - D_{ij}^P \rho_p \frac{\partial X_j}{\partial \zeta} \tag{A.27}$$

where

$$D_{ii}^{P} = \frac{B_{ii}}{\rho_p}\left(1 + X_i\frac{\rho_p}{\rho_i}\right) + \frac{B_{ji}}{\rho_j}X_i \tag{A.28}$$

$$D_{ij}^{P} = \frac{B_{ij}}{\rho_p}\left(1 + X_i\frac{\rho_p}{\rho_i}\right) + \frac{B_{jj}}{\rho_j}X_i \tag{A.29}$$

Finally, we can reformulate the equations in polymer coordinates as

$$\frac{\partial X_1}{\partial t} = \frac{\partial}{\partial \zeta}\left(D_{11}^{P}\frac{\partial X_1}{\partial \zeta} + D_{12}^{P}\frac{\partial X_2}{\partial \zeta}\right) \tag{A.30}$$

$$\frac{\partial X_2}{\partial t} = \frac{\partial}{\partial \zeta}\left(D_{22}^{P}\frac{\partial X_2}{\partial \zeta} + D_{21}^{P}\frac{\partial X_1}{\partial \zeta}\right) \tag{A.31}$$

In this system of reference, the boundary conditions are defined on the film surface as

$$j_i^{P}\big|_{\zeta=\zeta_{\max}} = -D_{ii}^{p}\rho_p\frac{\partial X_i}{\partial \zeta}\bigg|_{\zeta=\zeta_{\max}} - D_{ij}^{p}\rho_p\frac{\partial X_j}{\partial \zeta}\bigg|_{\zeta=\zeta_{\max}} = \frac{dm_i}{dt} \tag{A.32}$$

Just as introduced in section 6.1.5 we have in the gas phase

$$\frac{dm_i}{dt} = -\beta_{ig}\rho_{i,g}\left(y_{i,\mathrm{ph}} - y_{i,\infty}\right) \approx -\beta_{ig}\frac{\rho_{i,g}p_i^{*}}{\bar{\rho}_f p}c_{i,ph}^{V} \tag{A.33}$$

where $\bar{\rho}_f$ is the average density of the film on the surface and we assume an unloaded carrier gas $y_{i,\infty} = 0$. On the bottom surface of the film we have no evaporation and thus

$$j_i^{P}\big|_{\zeta=0} = -D_i^{p}\frac{1}{\rho_p}\frac{\partial X_i}{\partial \zeta}\bigg|_{\zeta=0} = 0. \tag{A.34}$$

These equations are not yet solvable. However, with Equation A.22, we can translate $c_{i,\mathrm{ph}}^{V}$ into $X_1(\zeta_{\max})$ and $X_2(\zeta_{\max})$ respectively and solve the PDE system only using the solvent contents.

A1.5. Solving diffusion equations with the numerical toolkit 'FEniCs'

FEniCs is a versatile and open source solver for partial differential equations. It is based on DOLFIN, a C++/Python library for data structures and algorithms for solving finite element problems. For solving Equations A.30-A.31, they have to be transferred to their weak form:

$$\int_0^{\zeta_{max}} \frac{\Delta X_1}{\Delta t} v_1 d\zeta + \int_0^{\zeta_{max}} D_{11}^P \frac{\partial X_1}{\partial \zeta}\frac{\partial v_1}{\partial \zeta} d\zeta + \int_0^{\zeta_{max}} D_{12}^P \frac{\partial X_2}{\partial \zeta}\frac{\partial v_1}{\partial \zeta} d\zeta + \int_0^{\zeta_{max}} \frac{\Delta X_2}{\Delta t} v_2 d\zeta + \int_0^{\zeta_{max}} D_{22}^P \frac{\partial X_2}{\partial \zeta}\frac{\partial v_2}{\partial \zeta} d\zeta + \int_0^{\zeta_{max}} D_{21}^P \frac{\partial X_1}{\partial \zeta}\frac{\partial v_1}{\partial \zeta} d\zeta + v_1 \frac{dm_1}{dt}\Big|_0^{\zeta_{max}} + v_2 \frac{dm_2}{dt}\Big|_0^{\zeta_{max}} = 0 \qquad \text{(A.35)}$$

using test functions v_1 and v_2 that vanish on $\zeta = 0$ per definition.

We note that the system above can be solved in FEniCs for situations, where the diffusion gradients in the film are sufficiently small. However, in the case where large concentration gradients are present, the inter-diffusion terms become increasingly problematic. The reason is most probably that they easily lead to a dependency $\partial^2 X_1/\partial t^2 = D_{12}^P D_{21}^P \partial^2 X_1/\partial \zeta^2$ giving rise to so called-diffusion waves. When these waves occur, they can grow very fast in amplitude and, in this case, violate mass conservation if $X_1 > 0$ and $X_2 > 0$ is not enforced properly. Although the formalism derived herein should theoretically not violate this condition, in practice, the solvers diverge due to negative values of X_1 and X_2, which can probably be attributed to the limited machine precision. If, for example, X_1 takes a value only sightly smaller than 0, it might create a self-amplifying diffusion wave.

The instabilities detailed above are the reason, why in the following only self-diffusion will be considered, which is consistent with most of the literature on the topic ([207, 206, 208]). In other words, we assume $D_{12}^P = D_{21}^P = 0$, effectively decoupling the diffusion of the first solvent from the second solvent. This decoupling is plausible in a situation where low solvent contents

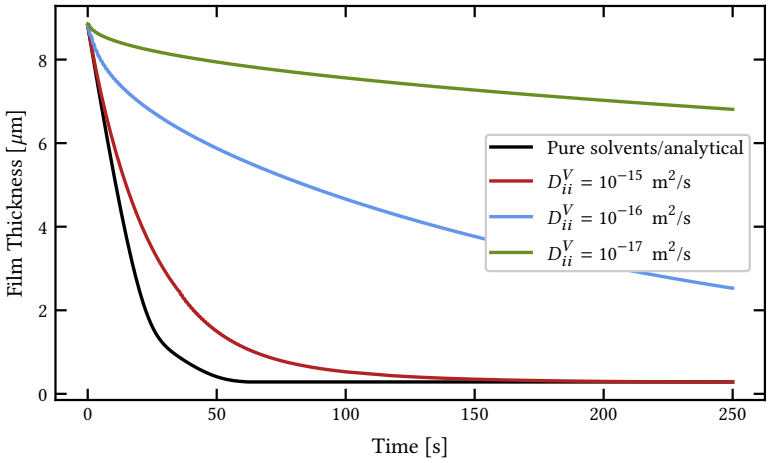

Figure A1.4.: Film thickness evolution for different diffusion coefficients and a wet film thickness of 8.5 μm and $\alpha = 240\,\mathrm{W\,m^{-2}K^{-1}}$ at $T = 5°\mathrm{C}$.

are present in the film, because the probability of different solvent molecules 'to meet' is very low in this scenario. Therefore, only the diffusion of each individual solvent molecule in the solute material is of importance. Fortunately, this assumption is in good accordance with the assumed exponential concentration dependency of the diffusion coefficient explained in the last section.

At first, let us however investigate a situation with a constant diffusion coefficient. The simulation results are depicted in Figure A1.4. We find that at diffusion coefficients on the order of $10^{-14}\,\mathrm{m^2\,s^{-1}}$, there is no significant difference between the analytical model derived in section 6.1.5 and the numerical calculations (black curve). Considering the initial film thickness of 8.5 μm, this corresponds to $\mathrm{Bi}_d = 10^8$ or $\mathrm{Bi}_d^{\mathrm{an.}} = 10^4$.

If the order of magnitude of the diffusion coefficients (we assumed equal values for D_{11}^V and D_{22}^V) is decreased, a significant deviation of the drying dynamics can be seen. Instead of the typical shape of first DMF and then DMSO evaporation, the curves follow a smoother exponential decay of the film thickness, which becomes slower with decreasing diffusion coefficients.

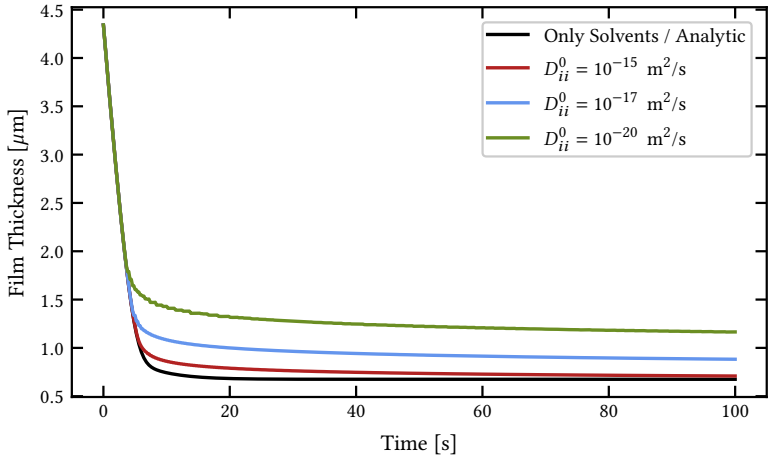

Figure A1.5.: Film thickness evolution for different diffusion coefficients at zero solvent loading D_{ii}^0 using the exponential decrease of the diffusion coefficient according to equation A.5 and a wet film thickness of 4.5 μm and $\alpha = 42\,\mathrm{W\,m^{-2}K^{-1}}$ at $T = 40°\mathrm{C}$. The parameters were chosen to match with Figure 6.8 for better comparison.

In a second step, we use the exponential decrease of the diffusion coefficient according to Equation A.5 with a constant $B = 100$ with different final values of the diffusion coefficient D_{ii}^0 (see Figure A1.5). We find consistently, that for $D_{ii}^0 < 10^{-14}\,\mathrm{m^2\,s^{-1}}$ (that is $\mathrm{Bi}_{8\mu\mathrm{m}} < 10^8$), the solution is indifferent from the analytical model, hinting to the same order of magnitude of the corresponding Biot number. Only when the diffusion coefficients take smaller values, a deviation is visible starting from a certain point in time. This is consistent with the well-studied observation that the decreasing diffusion coefficient on the film surface might create a capping layer acting as a diffusion barrier for the remaining solvent[209]. The more the diffusion coefficient decreases, the earlier this layer forms and the thicker it is. Interestingly however, the drying rate of such a layer does not show a strong dependence on the final diffusion coefficient. We note that this model prediction contradicts the data observed in the actual measurement of a drying triple cation perovskite film described in section 6.1.7, because drying rate in the film limited drying is much smaller than the one measured by interferometry.

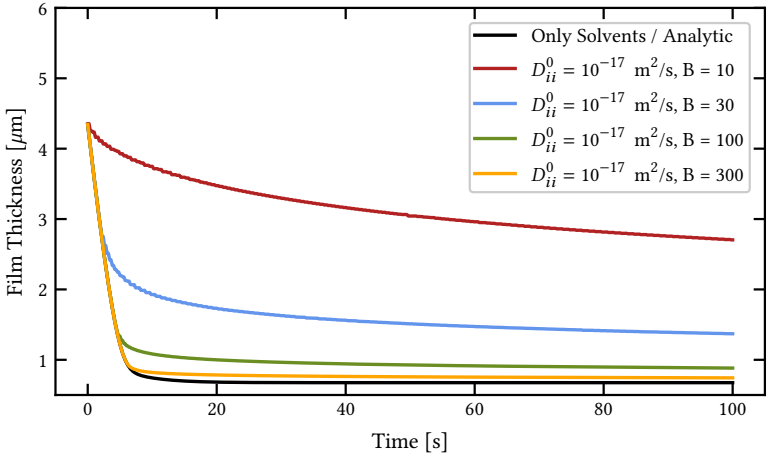

Figure A1.6.: Film thickness evolution for different diffusion coefficients at different constants B using the exponential decrease of the diffusion coefficient according to equation A.5 and a wet film thickness of 4.5 μm and $\alpha = 42\,\mathrm{W\,m^{-2}K^{-1}}$ at $T = 40°\mathrm{C}$.

In a last step, we want to investigate the effect of different coefficients, B, in the exponential dependence of the diffusion coefficient in Equation A.5. Again, we observe that, at high enough B, the solution will asymptotically approach the analytical solution. Lower values in B can change the slope of the drying of the capping layer, however also the onset of the forming of such layer at the same time. This is again not compatible with the data measured by interferometry discussed in section 6.1.7 because the onset of the decelerated drying regime is quite low, however the drying rate is too high to be reproducible with a corresponding value of B. In conclusions, our observations show that the deviation from the analytic drying model of the triple cation perovskite precursor is most-probably not caused by a capping layer, strongly favouring the original hypothesis, which is a reduction of the solvent activity.

A2. Photographs of setups

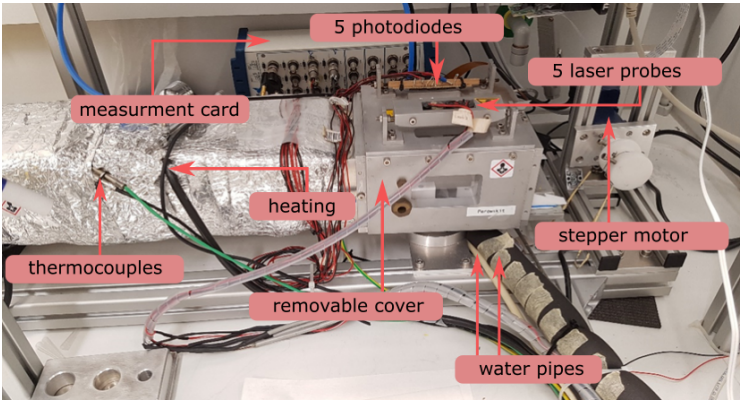

(a) Closed setup for processing and *in situ* interferometry measurements

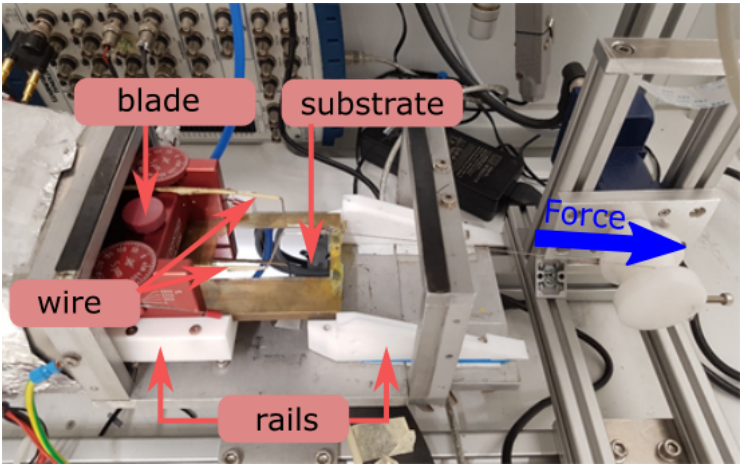

(b) Open setup for initiating the coating process

Figure A2.7.: Photographs of flow channel setup used in all three main publications[19, 20, 21]. Reproduced with permission from [19]

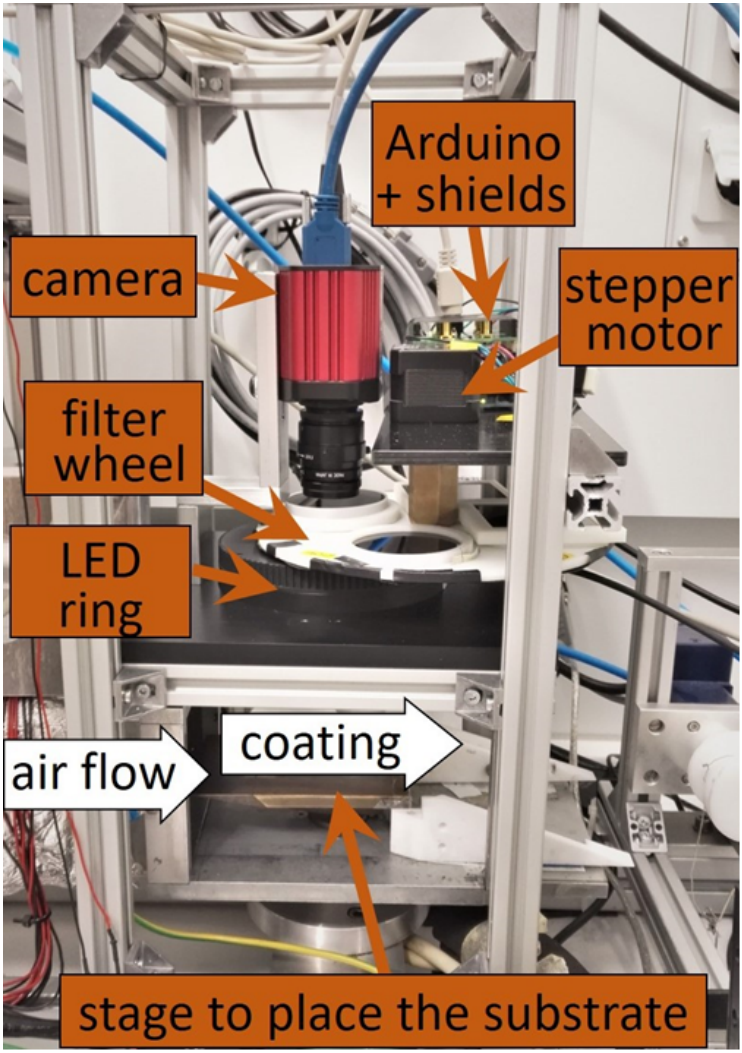

Figure A2.8.: In Situ Multichannel imaging setup [20]. Graphic created in cooperation with Felix Laufer.

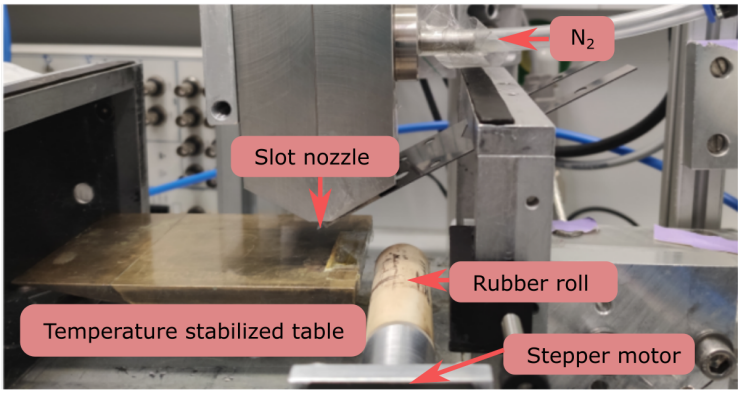

Figure A2.9.: Roll coating apparatus to simulate large-scale perovskite solution printing and drying [21].

A3. Abbreviations

The following abbreviations are used within this work:

Abbrev.	Full name
PV	Photovoltaic(s)
LCOE	Levelized cost of electricity
PCE	Power conversion efficiency
m^2	Square metres
cm^2	Square centimetres
MAPI	Methylammonium lead iodide
TCP	Triple cation perovskite
DCP	Double cation perovskite
DMF	N,N-Dimethylformamide
NMP	N-Methyl-2-pyrrolidone
2-Me	2-Methoxyethanol
DMSO	Dimethylsulfoxide
EGBE	ethylene glycol monobutyl ether
CO^2	carbon dioxide
N_2	nitrogen
IPCC	Intergovernmental Panel on Climate Change
IEA	International Energy Agency
MAI	Methylammonium iodide
FAI	Formimadinium iodide
MABr	Methylammonium bromide
MACl	Methylammonium chloride
$CH(NH_2)_2^+$	Formimadinium cation
Cs^+	Caesium cation
CsI	Caesium iodide
Pb^{2+}	lead cation
Sn^{2+}	tin cation
Ge^{2+}	germanium cation
I^-	iodine anion
Br^-	bromide anion
Cl^-	chlorine anion
PbI_2	lead iodide
$PbBr_2$	lead bromide
$PbCl_2$	lead chloride
$Pb(CH_3CO)_2 \cdot 3H_2O$	lead acetate trihydrate

Abbrev.	Full name
TiO_2	titanium oxide
SnO_2	tin oxide
H_2O	water
Au	gold
Alpha-LP	L-α-Lecithin
RFC	reasons for concern
SSP	socio-economic pathway
GDP	gross domestic product
BECCS	bio energy with carbon capture and storage
CCS	carbon capture and storage
$CH_3NH_3^+$	Methylammonium cation
CIGS	Cadmium indium gallium selenide
CdTe	Cadmium telluride
Si	mono-crystalline silicon
MW	Megawatt
GW	Gigawatt
UV	ultra violet
IEC	International Electrotechnical Commission

Abbrev.	Full name
CMR	Carcinogenic, mutagenic and reprotoxic
JV	Current density-voltage
UV-VIS	ultra violet-visible
PL	photoluminescence
EL	electroluminescence
EQE	external quantum efficiency
DDAB	Didodecyldimethylammoniumbromide
HDTMAB	Hexadecyltrimethylammoniumbromide
NREL	National Renewable Energy Laboratory
PSC	perovskite solar cell
TCO	transparent conductive oxide
IQE	internal quantum efficiency
ETL	electron transport layer
HTL	hole transport layer
i	intrinsic
n	n-doped
p	p-doped
AM1.5	1.5 times the atmospheric mass

Abbrev.	Full name
FF	Fill Factor
rpm	revolutions per minute
ITO	indium tin oxide
SEM	Scanning electron microscopy
AFM	Atomic force microscopy

Abbrev.	Full name
WLI	Whitelight Interferometry
TLC	thermochromic liquid crystal
FWHM	full width half max.
IMI	In situ multichannel imaging
1D,2D	one-dimensional, two-dimensional

A4. Physical quantities and their typical order of magnitude

Since this work combines different fields of engineering duplicate naming of variables is inevitable. We will therefore introduce these variable spaces here separately, giving a short introduction each time. The column 'typical value' should not be seen as an exact calculation, but rather an estimation of the order of magnitude of physical quantities in a typical example.

We will start with semiconductors and optoelectronics. We assume the example of an external field of $1\,\mathrm{V}\,\mu\mathrm{m}^{-1}$ to a perovskite thin film, which is the typical bias used for perovskite solar cells. The values for m^*, $\mu_{i,n}$ and $n_{i,n}$ are taken from literature[210, 211, 212] (the absolute values of energy levels are undefined sine they depend on the zero reference energy.)

Symbols used in solid state physics and PV research:

Symbol	Typical value	Unit	Physical Quantity
m^*	$0.3 \cdot 511$	$\mathrm{keV}\,\mathrm{c}_0^{-2}$	Effective mass (tensor or average)

Symbol	Typical value	Unit	Physical Quantity
$\varepsilon_n(\vec{k})$	undef.	eV	Dispersion relation (energy over momentum) of band n
$\vec{k}$	1	Å^{-1}	Wave number ($\propto$ momentum)
$\vec{v}_{i,n}$	10^3	m s^{-1}	Velocity of species i in band n
$\vec{a}_{i,n}$	10^{17}	m s^{-2}	Acceleration of species i in band n
$\vec{F}$	10^4	eV cm^{-1}	External force
$\vec{E}$	10^4	V cm^{-1}	External electrical field
$n_{i,n}$	10^5	cm^{-3}	Density of species i in band n
z_i	1,-1	–	Polarity of species i
$\tau_{i,n}$	10^{-15}	s	Time constant of free drift of species i in band n
$\mu_{i,n}$	10	$\text{cm}^2\,\text{V}^{-1}\text{s}^{-1}$	Charge carrier mobility of species i in band n
$\sigma_{i,n}$	10^{-13}	$1\,\Omega^{-1}\text{cm}^{-1}$	Charge carrier conductivity of species i in band n
$j_{i,n,\text{ind}}$	10^{-9}	A cm^{-2}	Respective drift or diffusive mono-polar charge carrier density of species i in band n
$j_{\text{bi},n,\text{ind}}$	$2 \cdot 10^{-9}$	A cm^{-2}	Respective drift or diffusive bi-polar charge carrier density of species i in band n
$D_{i,n}$	10^{-1}	$\text{cm}^2\,\text{s}^{-1}$	Diffusion coefficient of species i in band n
F	undef.	eV	Gibbs free energy
E	undef.	eV	Potential and kinetic energy
S	undef.	eV K^{-1}	(Gibbs) Entropy

Symbol	Typical value	Unit	Physical Quantity
T	273 - 400	K	Absolute temperature
$f_e(\varepsilon_e)$	0-1	–	Fermi-Dirac distribution
$D_e(\varepsilon_e)$	–	$cm^{-3}eV^{-1}$	Density of states
N_C	10^{18}	cm^{-3}	Effective density of states in conduction band
N_V	10^{18}	cm^{-3}	Effective density of states in valence band
n_e^0	10^5	cm^{-3}	Density of electrons in the dark
n_h^0	10^5	cm^{-3}	Density of holes in the dark
n_i^0	10^5	cm^{-3}	Intrinsic charge carrier density in the dark
n_e	10^{15}	cm^{-3}	Density of electrons under illumination
n_h	10^{15}	cm^{-3}	Density of holes under illumination
n_i	10^{15}	cm^{-3}	Intrinsic charge carrier density under illumination
ε_C	undef.	eV	Position of conduction band edge
ε_F	undef.	eV	Position of Fermi level (=electrochemical potential)
ε_V	undef.	eV	Position of valence band edge
ε_G	1.58	eV	Bandgap
ε_{FC}	undef.	eV	Quasi Fermi level of the electrons under illumination
ε_{VC}	undef.	eV	Quasi Fermi level of the holes under illumination
$\Delta\eta$	1.32	eV	Quasi Fermi level of the holes under illumination

Symbol	Typical value	Unit	Physical Quantity
$j_\gamma(x)$	$3 \cdot 10^{21}$	$\mathrm{m^{-2}s^{-1}}$	Flux of photons per unit area at position x
$dj_{\gamma,\mathrm{em}}(E)/dE$	10^{18}	$\mathrm{m^{-2}s^{-1}eV^{-1}}$	Flux of photons emitted at energy $E = h\nu$ per energy
$\alpha(E)$	$10^{-11} - 10^{5}$	$\mathrm{cm^{-1}}$	Absorption coefficient at photon energy E
$a(E)$	$0 - 1$	–	Absorptance at photon energy E
$r(E)$	$0 - 1$	–	Reflectivity at photon energy E
ν	$400 - 800$	THz	Frequency of photon(s)
Ω	4π	–	solid angle in radiant
$\phi_{\mathrm{BB}}(E)$	10^{19}	$\mathrm{m^{-2}s^{-1}eV^{-1}}$	Planck black body spectrum
$\tau(n)$	$10^{-3} - 10^{-9}$	s	Lifetime of charge carriers depending on the their density, n
IQE	$0 - 100\%$	–	Internal quantum efficiency
EQE	$0 - 100\%$	–	External quantum efficiency
G	10^{17}	$\mathrm{cm^{-3}s^{-1}}$	Excited charge carrier generation rate
R	10^{17}	$\mathrm{cm^{-3}s^{-1}}$	Excited charge carrier recombination rate
J_{Q}	$-30 - 30$	$\mathrm{mA\,cm^{-2}}$	Resulting Charge carrier density flowing over a device
V	$-2 - 2$	V	Voltage apparent at the device terminals
J_{S}	10^{-20}	$\mathrm{mA\,cm^{-2}}$	Reverse saturation current density
J_{SC}	$0 - 30$	$\mathrm{mA\,cm^{-2}}$	Short circuit current density
V_{OC}	$0 - 2$	V	Open circuit voltage

Symbol	Typical value	Unit	Physical Quantity
V_{MPP}	$0-2$	V	Maximum power point voltage
J_{MPP}	$0-30$	$\mathrm{mA\,cm^{-2}}$	Maximum power point current density
FF	$0-90\%$	–	Fill Factor
PCE	$0-30\%$	–	Power conversion efficiency
P_{in}	100	$\mathrm{mW\,cm^{-2}}$	Total irradiation power
η_{OC}	$0-1$	–	Outcoupling efficiency
I_{ind}	10^{-3}	A	Total current with respective function
R_{S}	$0-1$	Ω	Series resistance
R_{P}	$100-1$	kΩ	Parallel (or shunt) resistance
$C_{\mathrm{i,acc}}$	–	F	Capacitance

Symbols used in coating and drying engineering:

For coating and chemical engineering, we consider the drying process of a TCP solution film of final thickness 0.8 μm that is dried at 40°C in a laminar air stream with constant heat transfer coefficient $\alpha = 20\,\mathrm{W\,m^{-2}K^{-1}}$ (see sections 5.1 for details).

Symbol	Typical range	Unit	Physical Quantity
h_∞, d_{wet}	4.8	μm	Thickness of liquid film after blade coating
h_0	100	μm	Height of blade over substrate
$d(t)$	$4.8 - 0.8$	μm	Film thickness as a function of time
d_{p}	0.8	μm	Thickness of dry perovskite film
$\tilde{\rho}_{\mathrm{p}}$	6	$\mathrm{mmol\,cm^{-3}}$	Molar density of perovskite
ρ_{p}	4	$\mathrm{g\,cm^{-3}}$	Mass density of perovskite
$\tilde{\rho}_{i,\mathrm{l}}$	13, 14	$\mathrm{mmol\,cm^{-3}}$	Molar density of liquid solvent (DMF,DMSO)
$\rho_{i,\mathrm{l}}$	0.95, 1.1	$\mathrm{g\,cm^{-3}}$	Mass density of of liquid solvent (DMF,DMSO)
$\tilde{m}_{\mathrm{p}}$	1.3	M ($\mathrm{mmol\,ml^{-1}}$)	Molar mass of perovskite per added solvent ($\neq$ concentration)
$\tilde{j}_{i,\mathrm{p}}$	$50 - 300$	$\mathrm{mmol\,cm^{-2}s^{-1}}$	Molar flux of solvent molecules in the solute
$\tilde{D}_i^V$	10^{-9} (10^{-26})	$\mathrm{m^2\,s^{-1}}$	Diffusion coefficient of solvent in solute
$\tilde{c}_i^V$	$8.6 - 0, 2.3 - 0$	$\mathrm{mmol\,cm^{-3}}$	Molar concentration of solvent in film (DMF,DMSO)
$\tilde{c}_{\mathrm{p}}^V$	$6 - 1$	$\mathrm{mmol\,cm^{-3}}$	Molar concentration of solute in film

Symbol	Typical range	Unit	Physical Quantity
c_i^V	$0.6 - 0.2$	$\mathrm{g\,cm^{-3}}$	Mass concentration of solute in film
c_p^V	$4 - 0, 0.7 - 0$	$\mathrm{g\,cm^{-3}}$	mass concentration of solvent in film (DMF,DMSO)
$\tilde{D}_\mathrm{ii}^V$	10^{-9} (10^{-26})	$\mathrm{m^2\,s^{-1}}$	Self diffusion of solvent i in film
$\tilde{D}_\mathrm{ij}^V$	10^{-9} (10^{-26})	$\mathrm{m^2\,s^{-1}}$	Inter diffusion of solvent i into solvent j in film
$\tilde{x}_{i,\mathrm{ph}}$	0.72, 0.19	$\mathrm{mol\,mol^{-1}}$	Molar ratio of gaseous solvent (DMF,DMSO) in the gas phase at the phase boundary
$\tilde{y}_{i,\mathrm{ph}}$	$9.6 \cdot 10^{-4}, 4.2 \cdot 10^{-5}$	$\mathrm{mol\,mol^{-1}}$	Molar ratio of gaseous solvent (DMF,DMSO) in the gas phase at the phase boundary
$\tilde{c}_{i,\mathrm{ph}}$	$9.3 - 0, 2.3 - 0$	$\mathrm{mol\,mol^{-1}}$	Molar ratio of liquid solvent (DMF,DMSO) in the liquid phase at the phase boundary
$\phi_{p,i}$	1	–	Fugacity coefficient
p	10^5	Pa	Atmospheric pressure
p_i^*	1340, 220	Pa	Vapour pressure of the solvent (DMF,DMSO at 40°C)
γ_i	1, 0.045	–	Activity coefficient (at begin of drying and for intermediate phase with DMSO)
j_{ig}	$3.8 \cdot 10^{-4} - 0, 1.6 \cdot 10^{-5} - 0$	$\mathrm{mmol\,cm^{-2}s^{-1}}$	Flux of gaseous solvent (DMF,DMSO)
δ_{ig}	$1.1 \cdot 10^{-5}$	$\mathrm{m^2\,s^{-1}}$	Diffusion coefficient of gaseous solvent in the gas phase
$\tilde{\rho}_g$	0.4	$\mathrm{mmol\,cm^{-3}}$	Molar density of the gas phase

Symbol	Typical range	Unit	Physical Quantity
$\tilde{\beta}_{ig}$	0.01 (up to 1)	$\mathrm{m\,s^{-1}}$	Molar density of the gas phase
ΔS_C	1	mm	Concentration boundary layer thickness
J_{ig}	$3.8 \cdot 10^{-4} - 0, 1.6 \cdot 10^{-5} - 0$	$\mathrm{mmol\,cm^{-2}s^{-1}}$	Flux of solvent molecules away from film surface
T	313	K	Absolute temperature
α	20	$\mathrm{W\,m^{-2}K^{-1}}$	Heat transfer coefficient
$\dot{q}$	2	$\mathrm{W\,cm^{-2}s^{-1}}$	Heat flux out of film surface for $\Delta T = 100\,\mathrm{K}$
u_0	2	$\mathrm{m\,s^{-1}}$	Laminar air flow velocity/ nozzle output velocity
Re_x	1160	–	Local Reynolds-Number for $x = 1\,\mathrm{cm}$
ν	$1.72 \cdot 10^{-5}$	$\mathrm{m^2\,s^{-1}}$	Kinematic viscosity
η	$2.2 \cdot 10^{-5}$	Pa s	Dynamic viscosity
Sc	2	–	Schmidt number
Pr	1.1	–	Prantl number
Sh_x	9	–	Local Sherwood-Number for $x = 1\,\mathrm{cm}$
Nu_x	7.4	–	Local Nusselt-Number
k	0.027	$\mathrm{W\,m^{-1}K^{-1}}$	Thermal conductivity
Bi_d	$1 - 1000\,(4 \cdot 10^{19})$	–	Biot number for $d = 10\,\mu\mathrm{m}$, $D_i^V = 10^{-9}\,\mathrm{m^2\,s^{-1}}$ and different β_{ig} ($D_i^V = 10^{-27}\,\mathrm{m^2\,s^{-1}}$)
D	0.6	mm	Hydrodynamic width of slot nozzle
B	0.3	mm	Physical width of slot nozzle
θ	90°	rad	Mounting angle of slot nozzle

Symbol	Typical range	Unit	Physical Quantity
$N_i/\delta A, n_\mathrm{i}$	$1.1 \cdot 10^{-3}$,$4.2 \cdot 10^{-3}$	$\mathrm{mmol\,cm^{-2}}$	Number of molecules per area (DMSO,DMF)
$N_\mathrm{p}/\delta A, n_\mathrm{p}$	$4.8 \cdot 10^{-4}$	$\mathrm{mmol\,cm^{-2}}$	Number of perovskite unit cells per area
K_{12}	0.16	–	Ratio between mass transfer coefficients and partial pressures of solvents DMF and DMSO at 40°C
χ^2	–	–	Sum of squared residuals
P_i	229, 203	$\mathrm{cm^3 g^{0.25}\ s^{-0.5}\ mol^{-1}}$	Parachor (DMF,DMSO)
v_i	77, 71	$\mathrm{cm^3\ mol^{-1}}$	Specific volume of solvent i
σ_i	78, 67	$\mathrm{mN\,m^{-1}}$	Surface tension
Φ_p	0.16	–	Volume ratio of the perovskite
$\delta m_i, \delta V_i$	–	$\mathrm{g, cm^3}$	Mass or volume element occupied by a species i
X_i	0.86, 0.29	$\mathrm{g\,g^{-1}}$	Solvent content of solvent i
c_i^p	$3.44 - 0, 1.2 - 0$	$\mathrm{g\,cm^{-3}}$	Concentration in polymer coordinates
j_i^V	$0 - 0.02$	$\mathrm{mmol\,cm^{-2}s^{-1}}$	Solvent flux in Cartesian coordinates
j_i^p	$0 - 0.13$	$\mathrm{mmol\,cm^{-2}s^{-1}}$	Solvent flux in polymer coordinates
D_{ij}^p	$10^{-11}(10^{-28})$	$\mathrm{m^2\ s^{-1}}$	Diffusion constant in polymer coordinates

Symbols used in crystallization research: For the crystallization models, we continue partially with the example of the perovskite precursor drying. However, since we did not measure most of the physical quantities, for example the nucleation and crystal growth rates, and only made a qualitative analysis of crystallization we will simply use typical order of magnitude estimations as provided by Markov [24].

Symbol	Typical range	Unit	Physical Quantity
c_{p}^{V}	$0.7 - 4$	$\mathrm{g\,cm^{-3}}$	Solute mass concentration
$\tilde{c}_{\mathrm{p}}^{V}$	$1 - 6$	$\mathrm{mmol\,cm^{-3}}$	Molar solute concentration
$c_{\mathrm{p,0}}^{V}$	> 0.7	$\mathrm{g\,cm^{-3}}$	Equilibrium (solute mass) concentration
$c_{\mathrm{p,c}}^{V}$	> 0.7	$\mathrm{g\,cm^{-3}}$	Critical (solute mass) concentration
$\Delta\mu$	10	eV	Supersaturation (as chemical potential difference)
σ	$10^{-2} - 10^{2}$	–	Supersaturation
f_i	10^{3}	$\mathrm{erg\,cm^{-2}}$	Surface energy density of crystal facet i
$\bar{\gamma}$	10^{3}	$\mathrm{erg\,cm^{-2}}$	Mean surface energy density of all crystal facets
v_p	10^{-22}	$\mathrm{cm^{3}}$	Volume of a perovskite unit cell
r^*	100	Å	Critical radius of nucleus
n^*	10^{4}	–	Particles in a nucleus
ΔG^*	1	eV	Critical free energy
V^*	10^{-18}	$\mathrm{cm^{3}}$	Volume of nucleus forming on surface
V_0	10^{-18}	$\mathrm{cm^{3}}$	Volume of nucleus forming in bulk
J_0	10^{-3}	$\mathrm{cm^{-3}s^{-1}}$	Nucleation rate
ω^*	–	$\mathrm{s^{-1}}$	Frequency of attachment of particles

Symbol	Typical range	Unit	Physical Quantity
Γ	10^{-2}	–	Zeldovich factor
N^*	$1 - 100$	cm^{-3}	Equilibrium concentration of critical nuclei
ν	10^{13}	s^{-1}	Frequency factor
λ	10^{-8}	cm	Mean free path
ΔU	0.1	eV	Energy barrier of desolvation
R_{face}	10^{-8}	$cm\,s^{-1}$	Rate of step advance of a growing crystal facet
Q_0	1	$mmol\,cm^{-3}s^{-1}$	Molar concentration change as induced by drying (drying rate 0.5 $\mu m\,s^{-1}$)
p_T	–	cm^{-3}	Number of nuclei per volume
$D(n_i)$	–	cm	Diameter of n_i existing nuclei with approx. the same size

Symbols used when describing the measurement methods:

Symbol	Typical range	Unit	Physical Quantity
$\Delta(d, n_f)$	10	μm	Difference in optical path at film thickness, d, and refractive index, n_f
λ	660	nm	Laser wavelength
α	24	°	Impingement angle of incident laser
I_i	–	Cnts	Integrated light intensity predicted by optical model
λ_0	790	nm	Centre emission wavelength of photoluminescence
FWHM	30	nm	Full width half maximum of photoluminescence

Symbol	Typical range	Unit	Physical Quantity
$R_{\text{det}}(\lambda)$	$0-1$	–	Reflectance of detector
T_{lens}	$0-1$	–	Transmittance of lenses
$T_{i,\text{filters}}(\lambda)$	$0-1$	–	Transmittance of filter(s) at position i
$c_{p,w}$	2	$\text{J g}^{-1}\text{K}^{-1}$	Heat capacity
λ_w	0.2	$\text{W m}^{-1}\text{K}^{-1}$	Heat conductivity
ρ_w	1.2	g cm^{-3}	Mass density
$T_w(t)$	$293-353$	K	Temperature of plate
T_0	353	K	Temperature before heat transfer
T_∞	293	K	Temperature after heat transfer
h_s	$1-5$	cm	Height of spray gun over sample
Δp	$1-5$	bar	Over pressure present at spray gun

Used physical constants:

Symbol	value	Name
$\hbar$	$6.58 \cdot 10^{-16}$ eV s	Reduced Planck's constant
h	$4.13 \cdot 10^{-15}$ eV s	Planck's constant
c_0	$3.0 \cdot 10^{8}$ m s^{-1}	Speed of light in vacuum
k	$8.62 \cdot 10^{-5}$ eV K^{-1}	Boltzmann constant
R	8.31 J $\text{K}^{-1}\text{mol}^{-1}$	Ideal Gas constant
N_A	$6.02 \cdot 10^{23}$ mol^{-1}	Avogadro constant

A5. Acknowledgements

This work would not have been possible without the continuous assistance and support by excellent colleagues, good friends and family members.

At first, I would like to express my gratitude to T.T. Prof. Dr. Ulrich W. Paetzold, whose expertise was crucial for the realization of this work. His continuous factual as well as emotional support and feedback was invaluable, especially in hard times at the beginning of this work. Special thanks for seeing the potential in me for accomplishing tasks that I did not consider myself capable of before. I would like to acknowledge Prof. Dr. Bryce Richards for his continuous feedback from the viewpoint of a silicon photovoltaics expert, his detailed language and factual corrections and support throughout my journey. In particular, I would also like to thank Dr. Ian A. Howard for believing in my ideas to advance *in situ* characterization and providing me with excellent expertise on spectroscopy. Additionally, I would like to thank Dr. Philip Scharfer and Prof. Dr. Wilhelm Schabel for introducing me to the field of drying technology and providing me with the necessary tools and knowledge for investigating drying on a scientific level. To close this paragraph, I want to mention the support of Prof. Dr. Ulrich Lemmer who was constantly working in the background to keep the institute running during times of the pandemic.

Second, I want to thank the Perovskite Taskforce at KIT as a whole. Without the continuous cooperation, technical maintenance tasks, conceptual discussions and sharing of knowledge and experience this thesis would probably lack most its core results. In particular, I want to thank Felix Laufer and Fabian Schackmar, with whom I worked closely together during the continuing development of the IMI technique and also co-supervised many student theses. I would also like to thank Dr. Ihteaz M. Hossain, Dr. Jonas A. Schwenzer and Dr. Somayeh (Sara) Moghadamzadeh for their meticulous work of optimizing many of the solution processes used herein. Beyond that, I want to thank Julie Roger, Isabel Allegro, Diana Rueda Delgado and Thomas Feeney for countless (more or less) productive coffee breaks giving conceptual and emotional support for pursuing this work and many more unforgettable events.

Third, I want to thank the thin-film technology (TFT) group lead by Prof. Dr. Schabel for giving me space, resources and knowledge to make the transition from my Physics background to Chemical Engineering. Thanks for letting

me participate in a lot of professional events, even though I was part of another group, as well. In particular, Dr. Tobias Börnhorst and Jonas Mohacsi merit my gratitude for introducing me to the field of industrial-scale drying, diffusion-evaporation models and heat transfer measurements. Furthermore, I want to thank Dr. Benjamin Schmidt-Hansberg, from whom I inherited the drying channel setup and who helped a lot with the transition of the necessary knowledge for operation.

Fourth, a large group of people contributed to this work directly or indirectly who are not (any more) part of the above mentioned taskforce or the TFT group. To begin with, I am grateful to all the students I had the honour the supervise during my work. These are in chronological order: Teresa Dagenbach, Waldemar Mehlmann, Louis Kressibuch, Katrin Schmitt, Aynur Demir, Virajini Palakonda, Felix Laufer, Kristina Geistert, Alexander Diercks, Malte Haupt, Vashu Kamboj, Huang Minh Pham, Meriç Arslan, Ryan Schork, Nico Lüdke and Roja Thatichetty Sudhakumar. In particular, I am thankful to Nico Lüdke, Huang Minh Pham and Meriç Arslan for committing a lot of energy and thought process into the dynamic coating and drying line and performing an extensive range of coating experiments. I also want to express special thanks to Dr. Johannes Küffner from "Zentrum für Sonnenenergie- und Wasserstoff-Forschung" (ZSW) in Stuttgart for numerous fruitful discussions and cooperation. Other people who helped me to accomplish the hard-earned results are the employees at the Light Technology Institute (LTI), the Micro-Technology institute (IMT) and the Institute of Thermal Process Engineering (TVT). Thanks to Felix Geiselhöringer for his expertise and practical help on electronics, Astrid Henne, Claudia Holeisen, Margit Morvay and Nicole Klöfer for countless explanations and corrections of university administration processes, Richard Thelen for precise explanations, access and practical guidelines of profilometric measurement techniques, Christian Kayser for his clean room maintenance and the workshop staff of LTI and TVT for realising and correcting many hardware parts.

At last, I want to acknowledge the people who supported me in my private life on the bumpy road to finishing this work with their love and compassion. To mention only some: Jan Müller, Franziska Runkel, Jonas Rausch, Andreas Ternes, Ute Thielmann and, especially for the final two years, Flore Colonna and her family. Above all, I am grateful for the continuous support of my father, Thomas Ternes, who never left my side even in hard times and was always ready to give me tips about scientific work, and my mother, Annette Ternes, who never ceased gifting me stability and spiritual support despite

traversing testing times herself. It is in commemoration of her that I am joyfully celebrating the accomplishment of finishing this work.

A6. Funding

This work could not have been conducted without numerous funding organizations, who provided the financial support (mainly to T.T. Prof. Dr. Ulrich W. Paetzold) and merit my gratitude. These are:

- Federal Ministry of Education and Research (PRINTPERO, funding code: 03SF0557A),
- Initiating and Networking funding of the Helmholtz Association (HYIG of U.W.P. (funding code: VH-NG1148), the Helmholtz Energy Materials Foundry (HEMF),)
- Karlsruhe School of Optics & Photonics (KSOP).
- Research Field Energy—Program Materials and Technologies for the Energy Transition—Topic 1 Photovoltaics)

Schriften des Instituts für Mikrostrukturtechnik
am Karlsruher Institut für Technologie (KIT)

ISSN 1869-5183

Band 1 Georg Obermaier
Research-to-Business Beziehungen: Technologietransfer durch Kommunikation von Werten (Barrieren, Erfolgsfaktoren und Strategien).
ISBN 978-3-86644-448-5

Band 2 Thomas Grund
Entwicklung von Kunststoff-Mikroventilen im Batch-Verfahren.
ISBN 978-3-86644-496-6

Band 3 Sven Schüle
Modular adaptive mikrooptische Systeme in Kombination mit Mikroaktoren.
ISBN 978-3-86644-529-1

Band 4 Markus Simon
Röntgenlinsen mit großer Apertur.
ISBN 978-3-86644-530-7

Band 5 K. Phillip Schierjott
Miniaturisierte Kapillarelektrophorese zur kontinuierlichen Überwachung von Kationen und Anionen in Prozessströmen.
ISBN 978-3-86644-523-9

Band 6 Stephanie Kißling
Chemische und elektrochemische Methoden zur Oberflächenbearbeitung von galvanogeformten Nickel-Mikrostrukturen.
ISBN 978-3-86644-548-2

Die Bände sind unter www.ksp.kit.edu als PDF frei verfügbar oder als Druckausgabe zu bestellen.

Band 7 Friederike J. Gruhl
Oberflächenmodifikation von Surface Acoustic Wave (SAW) Biosensoren für biomedizinische Anwendungen.
ISBN 978-3-86644-543-7

Band 8 Laura Zimmermann
Dreidimensional nanostrukturierte und superhydrophobe mikrofluidische Systeme zur Tröpfchengenerierung und -handhabung.
ISBN 978-3-86644-634-2

Band 9 Martina Reinhardt
Funktionalisierte, polymere Mikrostrukturen für die dreidimensionale Zellkultur.
ISBN 978-3-86644-616-8

Band 10 Mauno Schelb
Integrierte Sensoren mit photonischen Kristallen auf Polymerbasis.
ISBN 978-3-86644-813-1

Band 11 Daniel Auernhammer
Integrierte Lagesensorik für ein adaptives mikrooptisches Ablenksystem.
ISBN 978-3-86644-829-2

Band 12 Nils Z. Danckwardt
Pumpfreier Magnetpartikeltransport in einem Mikroreaktionssystem: Konzeption, Simulation und Machbarkeitsnachweis.
ISBN 978-3-86644-846-9

Band 13 Alexander Kolew
Heißprägen von Verbundfolien für mikrofluidische Anwendungen.
ISBN 978-3-86644-888-9

Band 14 Marko Brammer
Modulare Optoelektronische Mikrofluidische Backplane.
ISBN 978-3-86644-920-6

Band 15 Christiane Neumann
Entwicklung einer Plattform zur individuellen Ansteuerung von Mikroventilen und Aktoren auf der Grundlage eines Phasenüberganges zum Einsatz in der Mikrofluidik.
ISBN 978-3-86644-975-6

Band 16 Julian Hartbaum
Magnetisches Nanoaktorsystem.
ISBN 978-3-86644-981-7

Band 17 Johannes Kenntner
Herstellung von Gitterstrukturen mit Aspektverhältnis 100 für die Phasenkontrastbildgebung in einem Talbot-Interferometer.
ISBN 978-3-7315-0016-2

Band 18 Kristina Kreppenhofer
Modular Biomicrofluidics - Mikrofluidikchips im Baukastensystem für Anwendungen aus der Zellbiologie.
ISBN 978-3-7315-0036-0

Band 19 Ansgar Waldbaur
Entwicklung eines maskenlosen Fotolithographiesystems zum Einsatz im Rapid Prototyping in der Mikrofluidik und zur gezielten Oberflächenfunktionalisierung.
ISBN 978-3-7315-0119-0

Band 20 Christof Megnin
Formgedächtnis-Mikroventile für eine fluidische Plattform.
ISBN 978-3-7315-0121-3

Band 21 Srinivasa Reddy Yeduru
Development of Microactuators Based on the Magnetic Shape Memory Effect.
ISBN 978-3-7315-0125-1

Band 22 Michael Röhrig
Fabrication and Analysis of Bio-Inspired Smart Surfaces.
ISBN 978-3-7315-0163-3

Band 23 Taleieh Rajabi
Entwicklung eines mikrofluidischen Zweikammer-Chipsystems mit integrierter Sensorik für die Anwendung in der Tumorforschung.
ISBN 978-3-7315-0220-3

Band 24 Frieder Märkle
Laserbasierte Verfahren zur Herstellung hochdichter Peptidarrays.
ISBN 978-3-7315-0222-7

Band 25 Tobias Meier
Magnetoresistive and Thermoresistive Scanning Probe Microscopy with Applications in Micro- and Nanotechnology.
ISBN 978-3-7315-0253-1

Band 26 Felix Marschall
Entwicklung eines Röntgenmikroskops für Photonenenergien von 15 keV bis 30 keV.
ISBN 978-3-7315-0263-0

Band 27 Leonardo Pires Carneiro
Development of an Electrochemical Biosensor Platform and a Suitable Low-Impedance Surface Modification Strategy.
ISBN 978-3-7315-0272-2

Band 28 Sebastian Mathias Schillo
Prozessentwicklung für die Automatisierung der Herstellung und Anwendung von hochdichten Peptidmicroarrays.
ISBN 978-3-7315-0274-6

Band 29 Nicole E. Steidle
Micro- and Nanostructured Microfluidic Devices for Localized Protein Immobilization and Other Biomedical Applications.
ISBN 978-3-7315-0297-5

Band 30 Jochen Heneka
Prozessentwicklung eines industrietauglichen Verfahrens zur Fertigung von vereinzelten LIGA-Mikrobauteilen.
ISBN 978-3-7315-0326-2

Band 31 Seoung-Eun Kim
Konzeption und prototypische Fertigung einer nicht-invasiven mikrofluidischen Plattform für die Elektrophysiologie (NIMEP) zur Zellenanlyse.
ISBN 978-3-7315-0378-1

Band 32 Elisabeth Wilhelm
Entwicklung eines mikrofluidischen Brailledisplays.
ISBN 978-3-7315-0385-9

Band 33 Viktor Pinneker
Entwicklung miniaturisierter Aktorsysteme basierend auf magnetischen Formgedächtnislegierungen.
ISBN 978-3-7315-0500-6

Band 34 Ali Caglar Özen
Novel MRI Technologies for Structural and Functional Imaging of Tissues with Ultra-short T_2 Values.
ISBN 978-3-7315-0657-7

Band 35 Anne Bäcker
Veränderliche 3D Zellgerüstträger auf Cryogelbasis zur Kultivierung von Prostatakarzinomzellen.
ISBN 978-3-7315-0676-8

Band 36 Frieder Johannes Koch
X-ray optics made by X-ray lithography: Process optimization and quality control.
ISBN 978-3-7315-0679-9

Band 37 Tobias Jörg Schröter
Vergrößerung des Sehfeldes der Röntgen-Phasenkontrast-Bildgebung für die klinische Anwendung.
ISBN 978-3-7315-0731-4

Band 38 Felix Vüllers
Bioinspired Superhydrophobic Nano- and Microstructured Surfaces for Drag Reduction and Optoelectronics.
ISBN 978-3-7315-0816-8

Band 39 Frederik Kotz
Entwicklung neuer Materialien für die additive Fertigung und das Rapid Prototyping von Glas und Polymethylmethacrylat.
ISBN 978-3-7315-0835-9

Band 40 Michael Oldenburg
Photon upconversion heterostructures made from surface-anchored metal-organic frameworks.
ISBN 978-3-7315-0863-2

Band 41 Elisa Kornemann
Entwicklung einer Röntgenzoomlinse.
ISBN 978-3-7315-0885-4

Band 42 Hossein Davoodi
NMR micro-detectors tailored for multinuclear and electrochemistry lab-on-a-chip applications.
ISBN 978-3-7315-1118-2

Band 43 Florian Brüderlin
Advanced Elastocaloric Cooling Devices Based on Shape Memory Alloy Films.
ISBN 978-3-7315-1065-9

Band 44 Andreas Striegel
Werkzeug- und Prozessentwicklung des Roll-to-Roll-Hochdurchsatzverfahrens zur kontinuierlichen, großflächigen Mikrostrukturierung.
ISBN 978-3-7315-1106-9

Band 45 Marlene Kopf
Langzeitstabilität der Innendrücke von Kavernen benachbarter MEMS-Sensoren auf Siliziumbasis.
ISBN 978-3-7315-1121-2

Band 46 Simon Ternes
In Situ Characterization and Modelling of Drying Dynamics for Scalable Printing of Hybrid Perovskite Photovoltaics.
ISBN 978-3-7315-1255-4

SIMON TERNES

In Situ Characterization and Modelling of Drying Dynamics for Scalable Printing of Hybrid Perovskite Photovoltaics

Hybrid perovskite photovoltaics could play a vital role in future's renewable energy production, promising cost-effective industrial fabrication by high-throughput solution printing methods such as slot-die coating, spray coating or inkjet printing. Although remarkable power conversion efficiencies were demonstrated in small-scale perovskite solar cells (about 1 cm^2), there is a substantial performance drop when fabricating large area perovskite photovoltaics (> 100 cm^2). A major reason for these difficulties is the complexity of controlling the perovskite formation on larger scales. In detail, this formation process involves crystal growth and nucleation as well as solvent evaporation – all of which are closely entangled. The present work sheds light onto this complex entanglement via quantitative analysis of the drying dynamics of blade coated perovskite solution films in well-defined laminar and slot-jet air flows. The main results are a quantitative model of perovskite drying dynamics and a novel in situ photoluminescence and reflectance imaging technique. With these tools at hand, process parameters for large-scale drying machines can be predicted and the quality of the forming perovskite thin-films can be assessed early on. The effectiveness of the methodology is demonstrated by investigating perovskite solar cell performance on small sample areas for different scalable fabrication methods. This work paves the way toward feedback-controlled printing of large-scale perovskite photovoltaics relying on the combination of perovskite drying models and continuous quality monitoring of the evolving thin-film morphology.

ISSN 1869-5183
ISBN 978-3-7315-1255-4

Gedruckt auf FSC-zertifiziertem Papier